Observations of the inner regions of winds around young T Tauri type stars

Vanessa Agra-Amboage

To cite this version:

Vanessa Agra-Amboage. Observations of the inner regions of winds around young T Tauri type stars. Astrophysics [astro-ph]. Université Joseph-Fourier - Grenoble I, 2009. English. NNT : . tel-00474379

HAL Id: tel-00474379

https://theses.hal.science/tel-00474379v1

Submitted on 19 Apr 2010

HAL is a multi-disciplinary open access archive for the deposit and dissemination of scientific research documents, whether they are published or not. The documents may come from teaching and research institutions in France or abroad, or from public or private research centers.

L'archive ouverte pluridisciplinaire **HAL**, est destinée au dépôt et à la diffusion de documents scientifiques de niveau recherche, publiés ou non, émanant des établissements d'enseignement et de recherche français ou étrangers, des laboratoires publics ou privés.

UNIVERSITÉ GRENOBLE I – JOSEPH-FOURIER
ÉCOLE DOCTORALE DE PHYSIQUE

THESIS by

Vanessa AGRA AMBOAGE

to obtain the degree of Doctor of science in the Université Joseph-Fourier

Speciality : ASTROPHYSICS – PHYSICS & DILUTED ENVIRONMENTS

Observations of the inner regions of winds around young T Tauri type stars

Public presentation on the 9^{th} of October 2009
in front of the jury composed by

Ms.	Francesca BACCIOTTI	Referee
Ms.	Sylvie CABRIT	Thesis co-supervisor
Ms.	Cecilia CECCARELLI	Jury president
Ms.	Catherine DOUGADOS	Thesis supervisor
Mr.	Thierry MONTMERLE	Thesis supervisor
Ms.	Brunella NISINI	Referee

Laboratoire d'AstrOphysique de Grenoble
UMR-5571 (OSUG/UJF/CNRS), BP 53, F-38041 Grenoble Cedex 9

Strong in the rain
Strong in the wind
Strong against the summer heat and snow
He is healthy and robust
Unselfish
He never loses his temper
Nor the quiet smile on his lips

(...)

That is the sort of person
I want to be

雨ニモマケズ
風ニモマケズ
雪ニモ夏ノ暑サニモマケヌ
丈夫ナカラダヲモチ
慾ハナク
決シテ瞋ラズ
イツモシズカニワラッテイル

ソウイウモノニ
ワタシハナリタイ

Kenji Miyazawa

Acknowledgments

This part is the last one I have written, but it is as important as the rest of my thesis because I would have never been able to achieve this work without the help and the support of all the people who was around me during all these years. For me, this period was not only a working experience, but a very enriching moment of my life and every person I met has contributed to it. Specially, I would like to thank the people who most participated in the good-ending of this project. I also thank each one of my friends, for being always there for me when I needed them.

I have written the acknowledgments in three different languages depending on the people I want to thank. The use of these three languages was also one of the main characteristics on my day to day life, something that I have loved to do and that I hope to keep doing in the future.

I start thanking the members of the jury for taking the time to read my manuscript. Specially I would like to thank the two referees, Dr. Brunella Nisini and Dr. Francesca Bacciotti, for the detailed reports they did and the suggestions for improving the quality of the manuscript. I would also like to thank Gareth and Emma for helping me with English; without their corrections, the manuscript would be very difficult to understand!.

Un remerciement très spécial pour mes directeurs Catherine Dougados, Sylvie Cabrit et Thierry Montmerle. Catherine et Sylvie m'ont donné non seulement l'opportunité de faire ma thèse en France, mais aussi d'intégrer le réseau du JETSET. Cette opportunité a été une très grande expérience, d'un point de vue scientifique, mais aussi personnel. On dit souvent qu'avoir plusieurs directeurs de thèse est très dur pour l'étudiant, c'est sûr que cela n'est pas facile et demande de l'énergie et du temps, mais dans mon cas, ils se sont coordonnés très bien et tous les trois m'ont beaucoup apporté. J'ai énormément appris et j'ai beaucoup apprécié les discussions avec Catherine et Sylvie qui ont toujours été très intéresssantes (même si elles ont été longues parfois...!). Les deux, avec ses différences, m'ont transmit une connaissance dans le domaine de la formation stellaire très complète, qui va de l'observation aux modèles et que je n'aurais pas pu imaginé avoir lorsque j'ai commencé. Elles m'ont montré aussi la vision critique et minutieuse nécessaire à un chercheur pour faire son travail, tout en gardant de l'enthousisme pour le travail que l'on fait. Elles ont toujours été là pour me pousser à aller encore plus loin et elles ont réussi à faire que je sois très fière de mon travail et des résultats obtenus dans cette thèse. Thierry a toujours été un soutien pour moi et j'ai beaucoup apprécié nos discussions, pas seulement scientifiques et toujours passionnantes.

Je voulais aussi remercier l'ensemble du Laboratoire d'Astrophysique de Grenoble pour le magnifique accueil que j'ai eu de leur part, prolongé d'une attention continue pendant ces quatre années, aussi bien les secrétaires, que le service informatique et l'ensemble de chercheurs.

Le soutien de mes amis tout au long de ces quatre années et surtout dans les derniers mois de rédaction, a été fondamental pour m'aider à réussir ce travail. Ils ont été près de moi pour me motiver, m'encourager et pour me faire rire dans les moments où j'en avais le plus besoin. Je voudrais remercier tout particulièrement mes trois collègues de bureau préférés : Celine, Evelyne et Eric. C'est ce dernier qui a le plus souffert de ma fin de thèse, merci ! Par ailleurs, j'ai eu la chance de partager les souffrances et les joies d'une thèse avec Myriam, Oscar, Philippe, Rémy, Tim, Johan, Morgan, Nico C, Nico T, Romain, et Benoît. On a aussi partagé beaucoup de bons moments : le lac, "le TEK", le laser-game... d'innombrables cafés et thés sur la terrasse... et aussi pas mal de bières, partagées en amitié et bonne humeur. Un grand merci à Myriam, Nico et Tim pour leur soutien inconditionnel. Aussi, outre les étudiants, ont fait mon intégration au laboratoire plus facile : Alex, Claire, Estelle, Guillermo et Jérôme. Je voudrais également remercier trois personnes qui sont arrivées à la fin de ma thèse, mais qui eux aussi, m'ont beaucoup soutenu et aidé : Olga, Rémi et Susana. Je voulais remercier Manue pour son soutien et pour sa participation à la preparation du pot de thèse, un super pot !

No me olvido de mi familia y amigos en España, que aunque lejos, siempre me han apoyado y respondido cuando he necesitado su ayuda. Un agradecimiento particular para mi hermana Ana que me ayudó mucho cuando llegué a Francia y siguió ayudándome después siempre que lo necesité. Mis amigas desde de la infancia: Ana Belén, Belén, Carolina y Fani. Mis amigos de la facultad: Alberto, Ana Belén F., Andrea, David, Raquel... y los "astro-locos" de La Laguna, junto a los cuales empecé a sumergirme en esto de la astrofísica y que a pesar de la distancia siempre han estado muy presentes: Alejandra, Ale, Antonio, Fran, Jorge, Juan, Isaias (que no es "astro-loco", pero como si lo fuera), Miguel, Paola, Raquel, Rebe, Sergio, Susi... Tantos y tantos, que no puedo poneros a todos. Un agradecimiento muy especial para Pedro que participó de manera muy personal y directa en el desarrollo de esta tesis y al que le debo mucho.

Thank you!
Merci !
¡Gracias!

Index

List of Figures

List of Tables

1

Thesis motivation

Jets from young stars are a ubiquitous part of the star formation process and their link with accretion processes is well established (Cabrit et al., 1990; Hartigan et al., 1995). They are launched almost certainly from the inner regions of the star-disk system, the same disk that ultimately may give rise to a planetary system. Although a number of models exist for their generation (see for example the review of Ferreira et al. (2006), Shang et al. (2007) and Pudritz et al. (2007)), the exact mechanism by which mass is ejected from accreting systems and collimated into jets is an open problem. It is thought that the same basic magnetohydrodynamic (MHD) mechanism is responsible for the launching of jets in objects as diverse as brown dwarfs (Whelan et al., 2005), planetary nebulae (e.g. García-Díaz et al. (2008), García-Segura et al. (2005)), micro-quasars and active galactic nuclei. It is also important for telluric planet formation models as they have implications on inner disc physics. Because of their proximity and their rich set of diagnostic emission lines, jets from young stellar objects represent the best test-bed we have of the MHD jet-launching paradigm (see the reviews of Bally et al. (2007) and Ray et al. (2007)).

I start by giving in this chapter my motivations for this work, the particular objectives of this thesis and the objects observed. Chapter 2 briefly reviews the current accepted theory of star formation and evolution, as well as a brief review of the accretion and ejection signatures in young stars, their connexion and the proposed models to explain the jet launching. In Ch. 2, I also review the observational works carried out using high spectral and angular techniques before the start of my thesis. Chapter 3 discusses the line diagnostic tools developed to analyze the data and derive physical conditions in the jet (n_e, T_e, x_e) and mass-loss rates. I explain in particular the diagnostics used in this thesis. Chapters 5 and 6 show the detailed study and the results obtained for the analysis in the optical of the RY Tau jet and DG Tau jet respectively. I finish in Ch. 7 with the global conclusions of the thesis and the perspectives obtained from it.

Objectives of this thesis

In order to better understand the physics of the ejection mechanism, this thesis concentrates on the study of the launching of jets in one kind of young stellar objects, the T Tauri stars, which are close enough to us and are no longer embedded to have access to the inner parts of the jet. Important advances have been made since the first evidence of the existence of jets produced in young stellar objects, from both a theoretical and observational point of view. However, important questions remain open in our understanding of this phenomenon. Notably, the origin of these jets, how exactly they are generated, which is the dominant launching mechanism and from where the jets are launched. We do not know if they come directly from the disc, the interaction zone between the stellar magnetosphere and the disc or even the star itself. Distinguishing between the different possible origins is crucial to discern between the proposed models and it would have an important influence in the evolution of the global disc-star system and therefore in the development of an eventual planetary system.

In my thesis, I obtain observational constraints on the ejection mechanism by comparing high-angular resolution observational data of the closest regions to the star (< 100 AU) with predictions from different MHD models. In particular, it is important to increase the number of sources studied in detail using high-angular resolution techniques, but above all I am interested in investigating the effects of source multiplicity and source mass on the jet properties. I analyze optical data of one of the most massive known T Tauri star and suspected binary. In addition, during the last years, more and more T Tauri jets were found out to show a NIR H_2 emission, but its origin is unclear and some questions have emerged: Is it a slow external component of the same disc wind or does it come from entrained material by the axial jet? In order to clarify the origin of this emission in T Tauri jets and how it is related to the atomic emission, I'll analyze NIR data of one of the most studied T Tauri jets, that of DG Tau.

From previous studies, the jet acceleration and jet collimation must occur within the 100 AU close to the star. This translates in a need in angular resolution of $\sim 0.1''$ or better for the closest regions (Taurus-Auriga cloud is at 140 pc from us) in order to probe the jet characteristics near this collimation zone. In addition, to complete the morphological studies, we are interested in carrying out a detailed study of the emission line ratios and velocity structure, which help us to distinguish between the different proposed launching mechanisms and clarify the nature of the emission observed in the inner regions. For this, a spectral resolution better than 3000 ($\Delta v < 100$ km/s) is required. One of the best techniques to simultaneously achieve high spatial resolution, over a reasonable field of view, along with sufficient spectral resolution, is to use Integral Field Spectroscopy (IFS). As part of my thesis I improve on this technique by combining it with adaptive optics to greatly increase the angular resolution. Two IFS instruments will be used, OASIS in the optical and SINFONI in the near-infrared. In particular, I carry out:

- **Morphological studies** in order to study the collimation properties as a function of the flow velocity. These studies will also allow the identification of knots.
- **Detailed kinematical studies**. I obtain, for the studied sources, the terminal flow velocity and the range of flow velocities. I investigate the influence of some parameters as the central stellar mass and the source multiplicity in the measured flow properties. Ferreira et al. (2006) show that these parameters are important to discriminate among MHD launching models as they predict different dependencies of the terminal velocity with these parameters. I also investigate the kinematic in the direction transverse to the jet axis in order to look for rotation signatures.
- **Study of the gas excitation conditions**, not only spatially but also as a function of the velocity. This study allows us to derive total jet densities necessary to get better mass-loss rate estimations, investigate variations with flow velocity, the flow structure and the shock conditions.
- **Determination of the ejection/accretion rate**. This ratio is an important test for the models (Ferreira et al., 2006).
- **Analysis of the molecular component**. As for the atomic jet, I analyze its morphology and kinematics and I determine its mass-loss rate. Observational data will be compared to models to find constrains to its origin.

At the time I started my thesis, only a handful of objects had been observed with a combination of high-angular resolution and spectroscopy techniques, and in particular, only two had been observed using Integral Field Spectroscopy (DG Tau and RW Aur). It was thus crucial to increase the sample of sources studied in detail, which is one of the specific objectives of this thesis. At the same time, more concrete objectives were considered and the objects analyzed here were chosen following these more concrete aims:

1) Influence of the central stellar mass: the jet from the intermediate T Tauri star RY Tau

The first star studied is RY Tau which was observed using the integral field spectrograph OASIS (Optically Adaptive System for Imaging Spectroscopy) combined with the adaptive optics bonnette PUE'O at the Canada France Hawaii Telescope (CFHT). Previous studies have already suggested the presence of the jet from detected [OI] blueshifted emission (Cabrit et al., 1990; Hartigan et al., 1995), but no detailed study of its morphology and kinematics has been performed using spectro-imaging techniques. Hence, this star was observed in the aim of studying the impact of higher central mass on the jet properties. Besides, this star is a suspected close binary from Hipparcos observations. These two particular properties will allow to directly probe the effect of the central star properties in the jet properties.

2) Origin of the H_2 emission in T Tauri jets: the case of DG Tau

DG Tau was observed using the spectrograph for INtegral Field Observations in the Near Infrared (SINFONI) at the Very Large Telescope (VLT) in the H and K band. Most of the studies with high angular resolution, high spectral resolution or using IFS were carried out in the optical domain. However, as I have mentioned, recent studies showed that strong NIR H_2 lines are present in the spectrum of T Tauri objects. Therefore, the SINFONI data will allow me, firstly to study in detail not only the atomic component but also the molecular one simultaneously, and secondly constrain the origin of the molecular emission, including a test of the disc-wind scenario.

2

Introduction

In this first chapter, I introduce the concept of T Tauri star, placing it in the context of the currently accepted star evolution diagram. I point out the importance of the study of the jet phenomenon in this particular type of young stellar object (YSO) and I review the observational efforts carried out in the last years in order to understand this fascinating stage of the star formation, also so important for other astrophysical domains. I finish giving a brief review of the models discussed for jet launchings.

2.1 Young stellar objects

Stars form in the molecular clouds such as Orion or Taurus-Auriga. They are mainly composed of molecular hydrogen and contain significant amounts of interstellar dust. Stars form through the gravitational collapse of molecular cores inside these clouds. Initially, the internal pressure of the fragment are balanced by gravity, but this equilibrium can be lost because of ambipolar diffusion, the dissipation of turbulence or because of an outside force (Andre et al., 2000), and the stellar mass cloud begins to collapse. However, it is still uncertain what initiates this collapse. This is the first stage in the formation of the star. As it collapses, the cloud becomes hotter since the density is increasing and the radiation cannot escape, heating the cloud. A temperature gradient and hence an internal pressure gradient begins to balance gravity. It is considered that a protostar has formed when this balance is nearly achieved. In addition, the conservation of angular momentum causes the rotation velocity to increase as the nebula becomes smaller. This rotation causes the cloud to flatten out and take the form of a disk. The result is a slowly contracting central core surrounded by a disc and an infalling envelope. It continues to evolve through the accretion of this ambient material onto the star and onto the circumstellar disc which will then also accrete material to the star by accretion funnels or by the interacting region between the star and the disc. At the same time, this causes the launching of bipolar outflows. This ejection is related to the accretion by the disk (e.g. Cabrit et al., 1990) but how exactly it is produced is an open question. The current models propose an origin on the disc, on the star or the interaction region between the disc and the star atmosphere.

The last stage of the star formation involves the dissipation of the gas and the slowing down of accretion and outflow activities. The circumstellar disc starts the first stage of planet formation and the star joins the main sequence.

2.1.1 Classification and evolution

Low mass stellar objects ($M_* \leq 2M_\odot$) are divided in four different classes based on their infrared emission. This infrared emission is produced by the dust surrounding the star. The spectral energy distributions (SEDs) of these objects are, in fact, modelled as a blackbody contribution from the star plus the infrared/millimeter contribution from the circumstellar material. As the young star evolves this radiation changes because the material distribution changes due to accretion and the action of outflows. Hence, this classification can be considered as a sequence of the young star evolution. It was proposed by Lada (1987) and Andre (1997) (Fig. 2.1), the different stages are:

Class O objects would correspond to the first stage in the star evolution with an age of $\sim 10^4$ years. The main characteristic is that most of the material (more than 50% (Andre, 1997)) is still in the circumstellar environment. Hence, they are very deeply embedded objects whose spectral energy distribution is completely dominated by the surrounding material. They are observed mostly at sub-millimeter or radio wavelengths with no emission at wavelengths shorter than 10μm. They produce powerful molecular outflows. Well collimated molecular jets in CO and SiO lines extend to 0.05-0.1 pc from the source, and within 100 AU, 40% of the Class O objects excite H_2O masers tracing very dense shocks. Figure 2.2 shows the example of the class O jet associated to the source HH 211, from Gueth & Guilloteau (1999). Further than 0.1-1pc chains of compacts, fast molecular bullets are detected, often associated with shock-excitated regions in the H_2 line at 2.12μm (e.g. Bachiller et al., 1990).

Class I objects have an age of $\sim 10^5$ years and most of the mass of the system is already in the star. They show a strong infrared excess and they are detected in the far and near infrared. This emission cannot be explained only by the presence of a disc around the star, it is due to the residual envelope which is strongly accreting onto the star-disc system. The near infrared emission is produced by light diffusion of the star radiation by the dust in the disc. Powerful outflows are also associated with these sources. They are still seen in radio, but shock-excitated H_2 and molecular outflows are weaker than in the previous class O objects. Jets become visible in lines such as H_α, [OI]λ6300, [SII]λ6731,λ6731, and [NII]λ6583, and in the near-infrared in the [FeII] lines. They extend to pc scales from the central sources and they contain small bright knots with separations of 500-1000AU and a large scale shock structure with typical distances of 0.1 pc. Figure 2.3 shows an example of this kind of jets. The jet from HH 34 is very collimated and has several knots of typical spacing 0.05-0.2 p.c.. Bow-shaped structures are also seen in both sides of the outflow. These knots are known as Herbig Haro objects and they are characterized by a shock emission line spectrum.

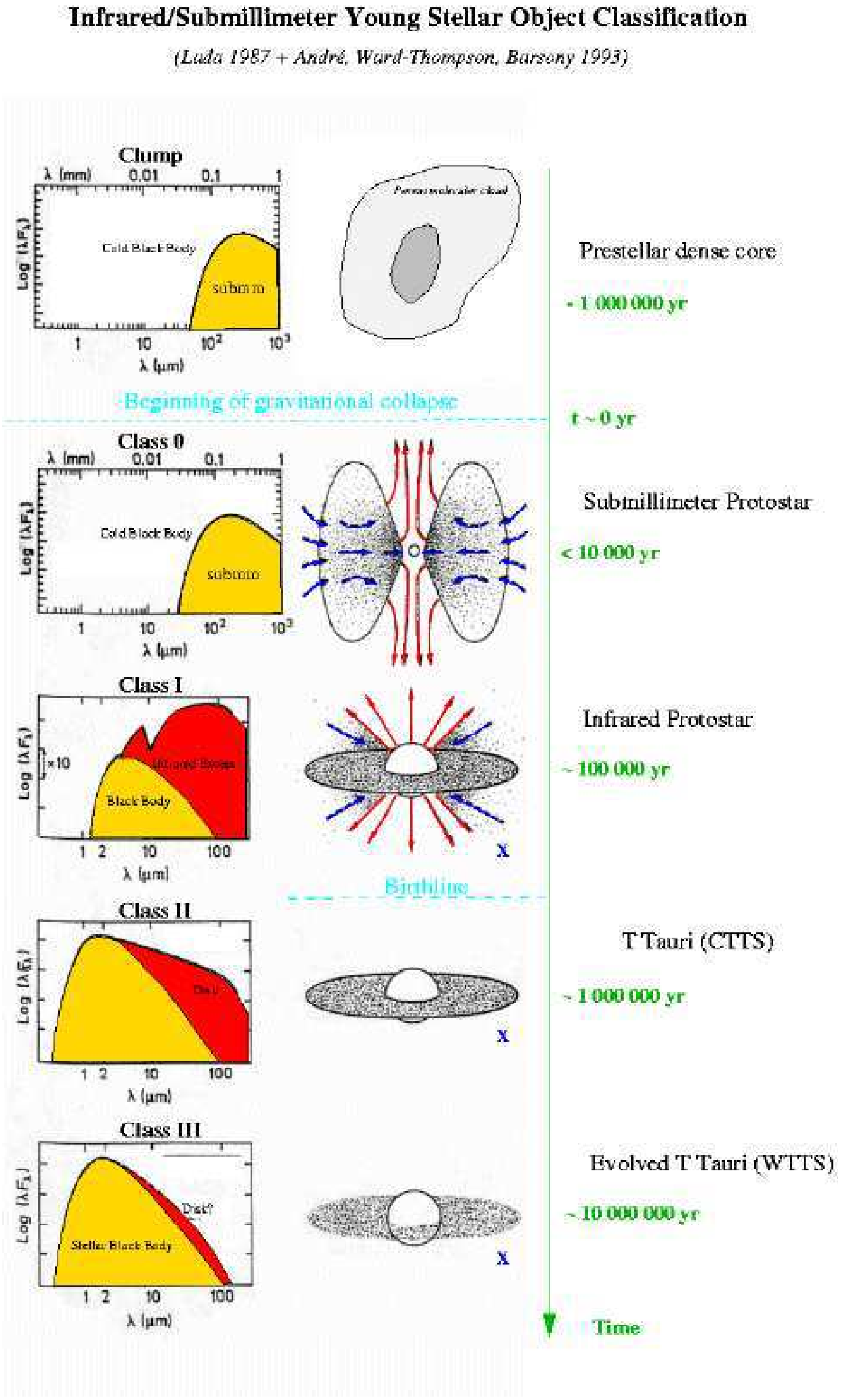

Figure 2.1: Classification of low mass young stellar objects and schema of their evolution.

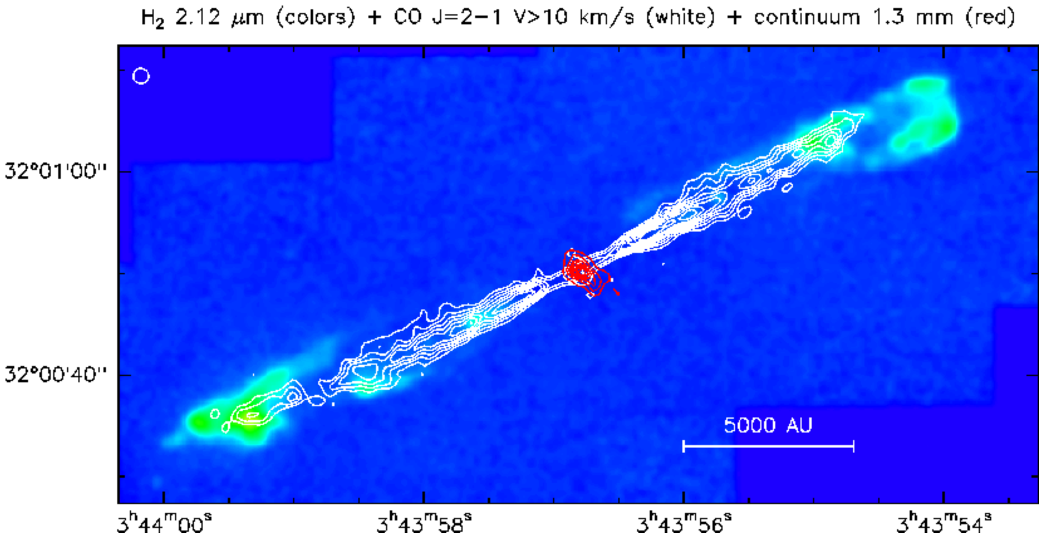

Figure 2.2: Example of a class 0 jet: HH 211. IRAM Plateau de Bure observations: H2 emission in the background color image, the CO J=2-1 emission at high-velocities in white contours, and the 230 GHz continuum emission in red contours (Gueth & Guilloteau, 1999).

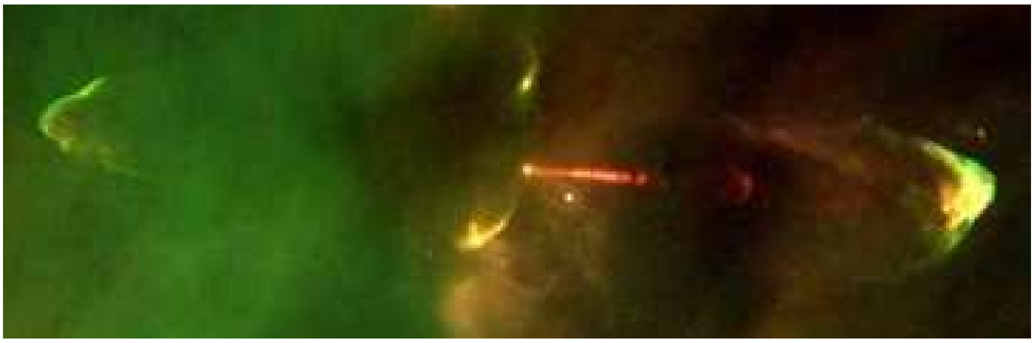

Figure 2.3: Example of a class I jet: HH 34. Images taken with the Hubble Space Telescope (HST).

Class II objects are observed in the optical domain and correspond to the sources named Classical T Tauri stars (cTTs). These stars have an age of $\sim 10^6$ years and they are formed by the central star surrounded by a disc and an outflow of material perpendicular to the disc, as shown in Fig. 2.4 for one of the typical examples of class II objects, HH 30. They also have a strong infrared excess but less important than in the Class 0/I objects because the outflow has already dispersed much of the circumstellar gas and dust. The infrared excess is produced then by the accretion disc around the star. The outflows are mainly traced by blueshifted forbidden lines of [OI]λ6300, [SII]λ6731, and [NII]λ6583 in smaller scales, they arises on scales of 100 AU. These objects also show strong Balmer emission lines and HeI and NaD with a blueshifted absorption component which is related also to the ejection. They show a high variability of intensity of the order of one magnitude in a few days. Besides the infrared excess, this objects show an excess in the UV domain, producing a "filling" of the photospheric absorption lines at these wavelengths

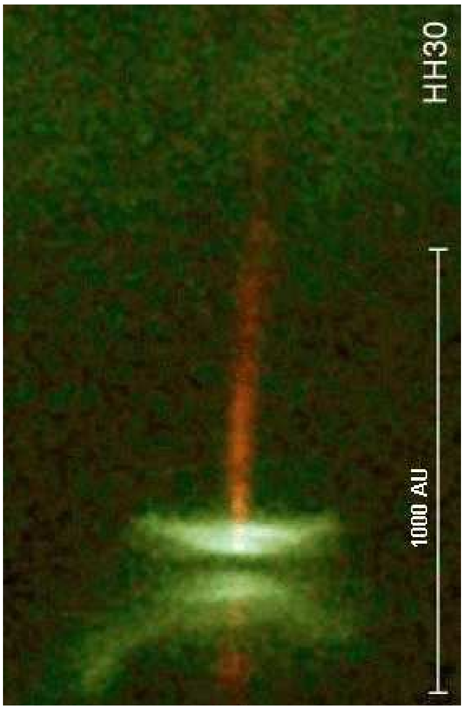

Figure 2.4: Example of a class II jet: HH 30. Images taken with the Hubble Space Telescope (HST).

("veiling"). This veiling is interpreted as an indication of accretion. It would be caused by the material coming from the disc falling onto the star, probably by the mediation of accretion columns produced by the interaction between the stellar magnetosphere and the magnetic field lines from the disc (Edwards, 1997).

Class III objects have an age similar to the class II objects, between $\sim 10^6$ or $\sim 10^7$ years. They are also called Weak T Tauri stars (WTTS) because they show weak emission lines and a very small infrared excess. In this case two explanations are possible: either the disc is tenuous and optically thin or there is no more material surrounding the star.

2.2 Accretion/ejection process in T Tauri stars

2.2.1 Evidence for accretion on young stars

In addition to the signatures of outflows shown before in detail for each class of young stellar objects, evidence of accretion from the disc onto these young stars is observed. These evidences come mainly from an ultraviolet (UV) excess in the continuum, an Infrared (IR) and millimeter excesses at wavelengths higher than 1mm (Bertout et al., 1988). Other evidence come from observations of redshifted absorption features in the Balmer lines (e.g. Edwards et al., 1994). Bertout et al. (1988) modeled these excess by a Keplerian disc of gas and a boundary layer of gas and dust accreting onto the star. They found that the disc contributes both an infrared excess due to accretion energy dissipation and reprocessing of stellar light, and the ultraviolet excess comes from the boundary layer between the disc and the star where half of the total accretion luminosity is generated. However, this infrared excess certainly probes the existence of an optically thick disc but it is not necessarily accreting material onto the star. The new models accept that the disc is disrupted somewhere in the vicinity of the co-rotation radius and the accretion flow is redirected to free-fall toward the star in a magnetic *funnel flow* (e.g. Koenigl, 1991; Hartmann et al., 1994). Some of the empirical support to the existence of these funnel flows are the inverse P Cygni features observed in hydrogen and permitted metallic lines (Edwards et al., 1994) with redshifted absorption components indicating mass in free-fall infall. The broad, asymmetric and centrally peaked hydrogen emission line profiles (Balmer, Paschen and Brackett lines) are well reproduced by radiative transfer models considering funnel flow (Muzerolle et al., 1998a). The spectral energy distributions observed between 1-5μm are better reproduced assuming that the inner disc is truncated at or inside the co-rotation radius (Bertout et al., 1988; Meyer et al., 1997). Other evidence of funnel flows is that some TTS show signatures of spots hundreds to thousands of degrees hotter than the photosphere due to accretion shocks on the stellar surface (Bertout, 1989) and the detection of kG magnetic fields on T Tauri stars (Johns-Krull, 2009; Valenti & Johns-Krull, 2004).

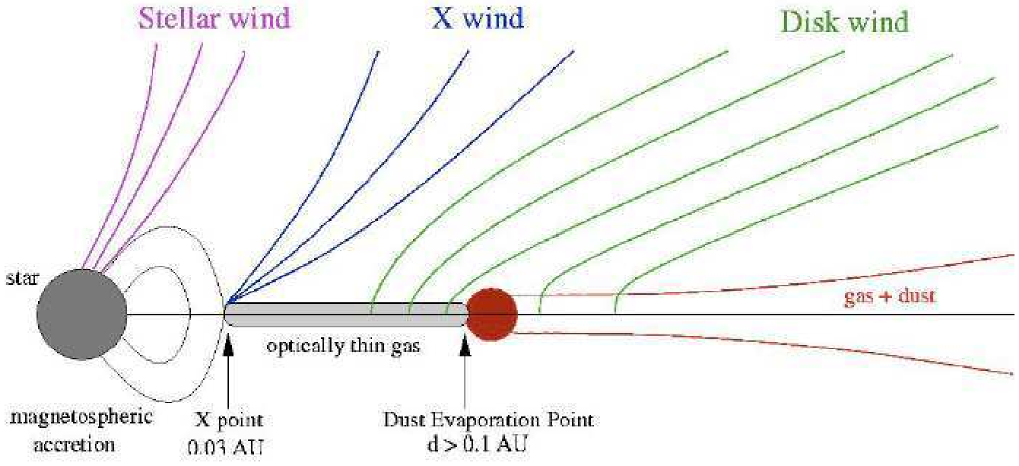

Figure 2.5: Schema of the star-disc-wind system with the scales involved both in the accretion and ejection processes (gently provided by Dr. Podio).

Figure 2.5 shows the different scales involved in this star-disc interaction, including the main proposed models to explain the observed outflows and explained more in detail later. The accretion of material from the disc onto the star would occur, by the means of accretion funnels, from very small distances, on the order of the co-rotation radius, i. e., 0.03 AU. In the case of the ejection, three main origins are proposed: either the wind comes from the star, “Stellar wind”, from the region of interaction between the stellar magnetosphere and the disc, at the co-rotation radius, “X-wind”, or from a large range of radii in the disc, “Disc wind”. The dust evaporation radius is also shown.

Nowadays, the more reliable estimations of the mass accretion rate, in the case of TTS, comes from the optical/ultraviolet emission in excess of photospheric radiation known as "veiling" in spite of the IR excess because it is not clear the percentage of IR emission is due to the accretion. More recently Muzerolle et al. (1998b) propose to use the Br_γ luminosity to estimate the accretion luminosity and therefore the mass accretion rate. This last one method will be used in this thesis to obtain a new estimation of mass accretion rate in the case of the DG Tau system (Cp. 6).

2.2.2 Ejection/Accretion connection

Cabrit et al. (1990) and Hartigan et al. (1995) demonstrated observationally the existing correlation between ejection and accretion signatures in the case of T Tauri stars. First, they showed that when there is a wind there is also a disc, i.e., stars showing near infrared excess, show also forbidden [OI] emission. More important is the correlation between the accretion luminosity, measured from the veiling of absorption lines, and the forbidden lines luminosity. This relation suggests that in fact winds not only need the presence of a disc, but they are also powered by accretion. How the energy is transmitted to the wind is still an open question of the star formation theory.

The evidence for an accretion/outflow connection in the more embedded Class I and Class 0 sources, covering a wider range of evolutionary states and masses than the TTS, is less firmly established. Outflow diagnostics in these cases, such as CO momentum fluxes or H_2 line luminosities, are well correlated with the source bolometric luminosity. However, the bolometric luminosity does not differentiate between photospheric and disc/envelope contributions. Hence, we only have indirect evidences of the ejection/accretion in these evolutionary states.

A crucial diagnostic of the ejection/accretion connection and for models trying to explain the ejection as powered by the accretion phenomenon, is the ejection/accretion mass rates ratio. However, even for the TTS this is a parameter not well constrained and needs to be reviewed in order to assess whether it is the same for all the evolutionary state, mass of the central star or other factors.

2.3 Jets in T Tauri stars

My thesis focuses on one particular type of young star, the classical T Tauri stars (cTTs), which are thought to be analogs of the young Sun, and in the jets emanating from these objects.

Many studies have been made of large-scale bipolar outflows (some parsecs) and our understanding of them has significantly increased. However, in order to probe the launching regions, as well as how jets become collimated and interact with the surrounded discs, observations of jets on scales comparable to the central engine are crucial. This is possible in the micro-jets associated to T Tauri stars. The presence of jets in this kind of object were first suspected from high-resolution profiles of emission and absorption lines (see for example Kuhi (1964) or Mundt (1984). Some T Tauri stars showed P Cygni profiles at the H_α profiles, indicating that mass loss is taking place. Clearer indications of atomic collimated winds come from the forbidden line emission regions (FLER). Blueshifted forbidden lines of [OI]λ6300, [SII]λ6731 and [NII]λ6583 were observed (Appenzeller et al., 1984; Edwards et al., 1987). Long-slit spectroscopy, after a careful continuum subtraction, revealed high velocity collimated microjets extended over a few 100 AU (Hirth et al., 1997). Finally, the first images using HST observations were carried out by Ray et al. (1996). These stars are optically visible and not very embedded giving access to the closest parts of the jets ($<$ 100AU). It is crucial to have access to the regions on scales of $\sim1''$ (for the distances to the nearest star-formation regions such as Taurus region). These objects show a rich atomic and molecular emitting spectrum allowing the access to both the morphology and kinematics of the jet launching. The major difficulty is to evade the stellar radiation but spectroscopy and Integral Field Spectroscopy (IFS) enables this contribution to be removed, revealing the jet on scales lower than $1''$.

2.4 MHD Models

Different models have been proposed to explain the jets produced in these objects and the observed emission spectra. One of the first models proposed was that of Edwards et al. (1987). This model considered only one kinematical component and the double peak profiles were reproduced by changing the projection angle but the model could not produce an emission peak at the velocity of the star as it is actually observed. Kwan & Tademaru (1988) proposed a two-component disc-wind model. The first component at high velocities (HVC) represented a fast well collimated jet and the second one at low velocities (LVC) represented a much slower, less focussed wind from the circumstellar disc. As I mentioned, observations carried out by Hartigan et al. (1995) or Hirth et al. (1997) confirm that the HVC and LVC come from physically distinct regions with different forbidden emission lines (FEL) properties, rather than be the same kinematical flow seen from two different projections.

Nowadays it is generally accepted that jets from young stars are launched centrifugally along magnetic field lines. On one hand, models based on hydrodynamic pressure fail to reproduce the collimation properties observed in jets. Disc thermal pressure alone does not produce a well-collimated jet beam, and dense confining envelopes would produce excessive extinction towards Class II objects. Collimation by external magnetic pressure gradients is another possibility, however it would require a magnetically dominated region with a poloidal or turbulent field strength of $\sim$10 mG over at least 100 AU and it is not clear how such a region may be formed and maintained. However MHD winds from the disc or from the star, satisfactorily reproduce the jet width, collimation and opening angles in Class II jets for realistic parameters (see the review by Cabrit (2007a)).

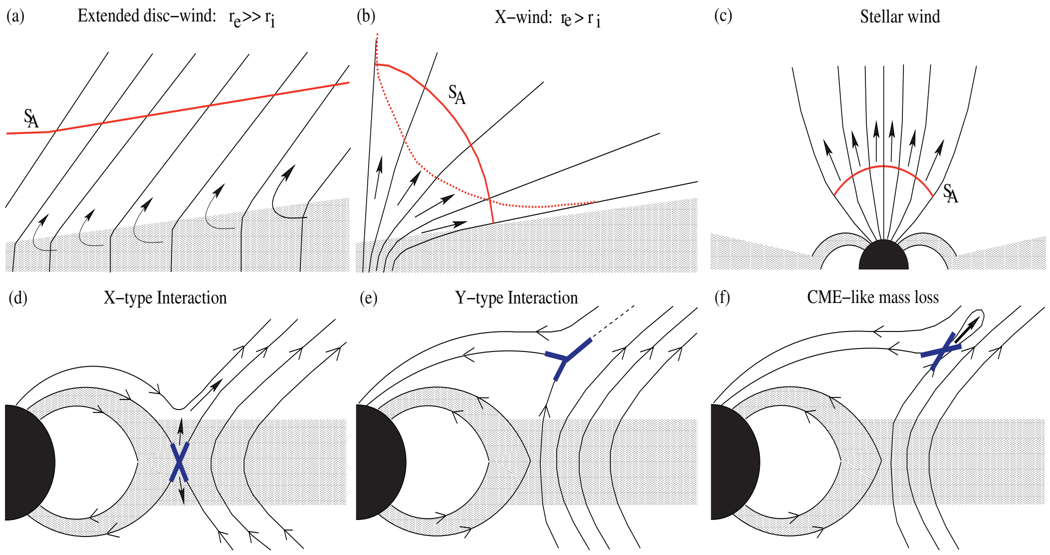

Fig. 1. *Top*: classes of published stationary MHD jets for YSOs. When the magnetic field is threading the disc on a large radial extension **(a)** extended disc wind) or a small disc annulus **(b)** X-wind), jets are accretion-powered. They are mostly pressure-driven when the field lines are anchored onto a slowly rotating star **(c)** stellar wind). The corresponding Alfvén surfaces S_A have been schematically drawn (thick lines). In the X-wind case, two extreme shapes have been drawn: convex (solid line) and concave (dashed). *Bottom*: sketch of the two possible axisymmetric magnetospheric configurations: **d)** X-type neutral line driving unsteady Reconnection X-winds, when the stellar magnetic moment is parallel to the disc field; **e)** Y-type neutral line (akin the terrestrial magnetospheric current sheet) when the stellar magnetic moment is anti-parallel (or when the disc field is negligible). **f)** A CME-like ejection is produced whenever the magnetic shear becomes too strong in a magnetically dominated plasma. Such a violently relaxing event may occur with any kind of anti-parallel magnetospheric interaction (even with an inclined dipole). The thick lines mark the zones where reconnections occur.

Figure 2.6: Schema of the current proposed MHD ejection models for young stellar objects, from Ferreira et al. (2006).

On the other hand, the observed jet energetics (mass, momentum, and kinetic energy flux), as well as the high ejection efficiencies, i. e., the ratios of jet energetics to the accretion rate or accretion luminosity, require also MHD processes to be explained. Acceleration by radiative pressure on dust cannot provide the high momentum efficiencies observed and hydrodynamic acceleration by thermal or wave pressure gradients requires an energy input rate in heat or coherent Alfvén waves that is at least comparable to L_{acc} (Cabrit, 2007a).

Therefore, magneto-centrifugal driving models appear as the most promising models capable to both accelerate and self-collimate the jet in good agreement with observations on the observed scales. The main difference between the MHD models proposed is from where precisely jets are launched. A completed description of the currently discussed models and a thorough comparison with observational results of the inner parts of jets in T Tauri stars is presented in Ferreira et al. (2006). Figure 2.6, taken from Ferreira et al. (2006), shows a schema of the different models described in the paper. The most discussed scenarios to explain jets in young stellar objects, are the stellar wind and accretion-powered disc winds. Among the last kind of models, two are the most widely favored models: the X-wind model (Shu et al., 2000) and the magneto-centrifugally driven disc-wind model (Konigl & Pudritz, 2000). I discuss here only the steady models, shown in top panels of Fig. 2.6, with those I will compare my results. Some recent studies have been made in unsteady ejection models but such ejection may not be collimated on large scales, see for example the works by Ferreira et al. (2000) for the case of unsteady Reconnection X-winds or Romanova et al. (2009) for the Y-type interaction (bottom panels in Fig. 2.6).

Stellar winds: Fast rotating stars can produce the energy needed to magnetically accelerate stellar winds. However, T Tauri stars are slow rotators and in this case winds must be driven by their pressure gradient either due to thermal effects (Sauty & Tsinganos, 1994; Sauty et al., 2002) or to turbulent Alfvén waves (Hartmann & MacGregor, 1980; Decampli, 1981; Hartmann et al., 1982). Hartigan et al. (1995) show the correlation of the forbidden line emission in T Tauri jets and the accretion luminosity suggesting that winds are powered by accretion energy. Both thermal and turbulent pressures can be generated by the magnetospheric accretion shock and therefore produce accretion-powered stellar winds (Matt & Pudritz, 2005).

Accretion-powered disc winds: A large scale magnetic field which thread the disc from a inner radius to some external radius is assumed. When the ejection occurs from a large range of radii one gets the *extended disc wind* and when it is from only one annulus at the co-rotation radius one gets the *X-wind*. The difference between these two models is in the origin for the large scale vertical magnetic field but the ejection process is computed identically. The two models give different predicted terminal velocities and angular momentum fluxes because of the range of launching radii and of the different Alfvén surface.

Ferreira et al. (2006) favor the extended disc wind interpretation ("warm" solution), excluding the so-called extended "cold" disc wind models but without excluding some X-winds solutions. They also propose that, although X-winds and disc-winds likely do not co-exist, pressure-driven stellar winds may probably be present in a jet mainly dominated by a disc-wind. Most of the mass would be carried by the disc wind and the stellar wind contribution would be in the inner parts of the flow, inside the T Tauri jets, carrying out only a small fraction of the mass flux.

2.5 Observational studies of T Tauri jets at high-angular resolution

Observations suggest that jets are launched and collimated within 100 AU from the central source. In the case of the closest regions (for example the Taurus-Auriga cloud is at 140 pc), this translates to a resolution of 0.1″ or better. Besides a high-angular resolution, a spectral resolution higher than 3000 is desirable to well resolve the kinematics of the jet. In this section I review the most important observational efforts carried out in the last years in the detection and study of jets in T Tauri stars, in particular using high-angular resolution techniques.

Different *techniques* have been used with the aim of increasing the angular resolution and to have access to the inner regions as possible:

- **Imaging:** Ray et al. (1996) gave the first high spatial resolution images of the HL Tau jet using narrow-band imaging with the Hubble Space Telescope (HST).
- **Long-slit spectroscopy:** One of the first exhaustive studies over a dozen of CTTs was that of Hirth et al. (1997). Using long-slit spectroscopy and thanks to a good subtraction of the continuum emission, authors studied the forbidden line emission of these stars with few arcsecond resolution.
- **Adaptive Optics (AO):** Lavalley et al. (1997) and Dougados et al. (2000) combined both 4m-class telescope narrow-band images and intermediate spectral resolution spectra with AO to obtain $0.2''$ angular resolution data of DG Tau, CW Tau and RW Aur jets.
- **Integral Field Spectroscopy (IFS):** Lavalley-Fouquet et al. (2000) combined an innovating technique, the IFS, with AO to obtain 3D data cubes of the DG Tau jet. Authors probed the regions of the jet base, a few hundred AU, with a spatial resolution of $0.5''$ ($\sim$70 AU at the Taurus distance). This technique allows the construction of 2D images of the jet at different velocity intervals in the same way as channels maps in radio interferometry. I describe in detail this technique, which is used in all the data analyzed in this thesis, in Ch. 4.
- **Hubble Space Telescope (HST) Spectroscopy:** Bacciotti et al. (2000) and Woitas et al. (2002), using HST long-slit observations with the Space Telescope Imaging Spectrograph (STIS), constructed also 2D images in individual lines, over a range of velocities (channel maps) for RW Aur and DG Tau. They took multiple parallel exposures of $0.1''$-width slit and placed the slit every $0.07''$ across the outflow.

  Hartigan et al. (2004) carried out slit-less spectroscopy, also using STIS, of the objects CW Tau, HN Tau, UZ Tau E, DF Tau and DD Tau. This alternative approach allowed them to construct high spatial resolution images in a large spectral range, including lines where no narrow-band HST filters exist.
- **Multi-epoch observations:** Dougados et al. (2000), López-Martín et al. (2003) and Hartigan et al. (2004) compared images taken at different epochs (a few years between them) to measure proper motions on the knots of the DG Tau and RW Aur jets.
- **Spectro-astrometry:** García (1999), Takami et al. (2001, 2003) used the technique of spectro-astrometry to reveal jets on scales of $\sim$10 AU ($\sim 0.05''$ in the nearest regions) in a number of YSOs. Spectro-astrometry measures the positional centroid of the emission along the slit as a function of wavelength. If there is an outflow, the centroid will be shifted from the continuum. The centroid is determined with an accuracy of $0.5\mathrm{FWHM}_{seeing}/\sqrt{N}$ in miliarcseconds, where N is the number of photons detected.

Regarding the *morphology* of the jets, these studies were centered first of all in their detection, and once detected in the analysis of the observed knots and in the measurements of the jet diameter close to the source:

- Lavalley et al. (1997) and Dougados et al. (2000) showed the *bow-shaped morphology* of the knot observed at 3″ from the source in the DG Tau microjet. They also detected a wiggling which is considered as a sign of precession of the jet. These properties suggest that knots in T Tauri jets are likely to be internal working surfaces due to time variable ejection as in the younger Herbig-Haro (HH) flows.

- A number of works have been made to measure the *jet width* (FWHM) as a function of the distance to the star, using spectroscopy observations. HL Tau jet diameter was measured by Ray et al. (1996), Dougados et al. (2000) and Woitas et al. (2002) did it for DG Tau, CW Tau and RW Aur sources and Hartigan et al. (2004) show the same kind of measurements for HN Tau and UZ Tau E jets. All these studies show that the jet remains unresolved within 15 AU considering the best spatial resolution achieved of 0.1″ (14 AU for the Taurus cloud).

  In addition to the jet width, estimations of the opening angle (OA) were obtained. Opening angles between 20° and 30° on scales of 15-50 AU were derived for the HN Tau and UZ Tau E, indicating a width at the jet source smaller than 5 AU. For distances further than 50 AU, jet width increases with only an OA of a few degrees. Jets exhibit typically FWHM of 20-40 AU at distances of 100 AU to the star. This indicates that collimation must occur on scales of a few tens of AU. This variation of the jet width with the distance to the star is consistent with disc-wind models of moderate to high efficiency ($\dot{M}_{ej}/\dot{M}_{acc}$>0.03) (Garcia et al., 2001a; Dougados et al., 2004).

- Whelan et al. (2004) showed, using spectro-astrometry techniques, that the Pa$_\beta$ emission is not only caused by accretion (as was previously thought) but also that there is a wind contributing to the emission. This technique can be used to separate the part coming from the outflow from that coming from the accretion. In addition, the presence of an acceleration zone have been evidenced by the fact that the offsets in the centroid increase with velocity.

  Moreover, Whelan et al. (2005) used this technique to first detect an outflow produced in a brown dwarf, ρ Oph 102. Since then, this technique has been used to study more cases of brown dwarfs with very good results, see the works by Whelan et al. (2007, 2009).

Regarding to the *kinematics*, two kinematical components are usually observed in the forbidden emission lines from classical T Tauri stars (Hartigan et al., 1995). Hirth et al. (1997) show that these components have different emission properties and hence they are probably formed in different regions. The so-called high velocity component (HVC) (velocity of a few hundred km/s) is more extended and of higher excitation than the low velocity component (LVC), this last one with velocities of 10-50 km/s. Some studies of the kinematics of the different components were carried out especially using HST observations or IFS techniques:

- Lavalley-Fouquet et al. (2000) using IFS+AO techniques, and Bacciotti et al. (2000) and Woitas et al. (2002) both using HST observations revealed some important characteristics of the velocity components. Jets exhibit an *onion-like kinematic structure*. This means that jets are more collimated at higher velocities and higher excitation. Hence the LVC are wider, slower and less excited but images show a smooth transition between the HVC and the LVC when one moves further from the outflow axis.

  Along the jet, the LVC is located at distances from the star up to 50 or 80 AU, whereas the HVC extends to much larger distances. The acceleration of the flow appears to occur on scales of 50 or 100 AU.

- Takami et al. (2004) showed that the molecular emission in H_2 lines in the DG Tau jet extends this onion-like kinematic structure. The emission is slower ($\sim$15 km/s) and wider than the forbidden line emission suggesting an origin in a different component.

- This onion-like structure were actually predicted by magneto-centrifugal winds theory (ex. Pudritz et al. (2007)).

- Theoretical models predict *rotation* in order to be able to remove angular momentum from the star and disc system and to allow accretion. Hints of rotation had already been observed in HH 212 jet at distances of 10^4 AU (Davis et al., 2000) and Bacciotti (2002), Coffey et al. (2004) and Woitas et al. (2005) extend this work to other YSOs. They analyzed HST/STIS observations of DG Tau, RW Aur and Th 28 in the aim of testing these predictions on the first 100-200 AU from the star. Placing the slit both along and perpendicular to the jet axis, authors found clear radial velocity asymmetries between pairs of positions placed symmetrically with respect to the jet axis. Assuming that this asymmetries are due to rotation, authors derived velocities of 5-25 $\pm$ 5 km/s at 50-60 AU from the source and 20-30 AU from the jet axis.

  Coffey et al. (2007) extended this work to other sources (CW Tau and HH 30) and to the Near Ultra-Violet (NUV) domain (DG Tau and Th 28) using again STIS observations both in the NUV and in the optical. They found at optical wavelengths similar velocity shifts of 10-25 $\pm$ 5 km/s and they confirmed systemic radial velocity shifts for the DG Tau and Th 28 jets in the NUV domain, but in this case the shifts are lower, of 10 $\pm$ 5 km/s.

  Other similar studies were carried out in early stage class I objects. Chrysostomou et al. (2005) observed with the ISAAC spectrograph on the VLT, the $H_2\lambda2.12\mu$m line emission of the HH 26 and HH 72 jets. They also found velocity shifts of $\sim$5-10 km/s at 2-3$''$ from the source and 1$''$ from the axis.

Atomic		Molecular (NIR H_2)	Radio/mm (CO, PdBI)
Optical	NIR		
$2 \rightarrow 5$ ~10 long-slit HAR	$0 \rightarrow 1$ ~10 long-slit HAR	$0 \rightarrow 6$	HH 30 (Class I) HH 212 (Class 0)

Table 2.1: Synthetic table with the number of sources studied using high angular resolution techniques at the beginning of my thesis and the evolution at the moment of writing of this manuscript. In the case of atomic and molecular studies, the first numbers are for sources studied using IFS observations, and an approximative number for the studies made from high angular resolution long-slit is also given.

When I started my thesis only a few stars that show clear signs of ejection and/or accretion had been observed with high resolution instruments, and even less with IFS. In particular, 30 cTT stars over 65 observed in two surveys carried out ten years ago showed clear signs of ejection at the moment of the observation (Hirth et al., 1997; Hartigan et al., 1995). During almost 10 years only 15 have been observed using HST/STIS and only 2 using IFS (DG Tau and RW Aur). It was vital to increase the sample of objects observed with best accuracy to be able to consolidate some global conclusions and results which really constrain the models. During my thesis, new results increased considerably our understanding of the ejection/accretion problem in young stars and providing a big advance in this field. In particular, my work in the optical of the RY Tau jet (object of this thesis). Other works in the optical domain are that of Hartigan & Morse (2007) who carried out a study on the HH30 jet using HST/STIS observations, or Melnikov et al. (2008) and Melnikov et al. (2009), also using HST/STIS data, who did it on the LkH$_\alpha$ 233 and RW Aur sources respectively. In addition, a study of 6 sources was carried out in the NIR to analyze its molecular emission in the $H_2 \lambda 2.12 \mu$m line (Beck et al., 2008). This is a very innovating work which I also completed in this thesis with a deeper analysis of this emission in the DG Tau jet. Moreover, studies using Radio/mm interferometry have started to be carried out to also prepare the coming of the interferometer ALMA. In particular, the work by Pety et al. (2006) in HH30 and Cabrit et al. (2007) in the case of HH212. Table 2.1 summarizes this evolution and the present state. Even if the number of works has been highly increased, more similar studies are hardly necessary in order to be able to establish some statistics in the physical parameters of the jets in young stellar objects and how this parameters evolve within the evolutionary stage.

3

Line diagnostics

In this chapter I explain the observational diagnostics used to analyze the physical conditions of the gas in the jet. I explain the theoretical basis underlying this kind of study, which is similar to that used in the study of other emission nebulae, but some peculiarities must be considered in the case of jets because of their relatively low ionization, high densities and inhomogeneous conditions present in shocks. I start with a brief description of the observed emission of jets. Then I give the possible mechanisms of heating and cooling and I describe them briefly. Next, I center the discussion on the possible diagnostic analysis. In particular, after a more general description, I discuss the interest and validity of the diagnostics used in the analysis of the data studied in this thesis. I center my discussion, on the one hand, in the [OI]λ6300Å atomic forbidden line, in the optical wavelength domain, which will be used to derive the jet properties and, in particular, the mass-loss rate in the jet of the star RY Tau. On the other hand, in the near infra-red (1-2μm) dataset for DG Tau, both atomic and molecular lines are present. Hence, the discussion is also center on the atomic [FeII]λ1.64μm and [FeII]λ1.53μm lines which will allow me to derive an estimate of the electron density. The brightest of them, [FeII]λ1.64μm, will also be used to derive the mass-loss rate in the atomic jet. The molecular emission analysis will be centered on the $H_2\lambda2.12\mu$m line. I finish with a detailed description of the methods used to derive the mass-loss rate in the jet and the application to the emission lines of interest in this thesis.

3.1 Jet emission

Jets, in young stars, show a very rich emission line spectrum, mainly in atomic forbidden line emission but also in molecular lines. They are usually observed in the optical and in the IR domain, but lines in the UV and in X-ray have also been observed. These atomic lines are usually observed in neutral or singly ionized form, typical of a low excited spectrum, but molecular emission, mainly in H_2 is also observed. Figures 3.1 and 3.2 show an example spectrum of the emission of this kind of object in the optical and IR domain respectively. Figure 3.2 shows not only the atomic emission but also plenty of H_2

molecular lines. The atomic and the molecular components come however from separate regions in the jet. The origin of the molecular emission is unclear but the observed emission transitions come from a gas at temperatures not larger than 3000 or 4000 K. Several possible scenarios have been given. For example this component can be produced either in the external layers of an atomic jet beam, at the interface with the ambient medium or in the wings of a bow shocks, where the velocity of the shock is not high enough to ionize the gas. I will try to distinguish between all these possibilities in detail with the analysis of the molecular component observed in DG Tau and which will be discussed in Ch. 6.

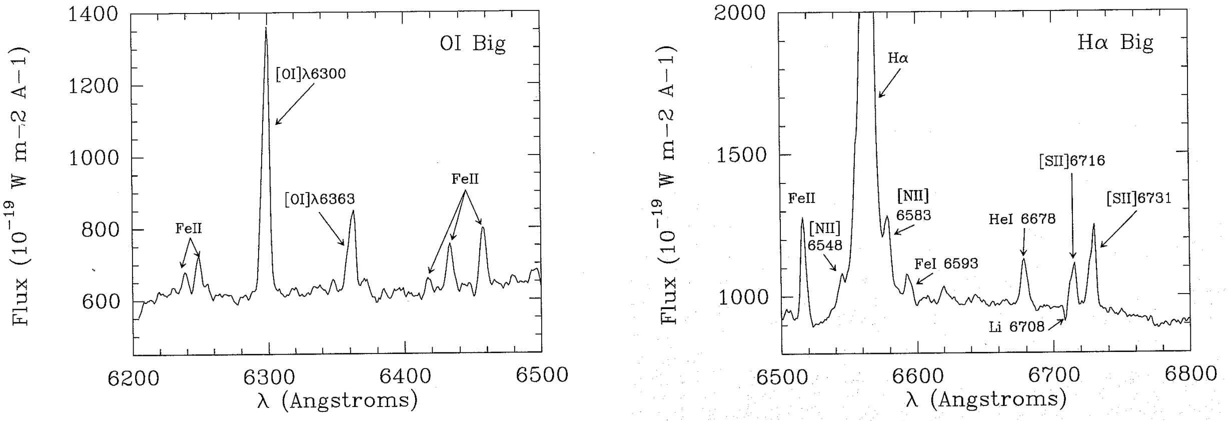

Figure 3.1: Example of the forbidden emission lines observed in an optical spectrum for a T Tauri microjet. In particular this spectrum was observed for the DG Tau star. It shows a variety of elements in both permitted and forbidden lines. Adapted from Lavalley (2000).

In order to understand the dynamics of jets and how they are connected with discs, one needs to learn about the mechanisms which heat the gas inside the jet, and its physical conditions such as the temperature, density, ionization fraction, magnetic fields and internal velocities. All the information about the physical properties of the gas, crucial to probe the models, can be straight-forwardly retrieved from the rich emission observed in the spectra. The technique that I am going to explain was first developed to the analysis of planetary nebulae and HII regions (Osterbrock, 1989) and then extended to other domains. The diagnostic techniques described in this chapter only assume that the gas is excited collisionally, but they are independent on the model for the heating mechanism. So the results allow the validation of one heating model over another, which in turn allows one to identify the most likely physical processes.

The main characteristic of emission lines in jets is that they are optically thin which makes their analysis easier because the emitted light escapes freely and there are no complex radiative transfer issues to consider. However, this is not the only hypothesis made to carry out this kind of study. I summarize in the following these hypotheses which are explained along the different sections of the chapter:

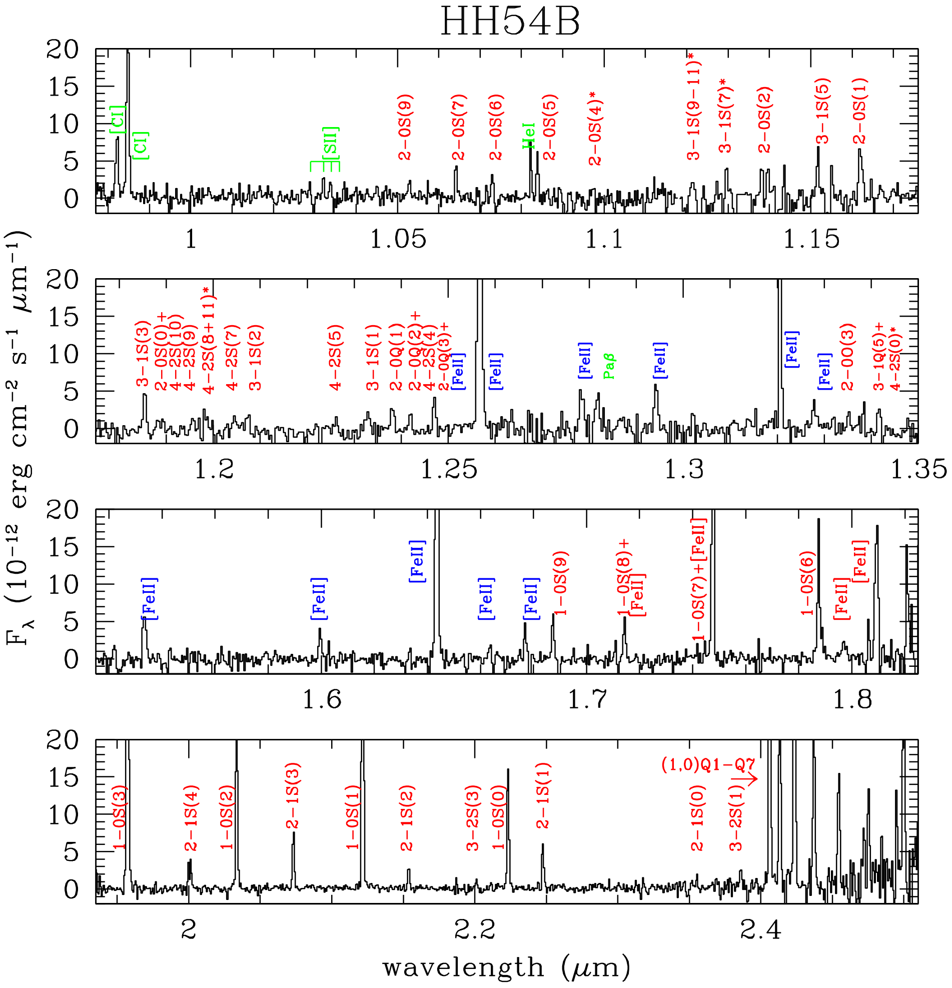

Figure 3.2: Example of the emission lines observed in the near-IR domain for the HH54B object. It shows a number of atomic lines but also molecular H_2 ones. Adapted from Giannini et al. (2006).

- Among the possible excitation processes producing an emission line, both photo-excitation and photo-ionization are neglected.

- Electron collisions are the main excitation process. We do not consider collisions with H atoms because they are an order of magnitude less efficient than that with electrons.

- The level population of atoms is given by statistical equilibrium.

- The atoms considered in the analysis are in ionization equilibrium with hydrogen.

3.1.1 Forbidden Line Emission (FLE): [OI] and [FeII]

Jets in young stellar objects were first observed in optical forbidden lines and one of the brightest lines observed is [OI]λ6300$\overset{\circ}{\text{A}}$. In excitation jet conditions, only the five first levels of the oxygen atom have the relevant energy levels to be considered. Figure 3.3 shows the energy level diagram for this atom. Ratios between transitions connecting $^1D_2$ with ^3P terms (nebular transitions) and transitions connecting $^1S_0$ and $^1D_2$ terms (auroral transitions) are sensitive to the electron temperature (see below). In the particular case of [OI] the ratio used is [OI]λ(6300+6363)/[OI]λ5577 which probes a range of temperatures between 5000 and 20000 K.

Our optical data covers a spectral range which only shows the [OI]λ6300$\overset{\circ}{\text{A}}$ line. This line was used to obtain an estimate of the mass loss rate in the jet, but it was not enough to determine electron temperature. I explain the method used, besides the general method to estimate the temperature from this kind of atomic lines, in the following sections.

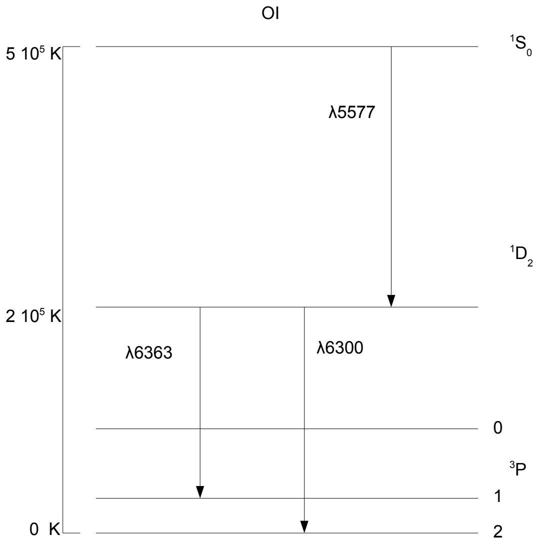

Figure 3.3: Energy level diagram of the neutral oxygen, [OI], with the main optical forbidden emission lines (wavelengths in $\overset{\circ}{\text{A}}$), adapted from Lavalley (2000).

Lately, the study of iron lines from jet spectra has become more and more common, mainly because of the availability of IR spectrographs. In particular, iron shows an extremely rich IR forbidden line spectrum, but also an optical spectrum being in fact one of the main gas coolants in dense atomic jets. In the physical conditions dominating jets environments, due to its rather low ionization potential, only 7.9 eV, it is almost all singly ionized. Moreover, the ionization energy for Fe$^+$ is 16.2eV, sufficiently high to exclude iron ionized twice or more. Figure 3.4 shows the energy level diagram for the 16 first levels of the [Fe II] atom and from which come the observed near and mid-IR iron transitions in jets. The brightest lines in the near-IR are those connecting the fine structure levels of the ^4D term with the levels of the ^4F and ^6D terms. As I will explain more in detail later, certain line ratios can be used to determine the electron density. The most common ratios are 1.533μm/1.644μm, 1.60μm/1.644μm and 1.67μm/1.64μm. The levels involved in these transitions have very similar excitations temperatures, ranging from ~11000 to ~12000 K, but different critical densities, between 10^4 and 10^5 cm^{-3}. Thus they are poorly sensitive to gas temperature but useful for determining densities. These ratios cannot be used as diagnostic tools in low density jets since lines need an electron density higher than 10^3 cm^{-3} to be excited, but they are useful to probe the dense inner parts of the jets.

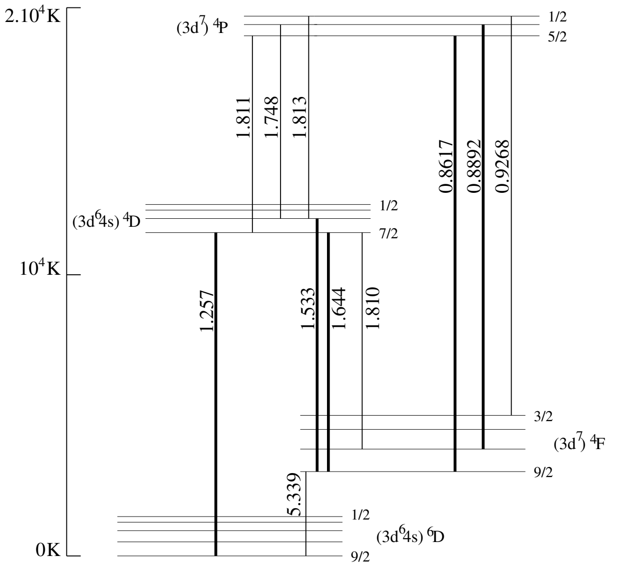

Figure 3.4: Energy level diagram of the more prominent optical and near-infrared [FeII] emission lines (wavelengths in μm) originating from the 16 first levels, adapted from Pesenti et al. (2003).

3.1.2 Molecular emission: H_2

The hydrogen molecule exists in two different states depending on the relative spin of the nuclei, the ortho-H_2 whose H nuclei have parallel spins, and the para-H_2 with antiparallel spins. Transitions between the ortho and para states may only occur through proton exchange reactions with H^0 and H^+. All the ro-vibrational transitions within the electronic ground state are quadrupolar. The selection rules in this case are that Δv=0, $\pm n$ and ΔJ=0, ±2, with v and J the vibrational and rotational quantum numbers, respectively. In jets of T Tauri stars and HH objects the main excitation mechanism producing molecular emission is collisions between H_2 molecules and neutral hydrogen. H_2 is also the only abundant shock molecular coolant observed by ground. Many molecular hydrogen lines are observed in near-IR spectra, which come from rotational transitions originating from the v=1-4 vibrational levels. One of the most studied lines is the 1-0 S(1)[1] line at 2.12μm. These lines can be used to probe the temperature and density of the gas, see below.

3.2 Heating mechanisms of the gas

What we observe in emission lines is the cooling of hot gas in the jet. Some heating mechanisms are invoked to maintain the needed temperatures to excite the gas, but these mechanisms must operate also along the length of the jet to allow their detection at distances far from the source. Below I summarize the main processes considered.

Ambipolar diffusion:

In a very simple way, the gas is heated due to the motion of ion and neutral atoms. In ideal MHD, charged particles are "frozen" to the magnetic fields lines, while neutral atoms are coupled by collisions to the charged particles. In non-ideal MHD, the dissipation of electric currents $\mathbf{J}$ provides a local heating term per unit volume. In a multi-component gas, with electrons and several ion and neutral species the generalized Ohm's law writes:

$$\mathbf{E} + \frac{v}{c} \times \mathbf{B} = \bar{\eta}\mathbf{J} - \left(\frac{\bar{\rho_n}}{\rho}\right)^2 \frac{\frac{1}{c^2}(\mathbf{J} \times \mathbf{B}) \times \mathbf{B}}{m_{in}\bar{n}_i\nu_{in}} - \frac{\nabla P_e}{en_e} + \frac{\mathbf{J} \times \mathbf{B}}{en_e c} \tag{3.1}$$

where $\mathbf{E}$ and $\mathbf{B}$ are the electric and magnetic fields, v the fluid velocity and c the speed of light. η is the fluid electrical resistivity, ρ and ρ_n are the total and neutral mass density, m_{in} the reduced ion-neutral mass, n_i the ionic density and ν_{in} the ion-neutral collision frequency. The overline stands for a sum over all chemical elements relevant to a given quantity.

The first term appearing in the right hand side of the equation is the usual Ohm's term, while the second describes the ambipolar diffusion, the third is the electric field due to the electron pressure and the last is the Hall term. This last term does not provide a net dissipation and the dissipation due to the electronic pressure is quite negligible (Garcia et al., 2001b). Hence, two terms mainly contribute to the gas heating: the Ohmic heating which arises mainly from ion-electron drag and the ambipolar diffusion heating due to ion-neutral drag.

The time scale for the magnetic field diffusion is inversely proportional to the ionization fraction, producing a slow diffusion for low-ionization jets. In Garcia et al. (2001b), authors presented the computed thermal and ionization structure of self-similar, magnetically-driven, atomic disc wind heated by ambipolar diffusion. They predicted temperatures of 10^4 K in atomic disc winds and of 2000 K in the case of molecular disc winds. In a more recent work, Panoglou et al. (2009) found similar results for the molecular component of a disc wind.

---

[1] Notation of H_2 transitions: v_{up}-$v_{low}\Delta$J(J$_{low}$), where v_{up}-v_{low} is the change in vibrational state and ΔJ=-2 is denoted by S, ΔJ=+2 by O and ΔJ=0 by Q.

Mechanical heating by turbulence:

When a supersonic jet is propagating in the ambient medium, the velocity difference across the layer between the two fluids causes the so-called Kelvin-Helmholtz instabilities. This interaction between the jet and the environment produces a turbulent mixing layer which grows both into the jet and into the environment. When it propagates into the jet, this turbulence heats the gas. This effect have been study and explained in detail by Canto & Raga (1991), among others, and in particular, they carried out an analytical study of this turbulence through a simplified model based on a simple turbulent viscosity description of the dissipation and transport associated with the turbulence. They found that the mixing layers can in principle substantially contribute to the emission from stellar jets, since they have a sizeable radiative luminosity. Taylor & Raga (1995) extended this work to incorporate a detailed treatment of the chemical history of the entrained molecular gas through a numerical calculation. They found that the mixing layer is hot, with temperatures of 10^4 K and only dissociates H_2 partially, which implies that a number of molecules can survive in the high velocity gas, contrary to the slower and cooler typical observed “molecular flows”.

Other authors, like Binette et al. (1999) resolved the energy equation in the radiative, steady mixing layer caused by a jet with high Mach number[2]. They carried out a non-equilibrium study of the ionization fraction taking into account the radiative processes considered in the MAPPINGS code to obtain the colling function. They found that the temperature cross-section changes from parabolic to flat-topped as the layer width increases. On the contrary, they found that the ionization fraction is always out of coronal equilibrium, because of turbulent diffusion of neutral gas from the jet and external medium into the layer.

Lavalley-Fouquet et al. (2000) carried out a deep comparison between line ratios from observations of DG Tau in the optical, with predictions for models of different heating mechanisms. In particular, they compared with the model by Binette et al. (1999) for the mixing layer heating mechanism. They found that the predictions for the mixing layer of Binette et al. (1999) where hotter and of lower ionization than observations but for environment densities higher than 10^7 cm^{-3}.

Photoelectric heating and X-rays:

Ultra-violet and X-ray radiation from the star are important sources of gas heating. The stellar radiation penetrates the disc and heats the material and dissociates the molecules in the uppermost surface layers of the disc. This radiation gets diluted with increasing distance from the star and as one goes deeper into the surface layer, the gas becomes molecular (Bergin et al., 2007).

---

[2] The Mach number, M, is the speed of an object moving through air, or any fluid substance, divided by the speed of sound as it is in that substance, $M=v_{object}/c_{sound}$.

In T Tauri stars, the Ly_{α} photons dominate the radiation field and play an important role in the photo-dissociation of molecules (Dullemond et al., 2007). The photoelectric heating process is often the dominant heating mechanism. The FUV photons are absorbed by a dust grain or a PAH molecule which emits an electron. This electron gets thermalized and heats the gas. The efficiency of this process depends on the shape of the radiation field but also on the grain charge, dust grain size and composition (Dullemond et al., 2007).

The X-ray radiation from the star can ionize hydrogen gas and be one of the important heating mechanism in protoplanetary discs (Nomura et al., 2007), but it heats mostly the uppermost surface layers, as their heating drops with the column density.

Shocks:

Nowadays, it is well accepted that in the jet front the heating is produced by shocks since a gas leaving the star at a supersonic velocity will create a shock when it interacts with the surrounded cloud.

Inside the jet body, this hypothesis is less obvious. Some scenarios producing shocks (steady or in movement) inside the jet were invoked to try to explain the knot morphology observed. For example they could be produced by ejection pulsation or by supersonic instabilities. Two kind of models exist, one is centered on the hydrodynamic or MHD evolution in large spatial scales and the second study the detailed microscopic processes for a single shock front. This first kind of model tries to obtain the evolutionary characteristics of the ejected material and the other kind of models tries to reproduce the observed emission in the stationary case. In this work I used models from the second group for the atomic iron lines and for the molecular emission in the H_2 lines and that I will describe briefly in the following.

Two types of shocks are present, J(ump)-type and C(ontinuous)-type shocks. The first ones have a discontinuity in the density, temperature and velocity at the front. The second type heats and compresses the gas gradually as magnetic fields accelerate ions through the neutral gas. In atomic gas, shocks are typically J-type, while molecular shocks are often of the C-type.

- In the context of atomic gas, shocks have been extensively modelled and specific diagnostics in optical forbidden line ratio diagrams have been developed. Some of these models designed to reproduce the optical and ultraviolet spectra have already predicted fluxes for infrared emission lines heated by atomic J-type shocks (Hartigan et al., 1994; Dopita & Sutherland, 1996). The codes include cooling from non-LTE atomic populations that are not in ionization equilibrium, follow atomic cooling, and solve radiative transfer of ionizing photons as gas travels throughout the cooling zone. They also include magnetic fields. However, these models did not include the iron atom. Hartigan et al. (2004) developed a shock model for Fe II based on the Raymond-Cox code described in detail in Raymond (1979). The code solves the total gas cooling at each grid point in the postshock flow. For Fe II this involves resolving a set of 159 equations for the non-equilibrium level populations. The radiation field is still included in the calculations both upstream and downstream of the shock front, even though there is not enough energetic photons to ionize the preshock gas, because of the low shock velocities considered in the model. I will use the results of this model to estimate the mass-loss rate in the atomic jet of DG Tau using the bright [FeII]1.64μm line under the assumption that this line is excited by shocks (Sec. 3.6.1).

- Moreover, important efforts have been made to extend this kind of prediction to the molecular emission. 2D and 3D bow shock models have been constructed by for example Fragile et al. (2005) and Smith et al. (2003), respectively. These models did not include detailed chemical reactions or the full set of magneto-hydrodynamical equations in a self-consistent manner. However Kristensen et al. (2008) following the 1D steady state, multi-fluid shock models of Flower & Pineau des Forêts (2003) combine for the first time both a self-consistent treatment of the chemistry and physics with the geometry. The model integrates in parallel the magnetohydrodynamic equations with chemical reaction rate equations in a self-consistent manner. Abundances of 136 species linked by 1040 reactions are calculated at each step of the model, as well as 100 H_2 rovibrational level populations (including transitions between rovibrational levels). The transverse component of the magnetic field is assumed to be frozen into the charged fluid of the preshock gas. I will use the result of these models in Sec. 3.6.2 to obtain a mass-loss estimate and constrain the heating mechanism in the molecular outflow observed in DG Tau and to fix upper limits to the magnetic field presented.

3.3 Excitation and ionization process

An emission line is observed in the spectrum because atom transitions from an excited bound state to a lower energy bound state occur, or also by electron recombination to a lower ionization state. A number of mechanisms to ionize, recombine and excite or de-excite an atom play an important role to populate or depopulate the different energy levels but not all of them are significantly in the case of jets.

3.3.1 Ionization and recombination process

Photoionization process in which an incident photon ejects one or more electrons from the atom usually does not dominate the ionization balance within stellar jets. T Tauri stars have relatively cool photospheres and do not emit substantial amounts of ionizing radiation. However, photoionization is an important process in the cooling zones of J-shock waves, where, for example, Lyman continuum photons propagate both upstream and downstream of the shock gas and they must be included in the shocks models (Hartigan & Morse, 2007).

Other processes taken into account in the ionization state determination are the collisional ionization, the radiative and dielectric recombination and the charge exchange with the hydrogen:

- Dielectric recombination occurs when a free electron gives almost all its kinetic energy to excite a bounded electron, and at the same time it is captured by the atom in a very excited level. In this case the atom is at the lower ionization state but with two excited electrons. This configuration is very unstable and cannot be maintained for a long time.

- Because of the high hydrogen abundance, charge exchange with the hydrogen must be considered, even if the probability of a collision between two atoms is lower than the electron-atom case (since the mean electron velocity much higher than atom velocity, due to the mass contrast).

In particular in stellar jets, as in all low-excitations nebulae, we assume that Sulfur and Iron are completely singly ionized. In addition, as I said before, photoionization is neglected, actually, Bacciotti & Eislöffel (1999) found that oxygen is completely regulated by charge exchange reactions with the hydrogen, while for nitrogen the neglect of photoionization is justified as long as x_e is lower than 0.5-0.6. In fact, for oxygen charge-exchange rates are four orders of magnitude larger than the recombination rates (and hence absolutely dominant) (Osterbrock, 1989),for nitrogen the charge-exchange rate coefficients are three orders of magnitude smaller than for oxygen, and only slightly larger than the recombination rates. However, the recombination time scale for nitrogen is about three times smaller than for hydrogen.

3.3.2 Excitation and de-excitation process

Given an ionization state, let us consider the processes that can excite or de-excite the atom. I begin by reviewing the radiative process. Let us consider two particular levels, i and j with i > j. The probability that a radiative transition from the i level to the j level occurs is given by the spontaneous emission coefficient A_{ij}, also called Einstein coefficient. This coefficient represents the rate at which an atom in the excited i level will decay to level j, emitting a photon of energy $h\nu_{ij}$ and it does not depend upon the level populations of other atoms in the gas and it is obtained from quantum mechanical considerations. In order of magnitude it is $\sim 10^6$-10^7 s^{-1} for the allowed lines and $\sim 10^{-6}$-10^{-2} s^{-1} for the forbidden ones. Hence, the de-excitation rate by spontaneous emission is given by $n_i A_{ij}$ where n_i is the number of Fe$^+$ ions excited at i level per unit volume.

In another emission mechanism, an electron, perturbed by a photon having the correct energy, may drop to a lower energy level. The stimulated emission rate is thus given by

$n_i u_{ij} B_{ij}$ where B_{ij} is the stimulated emission coefficient and u_{ij} is the monochromatic energy density at the wavelength of the transition. The induced and spontaneous emission coefficients can be related through the Einstein relation, obtaining:

$$A_{ij} = B_{ij} \frac{8\pi h}{\lambda_{ij}^3}$$

where h is the Planck constant and λ_{ij} is the wavelength of the transition. Assuming a black body emission, the spontaneous de-excitation is about four times the stimulated one for the observed optical and IR wavelengths. In the case of jets, far from the Local Thermodynamic Equilibrium (LTE), this difference is even bigger and the stimulated emission can be neglected. These processes occur if the population of the excited level is high enough. As well as this, other process can put an electron in a excited level.

- Photoexcitation and fluorescence:

Like photoionization, photoexcitation is a secondary process in stellar jets. The only transitions affected by photoexcitation in a significant way are permitted transitions where the lower energy level is populated enough to make the transition optically thick (resonant lines). These two processes can be neglected in the case of forbidden line emission in jets.

UV Fluorescence effect can be important in the case of the H_2 emission. The FUV radiation or Ly_α photons produced in the star or in shocks, pump the molecular hydrogen into an electronically-excited state populating the higher level which de-excites in cascade emitting Near-IR lines through the vibration-rotation transitions (e.g. Sternberg & Dalgarno, 1989). At high density and high FUV flux, which are the physical conditions of the gas at the base of the jet, the H_2 line is thermalized.

- Collisions:

The other important mechanism to both excite and de-excite an atom is by collisions. The jet is partially ionized making the collisions with the free electrons the more effective mechanism to excite or de-excite the atom. A free electron can collide with the atom, transfer some of its kinetic energy to the atom raising it to an excited state, or it also can de-excite the atom to a lower excited level. The parameters quantifying the collisional mechanism are the collisional coefficients. Let consider again two levels i and j (i > j), the collisional coefficient q_{ij} for the transition from i to j, is defined as the number of transitions per time, caused by electrons with velocity v and total density n_e, and integrated in velocity:

$$q_{ij} = \int_0^\infty f(v) v \sigma_{ij}(v) (4\pi v^2 dv) \tag{3.2}$$

where $f(v) \propto v^2 e^{-mv^2/2kT}$ is a Maxwell-Boltzmann velocity distribution and $\sigma_{ij}(v)$ is the cross section of interaction which can be written:

$$\sigma_{ij}(v) = \frac{\pi}{g_i}\Big(\frac{\hbar}{2m_e v}\Big)^2 \Omega_{ij} \tag{3.3}$$

where m_e is the electron mass, g_i is the statistical weight of level i and Ω_{ij} is the collision strength averaged on the electron energy:

$$\Omega_{ij} = \int_0^\infty \Omega_{ij}(E) e^{-E/kT} d(E/kT) \text{ with } E = \frac{1}{2}mv^2 \tag{3.4}$$

Ω_{ij} depends in general on the temperature, but this dependence varies depending on the electronic configuration of a given atom. It is more important for neutral atoms.

Therefore, the collisional de-excitation coefficient is given by:

$$q_{ij} \simeq \frac{8.63 \times 10^6}{g_i\sqrt{T_e}}\Omega_{ij}\ (cm^3 s^{-1}) \tag{3.5}$$

The collisional excitation coefficient is obtained assuming Local Thermodynamic Equilibrium (LTE). In this case the radiative rate is zero and the collisional excitation are balance by the collisional de-excitation: $q_{ij}n_i n_e = q_{ji}n_j n_e$. The relationship between the excitation and de-excitation collisional coefficients is thus given by the *detailed balance* equation:

$$\frac{q_{ij}}{q_{ji}} = \frac{g_j}{g_i} e^{-(E_j - E_i)/kT} \tag{3.6}$$

and the collisional coefficient is written as:

$$q_{ji} = \frac{8.63 \times 10^{-6}}{\sqrt{T_e} g_j} e^{-(E_j - E_i)/kT_e} \Omega_{ij} \tag{3.7}$$

where E_i and E_j are the correspondent energy for the i and j levels related to the ground, and k is the Boltzmann constant.

3.4 Emissivity

The volume emission coefficient, called emissivity, of one transition between level i and j is defined as the energy per unit volume, per second, per steradian in the emission line coming from the gas, that is:

$$\epsilon_{ij} = \frac{n_i A_{ij} h\nu_{ij}}{4\pi} \tag{3.8}$$

where n_i is the number density of atoms (cm^{-3}), A_{ji} is the Einstein coefficient for the transition (units s^{-1}), h is the Planck's constant and ν_{ji} is the line frequency. Hence the emissivity of the line, ϵ_{ji}, is in erg cm^{-3} s^{-1} str^{-1}.

The A_{ji} and ν_{ji} are calculated from quantum mechanical principals and the emissivity depends only on the upper level population which can be rewritten as follows:

$$n_j = n_H \left(\frac{n_X}{n_H}\right)\left(\frac{n_{X^k}}{n_X}\right)\left(\frac{n_j}{n_{X^k}}\right) \tag{3.9}$$

where n_H is the hydrogen density, X denotes the considered atom in the ionization state X^k. The line emissivity therefore depends on the elemental abundance, the ionization state and the excitation state of the element. The population on the upper limit will be obtained under the assumption of statistical equilibrium and the term $\frac{n_{X^k}}{n_X}$ is obtained by considering ionization equilibrium. In this manner, the line emissivity will be a function of the electron density and the temperature.

3.4.1 Ionization State

A given X element is in ionization equilibrium when its ionization fraction reaches a steady value: $\frac{d(X^i/X)}{dt} = 0$. The ionization state is then given by the equilibrium between the ionization terms and the recombination ones which, in an isolate system, are related to the local temperature and density.

In the case of LTE, the energy distribution of the gas particles is governed by the elastic collisions between them, the relative energy level populations are given by the Boltzmann equation and the ionization equilibrium by the Saha equation.

One of the hypothesis of the Boltzmann equation is that all the processes considered are balanced by their opposite. In the case of a low density gas the collisional ionization cannot be balanced by the three-body recombination (a free electron takes the energy lost by the recombined electron) because the probability of this process is very low. In this case the hypothesis is not satisfied and the *coronal equilibrium state* is defined as the state where the collisional ionization between an electron and an atom are balanced by the radiative and dielectric recombination. In this case the ionization fraction is given by the temperature.

In the low excitation conditions in the beam of stellar jets, the ionization state of the oxygen and nitrogen is dominated by charge exchange with the Hydrogen (Bacciotti & Eislöffel, 1999). The Hydrogen is not at the coronal equilibrium because of the slow recombination time against the dynamical time inside the beam (Lavalley, 2000). The ionization fraction is then a free parameter and it is found through dedicated diagnostics as the BE technique (Bacciotti et al. (1995) and explained in detail in Sec. 3.5.3). Keeping this in mind, lets first see the equilibrium equations derived for the case of the Hydrogen on one side, and the oxygen and nitrogen on the other side.

Hydrogen

The ionization coronal equilibrium in the case of the hydrogen can be written as:

$$n_e n_{H^0} C_H = n_e n_{H^+} \alpha_H \tag{3.10}$$

where C_H and α_H are the collisional ionization and radiative recombination coefficients for the hydrogen, respectively (Osterbrock, 1989). The dielectronic recombination has no meaning in this case. The ionization fraction is thus given by:

$$x_e = \frac{n_{H^+}}{n_H} = \frac{C_H}{C_H + \alpha_H} \tag{3.11}$$

Ionization equilibrium for oxygen and nitrogen

Although photo-ionization processes are probably not very important in the case of stellar jets, collisional ionization terms should be considered for the ionization state of O and N, given the presence of shocks along the beams. Moreover radiative plus dielectronic recombination can in principle compete with charge exchange:

$$n_e n(X^0) C_X + n_{H^+} n(X^0) \delta_X = n_{H^0} n(X^+) \delta'_X + n_e n(X^+) \alpha_X \tag{3.12}$$

where $n_e C_X$ is the collisional ionization rate par volume unit, $n_e \alpha_X$ the recombination (radiative and dielectronic) rate par volume unit, and $n_{H^+} \delta_X$ and $n_{H^0} \delta'_X$ are the ionization and recombination rates dues to the charge exchange par volume unit. The coefficients C_X,α_X,δ_X and δ'_X are calculated from atomic physic considerations and depend on the temperature.

The ionization fraction for the element X, considering the free electrons coming from the hydrogen ionization, can be written as:

$$\frac{n(X^+)}{n(X^0)} = \frac{x_e (C_X + \delta_X)}{x_e \alpha_X + \delta'_X (1 - x_e)} \tag{3.13}$$

From this equation, first introduced by Bacciotti et al. (1995), the ionization fraction of a particular atom depends on x_e and T_e which are independent variables. At the coronal equilibrium (x_e given by Eq. 3.11), the ionization fraction of the X element depends only on the electron temperature.

3.4.2 Statistical Equilibrium Equations (SEE) and level population

It is assumed that in a parcel of gas the level populations of atoms are in statistical equilibrium, that is, levels are populated at a rate equals to the rate at which they are depopulated. The characteristic time to establish the equilibrium depends on each radiative or collisional process. The de-excitation radiative rates are typically between 10^{-6} and 10^{-2} s^{-1}, and then the time scale is between 10^2 and 10^6 s. For the collisional process, it depends on the temperature and on the density. The collisional rates goes from 10^{-11} s^{-1} for T_e=10^3 K and n_e=10 cm^{-3}, to 10^{-4} s^{-1} for T_e=10^4 K and n_e=10^4 cm^{-3}. The worst case is if the level population is dominated by radiative process, hence the characteristic time is 10^6 s which is much less that the dynamic time, of some months in jets (t$_{dyn}$ > 7×10^6s for velocities < 300km/s in a 0.1″ resolution element at d=140 pc). Therefore, the statistical equilibrium hypothesis for jets is reasonable.

Two-level atoms

We are going to start to study a simple 2-level atom. In statistical equilibrium, we balance the rates in and out of the upper state, labeled level 2. For the same reason as we neglected photoionization processes when we studied the ionization state, photoexcitation processes will also be neglected in the derivation of the level population. Collisional excitation, de-excitation, and radiative decay are the dominant processes and must be balanced, then we have:

$$n_1 n_e q_{12} = n_2 A_{21} + n_2 n_e q_{21} \tag{3.14}$$

where n_e is the electron density, n_1 and n_2 are the lower and the upper level population and q_{12} and q_{21} are the rate coefficients for collisional excitation and de-excitation, respectively in units of cm^{3}s^{-1} and A_{21} is the Einstein coefficient for the 2→1 transition.

Therefore, we derive the ratio between the upper and lower level population as:

$$\frac{n_2}{n_1} = \frac{q_{12}}{q_{21}}\Big[\frac{1}{1 + n_{cr}/n_e}\Big] \tag{3.15}$$

where we define $n_{cr} = A_{21}/q_{21}$ as the *critical density* of level 2. This n_{cr} refers to the number density of electrons, not to the number density of the atoms that are the targets for the collisions. It is defined to be when collisional de-excitations are equal to the radiative de-excitations. It separates two regimes of electron density. If $n_e \ll n_{cr}$, equivalent to $n_e q_{21} \ll A_{21}$, each collisional de-excitation is followed by a radiative decay and the emission of a photon. Combining Eqs. 3.5 and 3.7, the ratio between the two levels populations in the case of low density is:

$$\frac{n_2}{n_1} \simeq \frac{n_e}{n_{cr}} e^{-(E_j - E_i)/kT_e} \tag{3.16}$$

In the contrary, if $n_e \gg n_{cr}$ ($n_e q_{21} \gg A_{21}$), the radiative de-excitations are negligible and collisonal processes are dominant. Every collisional excitation is balanced by a collisional de-excitation. We obtain:

$$\frac{n_2}{n_1} \simeq \frac{q_{12}}{q_{21}} = \frac{g_2}{g_1} e^{-(E_2 - E_1)/kT_e} \tag{3.17}$$

we identify in this last equation the Boltzmann function indicating that the atom is at LTE. The population in the second level does not depend on the density, n_e, but on the electron temperature, T_e.

Line	n_{cr} (cm^{-3})
[OI]λ6300 Å	1.8×10^6
[FeII]λ1.644 μm	5.6×10^4
[FeII]λ1.533 μm	4.6×10^4

Table 3.1: Critical densities for the three atomic lines studied in the thesis at an electronic temperature of T_e=10^4, typical in the case of jets in YSOs.

n-level generalization

In the general case of a n-level atom, we have a statistical equilibrium equation for each excited i-level and we have to resolve the set of equations together. In typical jet conditions, only the lowest levels are excited and we typically have a system of three to five equations, but for the general case, we can write:

$$\sum_{j\neq i} n_j n_e q_{ji} + \sum_{j>i} n_j A_{ji} = \sum_{j\neq i} n_i n_e q_{ij} + \sum_{j<i} n_i A_{ij} \tag{3.18}$$

We have an equation like this for each level and the set of equations are closed with the mass conservation equation, that is, the sum of each level number density must be the total ion density:

$$\sum_{j=1}^{n-level} n_j = n_{X^k} \tag{3.19}$$

The critical density for level i in this case is written as:

$$n_{cr}(i) = \frac{\sum_{j<i} A_{ij}}{\sum_{j\neq i} q_{ij}} \tag{3.20}$$

Table 3.1 gives the critical densities for the three lines studied in this thesis obtained for an electron temperature of 10^4 K that is a typical temperature for jets.

The generalization for the i level population in the two distinct density regimes can be written as:

- High density regime: collisional processes dominate and the population of level i is given by its Local Thermodynamic Equilibrium value.

  $$\frac{n_i}{n} \simeq \frac{g_i e^{-E_i/kT}}{\sum g_j e^{-E_j/kT}} \tag{3.21}$$

  where $n = \sum n_j$. As we saw in the 2-level atom case, the level population does not depend on the electron density and the line emissivity increases linearly with the total density n_H.

- Low density regime: collisions from level i are negligible.

$$\frac{n_i}{n} \simeq \frac{n_e}{A_{ij}} \sum_{j \geq i} q_{0j} \tag{3.22}$$

where q_{0j} is the collisional excitation coefficient to state j from the ground state. In this case emissivity increases as the square of the total density.

3.5 Diagnostics of physical conditions

In this section I will describe the common technique used to constrain the physical conditions in the jet. The concept underlying any diagnostic technique is to compare a grid of models of the emission with the observed data, and from this comparison to retrieve the most likely values of the physical quantities for the gas. It uses line ratios between forbidden line intensities both in the optical and in IR domains without any assumptions on the nature of the heating and ionization mechanisms. Depending on the lines chosen we can derive different important physical parameters of the gas as electronic density n_e, hydrogen ionization fraction x_e or electronic temperature T_e. It is important to keep in mind that the excitation conditions traced using IR lines are different from those traced using optical ones. The IR [FeII] lines probe denser and colder gas. The data analyzed in this work has the information needed to derive the electron density value from iron lines, thus I will detail the procedure followed with these lines.

3.5.1 Electronic density

To derive the electronic density from line ratios, one must use transitions from the same element, in the same ionization state and originating from upper levels of similar excitations energies to minimize the effect of electronic temperature but these lines have to show different critical densities. The determination of the electron density involves in general three levels, two transitions. We keep in mind the expression for the line emissivity and the level population, obtained from considering statistical equilibrium. Hence, the intensity ratio for a 3-level atom, in the low density limit, is given by $I_{31}/I_{21} = q_{13}/q_{12}$, and in the high density limit by $I_{31}/I_{21} = (q_{13}/q_{12}) \times (A_{21}/A_{31})$. Thus, the line ratio changes from one asymptotic value to a different one between the two regimes. When the electron density lies between the two, the observed ratio provides a good estimate of the electron density.

An example of such a density diagnostic in the optical is the [SII]λ6716 Å/[SII]λ6731 Å ratio. This line ratio traces electron densities up to 10^4 cm^{-3}. Our optical data does not show these emission lines and for the observed object, the electron density could not be estimated. However, another useful density diagnostic is the [FeII]λ1.533 μm/[FeII]λ1.644 μm ratio, these two lines are two of the strongest near-infrared lines in jets spectra from YSOs. In particular, our IR observations show these two lines and an estimate of the spatial electron density distribution was achieved (detailed below).

Many other important line ratios are presented in other wavelength domains and the trace other electron density ranges. In particular, the ratio between the two red lines [FeII]λ7155 Å and [FeII]λ8617 Å, in the optical, is sensible to electron densities of $n_e \sim 10^5$-10^7 cm^{-3} (Bautista & Pradhan, 1998; Hartigan et al., 2004). Other tracers for densities larger than 10^6 cm^{-3} are the permitted CaIIλ8542 Å and the forbidden [CaII]λ7291 Å transitions. These lines are good tracers of the electron density if we can ignore the influence of the fluorescence in the level population. For this reason this tracer has been used in HH objects where the dominant excitation mechanism appears to be through collisions (Hartigan et al., 2004; Nisini et al., 2005).

Electronic density from [FeII] lines

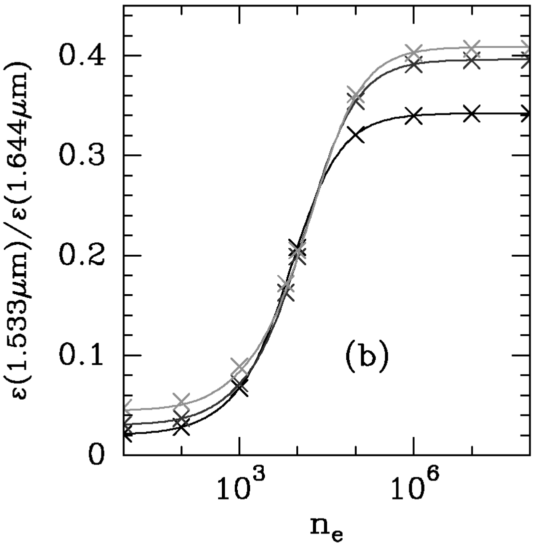

Figure 3.5: Theoretical [FeII]λ1.53μm/λ1.64μm ratio as a function of n$_e$ for three different electronic temperatures, 3000, 10 000 and 20 000 K, increasing from bottom to top. Adapted from Fig. 2 of Pesenti et al. (2003).

The ratio between the two strong [FeII] lines, [FeII]λ1.53μm and λ1.64μm is a very useful density diagnostic in the range between 10^3 and 10^5 cm^{-3}. The upper level of these two transitions comes from the same structure level ^{4}D (Fig. 3.4) having then similar excitations energies minimizing the effect of electronic temperature in the ratio but with different critical densities making this ratio directly related with n$_e$. This ratio has also the advantage of being little sensitive to reddening due to extinction in the line of sight.

From Eq. 3.8 and considering the three level involved (Fig. 3.4) in the transitions, we obtain an expression for the emissivity rate given by:

$$\frac{\epsilon_{1.53}}{\epsilon_{1.64}} = \frac{n_{^4D_{5/2}}}{n_{^4D_{7/2}}} \frac{\nu_{1.53}}{\nu_{1.64}} \frac{A_{^4D_{5/2} \rightarrow ^4F_{9/2}}}{A_{^4D_{7/2} \rightarrow ^4F_{9/2}}} \tag{3.23}$$

Figure 3.5 shows this theoretical ratio as a function of the electron density for three electron temperatures, modeling by Pesenti et al. (2003). The authors consider the first 16 levels of the [FeII] atom in the set of statistical equilibrium equations to obtain the level populations. It is a simple model, valid for excitation temperatures below 2×10^4 K, but it is generally applicable to stellar jets.

3.5.2 Electronic temperature

To derive electron temperature, intensity ratios of transitions of the same element with different excitation energy are used. The commonly used lines in the optical are the nebular and the auroral transitions in elements having a ^2p or ^4p configuration (Hartigan, 2008). In this case, in the low density limit, the collision rate coefficients depends also on the temperature, $I_{31}/I_{21}=q_{13}/q_{12}=\Omega_{13}/\Omega_{12}\times\exp(-(E_3-E_2)/kT)$. In the high density limit, the same dependence is kept. In this case, the intensity ratio depends both on the temperature and the electron density. To obtain a relation only depending on the temperature, a ratio involving three transitions coming from four different levels is usually considered:

$$\frac{\epsilon_{31} + \epsilon_{32}}{\epsilon_{43}} = \frac{n_3}{n_4} \frac{\nu_{31}A_{31} + \nu_{32}A_{32}}{\nu_{43}A_{43}} \tag{3.24}$$

Some examples of such a ratio are the [OI]λ(6300+6363)/[OI]λ5577 (Fig. 3.3) or [NII]λ(6548+6583)/[NII]λ5755, both in the optical. These lines are very good tracers of electron temperature being sensitive to a large range, between 5000 and 20000 K. However, in jet conditions the nebular lines are much stronger than the auroral ones making their use difficult to determine the temperature.

There are other useful diagnostics from iron line ratios. Transitions originated from the ^4P term, with excitation energies of ∼19000 K, are considered. One can use lines such as the 1.811, 1.813 or 0.8617 μm lines, or the ratio [FeII]1.644μm/[FeII]8620Å which probes temperatures between 4000 and 15000 K. The problem with those lines is that one needs to combine observations made with different instruments because they involve different wavelength domains (see Podio et al. (2006)), and some of them even need the use of spatial instruments due to the poor atmospheric transmission at some particular wavelengths.

Diagnostic diagrams

The diagnostic diagrams are a tool which combine line ratios sensitive to the electron density and ratios sensitive to the electron temperature. This kind of diagrams allows us to obtain the two parameters simultaneously.

In the optical, Lavalley (2000) analyzed in detail the dependence with n_e, T_e and x_e for some ratios between [SII], [NII] and [OI] lines. She found that the [SII]λ6731/[OI]λ6300 ratio depends on the three variables simultaneously, being very dependent on the temperature and independent on n_e for $n_e \leq 10^4$ cm^{-3}. She also showed that a diagnostic diagram combining this ratio with the [SII]λ6716/[SII]λ6731 ratio, which is very sensitive to the electron density, is a powerful tool to obtain both temperature and density, Fig. 3.6. The higher temperature is placed towards the left and the higher densities are placed towards the bottom of the graph. The region at the highest electron density (n_e ~10^4 cm^{-3}) are compacted at the lower part of the plot.

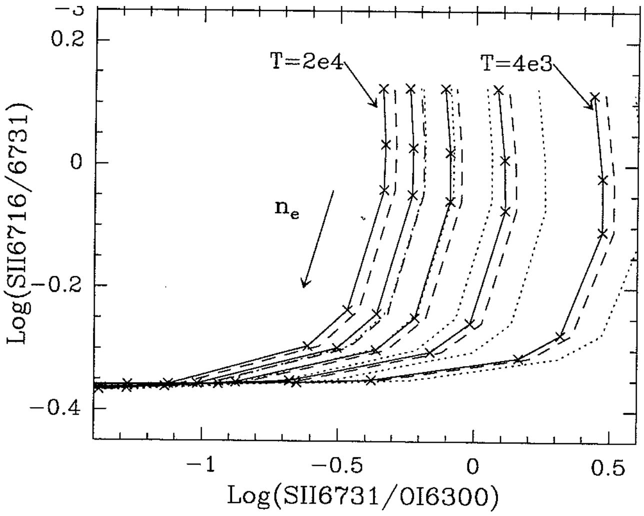

Figure 3.6: Diagnostic diagram from Lavalley (2000). Solid lines: x_e=0.01, dashed lines: x_e=0.1 and dotted lines: x_e=0.3 for temperatures increasing from 4×10^3 at the right of the graphic to 2×10^4 at the left. Each line connects different electron density values n_e=10^2, 5×10^2, 10^3, 5×10^3, 10^4, 5×10^4, 10^5, 5×10^5, 10^6, 5×10^6 cm^{-3}.

Pesenti et al. (2003) proposed a diagnostic diagram using [FeII] lines. The authors combine the density sensitive [FeII] 1.644μm/1.533μm ratio with the temperature sensitive [FeII] 0.8617 μm/1.257 μm ratio, to give a direct measure of (n_e, T_e). A similar diagram is presented in Nisini et al. (2005) using the same density sensitive [FeII] 1.644μm/1.533μm ratio but in this cas,e against [FeII] 1.644μm/0.862μm ratio. This two diagrams are presented in the Fig. 3.7.

The combination of optical and NIR analysis using a variety of diagnostic lines has shown to be a very powerful tool (Nisini et al., 2005; Podio et al., 2006). On the one hand, it allows the use of ratios between lines from the same species that are well separated in wavelength thereby providing more stringent constraints on excitation conditions, for example: [Fe II]8620Å/1.64 μm and the [SII]6716,6731Å/1.03 μm ratios, which are very

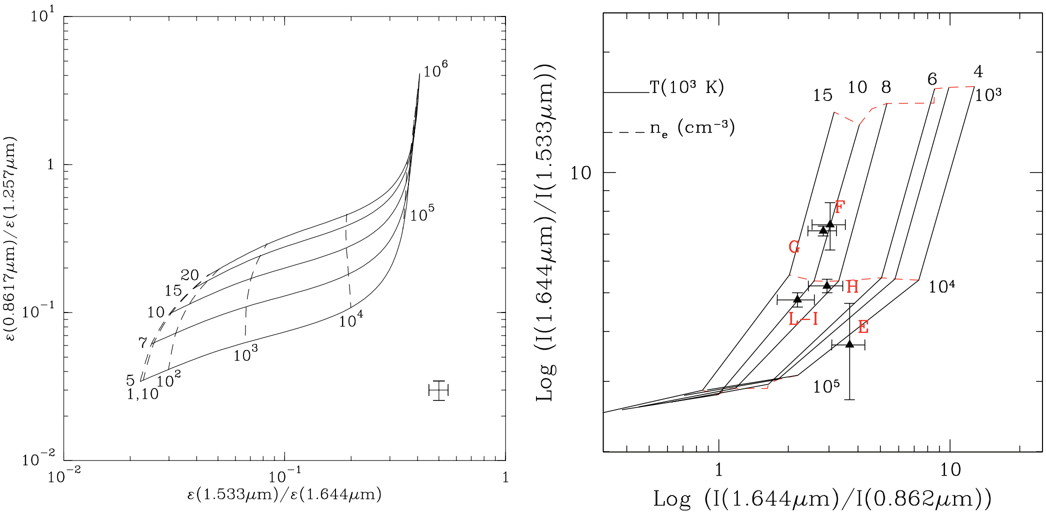

Figure 3.7: Diagnostic diagrams from Pesenti et al. (2003) on the left and Nisini et al. (2005) on the right from [FeII] lines in the IR domain. Left: dashed lines show n_e varying form from 1 to 10^6 cm^{-3} in factors of 10, solid lines show T_e varying from 5000 to 20 000 K. Right: dashed lines show electron densities of 10^3, 10^4 and 10^5 cm^{-3} and solid lines show electron temperatures of 4, 5, 6, 8, 10, 15 $\times 10^3$K.

sensitive to the gas electron temperature (Nisini et al., 2002; Pesenti et al., 2003). On the other hand, such an approach gives the possibility of probing the different components of the jet cooling layers, where strong gradients are expected along the jet axis, that are not spatially resolved with current instrumentation. The difficulty is that the observational settings should be chosen to obtain, as far as possible, homogeneous spectra in the two wavelength ranges. For example, the observations should be carried out over a short period of time and with similar spatial coverage in order to cover the same section of the jet. Finally, in order to use the line intensities, a careful inter-calibration, measuring the fluxes of the lines located in the overlapping spectral regions, must be achieved.

Temperature from H_2 lines

In the near-IR the spectra show a very rich set of rotational transitions originating from the v=1-4 vibrational levels. These transitions probe temperatures from ∼2000 K, for lines coming from v=1, to up to ∼4000 K for the higher levels.

The practical way to determine temperatures from a set of observed H_2 lines is through the construction of a Boltzmann diagram. Since the H_2 transitions are quadrupolar, their radiative rates, and consequently their critical densities, are low, typically critical density is 10^2-10^3 cm^{-3} at ∼2000 K and they are easily thermalised. In this case, the column density of a given level with respect to the total H_2 density, is given by the Boltzmann distribution:

$$\frac{N(v,J)}{N(H_2)} = \frac{g_{v,J}}{Q} e^{-E(v,J)/kT_{ex}} \tag{3.25}$$

And then the column density is related to the line intensity by:

$$I_{v,J} = \frac{h\nu}{4\pi} A_{v,J} N(v,J) \tag{3.26}$$

where v and J are the vibrational and rotational quantum numbers of the correspondent transition level, and N(v,J) is the column density of that transition.

An expression linking the line intensity and the total H_2 total density is easily deduced:

$$ln\frac{N(v,J)}{g_{v,J}} = ln\left(\frac{I_{v,J}4\pi}{g_{v,J}h\nu A_{v,J}}\right) = -\frac{E(v,J)}{kT_{ex}} + ln\frac{N(H_2)}{Q} \tag{3.27}$$

where Q is the partition function and the statistical weight $g_{v,J}$ is the product of the nuclear spin statistical weight, which in equilibrium has values of 1 and 3 for para and ortho-H_2 respectively, and the rotational statistical weight, which is (2J+1).

Hence, if we plot $ln\frac{N(v,J)}{g_{v,J}}$ versus the excitation energy E(v,J), Fig. 3.8, the observed values should fall on a straight line with a slope proportional to T_{ex}^{-1}, for a uniform temperature. In addition, the total column density of the H_2 is given by the interception to zero.

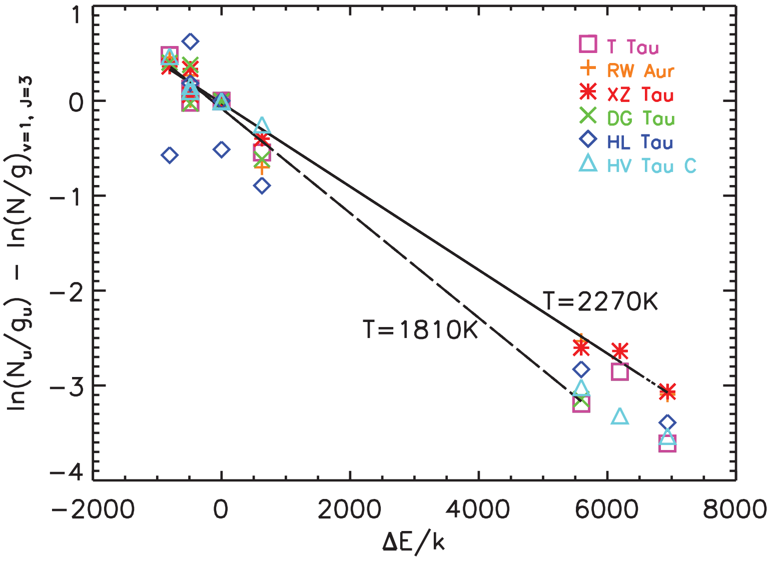

Figure 3.8: Example of a Boltzmann diagram obtained from different H_2 transitions, for several T Tauri stars, from Beck et al. (2008).

3.5.3 Ionization fraction: the BE99 technique

The electron temperature and density are very important parameters to describe the physics of flow, but to compare with models one needs to know the total hydrogen density n_H. This parameter can not be obtained directly from observations but can be deduced from the n_e estimation if the ionization fraction is known, $x_e = n_e/n_H$. However, to retrieve x_e from observations is not trivial. Bacciotti & Eislöffel (1999) developed a very powerful technique, called *BE technique*, to derive it from the ratio of some commonly observed optical emission lines in jets. I describe in this section the basis of this method.

In other astrophysical situations, the ionization fraction is computed assuming the so-called *coronal equilibrium*. Nevertheless, it is not applicable to the jet studies because recombination timescales are very long. Hence, in the case of jets, several authors use shock models to derive the ionization fraction by comparing the model outputs with the observed lines. These models make a lot of assumptions on the physical mechanism of gas heating, including the shock velocity and geometry, the pre-shock density or the pre-shock magnetic field. Hence, this method is highly model-dependent, and in addition, it is complex to apply.

The *BE technique* makes, in contrary, no assumptions about the heating mechanism, it only assumes that the gas is collisionally excited, and it derives the ionization fraction and the electron temperature from optical observed lines of S^+, O^0 and N^+. The basic idea of the method is that the dominant mechanism in the ionization balance of Hydrogen is the charge exchange between the oxygen and the nitrogen with the Hydrogen. This process is favored by the fact that the ionization potential of the N and O are very close to that of the H (E_{ion}=13.6 eV for H, 13.61 for O and 14.54 for N). The second important consideration of the method is that the Hydrogen is at any time in equilibrium with the nitrogen and the oxygen, even if it is not in equilibrium with the local temperature, because the processes that regulate the ionization balance of N and O are much faster that those that regulate the ionization balance of Hydrogen. This last consideration allows us to calculate the hydrogen ionization fraction from those of O and N.

This technique is applicable to low excitation conditions, which is the case of stellar jets, where neither S^{++}, N^{++} nor O^{++} are observed. Thus, the two ratios used are [OI]$\lambda\lambda$(6300+6363)/[NII]$\lambda\lambda$(6548+6583) and [SII]$\lambda\lambda$(6716+6731)/[OI]$\lambda\lambda$(6300+6363). These ratios depend not only on the electron density and temperature, but also on the ionization fractions and the abundances of the involved species.

Assuming that the Sulphur is all singly ionized in the jet beams, the N^+/N^0 and O^+/O^0 are computed considering that the dominant agent is charge-exchange with hydrogen. The relationship between this two ratios and the x_e is given by the following equations:

$$\frac{O^+}{O^0} = \frac{x_e(C(O,T)+\delta_O(T))}{x_e(\alpha(O,T)-\delta'_O(T))+\delta'_O(T)} \tag{3.28}$$

$$\frac{N^+}{N^0} = \frac{x_e(C(N,T)+\delta_N(T))}{x_e(\alpha(N,T)-\delta'_N(T))+\delta'_N(T)} \tag{3.29}$$

where $C(O,T)$,$C(N,T)$ are the collisional ionization rates for oxygen and nitrogen, $\alpha(O,T)$,$\alpha(N,T)$ are the direct plus dielectronic recombination rates, $\delta_O(T)$,$\delta_N(T)$ and $\delta'_O(T)$,$\delta'_N(T)$ are the direct and inverse charge exchange ionization rates, respectively.

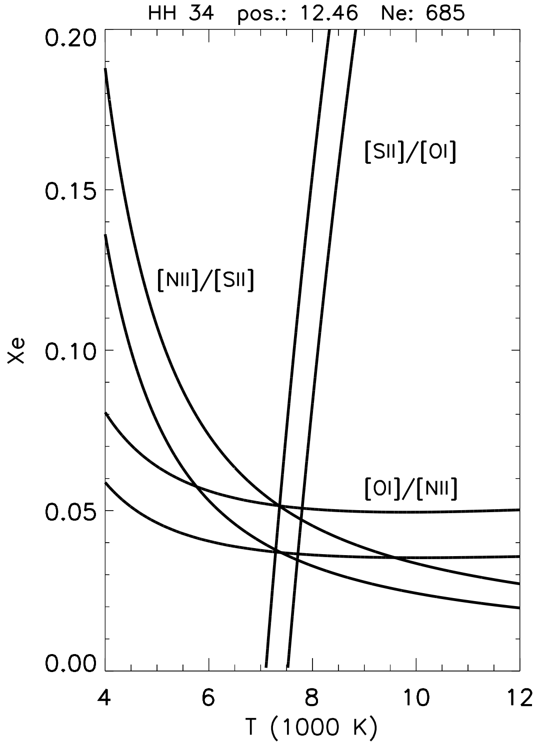

Figure 3.9: Example of the BE technique to derive the electron temperature and the ionization fraction in the jet of the HH 34 object. The values of x_e and T, and their uncertainty, are found from the intersections of the curves. Adapted Bacciotti & Eislöffel (1999).

Thus, combining these two last equations with that for the population of levels in statistical equilibrium, and assuming a given abundance set, the two ratios can be calculated numerically. The ratios are functions of the electron density, temperature and ionization fraction. As I explained before, the electron density can be estimated from the sulphur doublet and then the ratios depend only on the electron temperature and on the ionization fraction. In particular the second ratio is essentially only sensitive to the ionization fraction variations. In the (x_e,T_e) parameter space, Fig. 3.9, the two ratios define two surfaces and the observed values will be in one curve of each surface. In practice, the calculation of the physical quantities is calculated with an automated inversion code from the observed line ratios. The level populations are determined with a five-level model for the considered atoms, using transition probabilities and coefficients for electron collisions from Mendoza (1983), while the ionization fractions for O and N are found using collisional ionization and radiative recombination rates from Landini & Monsignori Fossi (1990), dielectronic recombination rates from Landini & Monsignori Fossi (1990) and Nussbaumer & Storey (1988), and charge exchange rates from Kingdon & Ferland (1996) and Arnaud & Rothenflug (1985).

The total density estimate allows one to derive the jet mass, energy and momentum fluxes, which are critical parameters to understand the relationship between the jet and its environment, the jet launching mechanism and the properties of the flow propagation.

3.5.4 Uncertainties

This technique is very useful to derive physical parameters in a simple way and without any assumption on the heating mechanism. Lavalley (2000) and Bacciotti & Eislöffel (1999) theirselves have analyzed the uncertainties and limits on the validity of the technique. I summarize here the main conclusions obtained which must be kept in mind.

One important assumption we made was neglecting photoionizations effects. In fact, this effect becomes important in the bow-shocks produced at the head of the jet when it impacts the interstellar medium. In order to analyze the physical conditions in this highly excited region, the photoionization should be included in the diagnostics. However, Bacciotti & Eislöffel (1999) and Lavalley (2000) studied in detail the validity of the approximation and they concluded that it is a good approximation for ionization fractions lower than 0.8. These authors also studied the effect of signal-to-noise on the accuracy of the derived values. They show that, in average S/N conditions, the electron density is obtained with an accuracy less than 3% (far from the critical density of the element used in the diagnostic). For the electron temperature and the ionization fraction is about 15-20% and 20-30% respectively.

The BE technique assumes solar abundances for the elements used (S,O and N) in the estimation of the ionization fraction and electron temperature. Some authors repeat the diagnostic using different abundances estimates. The differences in the derived values can amount to 30 or 40% with the most reliable value obtained using the most recent abundance value for the interstellar medium in the correspondent cloud.

Reddening is an important correction to do when we work with spectra to eliminate the effect of wavelength-dependent absorption of dust in line of sight. This correction is not easy to carry out in jets but the use of line ratios quite close in wavelength since it is done in the Be technique makes the reddening contribution small. Typically, for a T Tauri Star, the variation induced in the x_e and T_e values is at most 10% and 15%.

Lavalley (2000) studied also the effect due to the shocks on the jet. The diagnostics used assume that the line emission comes from a region with a single excitation condition. In fact, we observed the cooling zone behind a shock front, but generally this region is not resolved. We actually observe a region with important spatial gradients on temperature, density and ionization fraction. Lavalley (2000) found that the derived values are a good average value of the physical conditions in shocks with velocities less than 50 km/s and pre-shock densities less than 10^4 cm^{-3}.

3.6 Mass-loss rate derivation

Mass-loss rate is a very important parameter to constrain models and understand the mechanisms operating in jets formation and its link with accretion. A good estimation of the ionization fraction and total density are crucial to have a good estimate of mass-loss rate. However, a lot of uncertainties affect its estimation, for example, there may be cool material that do not radiate or dense material that fills a larger fraction of the volume in the jet than that observed. I am going to explain the different methods used during my analysis to obtain different independent estimations of the mass-loss rate and compare them.

3.6.1 From atomic lines: [FeII]λ1.64μm and [OI]λ6300A

We used three different methods, two of them based on the assumption of volume emission and the third assumes that the observed lines are excited by shocks. Next, I explain more in detail each method.

1^{st}*Method: Cross section and density*

For this first method, first introduced and described in detail by Hartigan et al. (1994), we consider the geometry and the density of the jet. In this method we do not make any assumption about the excitation mechanism and we assume that the considered beam is uniformly filled at the given density derived from the line ratio diagnostics. In fact, these two assumptions are unrealistic, on one hand the filling factor on the beam is not necessary equal to one, the line does not emit over the entire beam. On the other hand, this effect is partially compensated by the fact that there would be also some regions at higher density of that traced by the iron diagnostic (used in this work). Hence, this method gives an upper limit to the mass-loss rate which, for a collimated jet, can be estimated as follow:

$$\dot{M} = \mu' m_H n_H S_j V_j \tag{3.30}$$

where $\mu' = 1.35$ is the average weight per hydrogen nucleus, $\mu' = \mu \frac{n_{TOT}}{n_H}$ where $\mu = 1.24$ is the mean molecular weight for a neutral atomic gas, n_{TOT} is the total number of atoms in the beam and for solar abundances n_H/n_{TOT}=0.921. $n_H = n_e/x_e$ is the hydrogen number volume density and m_H is the proton mass. V_j is the jet velocity and $S_j = \pi r_j^2$ is the cross-section through which the flow passes. The jet radius, r_j, is calculated from the transverse width of the jet as $\frac{1}{2}FWHM$ of the line emission. Equation 3.30 can be written as:

$$\dot{M} = 1.23 \times 10^{-9}\left(\frac{n_H}{10^5 cm^{-3}}\right)\left(\frac{FWHM}{14AU}\right)^2\left(\frac{V_j}{100km/s}\right) \qquad (M_\odot/yr) \qquad (3.31)$$

2^{nd}*Method: Luminosity of uniform slab*

This method, described in detail in Hartigan et al. (1995), uses the observed luminosities of optically thin forbidden emission lines such as [OI] or [FeII]. It assumes that the electron temperature T_e, the electron density n_e and the ionization fraction x_e are uniform in each individual pixel and relates them to the mass inside the pixel.

The mass-loss rate of a given mass portion on the jet moving in the plane of the sky at V_t in an aperture also on the plane of the sky of l_t, is given by $\dot{M} = M_{TOT}V_t/l_t$, that could also be written as:

$$\dot{M} = M_{TOT} \times V_t/l_t = \mu' m_H \times (n_H Volume) \times V_t/l_t \qquad (3.32)$$

where, analogous to the *cross section and density* method, μ'=1.35 is the average atomic weight per hydrogen nucleus, m_H is the proton mass and $n_H = n_e/x_e$ is the hydrogen number volume density.

[FeII]λ1.64μm:

The total radiated energy in the line can be related with the total mass since this line is optically thin. Therefore, the total luminosity in this line is:

$$L_{[FeII]_{1.64}} = Volume \times \epsilon_{1.64}$$

where $\epsilon_{1.64}$ is the line emissivity and $Volume$ the total iron emitting volume. We used the emissivity values computed by Pesenti et al. (2003) for a 16-level model of the [FeII] emission that, under the assumption of optically thin lines, only depends on the electron density and temperature. As shown in Sec. 3.4 the emissivity of a transition depends on the upper level population, obtained resolving the statistical equilibrium equations for all the levels. It depends on the n_e and some other parameters depending on the electron temperature. Once we fix the temperature, the emissivity depends only on the electron density being proportional to $(C_1 + C_2 n_e)/C_3(n_e + n_{cr})$, with C_i constant values. In the 2-level atom approximation C_1=0, and thus the proportionality becomes $C_4(1{+}n_{cr}/n_e)^{-1}$. For an electron temperature of $\sim 10^4 K$, the computed emissivity $\epsilon'_{1.64}$ depending on the electron density is shown in Fig. 3.10. The fit obtained for the computed values, Eq. 3.33,

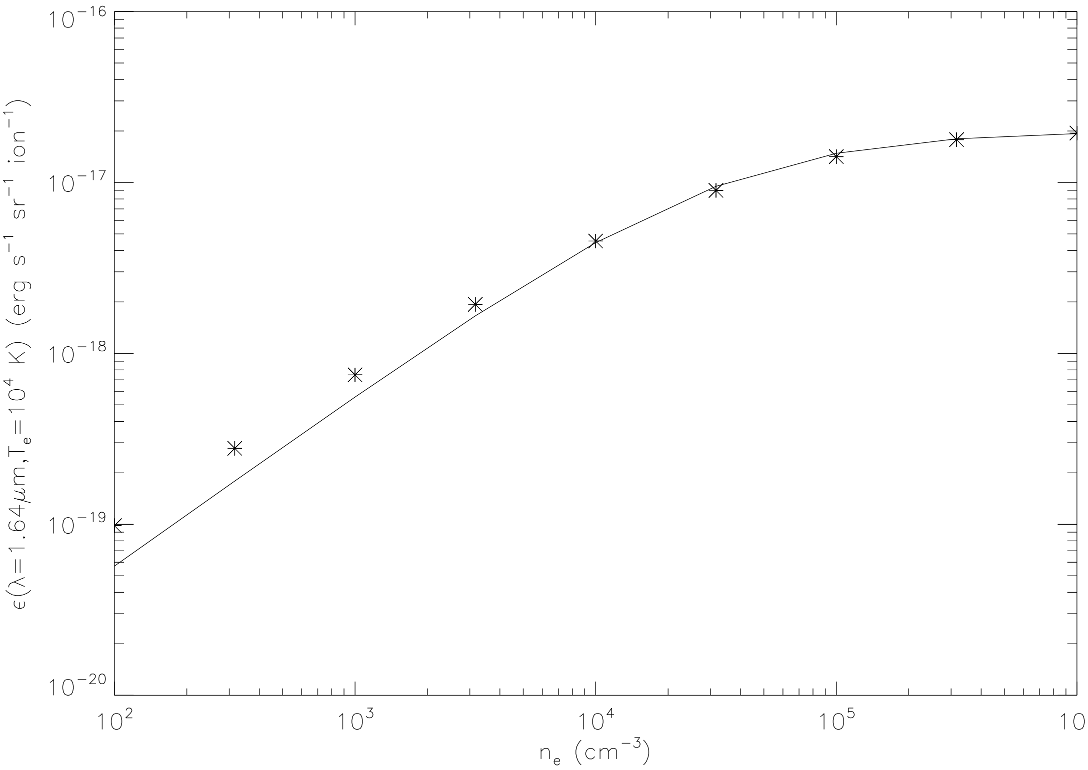

Figure 3.10: Computed emissivity by Pesenti et al. (2003) for [FeII]λ1.64μm line at an electron temperature T_e, of 10^4 K, as a function of the electron density, n_e. Points are the computed values and the line over-plotted is the fit used in our estimations of mass flux (see text).

is also over-plotted. The fit is especially good for electron densities higher than 10^4 cm^{-3} which is a typical value for jets.

$$\epsilon'(\lambda = 1.64\mu m, T_e = 10^4 K) = \frac{2 \times 10^{-17}}{1 + \frac{3.5 \times 10^4}{n_e(cm^{-3})}} \qquad (\mathrm{erg\,s^{-1}sr^{-1}ion^{-1}}) \qquad (3.33)$$

The emissivity given by this model, $\epsilon'_{1.64}$, is in units of erg s^{-1}sr^{-1}ion^{-1}, consequently we can write the emissivity in the expression of luminosity above as $\epsilon_{1.64}$=$\epsilon'_{1.64}\times 4\pi \times n_{Fe^+}$. Taking into account that we can write $n_{Fe^+} = \frac{n_{Fe+}}{n_{Fe}} \times \frac{n_{Fe}}{n_H} \times n_H$, the luminosity in the line can be written as follows:

$$L_{[FeII]1.64} = Volume \times \epsilon'_{1.64} \times 4\pi \times \frac{n_{Fe^+}}{n_{Fe}} \times \frac{n_{Fe}}{n_H} \times n_H \qquad (3.34)$$

We make the assumption that all iron atoms are singly ionized which means $\frac{n_{Fe+}}{n_{Fe}} = 1$ and that all the iron is in gaseous form, so we can use the known solar iron abundance, $\left[\frac{n_{Fe}}{n_H}\right] = \left[\frac{Fe}{H}\right]_{\odot}$. In fact, we know that up to ~ 70% of Fe atoms can be locked into grains so, making this approximation, we obtain a lower limit to the mass-loss rate estimation (Nisini et al., 2005). Taking into account these two last approximations and the previous Eq. 3.34 we can derive an expression for the mass-loss rate as a function of only known parameters:

$$\dot{M} = \mu' m_H \frac{L_{[FeII]1.64}}{[\frac{Fe}{H}] \times \epsilon'_{1.64} \times 4\pi} \frac{V_t}{l_t} \tag{3.35}$$

Assuming a solar total iron abundance with respect to hydrogen of 2.82× 10^{-5} (Asplund et al., 2005), giving V_t in km/s, l_t in cm and $L_{[FeII]_{1.64}}$ in solar luminosities $L_\odot$, and normalizing to typical values in T Tauri jets, we find the following numerical expression for the mass-loss rate:

$$\begin{aligned} \dot{M} = 1.45 \times 10^{-8} \left(1 + \frac{3.5 \times 10^4}{n_e(cm^{-3})}\right) \left(\frac{L_{[FeII]1.64}}{10^{-4} L_\odot}\right) \left(\frac{V_t}{150 km/s}\right) \times \\ \times \left(\frac{l_t}{2 \times 10^{15} cm}\right)^{-1} \left(\frac{[Fe/H]}{[Fe/H]_\odot}\right)^{-1} \quad (M_\odot/yr) \end{aligned} \tag{3.36}$$

[OI]λ6300A:

In the case of the oxygen and using the same basic equations and considering that the ionization state for the oxygen is dominated by the charge-exchange with the hydrogen, the ionization fraction for the oxygen is similar to that of the hydrogen. In this case, we obtain then that the total mass is given by:

$$M_{TOT} = 9.61 \times 10^{-6} \left(\frac{1}{1 - x_e}\right) \left(1 + \frac{n_{cr}}{n_e}\right) \left(\frac{L_{[OI]6300}}{L_\odot}\right) \quad (M_\odot) \tag{3.37}$$

Replacing this expression in the mass-loss rate equation and normalizing to typical values, then:

$$\begin{aligned} \dot{M}_J = 2.27 \times 10^{-6} \left(\frac{1}{1 - x_e}\right) \left(1 + \frac{n_{cr}}{n_e}\right) \left(\frac{L_{[OI]6300}}{L_\odot}\right) \left(\frac{V_t}{150 km/s}\right) \times \\ \times \left(\frac{l_t}{2 \times 10^{15} cm}\right)^{-1} \quad (M_\odot/yr) \end{aligned} \tag{3.38}$$

3^{th} Method: Shocks

Finally we used another method to estimate the mass-loss rate from the observed line luminosity but assuming that this emission is excited by single shocks inside the jet. In this case, the mass-loss rate in the shock, $\dot{M}_s$ is given by:

$$\dot{M}_s = \mu' m_H \times n_H V_s \times S_s \tag{3.39}$$

where μ', m_H and n_H are again the average atomic weight per hydrogen nucleus, the proton mass and the hydrogen density respectively. V_s and S_s are the shock velocity and cross section.

[FeII]λ1.64μm:

In the case of this line, we used the radiative shock models computed by Hartigan et al. (2004). They take into account 159 levels to predict fluxes of 1488 transitions, including [FeII]$\lambda 1.64\mu m$. The input parameters to the model are the shock velocity, the preshock density, the preshock ionization fraction of the hydrogen, the preshock magnetic field and the cutoff temperature. They assume an iron abundance with respect to the hydrogen of [Fe/H] $\sim 4 \times 10^{-5}$. The flux given, $F_{1.64}$ by the model is what emerges out the front of the shock, so to calculate the luminosity we should multiply by two and by the shock surface, $L_{1.64} = 2 \times F_{1.64} \times S_s$. Hence, taking the unknown variable S_s from the last expression and replacing it in Eq. 3.39 we can write the mass-loss rate in the shock as a function of the line luminosity:

$$\dot{M}_s = \mu' m_H \times \frac{1}{2}\left(\frac{n_H V_s}{F_{1.64}}\right) \times L_{1.64} \tag{3.40}$$

In this expression the shock velocity remains unknown, nevertheless as we can see in Fig. 3.11 where we plot the flux predicted by the model against the product of input parameters, $n_H V_s$, there is a clear proportionality between these two quantities. We conducted a linear fit to the points of the model and we obtained a constant value for $\frac{n_H V_s}{F_{1.64}}$= 1.032× 10^{13} (erg^{-1}). This proportionality allows us to evade the unknown variable, V_s, and write the mass-loss rate in the shock directly proportional to the observed luminosity in the [FeII]λ1.64μm line:

$$\dot{M}_s = 6.86 \times 10^{-17}\left(\frac{L_{1.64}}{L_\odot}\right)\left(\frac{n_H \times V_s}{F_{1.64}}\right) = 6.504 \times 10^{-4}\frac{L_{1.64}}{L_\odot} \qquad (M_\odot/yr) \tag{3.41}$$

As in the volume method based in the line luminosity estimation (the second method applied) there is indeed a dependence with the iron abundance coming from the luminosity. Thus, we have to keep in mind that the expression should be multiply by the term of abundance $[\frac{Fe}{H}]^{-1}$.

To convert the mass-loss rate in the shock into the jet mass-loss rate we have to multiply it by $V_j\, S_j/V_s\, S_s$ (factor obtained by comparison between Eq. 3.30 and Eq. 3.39). From simple geometrical considerations of a inclined shock related to the jet direction, $S_j/S_s = \cos\theta$ where θ is the angle between the two surfaces. As θ is small we assume $\cos\theta = 1$ and the mass-loss rate in the jet can be obtained from the shock mass-loss rate multiplying by the velocities ratio. Lavalley-Fouquet et al. (2000) found that $v_j/v_s = 4$ for typical T Tauri jets, so $\dot{M}_{jet} = \dot{M}_s v_j/v_s = 4\dot{M}_s$. A a factor N_{shocks}^{-1} must be included to take into account the number of shocks inside each integrated beam.

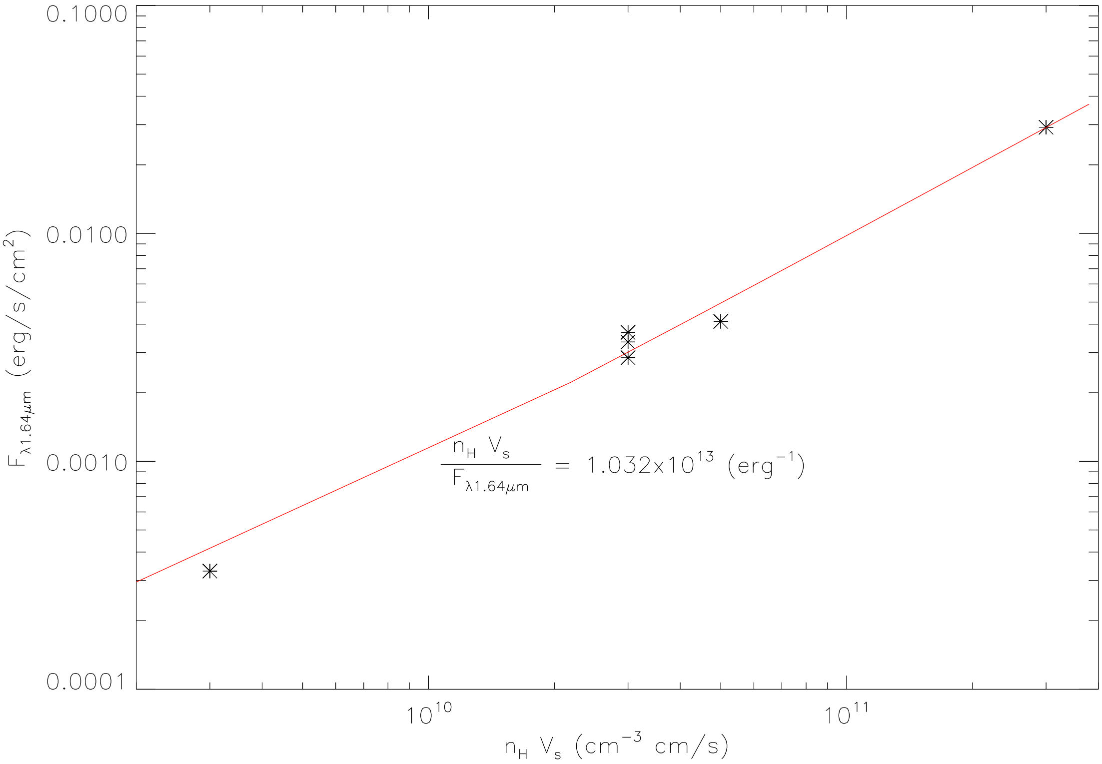

Figure 3.11: Flux in the [FeII]λ1.64μm line predicted by shock models computed by Hartigan et al. (2004) against the product of $n_H V_s$ (input parameters). The flux given is what emerges out the front of shock. We find a good agreement with a linear fit, also over-plotted. We use this proportionality to estimate the mass-loss rate in the shock (see Eq. 3.40 and the text).

[OI]λ6300A:

In this case we retake the expression for the mass-loss rate, which as a function of the shock surface can be written as:

$$\dot{M} = \mu m_H n_0 V_J S_s \tag{3.42}$$

where μ=1.24 is the mean molecular weight for a neutral atomic gas, n_0 is the pre-shock density, V_J the jet velocity and S_s is the shock surface.

The luminosity in the line, due to the shock, can be expressed as:

$$L_{[OI]6300} = N n_0 S_s V_s h\nu_{6300} \tag{3.43}$$

with N the number of photos emitted at 6300Å which pass trough the front shock.

Combining these two equations, and considering that that $n_J S_j \simeq n_0 S_s$ we can derive an expression for the mass-loss rate in the jet. As in the case of iron, we should take into account the existence of multiple (N_{shocks}) oblique shocks forming an angle between the normal to the shock front and the jet axis of θ. Therefore, the derived equation for the mass-loss rate is the following, where V_s is obtained by comparison between observed line ratios and shocks models :

$$\dot{M}_J = 6.616 \times 10^{-4} \left(\frac{V_J}{V_s}\right) \left(\frac{L_{[OI]6300}}{L_\odot}\right) \left(\frac{\cos\theta}{N_{shocks}}\right) M_\odot/yr \tag{3.44}$$

Comparison of the three methods

It is instructive to compare the results of the different methods as an indicator of their uncertainties. Such a comparison has been illustrated by Cabrit (2002) using the values obtained for the three bright Class I jets HH 34, HH 47 and HH 111, determined by Hartigan et al. (1994). Lavalley (2000) performed a similar comparison in the microjet of the Class II source DG Tau, as a function of distance and the jet velocity since both x_e and n_e actually vary along the jet and with the velocity component using optical data. I will present a similar comparison between the values obtained using these three methods for the NIR atomic iron emission in DG Tau (Ch. 6, Sec. 6.4.6).

Cabrit (2002), on the basis of the results of Hartigan et al. (1994) and Lavalley (2000), pointed out than among the two first methods, assuming uniform emission, the cross-section based estimate is always higher than the luminosity method. It suggests a filling factor less than one and hence, the first method tends to give an upper limit to the mass-loss rate. The most reliable methods appear to be the shock method and the first method corrected by a compression factor in the derived jet density ($n_j = n_H\sqrt{C^{-1}}$), assuming that emission comes from a shock wave. They give similar results beyond 100 AU for the T Tauri source DG Tau. On the contrary, close to the star, the two methods give different results, maybe due to extinction affecting the luminosity estimation and an overestimated jet radius.

Nevertheless, some limitations and possible sources of uncertainties can be directly deduced from the parameter dependence and the numerical expressions given above. The first method depends strongly on the jet width and on the total density, but the main uncertainty comes from the uncertainty in the ionization fraction. This value is difficult to obtain from observations and very few studies as a function of the distance to the source have been made. Bacciotti (2002) show that it can vary from 0.01 very close to the star to 0.5 at $1''$ to the star. A mean constant value along the jet will produce up two times the real value at some distances. I remind the reader that a filling factor of one is assumed, which implies a homogeneous distribution of the material in the jet, but also implies that the observed emission is dominated by the densest regions, giving in fact an upper limit to the mass-loss rate.

In the second method, the parameter which could cause discrepancies is l_t. In the case of IFS, this can considered as the transverse resolution element but in the case of long-slit spectroscopy, this value corresponds to the slit width which can be larger than the real emitting beam. In this case, the mass-loss rate obtained is a lower limit. The dependence with electron density in this method comes from the line emissivity which depends also on the electron temperature. At the same time, the choice of the emissivity function, as a function of the distance to the star, can also be a source of uncertainty. The model computed by Pesenti et al. (2003) used here gives a very good estimation for densities higher than 10^4cm^{-3}. Moreover, we have to keep in mind that this method assumes that the observed luminosity comes uniformly from all the mass confined inside the beam. However, this luminosity can originate only in the external layers shocking the environment medium. If it is the case, the mass assumed is higher than the real one.

In addition, it should be kept in mind that, the methods using the iron line luminosity are affected by the depletion onto the grains. Only the iron in gas form contribute to the line emission. Nisini et al. (2005) showed that up to 70% of the iron atoms can be locked into grains. Hence, the estimate given would be a lower limit to the real value.

3.6.2 Mass-loss rate in the molecular emission: H_2

As in the case of the atomic emission, the mass-loss rate in the molecular emission is derived using two different methods, one assuming a volume emission and the second assuming that the emission is caused by shocks. They are the same methods explained before, but I retake the expressions to apply them to the particular case of the H_2.

1^{st}***Method: Volume***

The surface brightness emitted by a volume of length L and a surface of A, in a particular transition between an upper level of density n_{up} and a lower level of density n_{low} is given by $F_{up\rightarrow low} = n_{up}A_{up}Lh\nu/4\pi$. Assuming a uniform density inside the volume, $n_{up}L$ is in fact the column density in the upper level N_{up}. Hence, we actually have a direct relation between the observed flux and the column density in the upper level of the transition. Likewise, from the Boltzmann distribution equation, we obtain a relation between the total column density in the H_2 molecule, N_{H_2}, and in the upper level, N_{up}:

$$N_{up} = \frac{N_{H_2}}{Q(T)} \times g_{up} exp\Big(\frac{-E_{up}}{kT}\Big)$$

where g_{up} is the degeneracy of the upper level, E_{up} is the energy of the level, k is the Boltzmann constant and T is the temperature. Q(T) is the *partition function* for a given temperature and it is given by $Q(T) = \sum_{level} g_{level} exp\big(-E_{level}/kT\big)$. Assuming the function fitted $Q(T) = 0.024T/(1 - exp(-6000/T))$ by Smith & Mac Low (1997) and Davis et al. (2001), we derive a relation between N_{H_2} and N_{up} for T=2000K of $N_{1-0S(1)}/N_{H_2} = 1.28\text{x}10^{-2}$.

In a similar way, the total luminosity in the transition is related to the column density in the upper level and therefore to the mass on this level, and using the relation derived before, it is also related to the total H_2 mass. Hence, using Eq. 3.45 we derive the total mass in the molecular hydrogen from the luminosity in the λ2.12μm emission line.

$$M_{H_2} = \frac{m_{H_2}}{1.28\text{x}10^{-2}} \frac{L_{\lambda 2.12\mu m}}{h\nu A_{up}} \tag{3.45}$$

Hence, in the case of an emitting volume, the mass-loss rate is given by:

$$\dot{M}_{H_2} = \frac{m_{H_2}}{1.28\text{x}10^{-2}} \frac{L_{\lambda 2.12\mu m}}{h\nu A_{up}} \times V_t/l_t \tag{3.46}$$

2^{nd}***Method: Shocks***

For this method we assume that the emission is produced in shocks. In this case, the flux in the 2.12μm line is proportional to the kinetic energy of the particles passing through the shock surface, S_s, at a shock velocity of V_s. The surface brightness can therefore be written in erg/s/cm^2/sr as:

$$F_{2.12\mu m} = K \times \mu m_H n_H \frac{V_s^3}{2} \frac{1}{4\pi} = K \frac{\mu m_H}{8\pi} n_H V_s^3 \tag{3.47}$$

where K is the factor of proportionality. Thus the line luminosity in erg/s results:

$$L_{2.12\mu m} = F_{2.12\mu m} \times 4\pi D^2 \times S_s(sr) = K \times \mu m_H n_H \frac{V_s^3}{2} \times D^2 \times S_s(sr)$$

The shock surface in cm^2 is in fact equal to $D^2 \times S_s(sr)$ and the mass-loss rate in the shock is actually $\dot{M}_s = density\ V_s S_s(cm^2) = \mu m_H n_H \times V_s \times D^2 S_s(sr)$. Taking this into account and the last equation for the line luminosity, the mass-loss rate in the shock can be written as a function of the luminosity in the 2.12μm line and the velocity in the shock.

$$\dot{M}_s = \frac{L_{2.12\mu m}}{K} \frac{2}{V_s^2} \tag{3.48}$$

The luminosity is obtained from observations but models are need to obtain the shock velocity. Models computed by Kristensen et al. (private communication, models based in those shown in Kristensen et al. (2008)) which calculate the expected flux for different H$_2$ lines assuming different input values of n$_H$, V$_s$ and magnetic field B, for both J and C-shocks will be used for the analysis of the DG Tau molecular emission. Comparing observed fluxes with those predicted by models, the total density and the shock velocity can be thus derived depending on the magnetic field. Beside these values, the factor K

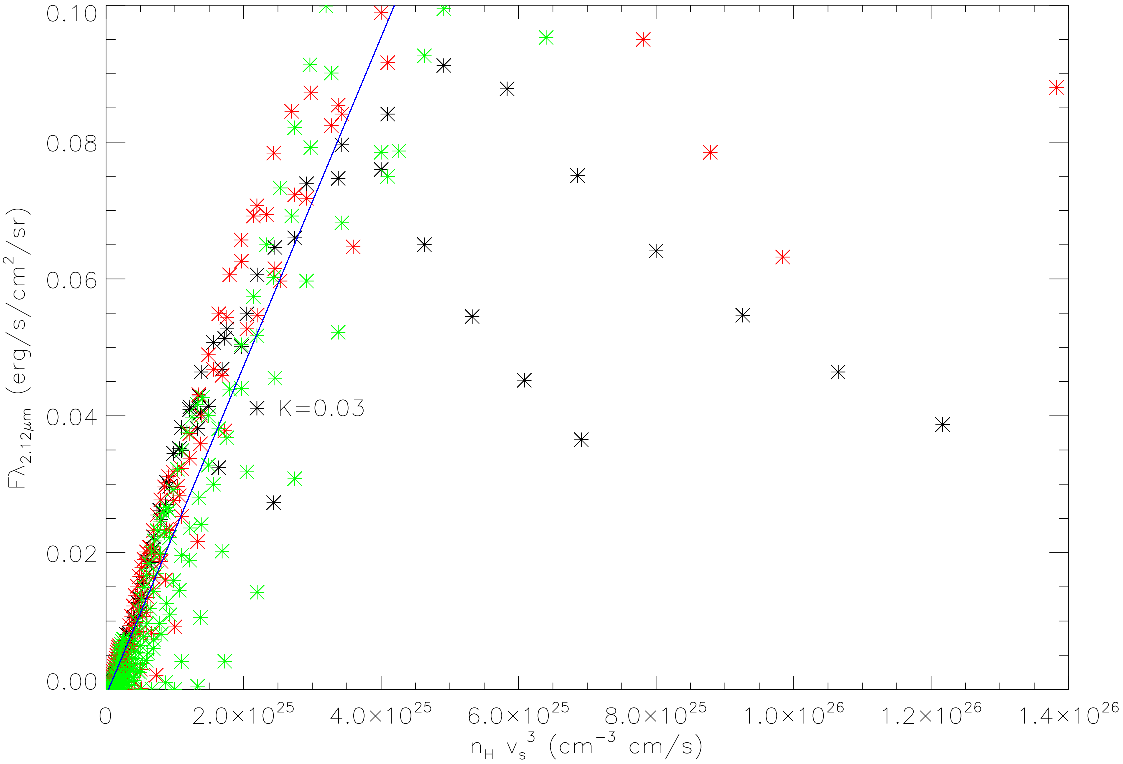

Figure 3.12: Computed H_2 brightness in the 1-0 S(1) ($\lambda = 2.12\mu m$) line against the product $n_H V_s^3$ to find the factor K in Eq. 3.47 as a linear fit. Different colors refers to models with different magnetic field, b=B/$\sqrt{n_H}$=0.5 (black), 1.0 (red) and 2.0 (green). In blue we plot the linear fit that gives us a value of K=0.03.

must to be estimated in order to obtain the mass-loss rate, as shown in Eq. 3.48. To obtain this factor K, a linear fit to the computed models as shown in Fig. 3.12 was carried out. Following Eq. 3.47 we present the $H_2\lambda 2.12\mu m$ flux against $n_H V_s^3$. Different colors refer to different magnetic field values. We accomplished the fit for values of $n_H V_s^3$ less than 5×10^{25} because for higher values the linear tendency described by Eq. 3.48 is not more valid. From the linear fit we obtain a factor of proportionality of K=0.03.

4

Integral Field Spectroscopy

The Integral Field Spectroscopy technique was used to obtain all the observational data analyzed in this thesis. Therefore, I consider it important to explain how it works and what are the differences between the instruments existing nowadays, and in particular for the instruments used in this thesis. I am going to explain also the steps needed in a data reduction for data taken with this observational technique. There are some differences with traditional spectroscopic data reduction which are very important to keep in mind. Finally I will describe some of the important analysis tools used to interpret the data.

4.1 Integral Field Spectroscopy

Integral Field Spectroscopy (IFS), often called 3D or 2D spectroscopy, produces spatially-resolved spectra over a two-dimensional field of view. It combines photometric (imaging) techniques with spectroscopic ones to obtain a spectrum for each two dimensional spatial element simultaneously with only one pointing of the telescope. Figure 4.1 illustrates this idea. It is an example for data taken from the integral field spectrograph INTEGRAL at the William Herschel Telescope in La Palma (Spain). In Fig. 4.1 I plot a bi-dimensional image reconstructed from the flux integrated in each individual spectra at a given wavelength, obtained from IFS data (see Sec. 4.5.1 for a description of how reconstruct maps from IFS data). The corresponding spectrum in the wavelength range, which contributes to the emission in the reconstructed image is overlaid for each spatial point.

As output of any kind of IFS technique, we obtain a data cube of a scalar quantity related to flux as a function of spatial coordinates in the field and wavelength. The main advantages of this technique, beyond the traditional long slit, are that (1) target acquisition is easier because it is not necessary to position the object carefully on a narrow slit and (2) the precise pointing may be determined after the observation by forming an image (of the continuum for example) from the spectral data. Moreover, it is less expensive in telescope time. For example, for an extended object, in long-slit, to record a spectrum from each part of the object, the long-slit has to be positioned across the target by mov-

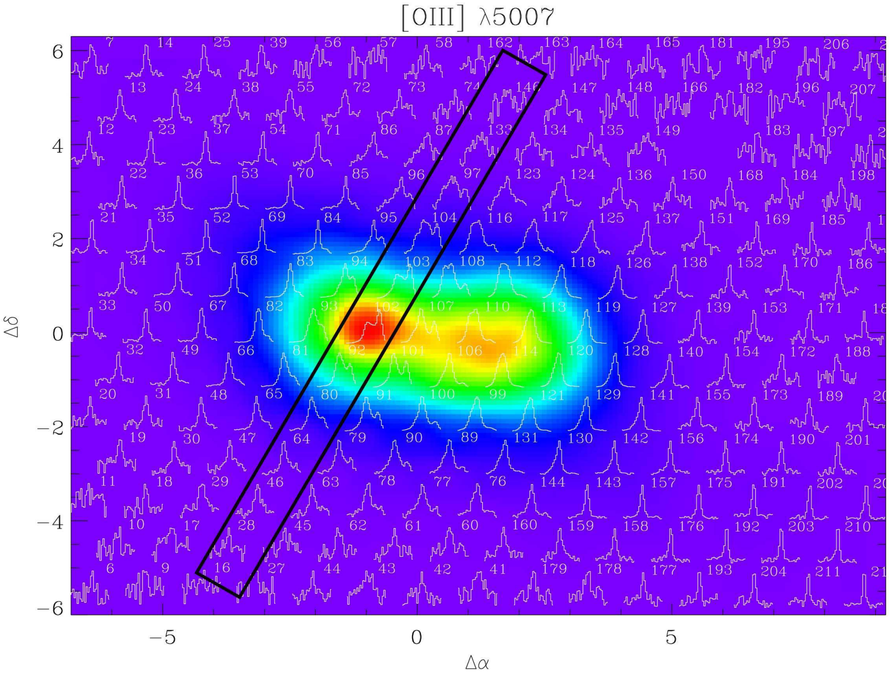

Figure 4.1: Reconstructed image for [OIII]λ5007 Å for an extended object from IFS data taken with the INTEGRAL spectrograph. For each spatial point we have the spectral information which contributes to the background reconstructed image. I over-plotted a simulated long slit to illustrate the information which would be averaged in this case.

ing the telescope and recording separate exposures for each position. There are other techniques such as Fabry-Perot scanning but they make inefficient use of telescope time and are potentially sensitive to changes in the instrumental or sky background. Other advantages are that errors in radial velocity (due to differences in the barycentre of the slit illumination obtained from the object and from reference sources) can be eliminated, and the global velocity field can then be recovered without bias imposed by the observer's choice of slit position and orientation. Additionally, a very important property of this technique is that the atmospheric dispersion effects can be corrected *a posteriori* and without loss of light.

In the case of jets in young stellar objects, a high variability was observed. On one hand, proper motions of 0.2″-0.3″/yr, measured in the jet knots, were observed (López-Martín et al., 2003). On the other hand, photometry variations or in the shape of line profiles have also been observed with time scales even shorter, of months or even days. The IFS technique is very useful for this scientific application, mainly because of the simultaneity in the acquisition of the spatial and spectral information. Besides the gain of telescope time already mentioned, and the fact of obtaining high angular and high spectral resolution in the same set of data, other advantages are the possibility of carrying out simultaneous studies of morphology, kinematics and even of excitation condition. All this properties result in a clearer and more direct analysis and interpretation of the observed features. Moreover, this technique has another advantage which is crucial in the study of micro-jets in young stellar objects. In these kind of systems the stellar continuum is very strong and the line emission coming from the micro-jet, in the regions very close to the star, is masked. IFS is especially useful for this study since it is easier to isolate the jet because of the simultaneous acquisition of the stellar continuum and the emission lines.

However, this technique has also some drawbacks. It is limited to a moderate spectral resolution and a small field of view. The existing integral field units have typically a few hundreds to a few thousands spatial elements each giving a spectrum with a typical length of 500-8000 pixels. That makes difficult to do surveys with these systems or to study objects of a few arc-minutes wide. In the case of the study of micro-jets in young stellar systems, the small field of view of some arc-seconds is not very problematic. They are adequate for the typical sizes of these systems and the typical velocity resolution of 100 km/s is good enough to resolve the high velocity component of the jet. However, to study the low velocity components and better separate the information from different components, a higher spectral resolution (which will be available in future instruments) is required.

4.2 Instruments

There are four kinds of possible techniques used in IFS instruments and they are summarized in Fig. 4.2. The first three are explained in detail by Allington-Smith & Content (1998) and the fourth is a more recent idea proposed by Content (2006). The main differences between them are in the way of sampling the focal plane and how they disperse the light. However, in the three cases, we obtain a 3D data cube with two spatial dimensions and the spectral information stored in a third dimension.

The first technique is based on lenslet arrays to segment the image formed by the telescope. Each small telescope pupil image formed is dispersed by the spectrograph. Because the detector is filled in two dimensions by the pupil images, the direction of dispersion has to be altered to avoid the overlap between the end of one spectrum and the beginning of other in the wavelength direction, as shown in Fig. 4.2. However, this overlap can not be completely avoided and a band-pass filter is necessary to isolate each spectrum. The main inconvenience of this technique is that, because of the overlapping, it does not use the detector surface optimally. This kind of systems are optimized for studies which require either low spectral resolution over a large wavelength range or high resolution over a small wavelength range. An example of an instrument which uses this technique is OASIS (explained in more detail in Sec. 4.2.1) which was one of the first instruments built using this technique. Other example is SAURON, *Spectrographic Areal Unit for Research on Optical Nebulae*, on the William Herschel Telescope in La Palma.

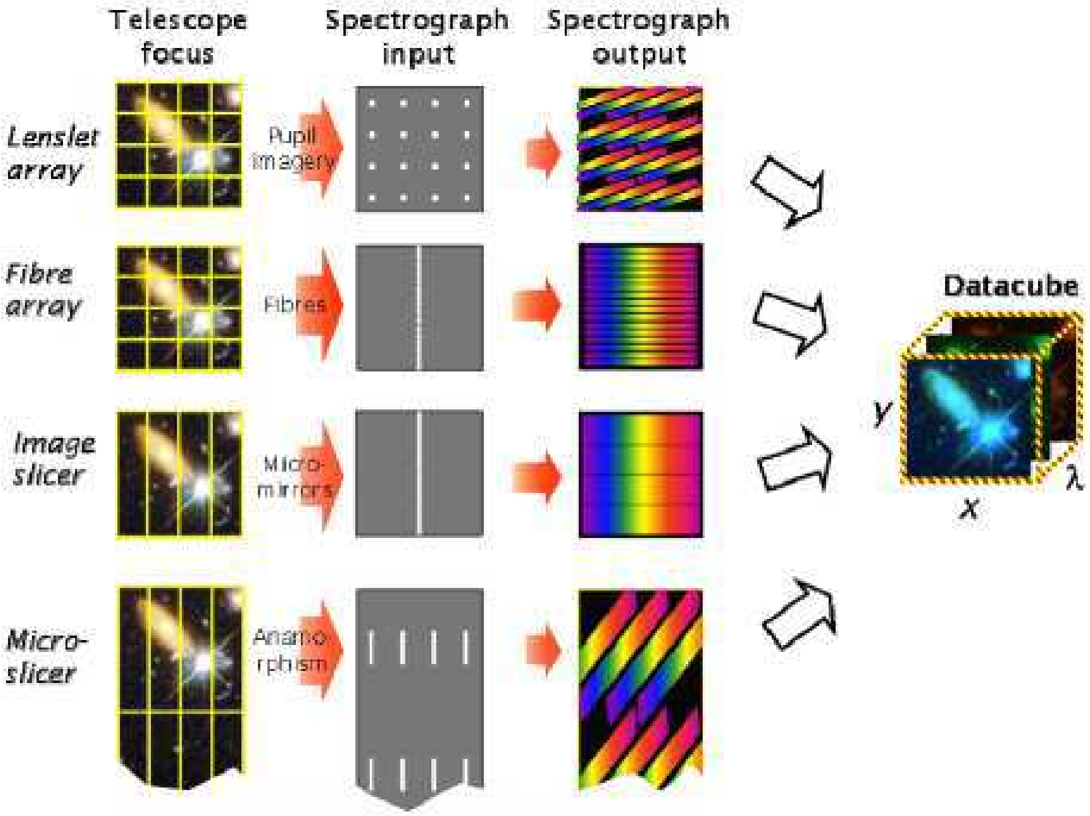

Figure 4.2: Schematic representation of the four kinds of integral field spectrographs existing nowadays.

The second method uses fibers to sample the image. In this case the sampling is done at the focal plane of the telescope. The fibers are then placed into a pseudoslit at the input of the spectrograph and the light is thus dispersed. In this case the spectrum can be as long as the detector size. The main disadvantage of this system is the light lost in the gaps between fibers, the typical filling factor being about 63%-75% in the optical domain. The second disadvantage is that for efficiency reasons, fibers should be used at focal ratios faster than f/5. This system shows an effect called "cross-talk" which is due to the use of fibers. It results in contamination in one fiber due to the light coming from the neighbor. I explain this effect a little more in detail and how to correct it in Sec. 4.3.2. This method is often used in combination with lenslets to improve it. The lenslets are placed at the input and optionally at the output of the fibers maximizing the filling factor and increasing the coupling efficiency with the telescope (if the input lenslets form a two-dimensional contiguous array). The disadvantage of this improvement is the greater manufacturing difficulty. Systems which uses this technique are INTEGRAL at the WHT (it only uses fibers); SMIRFS-IFU which is a near-infrared system for the UK Infrared Telescope, UKIRT; TEIFU at WHT operating with the ELECTRA and NAOMI adaptive optics systems; COHSI IFU for UKIRT; SPIRAL for the Anglo-Australian Telescope; VIRMOS for the Very Large Telescope, VLT, and the IFU unit for the GEMINI Multiobject Spectrographs, GMOS.

The third method consists in using image slicers which only use reflective optics. This technique is especially used for wavelengths longer than 1.8 μm because it is easier to cool the instrument. The image formed by the telescope is segmented into a number of narrow mirror slices and the light from each of the mirrors is rearranged to form the entrance slit of the spectrograph. Besides the possibility of cooling, other important advantages are that the spatial information is maintained along the slit and that diffraction affects only one dimension. In a fibre system, the diffraction is the same as would be obtained by passing the light through a physical aperture which subtends the same angle on the sky as each 2D IFU element. Hence, image-slicing IFU reduces the problem from two dimensions to one. A potential disadvantage is that it is hard to make the design compatible with existing spectrograph designs. An example of this technique is SINFONI in the VLT and explained in Sec. 4.2.2. Although it is not considered suitable for instruments which need to be cooled, fibers with integrated lenslets were developed for this instrument.

The last method is a hybrid between a lenslet array and an image slicer system. A set of rectangular lenslets divide the field in 2D, but each pupil image is replaced by a slice which contains the spatial information along its length. A second lenslet array reimage the microslices on the spectrograph, keeping the spatial information that is lost if the pupil is imaged instead. This kind of instruments takes many of the benefits of the image slicer reducing dead-space between spectra but reducing the spectral length to no more than a few hundreds pixels.

Instrument	Telescope	IFS-type	λ	Pixel	Spectral res.	Date
GMOS-IFU	Gemini	fibers+lens	0.4-1.1μm	200 mas	670-4400	2001
VIMOS	VLT	fibers+lens	360-1000 nm	330,670 mas	220-3100	2002
OASIS	WHT	lenslet	4200-8750Å	90,140,260 mas	200-4350	2003
SINFONI	VLT	slicer	1.05-2.45 μm	25,100,250 mas	2000-4000	2004
OSIRIS	Keck-II	lenslet	0.98-2.4 μm	20-100 mas	3500	2005
NIFS	Gemini	slicer	0.95-2.4 μm	40x100 mas	5000	2005
MUSE	VLT	slicer	0.46-0.93 μm	25-200 mas	2000-4000	2010
NIRSPEC	JWST		0.6-5 μm	100 mas	3000	2013

Table 4.1: A selection of IFS instruments.

Table 4.1 shows a list of the main instruments using IFS techniques and their characteristics. Although not all the current instruments are shown in the table, the main characteristics of two future projects or particular interest for the study of young jets have been included in order to give a global idea of the potential of this technique. Next, I am going to explain the two particular instruments used in this thesis which are two examples for the lenslet and the image slicer techniques.

Instrument	Object	Wavelength domain	Sky sampling	FOV	Spectral res.
OASIS	RY Tau	6209-6549 Å	160 mas	$6.2'' \times 5.0''$	3000
SINFONI	DG Tau	1.45-1.85 μm (H Band)	100 mas	$3'' \times 3''$	3000
SINFONI	DG Tau	1.95-2.45 μm (K Band)	100 mas	$3'' \times 3''$	4000

Table 4.2: Summary of the configurations used for our observations, for both the OASIS and the SINFONI data.

4.2.1 OASIS

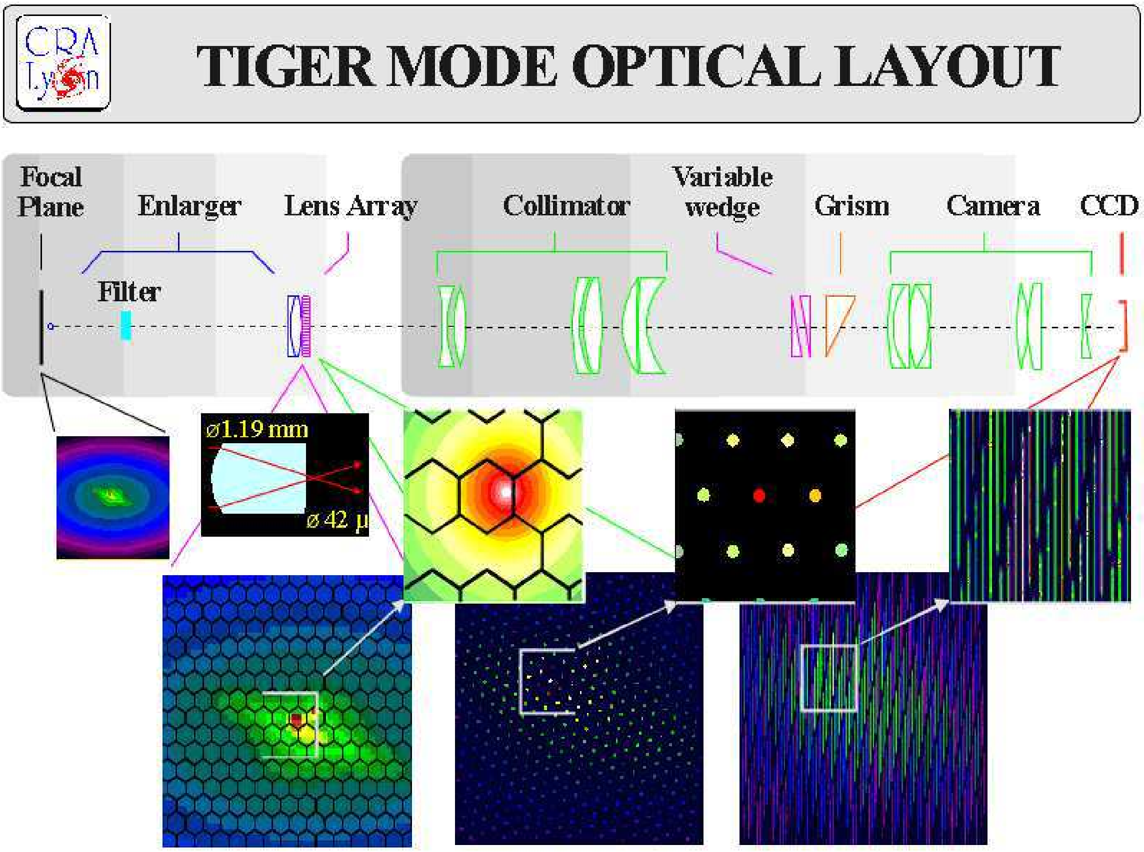

Figure 4.3: Schema of the optical path for the instrument OASIS.

The first dataset analyzed (Ch. 5) was obtained using the optical instrument OASIS, *Optically Adaptive System for Imaging Spectroscopy*, which is an example of integral field spectrograph based on lenslets. This instrument was developed by the Observatoire de Lyon team (Bacon et al., 1995). Figure 4.3 shows the optical path followed by the light coming from the scientific object. Light is spatially sampled using ~1000 hexagonal micro-lenses and then dispersed using a grism. The spectra are then recorded on the CCD obtaining at the end one spectrum for each field of view portion imaged with each lens.

This instrument was first placed at the CFHT, *Canada-France-Hawaii Telescope*, in the Mauna Kea observatory in Hawaii. The optical domain covered went from 4200Å to 10370Å. It worked at low to medium spectral resolution (1000-4295) and the sky sampling, depending on the field of view (FOV), was: 0.04″ for FOV 1.6″×1.2″, 0.11″ for FOV 4.1″×3.3″, 0.16″ for FOV 6.2″×5.0″ and 0.30″ for FOV 11″×9″. The data analyzed in Ch. 5 was taken in the third configuration (Table 4.2) combined with the adaptive optics system PUE'O to improve the angular resolution.

Since 2003, OASIS operates in the WHT, *William Herschel Telescope*, at the Roque de los Muchachos Observatory in La Palma. It can be used with or without adaptive optics and nowadays it offers three different sky samplings: 0.09″ (FOV 2.7″×3.7″), 0.14″ (FOV 4.0″×5.5″) and 0.26″ (FOV 7.4″×10.3″). It spectral resolution goes from two hundred to a little more than four thousand and it covers a wavelength domain which goes from 4000 to 10000 Å.

4.2.2 SINFONI

The second instrument used was SINFONI (Ch. 6), *Spectrograph for Integral Field Observation in the Near Infrared*, which has been developed by ESO and the Max-Planck-Institut für extraterrestrische Physik in Garching in collaboration with NOVA (Nederlandse Onderzoekschool Voor Astronomie) (Eisenhauer et al., 2003). This instrument is an example of the image slicer technique and it is placed in the VLT, *Very Large Telescope*, at Paranal observatory in Chile. Figure 4.4 shows a scheme of the functioning of the instrument. The field of view is sliced into 32 small slices which are recombined into a pseudo long slit before being dispersed using a standard spectrometer. Each one of the 32 slices is imaged onto 64 pixels of the detector, giving 2048 spectra of the imaged region. The dispersion direction overlays 2048 pixels of the detector. The final product is thus a 3D data cube where each plane of the cube is a monochromatic reconstruction of the SINFONI field of view.

SINFONI is installed at the UT4, at the VLT in Paranal Observatory. It is used in combination with an adaptive optics module and it covers the wavelength range from 1.1μm to 2.45μm. The spectrograph operates with four gratings (J, H, K, H+K) providing a spectral resolution which goes from 1500 in the H+K mode, 2000 in the J band, 3000 in the H band and 4000 in the K band. It can be used in three different spatial configurations, one with a spatial resolution of 0.25″ and a FOV of 8″×8″, another with 0.1″ spatial resolution and a FOV of 3″×3″ and the last with a spatial resolution of 0.025″ and a FOV of 0.8″×0.8″. The data analyzed in Ch. 6 were taken in the second spatial configuration in the H and K bands (Tab. 4.2).

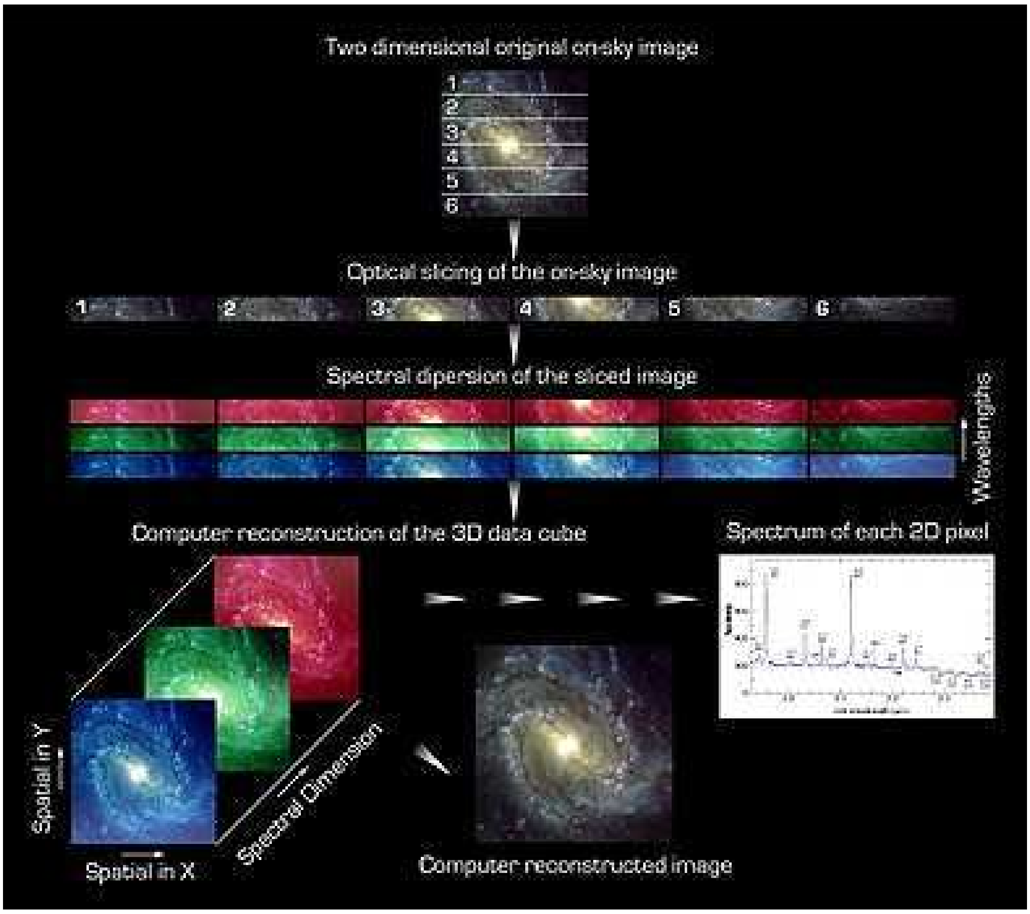

Figure 4.4: Schematic functioning for the instrument SINFONI.

4.3 Data reduction in IFS

The general reduction steps are summarized in Fig. 4.5. Generally speaking the same data reduction carried out in long slit spectroscopy is applied in integral field spectroscopy but with some particularities that we have to take into account. Some of these particularities are common to all the IFS techniques and some are specific to each one.

For the data analyzed in this thesis the corresponding pipelines were used in each case. For the optical data from OASIS, the XOasis software[1] was used. For the SINFONI data the corresponding version of the pipeline[2] was used. The details of each dataset reduction are explained in the corresponding sections in Ch. 5 and Ch. 6 respectively.

One important correction that we can make *a posteriori* is the atmospheric differential refraction correction. In traditional spectroscopy this correction has to be taken into

---

[1] http://www.cfht.hawaii.edu/Instruments/Spectroscopy/OASIS/Reduc/

[2] http://www.eso.org/sci/facilities/paranal/instruments/sinfoni/

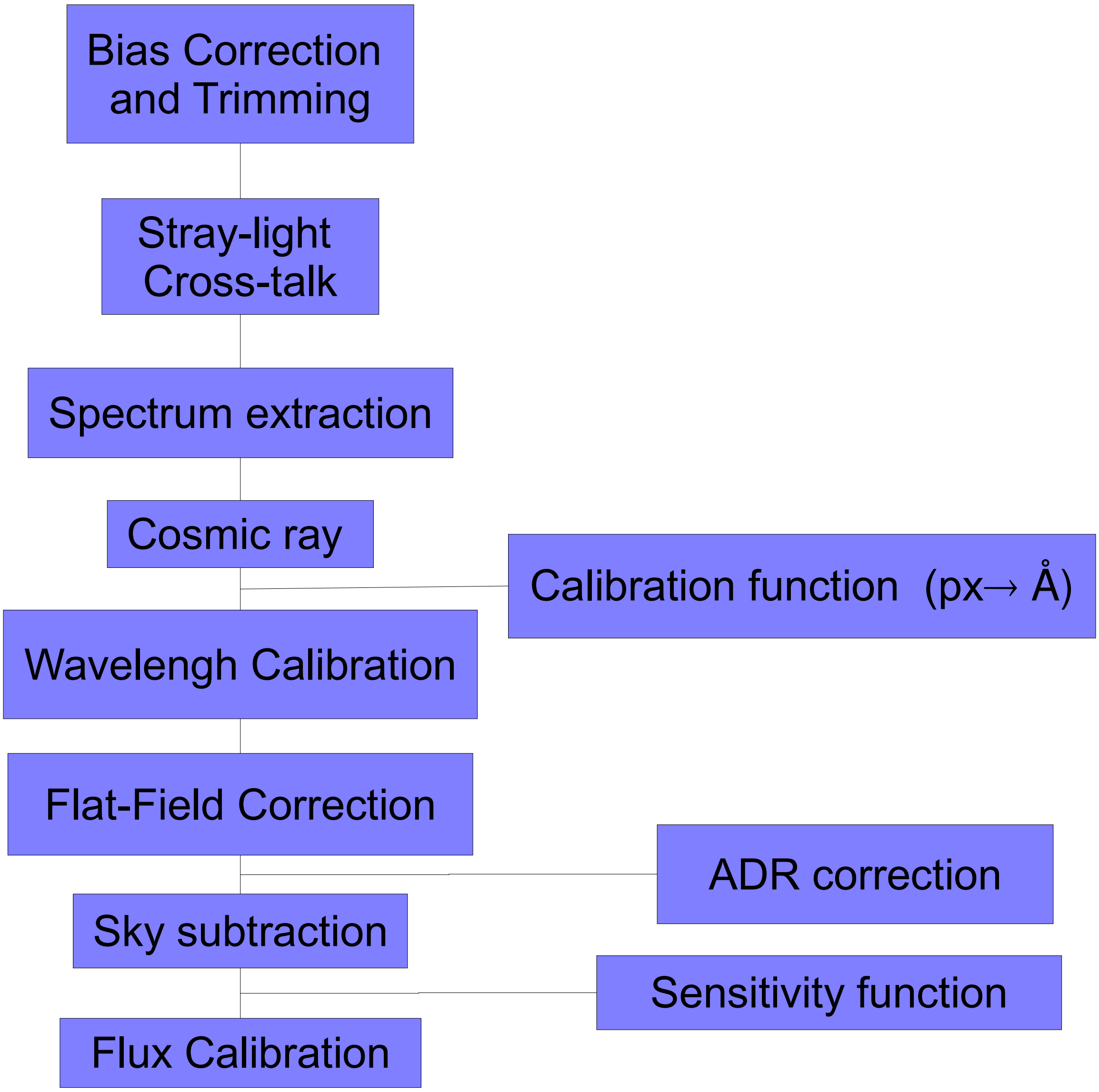

Figure 4.5: General steps for a data reduction of IFS.

account during the observation run making it difficult to accomplish. The spectrum extraction and the flat-field correction are two important steps which have to be done carefully. These specific steps just as the stray-light and cross-talk correction will be explained in detail in Sec. 4.3.2, 4.3.3, 4.3.6 and 4.3.7.

4.3.1 Bias and Dark Correction

The first step to be carried out in any data reduction is the bias subtraction. This bias level is introduced in the CCD to ensure that the measured data are always positive. A bias image is taken with an exposure time of 0s and it shows the electronic noise of the camera.

On the other hand, the dark current is a measure of the number of electrons with a high enough energy to end up in pixels without the need of an 'activating' photon. It is generated because the CCD has a non-zero temperature, although the current cameras are well cooled and this contribution is very small. To correct for this effect, some dark frames are taken during the observing run. Theses frames are taken with the same exposure time as the scientific data and then combined to reduce the noise introduced by this correction. The dark frames also contain the bias current.

In the case of SINFONI the final master dark is used to correct from the bias current but also to determine a hot pixels maps. Non-linear response pixels are obtained by evaluating the pixel response of a set of flat exposures of increasing intensity. In addition, a reference bad pixel map is already measured as the detector is known to have construction defects. Other bad pixels are determined on a set of flat fields.

In the case of OASIS a master bias image is also created by the combination of some bias frames taken during the observation run. To check the smoothness of the count level and be sure that any strange structure is added when the data are reading (corresponding to the dark current), a check is carried out in the overscan region of the CCD.

4.3.2 Stray-light and cross-talk

These two effects are specific for instruments which use fibers. Thus, they are not applicable to the data analyzed here but I explain them briefly for completeness. The stray-light is a background level recorded by the CCD which comes from several sources. One of the contributions for this background is the dispersion due to dust in the optical surfaces. Other contributions come from optical aberrations and defects in the dispersion net, the collimator or the spectrograph camera. In general, this stray-light background changes smoothly in both directions, spatial and spectral (Motta, 2003).

On the other hand, the cross-talk in one fiber is the amount of light coming from the neighboring fibers. This effect is important when the distance between fibers is small related to their size. This effect depends on the aperture profile, distance between apertures and the relative intensity distribution (Motta, 2003).

The best way to correct them is to fit both the spatial and the spectral direction at the same time and for each individual image before combining them. This fit gives a surface function which can be subtracted from the image.

4.3.3 Spectrum extraction

The spectra are recorded onto the detector in different ways depending on the IFS technique used but in general, depending on the instrument. To be able to recover the physical information, it is necessary to identify each spectrum with its position on the sky. In addition, because of optical distortions on the system, the spectra can not be completely aligned in the dispersion direction. Hence, the basic idea in this step is the same as in the standard extraction procedure in long slit spectroscopy, but we have to carry out a spatial calibration to associate each spectrum with a spatial position in the sky.

In the case of OASIS an image of the microlenses is taken during the observation run. This image consists in illuminating the instrument with a source of uniform light, a continuum flat-field image, but without dispersing the light to identify the lens center positions on the CCD by means of a gaussian fit. A cross-dispersion profile is evaluated for each spectrum and then fitted using a special algorithm which computes an optical model of the instrument dispersion on the detector. The positions of the spectra ridges are obtained from these cross-dispersion profiles. For every lens and every wavelength, the weighted sum of five pixels width centered on each particular spectrum ridge and wavelength is calculated. The weights are computed as 1 over the total signal variance over the pixel, using the photon noise of the fraction of the signal on the pixel and the known CCD readout noise. Finally, a extraction mask is created and the data are arranged in a data cube with the two spatial dimensions and a first estimation of the wavelength vector which will later be more finely calibrated.

In the case of SINFONI some raw frames are taken to be able to correct the image from the distortion effect and to calculate the slitlet distances. Some on/off lamp flats, arc lamp and fiber frames are required. These fiber frames are obtained by placing a fiber at different positions so that only the first column of each slitlet is illuminated through fibers. A fake slitlets-on and a slitlets-off frame are determined from the fiber frames. A wavelength calibration solution is determined from the undistorted arc lamp frames. The distortions parameters are calculated on the fake on-off frame and then the slitlet distances are also determined on this fake on-off frame. For that, a Gaussian fit along the spatial direction at each row is applied for each slit spectra. A position for each row is obtained and then they are averaged for each slitlet and computed regarding to one of reference.

4.3.4 Cosmic ray correction

Cosmic rays are in general removed directly in the CCD image. The standard procedures are more difficult to apply in the case of bidimensional spectroscopy. The median between neighboring pixels on the CCD can be determined only in the wavelength direction because in the spatial direction they correspond to different positions in the sky. In addition to this, some spectral unresolved lines coming from spatial unresolved regions can be mixed up with a cosmic ray and be awry corrected.

In the case of SINFONI, cosmic rays are corrected in the first step of the data reduction through the bad pixel master mask. In the contrary XOasis has a dedicate routine which is run before the sky subtraction, after the spectrum extraction, the wavelength calibration and the flat field correction. The integrals of the spectrum to be checked and of the neighbors inside a region where we can assume spectral similarity, are computed. The neighbors spectra are normalized to the central one and the median of the spectra is calculated. The difference between the central spectrum and the median spectrum is computed (median-filtered difference) and compared with the un-filtered difference. A sigma-clipping is then performed on this spectrum. The pixels above N times sigma are replaced, in the central spectrum, by the median value.

4.3.5 Wavelength Calibration

A very important step in any spectroscopic data reduction is the wavelength calibration. The standard procedure in the optical domain uses images of calibration lamps to obtain the transformation function from pixels in the detector to wavelength units, for example Å. The OASIS data are already calibrated to a good approximation (from a fraction of an Å to 2 Å, according to the configuration), in the extraction step. In this step, the residuals are fitted by a second-order polynomial to refine the calibration.

In the infrared domain is more common to uses the OH telluric lines exhibited in the sky images whose wavelength values are very well known, however the use of calibration lamps is also possible. The SINFONI pipeline uses by default the images of calibration lamps. In our particular case the wavelength calibration using lamps were not accurate enough to our purposes and a correction calculated from OH lines were carried out. All the details are explained in the corresponding section, Sec. 6.2.2, in the Ch. 6.

4.3.6 Flat field

The flat field correction is one of the most delicate step in IFS data reduction because of the 3D nature of data. Some effects present only in long-slit or only in photometry data are combined here and all of them must be corrected. The first correction is about the high spatial frequency variations because of the different pixel sensitivity of the detector, that is the traditional spatial flat-field. However, in spectroscopy we also have to care about the spectral uniformity response in the dispersion direction (spectral flat-field), not only about the spatial one. In addition to these two corrections, a low frequency spatial correction due to the different response in fibers or lenses, depending on the instrument, has to be considered.

In the case of OASIS the high spatial frequency variations seem to be not very important. Nevertheless, a correction can be carried out if enough continuum frames (about 50) are obtained. The low frequency both spatial and spectral flat effects are corrected in the same step. A continuum lamp exposure, wavelength calibrated and cosmic ray corrected, is normalized to the median integrated value of the central spectra. To remove any non-uniformity from the continuum lamp exposure, each sky spectrum is summed over the wavelength range and the resulting value is used to normalized the corresponding continuum lamp spectrum. A spline function is fitted to eliminate the high frequency residuals and obtain then the low frequency spectrum of reference. This spectrum of reference is compared to each continuum spectrum to obtain the correction by spectral pixel related to the low spatial frequency variations.

In the case of SINFONI some different types of flat field are taken. Standard flat fields with uniform light are used to determine the variation pixel to pixel and to detect bad pixel on the detector. This flat field correction is applied after the bad pixel removal. Other kind of flat fields are taken to test the detector's linearity and find highly non-linear pixels. They are taken by increasing the intensity of the uniform light. The last kind of flats are obtained together with fiber frames to compute the detector's distortion as I explain in the spectrum extraction section.

4.3.7 Atmospheric Differential Refraction (ADR)

The atmospheric differential refraction (ADR) effect consists on the change of the direction of light with wavelength when it passes through the earth atmosphere. It depends on the physical atmosphere conditions at the moment of the observation, the altitude of the observatory and on the wavelength at which we observe.

In long slit spectroscopy, the slit must be orientated in the direction given by the parallax angle if the relative fluxes in the spectra are preserved. If the slit is placed in a different angle, some spectral range will be affected by light loss. Nevertheless, one of the advantage of bidimiensional spectroscopy is the possibility of correcting ADR effects a posteriori. Without ADR, object images at any wavelength are coincident and the spectra are basically the same. However, when ADR is not corrected the object images at different wavelength are not in positional agreement. Differences increase quickly for higher zenith angle, and decrease with wavelength. In this case, each spectrum is different and fluxes at different wavelengths in a single spectrum are not comparable (Arribas et al., 1999).

To correct this effect, we fit the continuum displacement in the centroid for the two spatial directions at each wavelength related to one of reference and then we re-centered the images for each wavelength. For point sources this is easy to calculate from the reconstructed imaged at each wavelength. In the case of extended objects it is more complicated and a continuum image is used. Figure 4.6 shows an example of this effect in the case of OASIS data. On the left panel I show the ADR correction to apply in the X direction of the detector and on the right panel I show the correction for the Y direction. In black we plot the spatial displacement produced by this effect as a function of the wavelength, in this example we observed up to $0.016''$ over 300Å. A linear fit is carried out over all the displacements and then it is used to correct from this effect. The displacements corrected are over-plotted in blue.

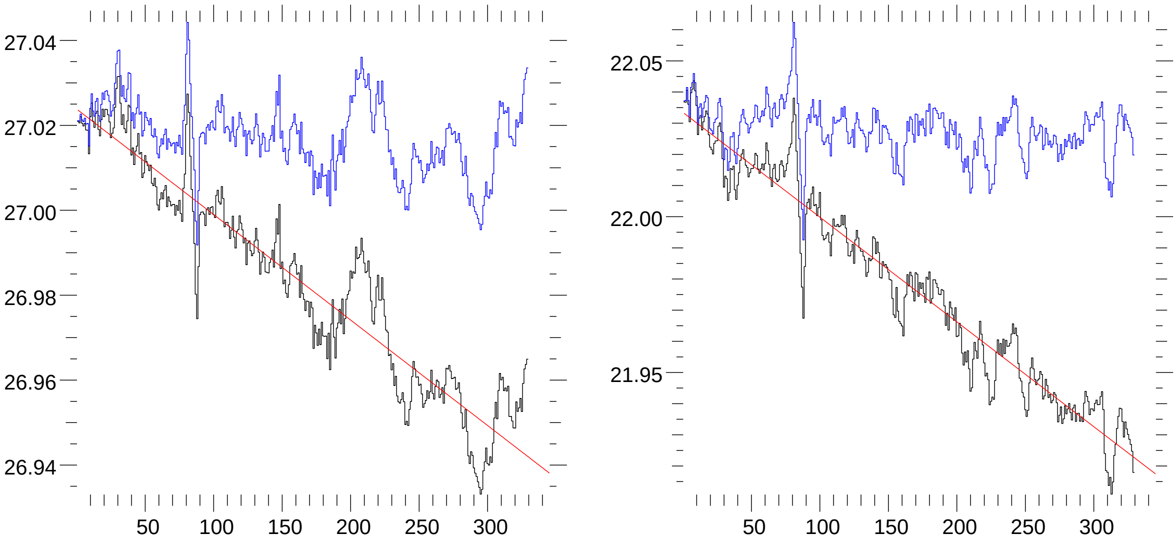

Figure 4.6: Example of the ADR effect from OASIS data (in the X direction of the detector on the left and in the Y direction on the right). The measured displacement as a function of the wavelength are plotted in black. In blue we show the same centroid displacement once the ADR effect has been corrected. The red line is the linear fit used to correct from this effect.

4.3.8 Sky subtraction and Flux Calibration

The two last steps in the data reduction, which are common to any kind of data reduction, are the sky subtraction and the flux calibration. For the first of them, in the case of SINFONI, some sky images are taken during the observing run and then combined to remove the sky background from the object images. The night sky emission lines are very bright and both spatially and timely variable in infrared. In order to completely eliminate the OH lines in the final data cube, the nearest (spatially and timely) sky frame must be used.

In the case of OASIS data, the sky is determined from the frame. A region assumed empty and consequently representative of the sky emission, is chosen from a reconstructed image from the spectroscopic data. The mean spectrum of this region is computed for each frame and subtracted from every spectrum of the data cube.

The flux calibration consists in convert the numerical intensity values on the detector to physical flux units. To achieve this calibration, some standard stars are observed during the night. The observed flux has to be integrated spatially within a certain radius, larger than the seeing disc radius, to obtain a total spectrum of the star and then it is compared with the total known flux of the star for each wavelength. This step was carried out during the data reduction with XOasis for our optical data. In the case of SINFONI, this step is not implemented in the pipeline and we carried it out by ourselves (detailed in Sec. 6.2.2 in the Ch. 6).

4.3.9 Combination of data cubes and re-sampling of data

During an observational run some exposures are taken and then combined to increase the signal to noise in the final image. Merging IFS data cubes has to be carried out carefully.

In the case of OASIS, the spatial shift between the different exposures must be known to avoid the field distortion in the final image. For that, for each exposure, a reconstructed image is created integrating in the whole wavelength range. On these images, some eye-catching detail (a star or a morphological detail), presented in all the images, is chosen. This point will became the zero point in the merged image. A special routine computes the parameters to achieve the merging process. It calculates the normalization factor to apply to the exposures to correct for the flux differences. It also obtains the optimal weights to be used during the merging process to maximize the resultant S/N. Finally, the data cube are merged and then re-sampling to a square spatial sampling grid, instead of the original hexagonal grid.

In the case of SINFONI, raw data are re-sampled using a wavelength map to remove the brick-wall pattern. Thus, a given image is re-sampled at discrete wavelength intervals using a polynomial interpolation so that each frame row is associated with a defined wavelength. The slitlets are then stacked into a cube taking into account the slitlets distances and the edge positions determined in the previous steps. At the end, each plane of the cube is a monochromatic image of the field of view. Reading some keywords and the exposure time, corresponding to each target, from the FITS header, the pipeline computes the spatial offsets to apply to each cube plane to properly merge them. The intensity of the final coadded cube is calculated, at each pixel, as the weighed mean of the corresponding overlapping pixel intensities. The weight is given by the exposure time of each target.

4.4 Integral Field Spectroscopy combined with adaptive optics

Previously, I discussed the importance of the integral field spectroscopy for the study of micro-jets in the closest regions to the star. I also mentioned that one of the main difficulties in these kind of studies is to separate the line emission coming from the jet and the bright stellar continuum. The emission line contrast can be increased either with a smaller PSF or with a better spectral resolution (ideally a combination of both). The required angular resolution for our study is $0.1''$ which can be achieved from space. However, in ground-based observations we are limited by the atmospheric turbulence at $\sim 1''$. Using adaptive optics in telescopes with diameter higher than 4m this required angular resolution can be achieved. The data analyzed in this thesis were obtained using integral field spectroscopy combined with adaptive optics. The combination of these two techniques allowed us to profit from the advantages that both of them provide. Thus, the data obtained had a good angular resolution, a good spectral resolution and a good spatial coverage, simultaneously.

4.4.1 Adaptive optics (AO)

The adaptive optics (AO) technique is one of the most powerful technique developed to be able to reach the diffraction limit of the telescope in ground-based observations. An adaptive optics system measures the wavefront perturbation due to refraction index fluctuations of the atmosphere to correct it quickly to follow the turbulence evolution during the observations. Nowadays, these systems are fundamental instruments in any 8-10 m class telescope. In this section, I am going to give a brief summary of this technique applied to our particular study, for a more detailed discussion of AO technique see for example Esposito & Pinna (2008).

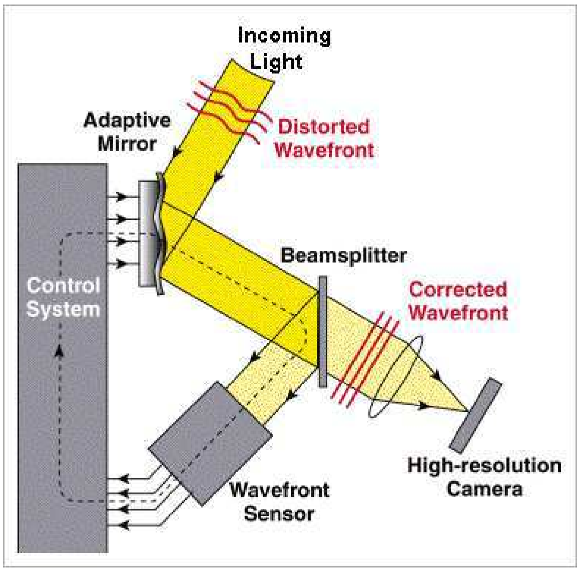

Figure 4.7: Diagram of an adaptive optic system. The main elements are represented: the wavefront sensor, the control system and the wavefront corrector (deformable mirror). The figure also shows the different optical paths of the light from the reference star and the scientific target.

Figure 4.7 shows the basic scheme of an adaptive optic system. Three are the main elements of this kind of systems. Firstly, the *wavefront sensor* measures the instantaneous wavefront aberration, which is computed by the *control system (or wavefront computer)* and then this last one gives the necessary instructions to the *wavefront corrector* (usually a deformable mirror) which corrects the phase fluctuation introducing different optical paths for different rays. The wavefront aberration are measured using a reference star which needs to be quite bright and not very far from the scientific target in order to be sure that the measured wavefront is representative of that present in the scientific target. The fundamental parameters which characterize the level of atmospheric turbulence are the Freid parameter, r_0, the size scale of turbulent cells and the correlation time t_0. These parameters depend on the wavelength and most of the AO systems are optimized to provide diffraction limit in the near-infrared domain. In fact,, current AO instruments in the 8-10 m class telescope can reach an angular resolution in the near-infrared similar to that of HST in the optical domain. However, because of the strong dependence with wavelength, the correction achieved in the optical is much worse.

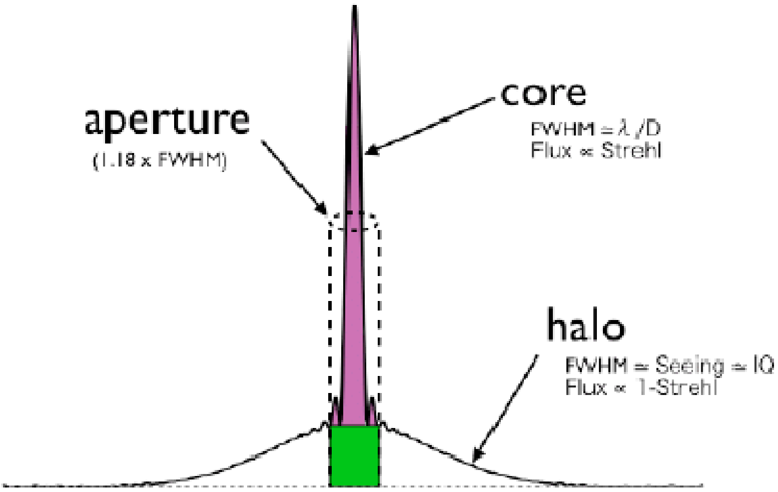

Figure 4.8: Profile of a point source image in an adaptively corrected telescope.

The quality of the AO correction is measured with the strehl ratio. This parameter is defined as the ratio between the peak intensity of a PSF image divided by the peak intensity of a diffraction-limited image with the same total flux. A PSF (point spread function) image is the image of a point source and in an adaptively corrected telescope, this image is the sum of the AO-corrected core (diffraction limited) and the uncorrected (seeing-limited) halo (see Fig. 4.8 for an example). Current AO systems provide typical strehl ratios of 50% in the near-infrared and a few % in the optical domain.

To analyze the wavefront perturbations induced by the atmosphere, a reference star is observed. In the natural guide star mode, this star has to be carefully chosen. It must be at an angular distance less than the isoplanetic angle ($\sim 30''$ at 2μm) of the scientific object in order to ensure that the turbulent wavefront analyzed is correlated to that of the scientific target. The reference star must also be bright enough to have a good signal to noise ratio on the wavefront sensor. In general, the limiting magnitude depends on the number of actuators which analyze the wavefront, but current AO systems in 8 m class telescopes need a 11-12th mag reference star to provides strehl ratios of 50%.

In the Laser Guide Star mode the requirement are similar but the limiting magnitude is less stringent, stars with 11-18th mag are good enough to have a good correction. However, this mode still needs a natural star for the tip-tilt correction.

4.4.2 Spectroscopy combined with AO

AO corrections can be also applied to spectroscopic observations. The improvement in angular resolution given by the AO allows to use smaller long slit widths increasing also the spectral resolution. However, due to the variations of the atmospheric turbulence with wavelength, the PSF changes across the spectrum and some spurious effects can be introduced if the slit width is close to or larger than the PSF. Because of this dependence of the PSF, artificial continuum slopes and wavelength shifts (the slit effect) can be observed. Moreover, if the adaptive optics correction is different in the telluric standard from the scientific object, the telluric correction becomes very difficult. Finally, the spatial profile of the PSF is composed by two components: a diffraction limited core and a seeing size halo which can have different spectral resolutions.

The use of integral field spectroscopy combined with adaptive optics minimizes the importance of these spurious effects. In particular, lenslet IFS technique does not suffer from the slit effect. Moreover, IFS combined with AO provides an instantaneous estimate of the 2D spatial PSF during the observations, but also its dependence with wavelength. This PSF estimate can be used in the deconvolution of reconstructed channels maps.

Deconvolution of maps

Once an image reconstructed (explained in Sec. 4.5.1) we can achieve a deconvolution of the PSF in the image as in traditional photometry. The deconvolution decreases the contribution of the PSF halo, i. e., it obtains a better Strehl ratio. Between the different available algorithms LUCY in IRAF gives good results for a combination of a bright point source and an extended source, which is the case of jets in young stars. In IFS it is, in theory, possible to carry out a 3D deconvolution. As it has been done in radio astrophysics, it is possible to do a global spatial deconvolution if we impose a spectral regularity condition. However, this technique has not yet developed in IFS.

The LUCY task restores a given image using an estimate of the PSF using the algorithm developed independently by Lucy (1974) and Richardson (1972). Using an iterative method, this algorithm generates a restored image using the maximum likelihood expression for data with a Poisson noise distribution. The method, in accordance with photon-counting statistics, forces the restored image to be positive. Moreover, the restored image will be properly normalized and the integrated flux in the image is conserved. The principle of the iteration is that the (n+1)th estimate of the restored image is given by the nth estimate multiplied by a correction image (asterisks represent convolution operators):

$$image_{n+1} = image_n \frac{original\ data}{image_n * PSF} * PSF(-x,-y)$$

In order to achieve a good deconvolution it is important to have a good estimation of the PSF and a good convergence criteria. The task allows the user to specify a number of iterations to be run and a limiting reduced chi-squared. From our experience, the χ^2 criteria is not very good, a criteria based in the final resolution is more robust. However, the difficulty is to find the appropriate number of iterations. If this number is too big, some artifacts can be formed in the restored frame. In theory the final resolution has to be two times the spatial initial sampling and it depends on the signal to noise and it will be different from one kind of source to another. We usually iterate so that jet widths measured from the convolved images does not evolve. Figure 4.9 shows, for the DG Tau micro-jet, the measured jet width as a function of the distance to the star for different number of iterations. As example, I show the results obtained for the deconvolved images from the channel maps shown in top panels of Fig. 6.12 in Ch. 6. The bottom panels in Fig. 6.12 were obtained for a number of iterations of 40. Here, the top left graphic shows the HVC observed in the atomic ([FeII]λ1.64μm) blue jet, the top right shows the red counterpart and the bottom one shows the case of the molecular ($H_2\lambda$2.12μm) emission.

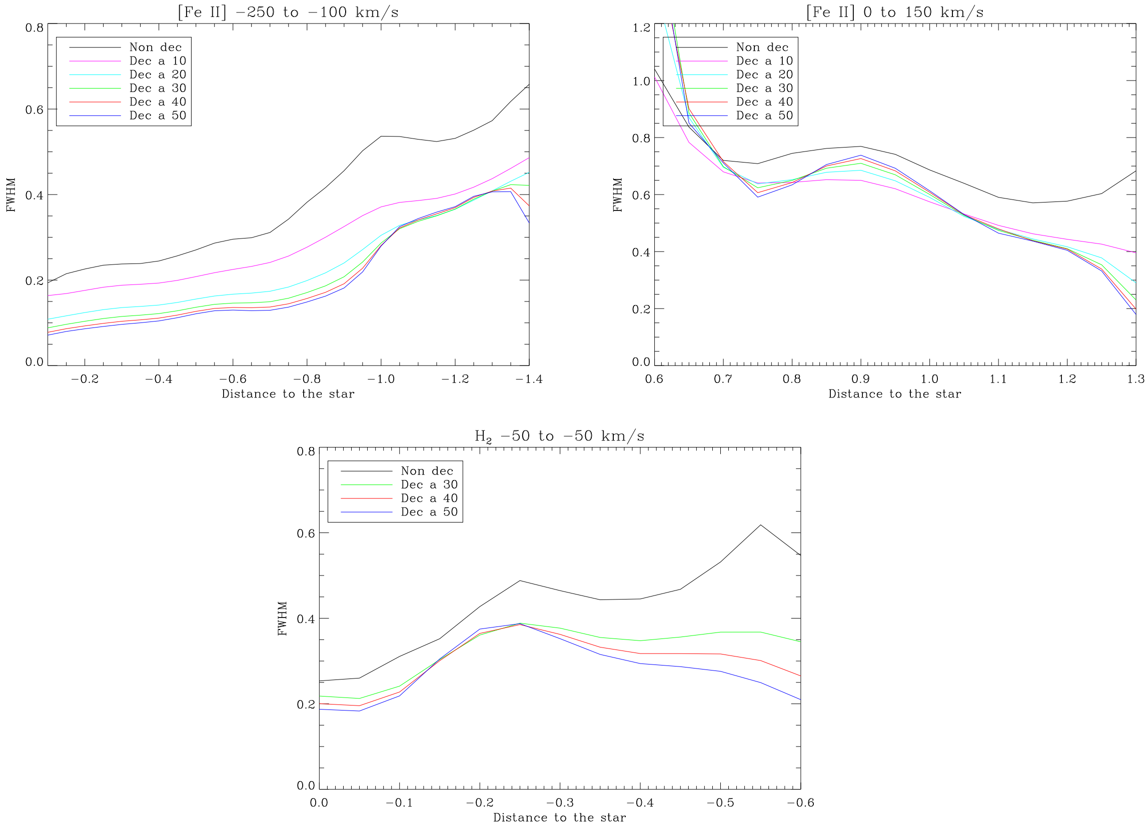

Figure 4.9: Deconvolved DG Tau jet widths measurements as a function of the distance to the star for different number of interactions. The original maps are that shows in top panels of Fig. 6.12 in Ch. 6. The final number of iterations taken to obtain the restored images shown in bottom panels of Fig. 6.12 is 40. The two top graphics correspond to the atomic jet (blue side in the left and red side on the right). The bottom graphics corresponds to the molecular emission.

Achieving the best results requires some preparation of the data. The result is better if the background data values are close to zero. In addition, bad pixels must be flagged or repaired to avoid the production of artifacts around the flawed pixels. The LUCY task automatically detects bad negative pixels that exceed the nominal distribution associated with the given read-out noise. The last thing is that the PSF estimation given to the algorithm, if it is extracted from observed data, must be corrected for any pixel defect and background removed. The PSF should be properly normalized and centered for the computation.

4.5 IFS visualization tools

The final information in a IFS data cube is given in a 3D or even 4D structure. The same data cube provides the two spatial dimensions, the spectral information and the intensity. Analyze and see all this information in 2D graphics is not easy, one or two of the dimensions must be eliminated or averaged. Two particularly useful visualization tools are the channel maps where the spectral direction is eliminated by integrating the emission over a given wavelength range, and the position-velocity diagrams where one of the spatial directions is averaged.

4.5.1 Channel maps

Bidimensional spectroscopy allows us to reconstruct a monochromatic image of the object in two dimensions from the spectra. However, it is also possible to integrate in a band width or in a velocity interval (channel map) to obtain the morphology of the object at a given velocity component.

For both set of data, OASIS and SINFONI, we developed routines in IDL to obtain these channel maps. For a given emission line each spectrum is integrated in a chosen velocity interval (see Fig. 4.10). Thus we obtain a value of intensity for each spatial point in a similar manner as traditional image from photometric observations. The advantage beyond the traditional photometry is that we can choose a posteriori the width of the band in which we want to integrate and we are limited by the spectral resolution of the instrument. Hence, it is possible to separate different velocity components for a single emission line.

The image reconstruction is carried out using the TRIANGULATE procedure which constructs a Delaunay triangulation of a planar set of points. After the data points have been triangulated, the function TRIGRID is invoked to interpolate surface values to a regular grid.

4.5.2 Position-velocity diagrams

Another visualization tool used in the data analysis of this kind of observations is to reproduce the same position-velocity diagrams which are used in long slit spectroscopy.

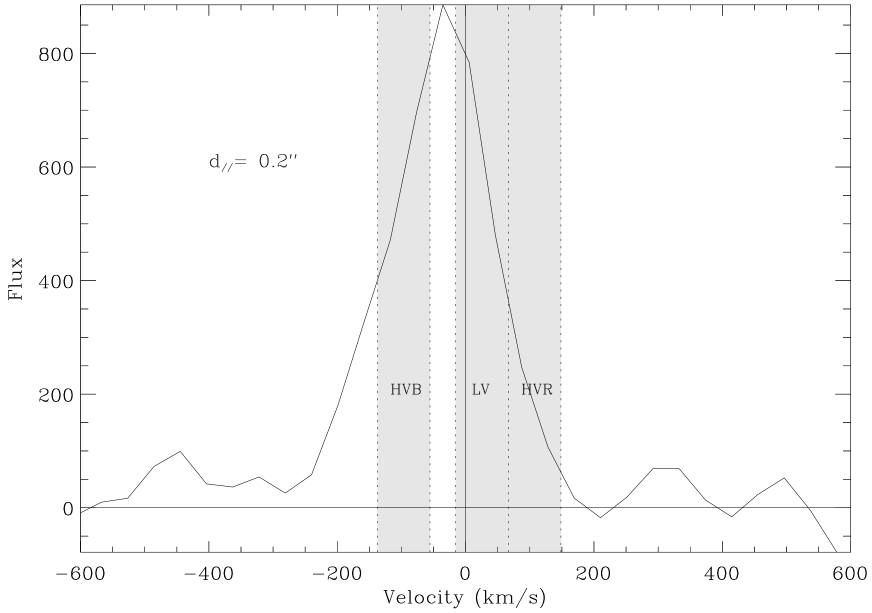

Figure 4.10: For a given emission line, one can choose the velocity intervals where the emission will be integrated to reconstruct each channel map. This is the example of the three velocity components (three channel maps) observed for the RY Tau jet (Ch. 5).

The advantage in the case of IFS is that we can create a PV diagram for which we choose not only the slit width in which integrate the emission, but also where we place the simulated slit and the orientation. To illustrate this, Fig. 4.1 shows one possible orientation of the simulated long slit, the spectra inside the slit width would be summed to obtain a spectrum for each spatial point along the long slit. It is also possible to choose the sampling in the preserved spatial direction. This kind of diagrams allows us to study the jet kinematics not only along the jet direction but also in the transverse direction.

Hence to reproduce this kind of diagrams, we developed a routine in IDL which estimate, for a given emission spectral line, the average flux from the spectra inside the simulated slit width and for each sampling element in the preserved direction. Thus, we obtain as a function of the velocity (or wavelength) an averaged spectrum for each spatial element along the jet direction or transverse to the jet axis.

4.5.3 Noise estimation

An estimation of the noise is carried out for each individual spectrum. This noise is obtained on the continuum subtracted spectra as the standard deviation at each side of the spectral line of interest. In the case of the channel maps, the signal to noise is calculated for each spectral pixel using this noise estimation. When several spectral channels are combined, the final noise is estimated by combining in quadrature the individual noise

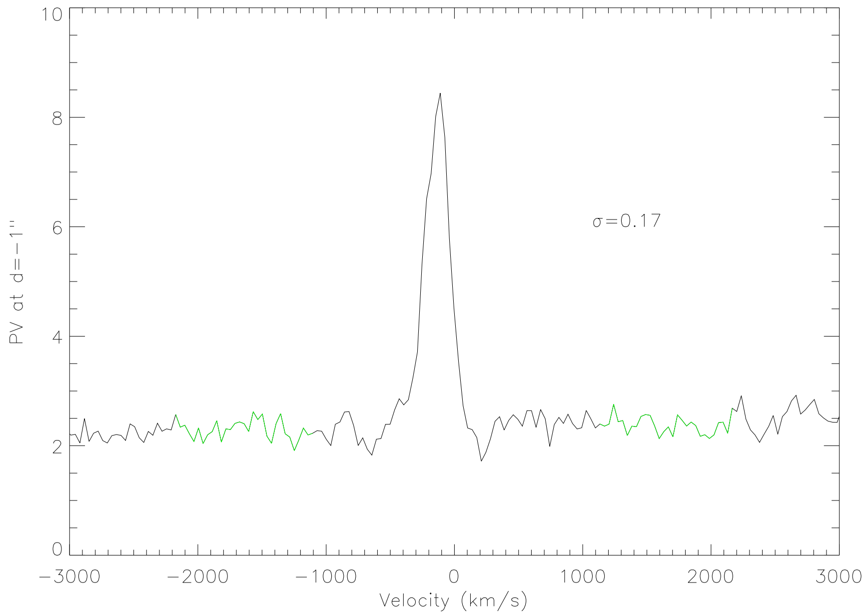

Figure 4.11: Example of the noise estimation in a spectrum of the PV diagram of DG Tau in the blue side of the jet, at a distance of 1″ from the star. The intervals in green are the regions where the standard deviation was computed.

($\sigma_{tot} = \sqrt{\sum_i \sigma_i^2}$). In the position-velocity, this error is calculated in the same way on the resulting averaged spectra. Figure 4.11 shows an example of a spectrum for the reconstructed position velocity for the blue jet in DG Tau in the [FeII]$\lambda1.64\mu$m line at a distance of 1″ from the star. The regions where the standard deviation was computed are marked in green.

5

RY Tau

In this chapter I present the analysis of optical spectro-imaging observations of the T Tauri star RY Tau which resulted in a publication in the Astronomy & Astrophysics journal (Agra-Amboage et al., 2009). All the analysis and results are given in detail in the article that I join to this chapter, but I will star with a brief summary of the aims and mains results obtained.

Following some of the main aims of this thesis, RY Tau was observed on one side, because this star is one of the most massive T Tauri stars studied so far with a mass of 2 $M_\odot$ (Mora et al., 2001) (intermediate between classical T Tauri stars and the Herbig Ae/Be counterpart). And on the other side, because this star has been classified as a binary from Hypparcos observations. These two particular properties allow to probe the influence of the star properties and the multiplicity in the properties of the resulting jet. In addition, it is important to increase the number of sources studied in detail, with a good combination of angular and spectral resolution. The previous works combining kinematical and imaging studies gave important advances in the field and showed the importance of extending this kind of works to other sources (e.g. Lavalley et al., 1997; Lavalley-Fouquet et al., 2000; Bacciotti et al., 2000).

RY Tau is a F8-G1 star located in the Taurus-Auriga cloud, at 140 pc. It has a mass of 2 $M_\odot$ (Mora et al., 2001) and stellar radius of 3 $R_\odot$ (Calvet et al., 2004). It is also an active accretor, with a veiling of $\sim$0.1 in the optical (Hartigan et al., 1995; Basri et al., 1991) and 0.8 in the UV (Calvet et al., 2004). The suspected binary is placed at a position angle of 304° ± 34° from the Hipparcos observations, and with a minimum separation of 3.27 AU (Bertout et al., 1999). In addition, it is a rapid rotator with a $v \sin i$ of 52 ± 2 km/s (Petrov et al., 1999).

RY Tau was studied using observations in the optical [OI]λ6300Å line taken using the integral field spectrograph OASIS combined with the adaptive optics system PUE'O at the Canada France Hawaii Telescope (CFHT), on January 15th 2002. The angular resolution achieved, after AO correction is 0.4″ and the velocity resolution is 135 km/s.

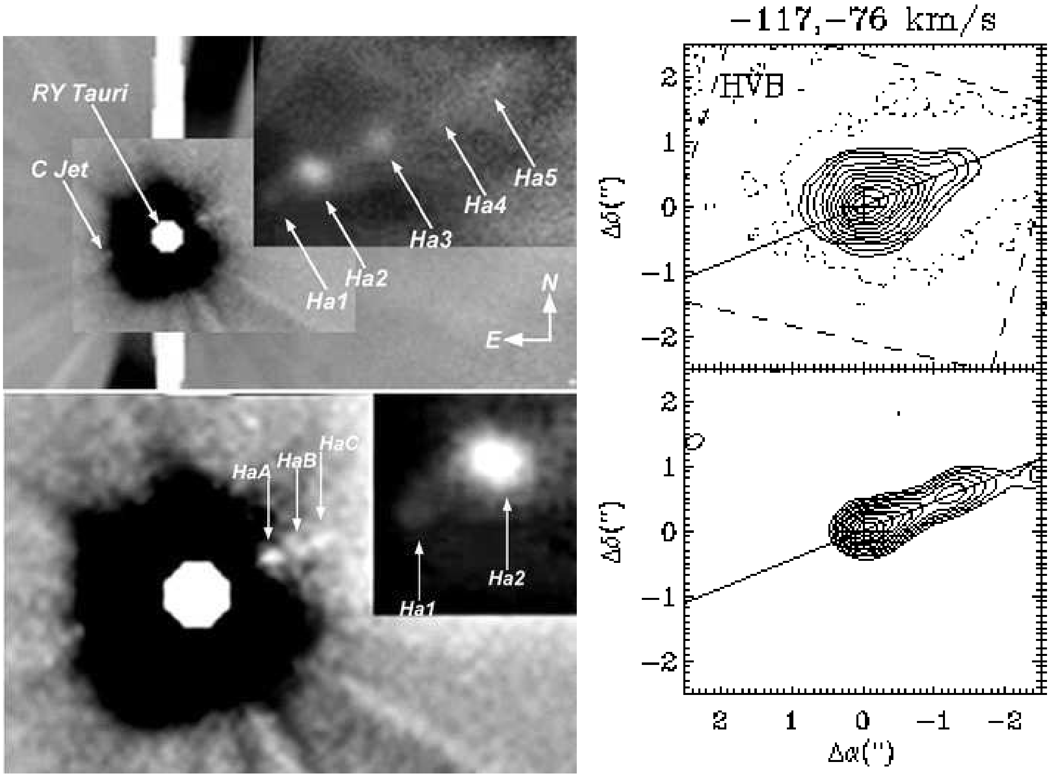

Figure 5.1: Left: Figure adapted from St-Onge & Bastien (2008) showing the RY Tau jet detected in H_α emission, out to several arcminutes. Right: The detected high velocity blue component detected in [OI] (this work) at spatial scales of several arcsecs for comparison.

Previous works have already suggested the existence of a jet (Cabrit et al., 1990; Hartigan et al., 1995) and St-Onge & Bastien (2008) confirmed this with the detection of a collimated H_α emission out to several arcminutes of the star (Fig. 5.1). In addition, Hartigan et al. (1995) and Hirth et al. (1997) carried out kinematical studies at high spectral resolution and identified a high-velocity component with radial velocities at -70,-80 km/s and a low-velocity component with velocities at -4km/s. The red counter jet has not been detected at the small-scales of some arcseconds.

Our IFS observations allowed to detect and map the blueshifted microjet associated to RY Tau within 2″ from the star and determine its position angle and its collimation degree. The good spatial resolution of the observations allows us to remove the PSF and derive the jet position and widths with better accuracy. A detailed morphological analysis was carried out, but also a kinematical one. The properties of the IFS technique allow to construct the traditional position-velocity diagrams, usually used in long-slit spectroscopy, but also to construct velocity maps by fitting each spectrum at each spatial position to an one-component Gaussian. In addition, a kinematical study of the transverse structure of the jet was carried out in order to look for the jet rotation. To finish a determination of the mass flux could be obtained as a function to the distance to the star.

In summary, the blueshifted microjet in RY Tau is detected with a position angle of 294° ± 1° and a full opening angle of 5° on spatial scales of 20-280AU. An emission knot at 1.35″ is shown, coincident with a peak in velocity. A high velocity component with average radial velocities of -70 km/s is identified in good agreement with previous studies. The red counter-jet is marginally detected and it is quite faint.

The transverse study reveals asymmetries in velocity with respect to the jet axis but the angular resolution of the data are not good enough to distinguish between jet rotation and asymmetries due to a bow-shock in the jet which will be placed at the knot position.

The mass loss rate estimate is 4 times higher than the previous estimation by (Hartigan et al., 1995) and reveals the importance of obtaining resolved spectro-imaging observations to derive more accurately this parameter, so important to probe the models.

Finally, the observed jet PA is comparable to the expected PA for the suspected binary system from the photocenter variations in the Hipparcos observations. This agreement calls into a question this interpretation. A possible alternative to explain this variations is that they could be caused by UXOr-like occultation events and/or scattering cavity relative to the occulted photo-sphere.

The main conclusions of this work are, on one hand, that the jet properties related to collimation, terminal velocity and ejection rate do not change compared to lower mass T Tauri stars. This conclusion support the common idea that the jet launching mechanism is universal over a large range of stellar masses. On the other hand, the influence of the binary status on the jet properties could not really be tested. The agreement between the position angle in the blue jet and the position angle derived from the photocenter variation detected by Hypparcos calls into a question the interpretation of binary made for this source. A deeper study to look for the possible companion should be performed.

A&A 493, 1029–1041 (2009)
DOI: 10.1051/0004-6361:200810025
© ESO 2009

Astronomy & Astrophysics

[O I] sub-arcsecond study of a microjet from an intermediate mass young star: RY Tauri*

V. Agra-Amboage[1], C. Dougados[1], S. Cabrit[2], P. J. V. Garcia[3,4,1], and P. Ferruit[5]

[1] Laboratoire d'Astrophysique de l'Observatoire de Grenoble, UMR 5521 du CNRS, 38041 Grenoble Cedex, France
e-mail: `[amboage;dougados]@obs.ujf-grenoble.fr`
[2] LERMA, Observatoire de Paris, UMR 8112 du CNRS, 61 avenue de l'Observatoire, 75014 Paris, France
[3] Departamento de Engenharia Fisica, Faculdade de Engenharia, Universidade do Porto 4200-465 Porto, Portugal
[4] Centro de Astrofisica, Universidade do Porto, 4150-752 Porto, Portugal
[5] Université de Lyon, 69003 Lyon; Université de Lyon-1, Observatoire de Lyon, 9 Av. Charles André, 69230 St. Genis Laval; CNRS, UMR 5574, Centre de Recherche d'Astrophysique de Lyon; École Normale Supérieure de Lyon, 69007 Lyon, France

Received 22 April 2008 / Accepted 21 October 2008

ABSTRACT

Context. High-resolution studies of microjets in T Tauri stars (cTTs) reveal key information on the jet collimation and launching mechanism, but only a handful of systems have been mapped so far.

Aims. We wish to perform a detailed study of the microjet from the 2 $M_{\odot}$ young star RY Tau, to investigate the influence of its higher stellar mass and claimed close binarity on jet properties.

Methods. Spectro-imaging observations of RY Tau were obtained in [O I]λ6300 with resolutions of $0\farcs4$ and 135 km s^{-1}, using the integral field spectrograph OASIS at the Canada-France-Hawaii Telescope. Deconvolved images reach a resolution of $0\farcs2$.

Results. The blueshifted jet is detected within 2″ of the central star. We determine its PA, collimation, 2D kinematics, mass-flux rate, ejection to accretion ratio, and transverse velocity shifts taking accurately into account errors due to finite signal to noise ratio. The RY Tau system is shown to provide important constraints to several models of steady MHD ejection.

Conclusions. The remarkably similar properties of the RY Tau microjet compared to jets from lower mass cTTs gives support to the common belief that the jet launching mechanism is universal over a broad range of stellar masses. The proximity between the jet PA and the PA of the photocenter variations observed by Hipparcos calls into question the interpretation of the latter in terms of binarity of RY Tau. Partial occultation events of the photosphere may offer an alternative explanation.

Key words. ISM: jets and outflows – ISM: individual objects: HH 938 – stars: formation – stars: individual: RY Tau – stars: winds, outflows

1. Introduction

One of the main open problems in star formation is to understand the physical mechanism by which mass in young stars is ejected from the accreting system and then collimated into jets. Magneto-hydrodynamic accretion-driven wind models best explain the efficient collimation and the large mass ejection efficiencies observed. However, different scenarios are proposed for the origin of the outflow, depending on whether it originates from the stellar surface (Sauty & Tsinganos 1994; Matt & Pudritz 2008), from the inner edge of the accretion disk (Shu et al. 1995), an extended range of disk radii (Pudritz & Norman 1986; Casse & Ferreira 2000), or from reconnexion sites in the stellar magnetosphere (Goodson et al. 1997; Ferreira et al. 2000).

Microjets from T Tauri stars offer a unique opportunity to probe the inner 100 AUs of the outflow where the acceleration and collimation processes occur, and therefore to place strong observational constraints on the ejection mechanism in young stars. Combined kinematic/imaging studies of microjets at sub-arcsecond resolution have allowed major advances in this field in recent years (Lavalley et al. 1997; Lavalley-Fouquet et al. 2000; Bacciotti et al. 2000; Ray et al. 2007, and refs. therein). That the jet phenomenon is very robust over orders of magnitude of central stellar mass is testified by the fact that both brown dwarfs and Herbig Ae/Be stars are known to drive collimated outflows (Whelan et al. 2005; Corcoran & Ray 1997). However, variation of jet properties (collimation, kinematics, mass-loss rates) with mass of the driving source has not yet been investigated in detail. It is thus important to extend the sample of microjets studied at high angular resolution to central sources of differing mass and binary status.

We concentrate here on the intermediate-mass classical T Tauri star RY Tau, located in the nearby Taurus-Auriga cloud (d = 140 pc). With spectral type F8-G1 and $M_{\star} \sim 2\ M_{\odot}$ (Mora et al. 2001; Calvet et al. 2004), RY Tau is of significantly higher mass than other nearby atomic jet sources previously spectro-imaged at high resolution, the most massive so far being RW Aur with 1.4 $M_{\odot}$ (Woitas et al. 2001). It thus allows us to probe jet formation in a mass range intermediate between standard classical T Tauri stars and Herbig Ae/Be stars (of mass >2 $M_{\odot}$). The presence of a jet in RY Tau was indirectly suggested by

---

* Based on observations obtained at the Canada-France-Hawaii Telescope (CFHT) which is operated by the National Research Council of Canada, the Institut National des Sciences de l'Univers of the Centre National de la Recherche Scientifique of France, and University of Hawaii.

[O I] emission blueshifted by -70 km s^{-1} in its spectrum (Cabrit et al. 1990; Hartigan et al. 1995). It has been recently confirmed by St-Onge & Bastien (2008) who detected a collimated string of Hα emission knots (HH 938) extending from 1.5$''$ out to several arcminutes on both sides of the star. RY Tau is also an active accretor, with veiling values of ~0.1 in the optical (Hartigan et al. 1995; Basri et al. 1991) and 0.8 in the UV (Calvet et al. 2004). The latter corresponds to an updated accretion rate of 6.4–9.1 × 10^{-8} $M_\odot$ yr^{-1}, 4 times higher than the previous determination by Hartigan et al. (1995).

Another important peculiarity of RY Tau besides its mass is a suspected close binary status from Hipparcos observations. The variability of the astrometric solution, indicating motion of the photocentre, is interpreted as indicative of a binary of PA = 304° ± 34° and minimum separation of 3.27 AU (Bertout et al. 1999). Such a close binary companion might have a strong impact on the ability of the inner disc regions to drive a collimated outflow, possibly leading to observable differences to microjets from single stars.

In addition to these specific properties, RY Tau shows a remarkably flat spectral energy distribution in the far-infrared, and a rather large degree of linear polarisation of a few percent in the optical, indicating a substantial amount of circumstellar material (Bastien 1982). RY Tau also shows a peculiar photometric variability with large variations of brightness accompanied by a near constancy of colour. Two abrupt brightnening events were recorded in 1983/1984 and 1996/1997 reminiscent of UX Ori events (Herbst & Stine 1984; Petrov et al. 1999). It is also a rapid rotator with a $v \sin i$ of 52 ± 2 km s^{-1} (Petrov et al. 1999). Petrov et al. (1999) argue that the photometric behavior can be interpreted as variable obscuration of the central star by a disc seen at high inclination. The large values of $v \sin i$ and polarisation further support this conclusion.

We present in this paper sub-arcsecond optical spectro-imaging observations of the RY Tau microjet in [O I] obtained with the OASIS integral field spectrograph coupled with adaptive optics correction at the Canada Hawaii telescope. The combination of high angular resolution and intermediate spectral resolution allows for accurate subtraction of the strong central continuum emission, critical to study the inner regions of the jet. Details on the observations and data reduction are given in Sect. 2. In Sect. 3, we discuss the main results regarding the jet morphology, the jet kinematics both along and transverse to the jet axis, the search for rotation signatures and the derivation of mass-loss rates. We analyze these results in the context of previous studies of microjets and discuss their implication for jet launching models and binarity of RY Tau in Sect. 4. We conclude in Sect. 5.

2. Observations and data reduction

Observations of the RY Tau microjet were conducted on January 15th 2002 at the Canada France Hawaii Telescope (CFHT), using the integral field spectrograph OASIS combined with the adaptive optics system PUE'O. The configuration used for the RY Tau observations provides a spectral resolution of $R \sim 3000$ (velocity resolution $FWHM$ = 135 km s^{-1} estimated from the width of the [O I] telluric emission line) and a velocity sampling of 41 km s^{-1} over a spectral range from 6209 Å to 6549 Å, including the [O I]6300 Å line. The field of view is 6.2$''$ × 5.0$''$ with a spatial sampling of 0.16$''$ per lenslet. After AO correction, the effective spatial resolution achieved is 0$''$.4 (Gaussian core $FWHM$). One exposure with an on-source integration time of 1800 s was obtained.

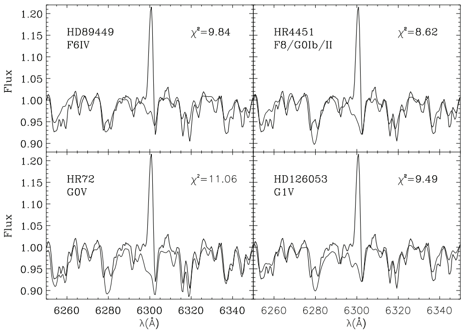

Fig. 1. Comparison between the EXPORT RY Tau spectrum (thick line, from Mora et al. 2001) and rotationally broadened EXPORT spectra of four reference stars (thin lines). The reduced χ^2, computed over our 6210−6550 Å wavelength domain (excluding the [O I] line region) is indicated in each panel. The reference star that best fits the photospheric spectrum of RY Tau is HR 4451.

The data reduction was carried out following the standard OASIS procedure (Bacon et al. 2001), using the XOasis software. A dedicated spectral extraction procedure was developed for the OASIS January 2002 run, to correct for a slight rotation of the lenslet array. Spectro-photometric calibration was performed using the standard star HD 93521. Final spectra are calibrated in units of 10^{-19} W m^{-2} Å^{-1}($''$)$^{-2}$. Atmospheric refraction correction was performed a-posteriori by recentering each spectral image on the continuum centroid, following Garcia et al. (1999). Subsequent analysis of the data (continuum subtraction, removal of [O I] sky emission, construction of images and PV diagrams) was performed under IDL.

As Fig. 1 illustrates, the red wing of the [O I] line in RY Tau is strongly distorted by an underlying photospheric absorption line. Therefore, the photospheric spectrum of RY Tau has to be carefully subtracted in order to retrieve the intrinsic jet kinematics and flux close to the source.

Since we did not observe a standard star of similar spectral type as RY Tau with OASIS, we retrieved from the litterature medium resolution (R = 6600) optical spectra of both RY Tau and standard stars obtained in the context of the EXPORT project, published in Mora et al. (2001). We investigated four different reference stars: HD 126053 (G1V), HD 89449 (F6IV), HR 4451 (F8/G0Ib/II) and HR 72 (G0V) to find the best fit to the continuum. Figure 1 shows the comparison between the EXPORT spectrum of RY Tau and the photospheric contribution predicted by the four stars, after rotational broadening by $v \sin i$ = 52 km s^{-1}. In accordance with Mora et al. (2001), we find that the best fit is obtained for HR 4451, of spectral type F8/G0.

We then developed a dedicated continuum subtraction procedure under IDL in order to remove the photospheric contribution from our OASIS [O I]λ6300 Å spectra at distances $d < 1''$ from the star. The EXPORT spectrum of HR 4451 is first rotationally broadened to the $v \sin i$ of RY Tau and smoothed to the OASIS spectral resolution. At each lenslet position, this standard spectrum is scaled to the continuum level in the current OASIS spectrum, as illustrated in the top-left panel of Fig. 2. It is then subtracted out, leaving a residual [O I]λ6300 Å line profile essentially free of photospheric features, shown by the solid curve in the bottom panel of Fig. 2. The good photospheric subtraction

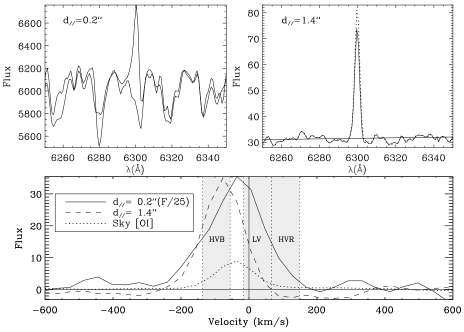

Fig. 2. *Top panels*: solid curves show the observed OASIS [O I]λ6300 Å spectra (thick lines) and the fitted continuum (thin lines) towards the blueshifted jet, offset by $0\farcs2$ (*top-left*) and $1\farcs4$ (*top-right*) from the star. Profiles before subtraction of the [O I] atmospheric line are shown with a dotted line (same as solid thick curve at $0\farcs2$). *Bottom panel*: residual continuum-subtracted [O I] line profiles at $0\farcs2$ and $1\farcs4$ from the star. The subtracted [O I] atmospheric line is shown as a dotted curve. The profile at $0\farcs2$ is divided by 25 for clarity. Velocity intervals contributing to the HVB, LV and HVR channel maps of Fig. 3 are shaded.

indicates no detectable veiling in our OASIS spectra, consistent with the low veiling $\simeq$0.1 in previous high-resolution optical spectra of RY Tau (Hartigan et al. 1995; Basri et al. 1991). At larger distances $d \geq 1''$, photospheric absorption lines no longer contribute significantly, and a simple linear baseline fit to the local continuum over two intervals on either side of the [O I] line is used, as illustrated in the top-right panel of Fig. 2. In each residual, continuum-subtracted spectrum, we also estimate the spectral noise σ equal to the standard deviation computed over two wavelength intervals bracketting the [O I] line. This noise estimate thus takes into account both the original data noise and the uncertainty in the photospheric continuum subtraction.

The residual [O I] line emission, especially in the red wing and close to the source, will depend strongly on the estimate of the photospheric line lying underneath. The depth of this absorption feature is seen to vary with the spectral type and/or the luminosity class. However, from the higher resolution spectra obtained by Mora et al. (2001), we see that the depth of the absorption line is well matched by the photospheric spectrum of HR 4451 (Fig. 1). We thus feel confident that our photospheric fitting procedure does not overestimate the red wing of the [O I] line emission close to the source.

[O I] atmospheric line emission is estimated from the average of 13 spectra located at the periphery of the field of view ($\alpha_c = 2'', \delta_c = -1''$). It is then subtracted from each spectrum. This average sky profile is shown with the dotted line in the bottom panel of Fig. 2. The average peak radial velocity is -41 km s^{-1} with respect to RY Tau and the average peak surface brightness is 9.6×10^{-19} W m^{-2} Å$^{-1}('')^{-2}$. We derive a velocity resolution of 135 km s^{-1} from the *FWHM* of the sky [O I] line profile. From the lens-to-lens dispersion in the [O I] sky line centroid velocities (estimated through Gaussian fitting), we derive a random uncertainty in the velocity calibration of 5 km s^{-1} (rms). The wavelength scale is converted to a radial velocity scale with respect to the central source, using a heliocentric radial velocity for RY Tau of $V_{\rm helio}$ = 18 km s^{-1} (Petrov et al. 1999).

3. Results

3.1. Morphology

3.1.1. Raw [O I] channel maps

Line emission maps in various velocity intervals are reconstructed by reprojecting the hexagonal OASIS lenslet array onto a square grid with $0\farcs1$ sampling. In the top row of Fig. 3, we display continuum-subtracted line emission maps in three velocity intervals, each covering two individual spectral channels of width 41 km s^{-1}: high-velocity blue (HVB): [−137.5: −55.5] km s^{-1}, low-velocity (LV): [−15.5: +66.5] km s^{-1}, high-velocity red (HVR): [+66.5: +148.5] km s^{-1}. These intervals are shaded in grey over the profiles in Fig. 2. The channel centered at −35 km s^{-1} shows a behavior intermediate between the HVB and LV intervals. It is thus left out from the channel maps, in order to better reveal the distinct morphologies between the high and low velocity ranges.

The continuum map, computed by integration of the estimated photospheric contribution over the velocity interval [−2400, −500 km s^{-1}], is also shown in the last top panel. Fitting the brightness radial distribution of the continuum map with a Moffat function, representative of a partially corrected AO point-spread function (PSF), gives a Gaussian core width of *FWHM* = $0\farcs4$. We determine the centroid continuum position with an accuracy (1σ) of $0\farcs015$ from 2D Gaussian fitting. In all figures, spatial offsets are plotted relative to this continuum centroid.

In the HVB map, tracing high blueshifted velocities, the [O I] jet emission is clearly detected out to distances of 2$''$ towards the north-west. The line emission peak is slightly displaced along the jet from the continuum centroid position ($\Delta\alpha = -0\farcs05$, $\Delta\delta = 0\farcs035$) and the emission is resolved (*FWHM* = $0\farcs5$). In the LV map, tracing low flow velocities, the emission is marginally resolved (*FWHM* = $0\farcs45$) and centered closer to the continuum position ($\Delta\alpha = -0\farcs032$, $\Delta\delta = 0\farcs018$). At high redshifted velocities (HVR map), the emission is dominated by an unresolved component (*FWHM* = $0\farcs4$) centered on the continuum position within positional uncertainties ($\Delta\alpha = -0\farcs025$, $\Delta\delta = -0\farcs016$). Some low level extended emission also appears towards the east. This extension is also faintly present in the LV map, although its relative contribution is much less important. We checked that this residual redshifted emission remains when using another reference star for the photospheric emission subtraction. This extended component shows a position angle significantly different from the one of the blueshifted jet emission and might trace strong brightness asymmetry in the counterjet emission. However this feature has a low signal to noise ratio (between 3 and 5, see Fig. 3), thus preventing us from a detailed analysis of its possible origin.

3.1.2. Deconvolved channel maps

In order to remove the non Gaussian wings of the partially corrected AO PSF and derive accurate estimates of jet position angle and jet emission widths, we have deconvolved the observed channel maps, using the continuum map as an estimate of the corresponding point spread function. We use the LUCY restoration routine as implemented in the STSDAS/IRAF package. We limit ourselves to 20−25 iterations (standard acceleration method) which yield χ^2 values of 1.4, 1.1, 2.0 for the 3 channels respectively and final resolution of *FWHM* = $0\farcs2$ (estimated by fitting a Gaussian profile to the central compact component in the HVR map). The maximum number of

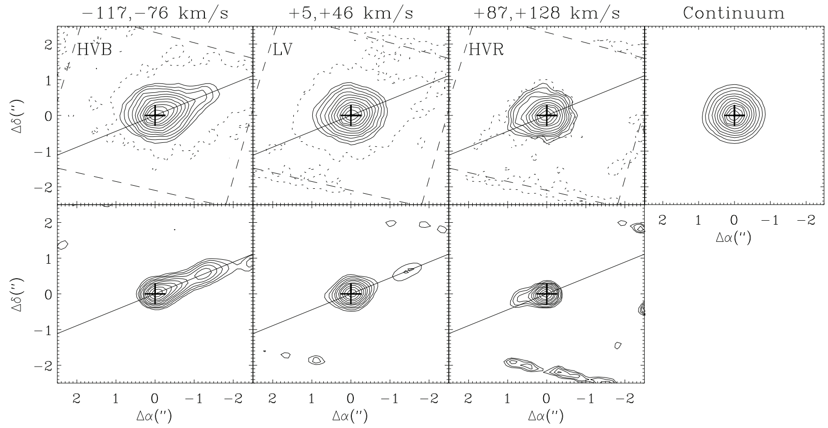

Fig. 3. Continuum-subtracted [O I]λ6300 Å emission maps of the RY Tau microjet, both raw (*top panels*) and deconvolved (*bottom panels*). Emission is integrated over three velocity intervals, with the *centers* of the corresponding velocity channels (each 41 km s^{-1} wide) indicated on top. The derived blueshifted jet position angle is plotted as a solid line. The continuum map is displayed in the *top-right panel*. In the *top row*, contours start at 2% of the maximum and increase by factors of $\sqrt{2}$. In the bottom row they start at 0.1% of the maximum and increase by factors of 2. Dotted contours correspond to a signal to noise ratio of 5 for the HVB and LV maps, 3 for the HVR map. The dashed line shows the OASIS field of view. Spatial offsets are relative to the continuum centroid (located with a cross). The spatial sampling used is 0″.1.

iterations was determined by ensuring that the derived image characteristics (such as intrinsic jet *FWHM*) did not change significantly with further iterations. The deconvolved maps are shown in the bottom panels of Fig. 3.

As already noticed in the raw maps, the line emission is dominated in all channels by a compact component very close to the star. It is unresolved and centered at the continuum position in the HVR map, and shows increasing *FWHM* and spatial offset towards more blueshifted velocities. The extended jet emission stands out more clearly in the deconvolved HVB map, with the low-level emission in the raw map sharpening into an emission knot located at $\Delta\alpha = -1''.23$, $\Delta\delta = 0''.55$, ie at a distance of 1″.35 (190 AU) from the star. In the HVR map, the low level extension towards the east stands out clearly (at a level of 0.2% of the peak emission).

From the HVB deconvolved map, we derive a position angle (PA) for the blueshifted jet of 294° ± 1°. This orientation agrees with the mean of the PA values of 292°–297° derived on larger scales for Hα knots by St-Onge & Bastien (2008). Our derived blueshifted jet PA is perpendicular to the direction of the velocity gradient in interferometric millimetric CO maps or RY Tau, PA $\simeq$ 21° (Koerner & Sargent 1995), indicating that the jet is parallel to the spin axis of the disk. It is also perpendicular to the average direction of the optical linear polarization vector derived by Bastien (1982) of 20°. Interestingly, the derived jet PA is also compatible with the direction of the photocenter variation seen by Hipparcos (PA = 304° ± 34°), interpreted as the direction to a possible binary companion (Bertout et al. 1999). We will return to this issue in the discussion section.

3.1.3. Jet widths

We show in Fig. 4 the variation of the intrinsic jet width as a function of the distance to the star. We estimate the intrinsic jet width as: $FWHM_0 = \sqrt{FWHM^2 - (0''.2)^2}$, where *FWHM* is measured from Gaussian fits to the 1D transverse jet emission profiles in the deconvolved HVB map, of effective resolution 0″.2. The RY Tau jet width increases slowly from 0″.2 (28 AU) at projected distances $0''.15 < d < 0''.6$ (20–84 AU) to 0″.3 (42 AU) at $d = 2''$ (280 AU) with a full opening angle of ~5°. This behavior is remarkably similar to that of other T Tauri microjets observed at sub-arcsecond resolution (see Fig. 4 and discussion section). We do not see any clear change of jet width at the location of the knot (projected distance along the jet of 190 AU), within our angular resolution.

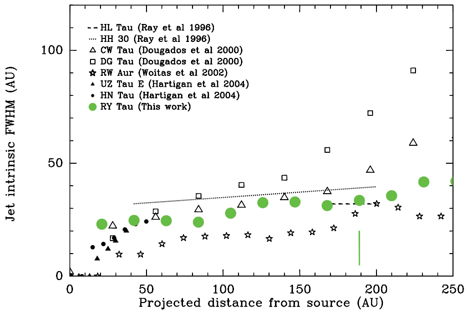

Fig. 4. Large filled circles: PSF-corrected width (*FWHM*) of the RY Tau jet forbidden line emission versus projected distance from the star, as derived from the [O I] HVB deconvolved map (see text). Measurements available on the same spatial scales for other TTS microjets are also plotted with various symbols, after correction for the corresponding PSF. The object-symbol correspondance and references are given at the top left corner of the plot. The position of the knot located at 1″.35 = 190 AU in the RY Tau microjet is denoted by the vertical line.

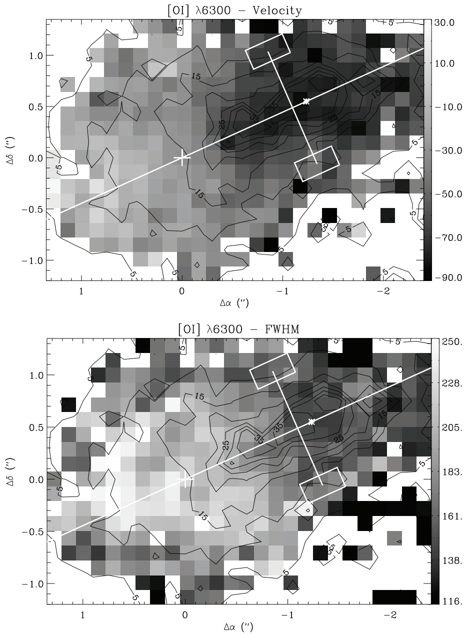

Fig. 5. Maps of the centroid radial velocity (*top*) and velocity width (*bottom*) of a one-component Gaussian fit to the [OI]λ6300 Å line profiles. Contours show the signal to noise ratio (*SNR*) at the line peak (from 5 to 35 by step of 5). Only lenslets with *SNR* > 5 are shown. The cross shows the continuum position, the asterisk denotes the HVB knot, and the straight line the blue jet PA. The two white boxes indicate the two regions that contribute to the transverse velocity shift detected at 1.″2 from the star and 0.″6 to the jet axis in Fig. 8.

3.2. Kinematics

3.2.1. Centroid velocity and line width maps

High spectral resolution integrated line profiles of [O I] in RY Tau show two distinct kinematical components, a high-velocity component (HVC) with peak radial velocities of −70, −80 km s^{-1} and a low-velocity component (LVC) peaked at −4 km s^{-1} (Hartigan et al. 1995; Hirth et al. 1997). Since both components contribute close to the star, we first tried to perform two-component Gaussian fits to each individual OASIS line profile. However, because of insufficient spectral resolution, the two velocity components cannot be well separated in our data (see bottom panel of Fig. 2) and a globally consistent fit could not be found over the whole field of view.

To obtain an overall view of the 2D kinematics of the RY Tau jet, we thus performed a single-component Gaussian fit to our spectra. We show in Fig. 5 the resulting maps of centroid velocity and profile *FWHM*. We overlay on these maps the contours of the signal to noise ratio (*SNR*) at the line peak. Note that due to combined strong photon noise and strong residuals of photospheric subtraction close to the central source, the maximum peak *SNR* is not reached at the star position but towards the blueshifted jet. In photon noise statistics, and for an infinite sampling, the standard deviation of the centroid estimate for a Gaussian distribution of rms standard deviation $\sigma_{\rm line}$ and peak signal-to-noise *SNR* is given by: $\sigma_{\rm cent} = \frac{\sigma_{\rm line}}{SNR}$ (Porter et al. 2004). Uncertainties in line centroid velocities derived from our Gaussian fitting procedure are thus typically: $\sigma_V = \frac{FWHM/2.35}{SNR}$, i.e. ≤11−16 km s^{-1} for a line peak $SNR \geq 5$ and a line *FWHM* ranging from 135 to 200 km s^{-1} typical of our observations.

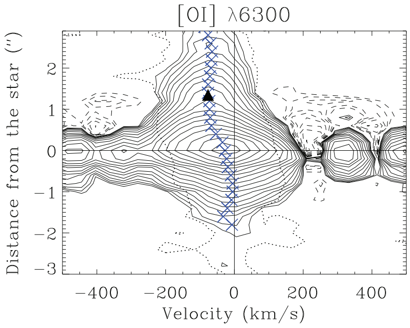

Fig. 6. Position-velocity map along the RY Tau jet in [O I]λ6300 Å after continuum subtraction, for a 1″ wide pseudo-slit sampled every 0.″2 along the jet. Centroid velocities derived from a single Gaussian fit are also plotted (blue crosses). Intensity contours start at 3 σ (1.32×10^{-19} W m^{-2} Å^{-1} (″)$^{-2}$) and increase by factors of $\sqrt{2}$. Negative contours are shown with dashed lines. The dotted line shows the 5σ level, based on the spectral noise in each spectrum. Close to the star, the far wings of the line ($|v| \geq 250$ km s^{-1}) are affected by continuum subtraction residuals. The location of the jet knot identified in the deconvolved HVB map is indicated by a filled triangle.

The centroid map shows that the extended blueshifted jet emission at PA = 294° has centroid velocities of average value −70 km s^{-1}, consistent with the HVC in previous high-spectral resolution observations. The jet shows a local peak in centroid velocity (−90 km s^{-1}) at $(\Delta\alpha, \Delta\delta) \sim (-1.''2, +0.''6)$, coincident with the emission knot identified in the deconvolved HVB channel map (denoted with an asterisk in Fig. 5). The profile width is narrow, and essentially unresolved beyond 1.″3 from the star.

Closer to the star, centroid velocities progressively decrease to values of ≃−30, −10 km s^{-1} while the line *FWHM* significantly increases. The available velocity information combined with the channel maps from Fig. 3 suggests that, towards the central source, emission from the spatially unresolved LVC component at −4 km s^{-1} centered at the continuum position strongly contributes to the line profile, resulting in intermediate centroid velocities and increased line widths.

In a small zone on the redshifted side, at $(\Delta\alpha, \Delta\delta) \sim (+0.''8, -0.''3)$, peak velocities appear slightly redshifted and line profiles become significantly broader with a fitted $FWHM \geq 200$ km s^{-1}, corresponding to an intrinsic *FWHM* > 140 km s^{-1}, suggesting a contribution from a third kinematical component. This region spatially coincides with the red extension identified in the reconstructed HVR channel map from Fig. 3.

3.2.2. Kinematics along the jet axis

Figure 6 shows a position-velocity map along the jet in [O I], reconstructed by averaging the lenslets transversally across a 1″ wide pseudo-slit, and sampling every 0.″2 along the jet. Centroid velocities derived from one-component Gaussian fits to the line profiles are also plotted. Beyond 0.″5, we clearly

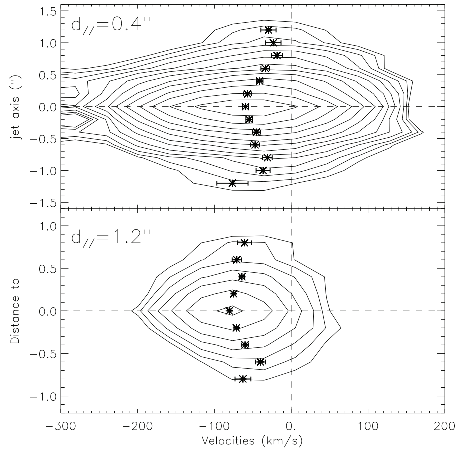

Fig. 7. Transverse position-velocity diagrams across the blue jet at distances of 0.″4 (*top*) and 1.″2 (*bottom*) from the star. Centroid velocities (crosses) derived from one-component Gaussian fits are also plotted with their estimated 1σ error bars (see text). The pseudo-slits are 0.″2 wide and are binned every 0.″2 in the transverse direction. Contours start at 5σ and increase by factors of $\sqrt{2}$.

detect the high-velocity blue jet (HVC) with an average centroid radial velocity of ~ -70 km s^{-1}. The profiles are essentially unresolved spectrally in the jet ($FWHM$ = 140 km s^{-1}). Average variations in radial velocities along the blue jet do not exceed 10% (7 km s^{-1}) beyond 0.″6 over the central 2.″5. Closer to the star, centroid radial velocities progressively decrease and converge to ~ -10 km s^{-1} on the redshifted side, consistent with the LVC. The lines become asymmetric and wider with an intrinsic $FWHM$ (deconvolved from the instrumental $FWHM$ = 135 km s^{-1}) of $\simeq 130$ km s^{-1} (see profile in bottom panel of Fig. 2).

3.2.3. Transverse position-velocity diagrams

We show in Fig. 7 transverse position-velocity maps reconstructed by integrating spectra within a 0.″2 wide pseudo slit positioned perpendicular to the jet axis at two different distances from the star along the jet axis. These two position-velocity diagrams illustrate the transverse structure of the jet. Close to the source (at d = 0.″4), where the LVC component still marginally contributes, the emission on the jet axis peaks at intermediate velocities (-60 km s^{-1}) and is marginally resolved transversally. At d = 1.″2, the emission is more resolved transversally and the radial velocities peak at -80 km s^{-1} towards the jet axis, consistent with the HVC component. In both cases, radial velocities decrease by 20 km s^{-1} in the external parts of the jet at transverse distances +/−0.″6.

3.2.4. Search for transverse velocity shifts

Transverse velocity gradients, indicative of possible rotation within the jet body, have been previously reported for 5 TTS microjets (Bacciotti et al. 2002; Woitas et al. 2005; Coffey et al. 2004, 2007).

The principle of the measurement of rotation is to search for radial velocity differences between pairs of spectra emitted at two symmetrical transverse offsets $\pm d_\perp$ on either side of the jet axis. In an axisymmetric flow, these velocity differences $\Delta V = V(+d_\perp) - V(-d_\perp)$ would be related to the rotation velocity by $V_\phi(d_\perp) = \Delta V/(2\sin i)$, where i is the inclination of the jet axis to the line of sight, provided $d_\perp$ is larger than the telescope PSF and on the order of the jet emission radius, to minimize convolution and projection effects (Pesenti et al. 2004).

The RY Tau transverse position-velocity diagrams presented in Fig. 7 do show a skewness in the outer contours indicative of transverse velocity gradients. Velocity shifts between two spectra can be measured either by the difference of the centroid velocities (determined by fitting a Gaussian profile to each line) or directly by cross-correlating the two profiles. We apply both methods to compute transverse velocity shifts at various transverse distances to the jet axis ($d_\perp$) and distances from the central source along the jet axis ($d_{//}$). We first averaged lenslets over boxes of width 0.″4 along the jet and 0.″2 across the jet, in order to increase the signal to noise ratio and to decrease the random wavelength calibration uncertainty (typically with 3−4 lenslets per box, the latter is down to $1\sigma \sim 2.5$ km s^{-1}). The results are shown in Fig. 8 for $d_\perp$ = 0.″2 and $d_\perp$ = 0.″6. Computed velocity shifts range between -10 km s^{-1} and $+10$ km s^{-1} for $d_\perp$ = 0.″2, and between -35 km s^{-1} and $+15$ km s^{-1} for $d_\perp$ = 0.″6, and show no clear trend with distance along the jet axis.

The random errors due to noise associated with our transverse velocity shift measurements are assessed through a Monte-Carlo study detailed in Appendix A. We show that the Gaussian fitting method is more accurate, and that the uncertainties associated with our velocity shifts measurements are well represented by the empirical formula $\sigma_{\Delta V} = 90/SNR$ km s^{-1}, as expected theoretically for our typical line width (Porter et al. 2004). Based on the above formula, we thus expect a 1σ uncertainty in velocity shifts derived from Gaussian fits of ≤ 4 km s^{-1} for peak $SNR \geq 20$, and ≤ 8.5 km s^{-1} for peak $SNR \geq 10$ (significantly larger than wavelength calibration errors). Of course these estimates are only valid as long as the observed profiles do not depart too much from a Gaussian profile, which is our case in the blueshifted jet of RY Tau. Otherwise, the cross-correlation technique should be preferred for measuring velocity shifts and the corresponding uncertainties will be larger (see Appendix A). For completeness, both the Gaussian centroid and the correlation method are shown here, and they give identical results.

The 3σ error-bars derived from the profile SNR using the above empirical formula from our Monte-Carlo study are plotted in Fig. 8, for each transverse velocity difference. The detected velocity shifts at $d_\perp$ = ±0.″2 are all compatible with zero (at the 3σ level), as expected from beam-convolution effects. Indeed, for transverse distances significantly smaller than the spatial PSF, contributions to rotation signatures from receding and approaching flow lines should cancel out in the beam (Pesenti et al. 2004).

For transverse distances of the order of the jet width and larger than our spatial resolution ($d_\perp$ = 0.″6) where rotation signatures should be optimized (Pesenti et al. 2004), the detected velocity shifts are also compatible everywhere with zero except marginally at two distances along the jet axis: $d_{//}$ = 0.″4 and $d_{//}$ = 1.″2 where we detect at a 2.5−3σ level transverse velocity shifts of $\Delta V = V(d_{\rm NE}) - V(d_{\rm SW})$ of $+15.4 \pm 5.9$ km s^{-1} and -19.6 ± 4.6 km s^{-1} respectively. These transverse asymmetries in velocities are clearly visible on the two transverse position-velocity diagrams shown in Fig. 7, which correspond to these same two distances from the source. We discuss in

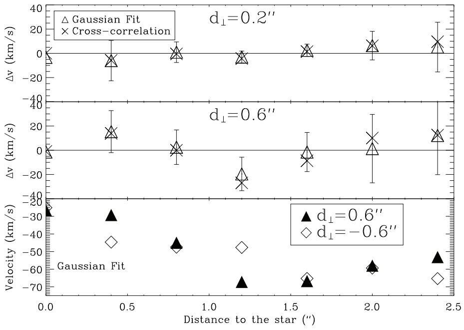

Fig. 8. *Top and middle panels*: velocity shifts between symmetric spectra taken at ±0.″2 (*top panel*) and ±0.″6 (*middle panel*) on either side of the jet axis, as a function of distance along the blue jet. Velocity shifts are measured by one-component Gaussian fitting (triangles) and cross-correlation (crosses). The 3σ error-bar deduced from the profile peak *SNR* is plotted. *Bottom panel*: centroid velocities (from Gaussian fits) measured on both sides of the jet axis at transverse offsets $d_\perp = \pm 0.''6$, as a function of distance to the star. Positive transverse offsets (filled triangles) correspond to the north-east side of the blueshifted jet. In all panels, lenslets are averaged inside boxes of width 0.″4 along the jet and 0.″2 across the jet.

Sect. 4.3 whether or not these two marginally detected velocity shifts could trace signatures of rotation within the jet body.

3.3. Mass-loss rate

We estimate the mass-loss rate in the blueshifted jet from the [O I] line luminosities using two different methods described in detail by Hartigan et al. (1995), hereafter HEG95, and Cabrit (2002). The first method assumes volume emission over the entire elementary aperture under uniform plasma conditions (n_e, T_e,$x_e = n_e/n_H$). The mass-loss rate is then expressed as:

$$\dot{M}_J = M_{\rm TOT} V_\perp / l_\perp \qquad (1)$$

where $V_\perp$ is the tangential flow velocity, $l_\perp$ is the projected size of the aperture on the plane of the sky along the jet axis, and $M_{\rm TOT}$ is the total gas mass inside the aperture given by:

$$M_{\rm TOT} = 9.61\times10^{-6}\left(\frac{1}{1-x_e}\right)\left(1+\frac{n_{\rm cr}}{n_e}\right)\left(\frac{L_{\rm [OI]\,6300}}{L_\odot}\right) M_\odot \qquad (2)$$

assuming $T_e = 8200$ K, with a corresponding line critical density $n_{\rm cr} = 1.97\times10^6$ cm^{-3} (HEG95). The term $(1-x_e)$ is added here to account for ionised oxygen, assuming that O$^+$/O = x_e due to resonant charge exchange with hydrogen (Cabrit 2002).

The second method assumes that [O I] line emission within each elementary aperture arises from shock fronts. The mass-loss rate is then expressed as a function of the shock velocity as:

$$\dot{M}_J = 6.616\times10^{-4}\left(\frac{V_{\rm jet}}{V_{\rm shock}}\right)\left(\frac{L_{\rm [O\,I]6300}}{L_\odot}\right)\left(\frac{\cos\theta}{N_{\rm shock}}\right) M_\odot\,{\rm yr}^{-1} \qquad (3)$$

where $V_{\rm jet}$ and $V_{\rm shock}$ are the jet speed and shock speed respectively, $N_{\rm shock}$ is the number of shocks within the elementary aperture and θ is the angle between the normal to the shock front and the jet axis. These last two parameters are not present in the original equation of HEG95, and are added to account for multiple shocks in the beam and for the fact that an oblique shock intercepts a surface of $1/\cos\theta$ times the jet cross-section (Cabrit 2002).

By comparing the above two methods applied to stellar jets observed with both small and large apertures, Cabrit (2002) concluded that on average $\cos\theta/N_{\rm shock} \simeq 1$ per 100 AU of jet length. We will thus assume a value of 1 here for this ratio (our flux apertures have $l_\perp = 0.4'' = 60$ AU along the jet, see below). We will adopt a jet speed of $V_{\rm jet} = 165$ km s^{-1}, and a tangential velocity $V_\perp = 150$ km s^{-1}, corresponding to a blue jet inclination to the line of sight of 65° (see Sect. 4.1 for estimates of the RY Tau jet inclination).

Since our present dataset of RY Tau only includes the [O I] line, values of x_e, n_e, and $V_{\rm shock}$ cannot be inferred directly from [S II] and [N II] line ratios, as done previously in our OASIS study of the DG Tau microjet (Lavalley-Fouquet et al. 2000) and we have to rely on estimates. We note that low shock velocities are expected from the non-detection of [N II] emission in RY Tau (Hartigan et al. 1995; Hirth et al. 1997). Indeed, planar shock models predict a sharp decrease of emissivity for this line for shock velocities below 30 km s^{-1} (Hartigan et al. 1994). We may thus assume in Eq. (3) that $V_{\rm shock}$ is in the range 20 to 50 km s^{-1}. For n_e and x_e in Eq. (2), we will adopt typical parameters inferred from high-angular resolution observations of the inner regions of the DG Tau, RW Aur, Th 28 and HH 30 microjets (Lavalley-Fouquet et al. 2000; Dougados et al. 2002; Bacciotti & Eislöffel 1999; Hartigan & Morse 2007). We thus assume an ionisation fraction $x_e = 10$ % and an electronic density decreasing with distance to the central source as $n_e = 5\times10^3(1''/r)$ cm^{-3} for $d \geq 60$ AU, and flattening to a constant value of 3×10^4 cm^{-3} inside 60 AU (Hartigan & Morse 2007).

We estimate the blueshifted HVC jet [O I] luminosities at different distances along the jet axis by integrating observed surface brightnesses over the 3 velocity channels centered at −117, −76 and −35 km s^{-1} (i.e. a total velocity range from −137.5 to −14.5 km s^{-1} taking into account the channel width). We now include the spectral channel centered at −35 km s^{-1} since it always contains a significant fraction of the total HVC flux, due to our moderate spectral resolution (see Fig. 2). The emission is summed *in the raw maps* over rectangular apertures of full longitudinal and transverse widths of $0.''4 = l_\perp$ and $1.''6 = d_\perp$ respectively. The chosen longitudinal width provides a sampling along the jet axis similar to our spatial PSF, while the full transverse width ensures that we include all of the jet emission over our field of view (measured transverse *FWHM* ≤ 0.″8 in our raw maps for distances along the jet axis ≤2.″). The derived HVC [O I] luminosities as a function of projected distance along the jet axis are plotted in Fig. 9. We observe a steep decrease in brightness with distance from the source, reaching two orders of magnitude at 2.5″. However, within 0.″6 from the central source, the measured [O I] luminosities are strongly contaminated by the strong low-velocity component, as indicated by centroid velocities lower than −70 km s^{-1} (see Fig. 6). Beyond distances of 2″, part of the transverse aperture falls outside the OASIS observations field of view. Distances between 0.″6 and 1.″8 from the star (hereafter denoted as the HVC-dominated region) thus give the best estimate of the HVC jet luminosity.

We also plot in Fig. 9 our estimates of mass-loss rates using the methods of volume (Eq. (2)) and shock (Eq. (3)) emission. Since we assume for simplicity a constant value of shock speed and $\cos\theta/N_{\rm shock} = 1$, and since $V_{\rm jet}$ also remains constant within 10% along the jet, the mass-flux rate we derive from the shock method is exactly proportional to the [O I] luminosity (see Eq. (3)) and thus follows the same steep decrease with distance

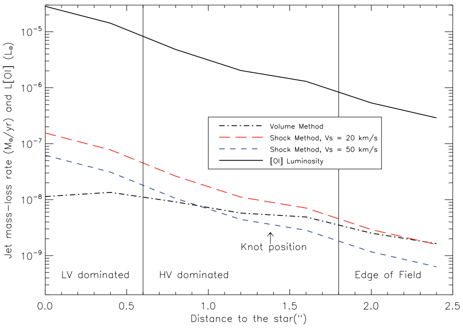

Fig. 9. Mass-loss rate in the RY Tau blueshifted jet as a function of projected distance, derived from the [O I] line luminosity with two different assumptions (see text): volume emission (*dot-dashed line*) and shock layer with shock speed 20 km s^{-1} (*red long-dashed line*) or 50 km s^{-1} (*blue short-dashed line*). The two methods are in good agreement in the region dominated by the HV component. The [O I] line luminosity, integrated over apertures of $0\farcs4 \times 1\farcs6$ and velocity interval −137 to −15 km s^{-1} is plotted as a *full line*.

to the central star. In particular, it drops by a factor of 5 from the $d = 0.8''$ to the $d = 1.6''$ apertures covering the HVC-dominated region. Although a real variation in $\dot{M}_J$ of this magnitude cannot be completely ruled out a priori over a time span of 4 yrs (crossing time of the HVC-dominated region), we suspect that this drop is mainly an artefact of our simplifying assumptions in the shock method. Our argument is that *all* TTS microjets images at sub-arcsecond resolution so far show a strongly decreasing [O I] jet luminosity over their inner 200 AU; If this decrease were proportional to a jet mass-flux variation, one would expect to also encounter stars with rising jet brightness over the same distance scales, whereas none have been seen. Therefore, the jet mass-flux is probably not strictly proportional to the jet luminosity over the jet length, and the factor 5 decline obtained by the shock method for a constant $V_{\rm shock}$ and $N_{\rm shock}$ is an upper limit to the true variation in $\dot{M}_J$ (e.g., $V_{\rm shock}$ and $N_{\rm shock}$ could easily decrease with distance from the star in a time-variable jet, causing a luminosity decline even for a constant mass-flux; see Eq. (3)).

In support of this conclusion, we note that the volume method gives values that are much more uniform along the jet, because the decline in [O I] luminosity is now compensated for by the drop of $n_{\rm e}$ (see Eq. (2)). Across the HVC-dominated region, values of the mass-loss rate derived by this method change by only a factor 2, and are well bracketed by the shock method for low to intermediate shock speeds (20−50 km s^{-1}). We thus take the average volume method mass-loss rate over distances of $0\farcs6$–$1\farcs8$ from the star of 6.6×10^{-9} $M_\odot$ $\rm yr^{-1}$ as our best estimate of the mean HVC mass-loss rate. The uncertainty on the jet velocity (see below), and on the typical electronic densities at projected distances 100−150 AU, suggests an uncertainty of at most a factor of 4 either way, consistent with the good agreement with the shock methods noted above. The mass-loss rate in the RY Tau blueshifted jet therefore is between 0.16 and 2.6×10^{-8} $M_\odot$ $\rm yr^{-1}$. Combining with the range of disc mass accretion rates determined by Calvet et al. (2004) of 6.4–9.1×10^{-8} $M_\odot$ $\rm yr^{-1}$, we derive an ejection to accretion rate ratio (one sided) of $\dot{M}_J/\dot{M}_{\rm acc}$ between 0.02 and 0.4, with a most probable value of 0.085.

Our best mass-flux estimate for the RY Tau blueshifted jet is 4 times higher than the value of 1.6×10^{-9} $M_\odot$ $\rm yr^{-1}$ previously derived by HEG95 from long-slit spectroscopy, despite using the same volume method (Eq. (2)) and same transverse jet speed (150 km s^{-1}). The main origin of this difference lies in the fact that our observations are spatially resolved while the ones of HEG95 were not. First, HEG95 assumed that their integrated [O I] HVC luminosity uniformly filled a large region of length $l_\perp = 1\farcs25$ originating at the star position. However, our [O I] maps show that most of the [O I] luminosity originates from a compact component located much closer to the source. Indeed, in our central aperture at $d = 0''$ we measure a similar HVC [O I] luminosity as HEG95 did (2.85×10^{-5} $L_\odot$ here vs. 3.4×10^{-5} $L_\odot$ in HEG95), but with a diaphragm 3 times smaller ($l_\perp = 0\farcs4$ here versus $1\farcs25$ in HEG95). Furthermore, we noted above that our HVC luminosity is overestimated in the central regions, due to contamination by the compact LVC, so that the best estimate of the RY Tau jet HVC mass-loss rate is in fact not obtained at the source, but at projected distances along the jet between $0\farcs6$ to $1\farcs8$. Although we observe at these distances an order of magnitude lower [O I] luminosities than that derived by HEG95, we now have 16 times lower $n_{\rm e}$ values (adopting the representative $n_{\rm e}$ observed on these spatial scales in other resolved microjets) and again 3 times lower $l_\perp$, resulting in our best estimate mass-loss rate being, in the end, higher by a factor 4 than the value derived by HEG95. This example illustrates the key importance of spatially resolved spectro-imaging observations to derive more accurate mass-flux rates in T Tauri microjets.

4. Discussion

4.1. Jet inclination angle and flow kinematics

The RY Tau system inclination to the line of sight is currently poorly constrained. Kitamura et al. (2002) derive a best fit disc axis inclination angle of 43.5° ± 5 from simultaneously fitting marginally resolved 2 mm dust continuum emission maps and the spectral energy distribution. On the other hand, Muzerolle et al. (2003) derive an inner disc rim inclination to the line of sight of 86° ± 10° from modelling of the near-infrared spectral energy distribution (from 2 to 5 μm). Recently, Schegerer et al. (2008) constrained the disc inclination axis to the line of sight to be less than 70° from fitting both the spectral energy distribution and N band visibilities obtained with MIDI at the VLTI. Here we reexamine constraints on the system inclination in an attempt to better estimate the true deprojected jet speed.

The observed variation of line-of-sight velocities with position along the RY Tau jet, $\Delta V_{\rm rad} \simeq 10\% V_{\rm rad}$, implies a typical shock speed $\simeq 10\% V_{\rm jet}$. Shock velocities in excess of 30 km s^{-1} at distances $\leq 1''$ from the source appear unlikely, since strong [N II] has never been observed in RY Tau (Hirth et al. 1997; Hartigan et al. 1995), while planar shock J-type models predict a sharp increase of [N II]6584 Å emission above $V_{\rm s}$ = 30 km s^{-1}. Hence the constraint derived above on shock velocities implies a true jet flow velocity lower than 300 $\rm km^{-1}$. With $V_{\rm rad} \simeq 70$ km s^{-1}, this would correspond to a *maximum* inclination to the line of sight of 76.5°. This maximum inclination is compatible with the fact that no dark lane is clearly visible in optical/near-IR images of the system (St-Onge & Bastien 2008).

We now derive an additional constraint on the *minimum* system inclination required to reproduce the photo-polarimetric behaviour of RY Tau reported by Petrov et al. (1999). As pointed out by these authors, the behaviour of RY Tau is reminiscent of that observed in UX Ori type stars, in particular the increase of linear degree of polarization when the system is fainter. Natta & Whitney (2000) model the optical photometric and polarimetric variability of UX Ors with partial occultation of the photosphere by circumstellar dust clouds, resulting in a relative increase of (polarised) scattered radiation from the surrounding circumstellar disc. In particular, these authors compute the degree of linear polarisation expected at minimum light as a function of the optical depth of the occulting screens and of the inclination of the disc to the line of sight. In RY Tau, the intrinsic linear polarisation in the V band increased from 0.7% at high brightness to 1.7% ± 0.1% at minimum brightness (Δmag = 1 mag; Petrov et al. 1999). According to the models computed by Natta & Whitney (2000) this behaviour indicates an inclination of the disc axis to the line of sight ≥45°. The models are computed for a 2 $M_\odot$ central star with effective temperature $T_{\rm eff}$ = 9000 K and luminosity $L_\star = 50\,L_\odot$, i.e. of similar mass as RY Tau, but of higher effective temperature and luminosity ($T_{\rm eff}$ = 5945 K and $L_\star = 9.6 \pm 1.5\,L_\odot$ is estimated for RY Tau by Calvet et al. 2004). The model predictions are mostly sensitive to the disc flaring parameter h/r, ranging between 0.01 and 0.03. For a passive irradiated thin disc, $T \propto L_\star^{1/4}$ so that $h/r \propto L_\star^{1/8}\ M_\star^{-1/2}$ and the difference of a factor 5 in stellar luminosities amounts to a 20% difference in h/r only. The conclusion on the minimum RY Tau inclination angle of 45° therefore appears quite robust.

Our conservative lower and upper limits to the jet inclination of 45° and 76.5° are compatible, within the errors, with the determinations of both Kitamura et al. (2002) and Muzerolle et al. (2003) but do not allow us to discriminate between the two. Within best available constraints, we will therefore assume a jet inclination angle to the line of sight within this range, implying a deprojected flow velocity between 100 and 300 km s^{-1} with a most probable value of 165 km s^{-1} (taking into account a random orientation of the jet axis in 3D space). This latter value was adopted to estimate the jet mass-flux rate.

We note that St-Onge & Bastien (2008) estimate a similar proper motion of 165 km s^{-1} for their brightest Hα knot (Ha2), from comparison to archival *HST* data. If we identify our HVB [O I] knot at 1.″35 with one of their inner Hα knots, we would infer proper motions of 140 km s^{-1} (HaB knot) to 247 km s^{-1} (HaC knot), again consistent with a moderate jet speed <300 km s^{-1}.

4.2. Origin of the Hipparcos photocenter variation

The jet position angle (294° ± 1°) is compatible with the position angle of the photocenter variation derived by Hipparcos observations (304° ± 34°), calling into question the proposed interpretation in terms of a close binary system (Bertout et al. 1999). One would expect close binaries to have their orbits coplanar with the disk and perpendicular to the jet. In an inclined system like RY Tau, the probability of catching the binary when it appears projected along the blueshifted jet axis would then be quite small. Furthermore, recent infrared interferometric measurements have failed to detect a close companion in RY Tau (Schegerer et al. 2008).

We investigate below whether the displacement of the photocenter seen by Hipparcos could be produced instead by line emission associated with the jet itself. A displacement of the photocenter in the direction of the blueshifted jet axis would result if the contrast between the extended jet and unresolved continuum photosphere varied during the Hipparcos observations (2.5 years between January 1990 and June 1992). Such a variation could be produced either by intrinsic jet variability due for example to knot ejections, or by variability in the photospheric continuum emission itself. The latter case seems to be favored in the RY Tau system, where the RY Tau photo-polarimetric behavior can be understood in terms of partial occultation episodes of the photosphere (Petrov et al. 1999).

We evaluate the total jet line flux expected in the Hipparcos photometric filter, covering the spectral range between 4000 Å and 6500 Å, by considering the predictions from the planar shock models of Hartigan et al. (1994) and HEG95 with pre-shock densities ranging between 10^6 and 10^2 cm^{-3}, pre-shock magnetic fields between 30 and 300 μG and shock velocities ranging between 20 and 100 km s^{-1}. The lines which could contribute significantly are: Hβ λ4861 Å, [N I]λ5200 Å, [O I]$\lambda\lambda$6300, 6363 Å, [N II]$\lambda\lambda$6548, 6583 Å, Hα λ6563 Å, and [S II]$\lambda\lambda$6716, 6731 Å. We consider first a single shock front of shock velocity $V_{\rm s}$, located at distance z from the source, and intercepting the total cross-section of the jet. The line emission can be expressed as:

$$F(z) = \frac{\pi R(z)^2}{2\pi D^2} \times f(V_{\rm s}(z), n_{\rm H}(z)) \tag{4}$$

where D is the distance from the source to the earth, $R(z)$ and $n_{\rm H}(z)$ respectively the jet transverse radius and pre-shock density at distance z along the jet. The function f gives the emitted flux per unit surface out of one face of the shock, and is taken from Hartigan et al. (1994) and HEG95. The function f increases strongly with shock velocity and is proportional to $n_{\rm H}$, the pre-shock density. Its dependence on the pre-shock magnetic field is weak in the conditions considered. If we further assume a constant mass-loss rate along the jet, equal to $\pi R^2 \mu n_{\rm H} V_{\rm jet}$, the line flux becomes independent of z and reduces to (for D = 140 pc):

$$\begin{aligned} F \ =\ & 2.1 \times 10^{-12} \times \left(\frac{\dot{M}_J}{10^{-8}\ M_\odot\ {\rm yr}^{-1}}\right) \times \left(\frac{165\ {\rm km\ s}^{-1}}{V_{\rm jet}}\right) \\ & \times f\left(V_{\rm s}, n_{\rm H} = 10^4\ {\rm cm}^{-3}\right)\ {\rm erg\ s}^{-1}\ {\rm cm}^{-2}. \end{aligned}$$

The function $f(V_{\rm s}, n_{\rm H} = 10^4\ {\rm cm}^{-3})$ increases from 10^{-2} for shock velocities $V_{\rm s}$ = 30 km s^{-1} to 0.2 for $V_{\rm s}$ = 100 km s^{-1}. Hence, the total optical line flux emitted by one single shock front is expected to be ≤ 2.1 × 10^{-14} erg s^{-1} cm^{-2} for shock velocities ≤30 km s^{-1}, ≤4.2 × 10^{-13} erg s^{-1} cm^{-2} for shock velocities ≤100 km s^{-1}.

The maximum photocenter displacement will occur at minimum photospheric brightness. During Hipparcos observations RY Tau V band magnitudes varied between 9.7 and 11.05. We thus estimate the continuum flux at minimum brightness in the Hipparcos photometric filter (*FWHM* ≃ 2000 Å) to be $F_{\rm cont} \simeq 3 \times 10^{-10}$ erg s^{-1} cm^{-2}. The maximum contrast between line emission from a single shock front and photospheric continuum emission is therefore expected to be 6.7×10^{-5} for $V_{\rm s} \leq 30$ km s^{-1} and 1.4 × 10^{-3} for $V_{\rm s} \leq 100$ km s^{-1}.

To produce the maximum displacement of the photocenter of 19.5 mas observed by Hipparcos would thus require a shock front located at a distance from the star ≥300″ for shock velocities ≤30 km s^{-1} and 14″ for shock velocities ≤100 km s^{-1}. But this is well outside the primary beam of Hipparcos (of diameter 30″ but with a strong attenuation starting at 5″ from center). Alternatively, more than one shock front may contribute within the beam of Hipparcos observations. The photocenter displacement produced by n shock fronts equally spaced along the jet within a radius R, i.e. with separations $\Delta x = R/n$, can be written as:

$$x_{\rm phot} = R \times \frac{n+1}{2} \times \frac{F}{F_{\rm cont}} \, . \tag{5}$$

To produce a photocenter displacement of 19.5 mas would then require ≃5 shock fronts located within 5″ of the central source for shock velocities ≃100 km s^{-1}, and an unrealistically large number of shock fronts (≥100) for shock velocities ≤30 km s^{-1}.

Knot separations ≃1″ are compatible with previous observations of the inner regions of TTS microjets (Dougados et al. 2000; Bacciotti et al. 2000; López-Martín et al. 2003; Woitas et al. 2005). Thus predictions of jet line emission from multiple shocks could marginally account for the observed Hipparcos photocenter displacement provided shock velocities are ≃100 km s^{-1}. This however seems inconsistent with the non-detection of [N II] emission in RY Tau. Progress on this issue will require more accurate determinations of shock velocities through line ratio observations in the RY Tau microjet.

Another possible source of photocenter displacement along the jet axis is bright scattered optical light from the surface of the circumstellar disc. At intermediate inclinations for the RY Tau system, the image of the disc in scattered light will be dominated by the blue lobe (see Natta & Whitney 2000 for an example). Occultation of the photosphere will enhance the contrast between scattered and direct stellar light, resulting in a displacement of the photocenter perpendicular to the disc plane, towards the blueshifted jet axis. The maximum degree of linear polarisation of 1.7% at minimum photospheric brightness (Petrov et al. 1999) gives a lower limit to the ratio of scattered to direct light during occultation. Indeed due to polarisation cancelling in a centro-symmetric scattering pattern, the true ratio of scattered to direct light can be much higher than the integrated polarisation. This interpretation should be checked with detailed disc image modelling.

From the fact that the photocenter displacement seen by Hipparcos lies along the jet axis, we thus conclude that a binary companion may not be the most relevant explanation. Our analysis above shows however that line emission from shocks in the jet is probably not bright enough to produce the observed photocenter displacement in the Hipparcos broad photometric filter. The most likely origin thus appears to be scattering off the surface of the disc seen at intermediate inclinations, combined with variable partial occultation of the central photosphere. This interpretation should however be checked with a detailed study of the observed variation of the Hipparcos photocenter with time. In particular, we predict a clear anti-correlation between system brightness and photocenter displacement.

4.3. Transverse structure and rotation signatures

We discuss below whether the transverse velocity shifts marginally detected at distances along the jet of $d_{//} = 0\farcs4$ and $1\farcs2$ from the star and transverse distances $d_{\perp} = \pm 0\farcs6$ from the jet axis could be due to rotation within the jet body. The 2.5σ detection at $d_{//}=0\farcs4$ is doubtful, since the inferred sense of rotation would be opposite to the disc rotation sense inferred from the velocity gradient observed in the millimetric CO observations of Koerner & Sargent (1995): from blueshifted in the north-east to redshifted in the south-west along PA ≃ 21°. In contrast, the 3σ detection at $d_{//} = 1\farcs2$ would indicate a sense of rotation in the jet in agreement with the disc rotation sense. The detection of jet rotation at this position and not at others could reflect the fact that both the *SNR* and the HVC contribution are maximized there: closer in, photospheric subtraction residuals are important and the low-velocity component contributes significantly, while further out, the signal to noise ratio rapidly decreases. However, interpretation as a rotation signature remains questionable due to the marginal 3σ level and to the fact that the detection happens to be very close to the jet knot detected in the HVB map. We plot in Fig. 5 as white boxes the two regions of the jet whose summed line profiles produce the detected transverse velocity shift at $1\farcs2$. The detected velocity asymmetry could also be caused by asymmetries in the wings of a bow-shock peaked at the position of the HVB knot, at $1\farcs35$ from the star (asterisk symbol in the figure). Higher angular resolution observations that better resolve the jet transverse structure are required to settle the origin of this velocity asymmetry.

4.4. Comparison with cTTS microjets

We analyze here the derived properties of the RY Tau microjet in the light of previous studies of T Tauri small scale jets. We compare in Fig. 4 the RY Tau blueshifted jet widths as a function of projected distance to the central source with previous studies of TTS microjets. Both the jet widths and opening angle appear similar to those derived on similar spatial scales for the other TTs microjets, suggesting similar collimation scale and properties.

The full range of centroid flow velocities observed on spatial scales of a few 100 AUs for the DG Tau (Pyo et al. 2003; Lavalley et al. 1997), RW Aur (Pyo et al. 2006), HL Tau (Pyo et al. 2006), HH 30 (Hartigan & Morse 2007) and CW Tau (Hartigan et al. 2004) microjets, where inclination angles are well constrained, is 130−300 km s^{-1} with an average value of 225 ± 55 km s^{-1}. Our possible interval of 100−300 km s^{-1} for the deprojected terminal velocity in the RY Tau microjet (Sect. 4.1) thus falls in the same range as previously investigated microjets from lower mass central sources.

Finally, our estimate for the (one-sided) ejection to accretion rate $\dot{M}_J/\dot{M}_{\rm acc}$ ratio, between 0.02 and 0.4 with a best value of 0.085, is also compatible with the average ratio ≃0.1 for lower mass cTTS sources found by Cabrit (2007) using jet mass-fluxes from HEG95 and revised accretion rates from Gullbring et al. (1998).

The overall properties (collimation, terminal centroid velocities, ejection to accretion rate ratio) of the RY Tau microjet therefore appear quantitatively similar to those of the microjets from lower mass cTTS investigated so far.

4.5. Implications for jet launching models

The remarkably similar collimation, terminal speed, and ejection efficiency of the RY Tau microjet compared to lower mass cTTs gives for the first time a firm support to the common belief that the jet launching mechanism is probably universal over a broad range of stellar masses. We examine below the implications of the derived RY Tau jet parameters for the three classes of *steady state* jet launching magneto-centrifugal models currently discussed in the context of cTTS microjets and for which detailed observational predictions are available (see Ferreira et al. 2006; Cabrit 2007, for detailed reviews).

Magnetized stellar wind models have been developped to account for the origin of collimated mass-loss in young stars, and to explain their spin-equilibrium despite active accretion (Sauty & Tsinganos 1994; Matt & Pudritz 2008). Since CTTS rotate at a small fraction of their break-up velocity (e.g. 15% in RY Tau), centrifugal acceleration from the stellar surface is insufficient to overcome the gravitational pull of the star, and a significant amount of energy must be deposited by pressure gradients at the base of the flow. This additional source of energy would presumably originate from the accretion process, e.g. in the form of enthalpy (hot wind) or Alfven-wave pressure (cool wind).

A recent analysis of UV emission lines in RY Tau by Gómez de Castro & Verdugo (2007) does indicate the presence of a hot stellar wind at $\simeq 6 \times 10^4$ K in this star. However, with the parameters derived by these authors for the UV line emitting region (emitting volume $(0.35\ R_\odot)^3$, total density $\simeq 10^{10}$ cm^{-3} and flow velocity $\simeq 150$ km s^{-1}), we estimate a mass-loss rate for the high-temperature UV emitting wind of $\simeq 10^{-11}\ M_\odot$ yr^{-1}. This is 2−3 orders of magnitude lower than the mass-loss rate in the optical jet. Thus, the hot stellar wind component does not contribute significantly to the bulk of the jet mass-loss seen at optical wavelengths, and enthalpy is not the main jet driving mechanism.

Pressure gradients from Alfvén waves allow one to drive cooler stellar winds (Decampli 1981), but the wave energy needed to power the observed jet mass flux is unrealistically large. Neglecting centrifugal acceleration, the fraction of accretion luminosity that needs to be transferred to the flow is $\epsilon_\infty \simeq \beta \dot{M}_j/\dot{M}_\mathrm{a}$ where $\dot{M}_j$ is the mass-flux in *one* jet and $\beta = 2 + V^2_\mathrm{jet}/V^2_{\mathrm{K},\star}$ parametrizes the amount of specific energy transferred to the flow by pressure gradients (Ferreira et al. 2006). In RY Tau, the estimated range of jet terminal speed is 100−300 km s^{-1} and the Keplerian speed at the stellar surface $V_{\mathrm{K},\star} = 350$ km s^{-1}(using $M_* = 2\ M_\odot$ and $R_* = 3\ R_\odot$; Calvet et al. 2004), yielding $\beta \simeq 2$−3 and $\epsilon_\infty \simeq 20\%$−30% for the one-sided ejection/accretion ratio of 0.1. Full MHD stellar wind solutions including magnetocentrifugal effects yield a similar result, with $\epsilon_\infty \simeq 20\%$−40% for a two-sided ejection/accretion ratio of 0.15−0.2 (Matt & Pudritz 2008). If only 20% of the Alfvén wave power is actually transferred to the flow, as the calculations of Decampli (1981) suggest, the total power in waves would have to be comparable to the accretion luminosity, which seems unrealistic.

We now examine the possibility that the jet originates from the inner regions of the circumstellar disc (X-wind or extended disc wind). The expression of the terminal poloidal flow velocity for a given streamline originating from a launching radius r_0 in the disc is given by (Blandford & Payne 1982):

$$V^\infty_\mathrm{p} = (GM_*/r_0)^{1/2}\sqrt{2\lambda - 3} \qquad (6)$$

where $\lambda = (r_A/r_0)^2$ is the magnetic lever arm parameter.

In the framework of the X-wind model developed by Shu and collaborators, all the streamlines originate from the co-rotation radius in the disc with λ values ranging between 3 and 6 (Shang et al. 1998), with most of the mass flux having $\lambda \simeq 3$. With the RY Tau stellar parameters $M_* = 2\ M_\odot$, $R_* = 3\ R_\odot$, and $v \sin i = 52$ km s^{-1}, we estimate a co-rotation radius of $0.05 \sin i^{2/3}$ AU. Thus, the range of terminal poloidal velocities predicted by the X-wind model in the case of the RY Tau microjet would be $\simeq 310$−$540 (\sin i)^{-1/3}$ km s^{-1}, with the jet line emission sharply peaked at the lower value (see predicted PV diagrams in Shang et al. 1998). The [O I] velocity centroid of 70 km s^{-1} in the RY Tau jet would then imply an inclination of the jet axis to the line of sight of 77°, at the upper limit of current observational constraints (see Sect. 4.1).

In the radially self-similar disc wind solutions first introduced by Blandford & Payne (1982), mass-loss originates from an extended range of radii in the disc, and the magnetic lever arm parameter λ is constant over all streamlines. Self-consistent calculations including the accretion disk dynamics show that super-Alfvénic solutions exist for λ between 2 and 100, depending on the toroidal field and heating at the disk surface (Ferreira 1997; Casse & Ferreira 2000). The *two-sided* ejection to accretion rate ratio is tightly related to λ and is given by $\frac{1}{2(\lambda-1)} \ln (r_\mathrm{out}/r_\mathrm{in})$ where r_out and r_in are the inner and outer radii of the region in the disc where the jet originates. As shown in Ferreira et al. (2006), these solutions reproduce the global properties (collimation, terminal poloidal velocities, rotation signatures, ejection to accretion rate ratio) of previously studied cTTs microjets for λ values in the range 2−15 and $r_\mathrm{out} \leq$ a few AUs. The global derived RY Tau jet parameters, being in the same range as previously investigated cTTS microjets, will therefore be compatible with similar disc wind solutions. We note in particular that the transverse kinematical structure of the blueshifted jet, illustrated in Fig. 7, is reminiscent of the kinematical behavior of magneto-centrifugal disc winds where outer streamlines originating from larger launching radii are predicted to flow at lower velocities than inner streamlines.

Our current best estimates of the RY Tau microjet parameters thus appear more compatible with an origin from the inner regions of the disc than with a stellar wind. Obviously, an accurate determination of the jet parameters (inclination and densities) is required to constrain more precisely the wind kinematics and the ejection to accretion ratio, allowing a detailed comparison with model predictions.

5. Conclusions

Using the OASIS spectroimager at CFHT, we have studied with 0.2″−0.4″ resolution the 2D morphology and kinematics of the inner 2″ of the RY Tau microjet in the [O I]λ6300 Å line. Our main conclusions are the following:

- The [O I] emission exhibits a bright compact low-velocity peak within 30 mas = 4 AU of the star, and an extended high-velocity blueshifted jet at PA = 294° ± 1°, with an emission knot at 1″.35. The PA is consistent with the Hα jet imaged on larger scales by St-Onge & Bastien (2008). The redshifted jet is faint and only marginally detected.
- We derive PSF-corrected jet widths of 30−40 AU and full opening angle of 5° on spatial scales 20−280 AU. These collimation properties are similar to those of lower mass cTTS microjets previously imaged at subarcsecond resolution.
- The mean jet centroid radial velocity is -70 ± 5 km s^{-1}. Best current constraints indicate an intermediate jet inclination to the line of sight (between 45° and 77°) and true flow velocities between 100 and 300 km s^{-1}, in the same range as microjets from lower mass cTTS. The most probable jet speed of 165 km s^{-1} agrees well with preliminary proper motion estimates.
- The transverse jet kinematic structure was studied in detail. A decrease of centroid velocity towards the jet edges is observed at all positions along the jet axis, as expected from MHD disk wind models. Asymmetries in velocity with respect to the jet axis, and their statistical errors, were also examined. A 3σ transverse velocity shift is found near the emission knot at 1″.35 from the source, but our angular resolution is insufficient to distinguish between jet rotation and bowshock asymmetries.
- From the measured spatially resolved [O I] luminosity along the jet, we derive for the HVC an ejection rate 4 times higher than the previous determination by Hartigan et al. (1995).

The one-sided ejection to accretion rate ratio is ≃0.1 (within a factor of 4), similar to its average value in lower mass cTTS (Cabrit 2007).

- The remarkably similar collimation, terminal speed, and ejection efficiency of the RY Tau microjet compared to lower mass cTTS gives firm support to the common belief that the jet launching mechanism may be universal over a broad range of stellar masses.
- The [O I] jet mass-flux exceeds by 2−3 orders of magnitude the mass-flux in the hot stellar wind component discovered in UV lines by Gómez de Castro & Verdugo (2007). This does not support thermal pressure as the main driving agent for the atomic jet. An Alfvén-wave driven, cool stellar wind is possible but energetically challenging.
- The PA we measure for the blueshifted jet is comparable to the PA of the photocenter variation detected by Hipparcos in RY Tau, calling into question its interpretation in terms of a binary system. We propose that the photocenter displacements may instead arise during UXOr-like occultation events, which enhance emission from the blueshifted jet and/or scattering cavity relative to the occulted photosphere. This would predict a clear anti-correlation between photocenter displacement and source brightness.

Acknowledgements. We are grateful to the anonymous referee for useful and constructive comments. V. Agra-Amboage, S. Cabrit, and P. Garcia wish to acknowledge financial and travel support through the Marie Curie Research Training Network JETSET (Jet Simulations, Experiments and Theory) under contract MRTN-CT-2004-005592. The work of P. Garcia was supported in part by the Fundação para a Ciencia e a Tecnologia through grant PTDC/CTEAST/65971/2006 from POTCI, with funds from the European program FEDER.

Appendix A: Random errors on transverse velocity shift measurements

In order to accurately estimate the uncertainties due to noise in our transverse velocity shift measurements, we perform a Monte-Carlo study adapted to our OASIS observational parameters. We simulate pairs of identical Gaussian spectra with total *FWHM* 135 km s^{-1} or 175 km s^{-1}, typical of our observations, and shift them by $\Delta V = 10$ km s^{-1} (comparable to the expected transverse velocity shifts due to rotation), using the same velocity sampling as in our data. We checked that the results shown below are in fact independent of the shift for $\Delta V \geq 10$ km s^{-1}. We then introduce random Gaussian noise typical of our observing parameters, i.e. a peak signal-to-noise ratio (*SNR*) varying between 5 and 40. For each Monte-Carlo realisation of the noise statistics, we "measure" velocity shifts between the two spectra with the two different methods: difference between the velocity centroids derived from single component Gaussian fits, and cross-correlation between the pair of spectra. We perform 300 such Monte-Carlo realisations at a given *SNR*, and then compute the rms standard deviation of the 300 measured velocity shifts.

The result is shown in Fig. A.1 where we plot the standard deviation of the measured velocity shift as a function of initial peak signal to noise ratio for the 2 methods, and for the two values of input *FWHM*. This study demonstrates that the Gaussian fitting procedure gives the best accuracy compared to cross-correlation, and that the error increases steeply with decreasing peak *SNR*.

The theoretical accuracy on the centroid of a single component Gaussian profile of dispersion $\sigma_{\rm line}$ dominated by photon noise and with infinite sampling is given by $\sigma_{\rm line}/SNR$ (Porter et al. 2004) where the *SNR* is the signal over noise ratio at the line emission peak. Since we compute the difference of two centroids, each affected by the same error, we would thus expect a 1σ dispersion in the velocity shifts of $\sigma_{\Delta V} \simeq \sqrt{2}(FWHM/2.35)/SNR$ ranging between $82/SNR$ km s^{-1} (for $FWHM = 135$ km s^{-1}) and $104/SNR$ km s^{-1} (for $FWHM = 175$ km s^{-1}). Our Monte-Carlo results in Fig. A.1 for the Gaussian method are well fitted by an empirical formula $\sigma_{\Delta V} = 90/SNR$ km s^{-1}, fully consistent with the theoretical expectations from Porter et al. (2004). We use this formula to compute 3σ error bars for the transverse velocity shifts plotted in Fig. 8.

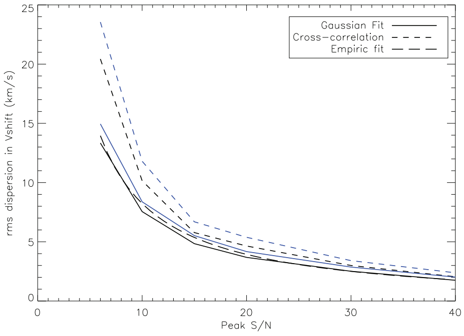

Fig. A.1. 1σ error on the velocity shift between two spectra as a function of the signal-to-noise ratio (*SNR*) at the line peak, as modelled from Monte-Carlo simulations. Two measurement methods are presented: cross-correlation of spectra (short-dashed curves) and centroid difference of Gaussian fits (solid curves). The input velocity shift is 10 km s^{-1}, and the input profile *FWHM* is 135 km s^{-1} (black curves) and 175 km s^{-1} (blue curves). The long dashed curve plots $\sigma_{\Delta V} = 90/SNR$ km s^{-1}, the expected theoretical error for infinite sampling (see text).

References

Bacciotti, F., & Eislöffel, J. 1999, A&A, 342, 717
Bacciotti, F., Mundt, R., Ray, T. P., et al. 2000, ApJ, 537, L49
Bacciotti, F., Ray, T. P., Mundt, R., Eislöffel, J., & Solf, J. 2002, ApJ, 576, 222
Bacon, R., Emsellem, E., Combes, F., et al. 2001, A&A, 371, 409
Basri, G., Martin, E. L., & Bertout, C. 1991, A&A, 252, 625
Bastien, P. 1982, A&AS, 48, 153
Bertout, C., Robichon, N., & Arenou, F. 1999, A&A, 352, 574
Blandford, R. D., & Payne, D. G. 1982, MNRAS, 199, 883
Cabrit, S. 2002, in EAS Pub. Ser. 3, ed. J. Bouvier, & J.-P. Zahn, 147
Cabrit, S. 2007, in IAU Symp. 243, ed. J. Bouvier, & I. Appenzeller, 203
Cabrit, S., Edwards, S., Strom, S. E., & Strom, K. M. 1990, ApJ, 354, 687
Calvet, N., Muzerolle, J., Briceño, C., et al. 2004, AJ, 128, 1294
Casse, F., & Ferreira, J. 2000, A&A, 361, 1178
Coffey, D., Bacciotti, F., Woitas, J., Ray, T. P., & Eislöffel, J. 2004, ApJ, 604, 758
Coffey, D., Bacciotti, F., Ray, T. P., Eislöffel, J., & Woitas, J. 2007, ApJ, 663, 350
Corcoran, M., & Ray, T. P. 1997, A&A, 321, 189
Decampli, W. M. 1981, ApJ, 244, 124
Dougados, C., Cabrit, S., Lavalley, C., & Ménard, F. 2000, A&A, 357, L61
Dougados, C., Cabrit, S., & Lavalley-Fouquet, C. 2002, in Rev. Mexicana Astron. Astrofis. Conf. Ser. 13, ed. W. J. Henney, W. Steffen, L. Binette, & A. Raga, 43
Ferreira, J. 1997, A&A, 319, 340
Ferreira, J., Pelletier, G., & Appl, S. 2000, MNRAS, 312, 387
Ferreira, J., Dougados, C., & Cabrit, S. 2006, A&A, 453, 785
Garcia, P. J. V., Thiébaut, E., & Bacon, R. 1999, A&A, 346, 892
Gómez de Castro, A. I., & Verdugo, E. 2007, ApJ, 654, L91
Goodson, A. P., Winglee, R. M., & Boehm, K.-H. 1997, ApJ, 489, 199
Gullbring, E., Hartmann, L., Briceno, C., & Calvet, N. 1998, ApJ, 492, 323

Hartigan, P., & Morse, J. 2007, ApJ, 660, 426
Hartigan, P., Morse, J. A., & Raymond, J. 1994, ApJ, 436, 125
Hartigan, P., Edwards, S., & Ghandour, L. 1995, ApJ, 452, 736
Hartigan, P., Edwards, S., & Pierson, R. 2004, ApJ, 609, 261
Herbst, W., & Stine, P. C. 1984, AJ, 89, 1716
Hirth, G. A., Mundt, R., & Solf, J. 1997, A&AS, 126, 437
Kitamura, Y., Momose, M., Yokogawa, S., et al. 2002, ApJ, 581, 357
Koerner, D. W., & Sargent, A. I. 1995, AJ, 109, 2138
Lavalley, C., Cabrit, S., Dougados, C., Ferruit, P., & Bacon, R. 1997, A&A, 327, 671
Lavalley-Fouquet, C., Cabrit, S., & Dougados, C. 2000, A&A, 356, L41
López-Martín, L., Cabrit, S., & Dougados, C. 2003, A&A, 405, L1
Matt, S., & Pudritz, R. E. 2008, ArXiv e-prints, 801
Mora, A., Merín, B., Solano, E., et al. 2001, A&A, 378, 116
Muzerolle, J., Calvet, N., Hartmann, L., & D'Alessio, P. 2003, ApJ, 597, L149
Natta, A., & Whitney, B. A. 2000, A&A, 364, 633
Pesenti, N., Dougados, C., Cabrit, S., et al. 2004, A&A, 416, L9
Petrov, P. P., Zajtseva, G. V., Efimov, Y. S., et al. 1999, A&A, 341, 553
Porter, J. M., Oudmaijer, R. D., & Baines, D. 2004, A&A, 428, 327
Pudritz, R. E., & Norman, C. A. 1986, ApJ, 301, 571
Pyo, T.-S., Kobayashi, N., Hayashi, M., et al. 2003, ApJ, 590, 340
Pyo, T.-S., Hayashi, M., Kobayashi, N., et al. 2006, ApJ, 649, 836
Ray, T., Dougados, C., Bacciotti, F., Eislöffel, J., & Chrysostomou, A. 2007, in Protostars and Planets V, ed. B. Reipurth, D. Jewitt, & K. Keil, 231
Sauty, C., & Tsinganos, K. 1994, A&A, 287, 893
Schegerer, A. A., Wolf, S., Ratzka, T., & Leinert, C. 2008, A&A, 478, 779
Shang, H., Shu, F. H., & Glassgold, A. E. 1998, ApJ, 493, L91
Shu, F. H., Najita, J., Ostriker, E. C., & Shang, H. 1995, ApJ, 455, L155
St-Onge, G., & Bastien, P. 2008, ApJ, 674, 1032
Whelan, E. T., Ray, T. P., Bacciotti, F., et al. 2005, Nature, 435, 652
Woitas, J., Leinert, C., & Köhler, R. 2001, A&A, 376, 982
Woitas, J., Bacciotti, F., Ray, T. P., et al. 2005, A&A, 432, 149

6

DG Tau

In this chapter I present a detailed analysis of the near infrared emission of the DG Tau microjet in the inner regions, ∼200 AU from the star. I analyze both the atomic and molecular components of the outflow from SINFONI observations in the H and K bands. Observing in the near-IR allows to reach higher angular resolution than in the optical because of a better performance of OA systems in the near-IR versus the optical regime (0.15″ for SINFONI observations while 0.3″-0.4″ for similar instruments in the optical). On the other side, these observations will allow to probe simultaneously atomic and molecular tracers and study their relationship.

Firstly, this study extends to NIR high angular resolution spectro-imaging techniques, the studies carried out in the NIR by Pyo et al. (2003) using long-slit techniques and in the optical using long-slit techniques (e.g Bacciotti, 2002; Coffey et al., 2008) but also using IFS techniques (Lavalley-Fouquet et al., 2000). In particular, the iron atomic lines observed in the H band trace densities higher than the optical [SII] doublet common tracer and they can be used to obtain the collimation and acceleration scales and the mass-loss rates so important to test disc wind models. In addition, an estimate of the iron depletion at the jet base is also possible which gives indicators of the jet origin. If the jet originates from disc regions, some depletion is expected but in contrary, if the jet has a stellar origin, no depletion will be observed.

Secondly, the H_2 emission observed in the K band allow to probe the structure of the flow in a broad range of excitation conditions and to study its relation with the atomic component. Molecular hydrogen is a primary constituent of cool gas in the circumstellar environments of young stars. A number of molecular studies were carried out in sources presenting outflows. However, these studies were centered in class 0/I objects and in the cooler component observed at millimeter wavelengths. To date, the spatial structure, excitation and variability of near IR molecular hydrogen emission in the inner 200 AU environment of most T Tauri stars remains unknown. Investigating the morphology, velocity structure in the H_2 transitions observed in the NIR and the relationship with the atomic jet could distinguish between excitation mechanisms and clarify the nature of the emission in these regions.

The most recent and detailed studies of the inner regions of warm H_2 outflows in T Tauri stars are those of Takami et al. (2004) using long-slit observations of DG Tau or those of Gustafsson et al. (2008) and Beck et al. (2008) using IFS observations. Gustafsson et al. (2008) analyzed SINFONI observations, similar to those shown here, for the T Tau case and Beck et al. (2008) carried out a study of 6 CTTs, including DG Tau, using the NIFS spectrograph on the Gemini North Telescope. Excitation by UV fluorescence pumped by FUV or Lyα photons, by stellar UV and/or X-ray and by shocks in the outflows are considered and discussed in depth in the three papers. In addition, the origin of the emission is discussed, does this emission come from the material on the disc, from an outflow or from material in the envelope? if it is an outflow, is it a disc wind or a X-wind? This previous works seem to indicate that gas is excited by shocks in a wide-angle wind component, but none of the possibilities is really excluded. I will summarize all the arguments presented in these studies and deeply discuss them within the new results present during the chapter in order to constrain as much as possible the origin of this molecular component.

6.1 Previous works

DG Tau is a prototypical T Tauri jet source, in transition between Class II and Class I objects and with the highest accretion rate among the TTs. Athough it is one of the most studied CTTs, a big uncertainty exists in its properties. Starting by the spectral type classification, Strom et al. (1989) classified DG Tau as K5, while Muzerolle et al. (1998b) gave K7-M0 and a more recent study classifies it as K3 ± 2 (White & Hillenbrand, 2004). Hartigan et al. (1995) give a stellar radius of 2.3 $R_\odot$ and a stellar mass of 0.67 $M_\odot$ from pre-main sequence tracks by D'Antona & Mazzitelli (1994), but White & Hillenbrand (2004) give a stellar mass of 2$M_\odot$ using tracks given by Siess et al. (2000). This last value results from a higher effective temperature and stellar luminosity determinations by White & Hillenbrand (2004). I will assume the first estimate because it is that generally accepted to date. The visual extinction, A_v, is a parameter very difficult to obtain and estimates between 0.8 and 3.3 are given in the literature. Different values for the $\dot{M}_{acc}$ and $\dot{M}_{ej}$ are found through the different authors, but I will discuss them in detail in the corresponding section of Ch. 6.

In the NIR the most recent studies of this object, that I will compare with the results of the work carried out in this thesis, are those of Pyo et al. (2003), Takami et al. (2004) and Beck et al. (2008). The first one studied the [FeII] atomic component using long-slit spectroscopy (slit width=0.3″ with the Infrared Camera and Spectrograph, IRCS) combined with the adaptive optics system of Subaru Telescope in Mauna Kea, Hawaii. Observations were taken on October 2001 using a configuration providing an angular resolution of 0.16″ and a velocity resolution of 30 km/s. They identified two clear velocity components, one named low velocity component (LVC) with a center velocity of ∼-100 km/s and a high velocity component (HVC) at ∼-220 km/s. They also identified a red-shifted component showing a gap due to a disc of 140 AU in radius. The authors give some interpretations to the origin of the two components and they conclude that the well-collimated HVC jet emanates from a region close to the star while the LVC is a wide disc wind component. They say that the LVC can be due to entrainment of material by the HVC or maybe two different mechanisms explain the two components. The HVC would be driven by reconnection of dipolar stellar magnetic fields anchored to an accretion disc and the LVC would be the result of the interaction of the inner part of the disc with open magnetic field lines.

Takami et al. (2004) and Beck et al. (2008) centered their efforts in understanding the molecular emission. Takami et al. (2004) was the first detection of a warm molecular wind in DG Tau in the near-IR H_2 lines. They used the same configuration of the IRCS on Subaru Telescope but in the K band to observe DG Tau in November 2002. The main conclusion of this work is the detection of the H_2 emission in DG Tau with a radial velocity of ∼-15 km/s. The authors discuss the origin of this emission and they conclude that the H_2 and the forbidden lines emission are originated in different regions of the flow: 1) from fast, well-collimated and partially ionized streamlines and 2) from slow, poorly-collimated and molecular streamlines. This interpretation is in good agreement with predictions from magneto-centrifugal disc wind models or by entrainment of the material by the fast jet, although the authors think this possibility unlikely. They also noted that the gas, observed at a temperature of ∼2000 K can be heated by shocks or ambipolar diffusion.

Beck et al. (2008) observed 6 stars, including DG Tau, with the Near IR Integral Field Spectrograph (NIFS) at the Gemini North Telescope in Mauna Kea, Hawaii. DG Tau was observed on October 2005 with a spatial resolution of $\leq 0.1''$ and a spectral resolution of ∼5300 at 2.2μm. The authors detected H_2 emission in the six CCTs observed and they derived excitation temperatures in the range 1800-2300 K. Observed line ratios are consistent with shock excitation while models of UV or X ray heating predict insufficient excitation temperature for the spatial extents of the observed H_2 emission. However, the authors do not exclude the possibility since models are developed for ISM environment which are quite different from the conditions surrounding CCTs. Finally, the authors conclude then that the bulk of the emission comes from shock excitations associated with the HH outflows rather than from a quiescent disc irradiated by the central star.

6.2 Observations and Data Reduction

6.2.1 Observations

Observations of the DG Tau microjet in H and K bands were conducted on October 15th 2005 at the Very Large Telescope (VLT), using the integral field spectrograph SINFONI combined with an adaptive optics (AO) module. The configuration used for the DG Tau observations, summarized in Table 6.1, provides a spectral resolution of R ∼3000 (veloc-

Band	Spatial scale	R	Spectral range	Spectral dispersion	t_{exp}(OBJ)	t_{exp}(SKY)
H	$0.05'' \times 0.1''$	3000	1.45-1.85μm	0.20 nm/px	540 s	270 s
K	$0.05'' \times 0.1''$	4000	1.95-2.45μm	0.25 nm/px	500 s	250 s

Table 6.1: Summary of the SINFONI observations of DG Tau.

ity resolution $\sim$ 100 km/s) over a spectral range from 1.45μm to 1.85μm and spectral dispersion of 0.20 nm/px (equivalent to ~ 35 km/s) in the H band, and a spectral resolution of R $\sim$4000 (velocity resolution $\sim$ 75 km/s) over a spectral range from 1.95μm to 2.45μm, with spectral dispersion of 0.25 nm/px in the K band. The field of view is $3'' \times 3''$ with a spatial scale of $0.05'' \times 0.1''$. After AO correction, the effective spatial resolution achieved is $\sim 0.15''$ in both bands (FWHM estimated from a Gaussian fit on the two spatial directions). One combined final datacube with total integration time of 540s for the object and 270s for the sky was obtained in the H band and of 500s and 250s in the K band for the object and the sky respectively.

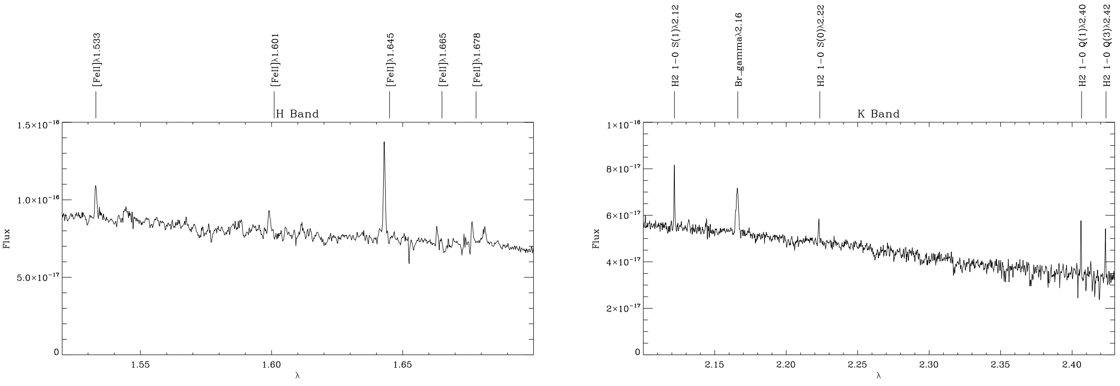

Figure 6.1: Average spectra, both in the H and K band, from a region with strong emission from the DG Tau jet. I label the strongest emission lines identified, most of them iron and molecular hydrogen lines, but also the Br_γ line at 2.16μm.

Figure 6.1 shows two spectra, one in the H band and the other in the K band, spatially averaged in a region with strong emission coming from the DG Tau jet. I mark the position for the main lines detected. In particular, the analysis will be centered on the [FeII]λ1.53μm and [FeII]λ1.64μm, but also on the molecular $H_2\lambda2.12\mu$m and the Br_γ emission lines.

6.2.2 Data Reduction

Data reduction was carried out using the SINFONI pipeline (see brief description in Ch. 4, section 4.3). Final provided cubes are corrected for bad pixels, dark, flat field, geometric distortions on the detector, sky background and calibrated in wavelength. Data were spatially re-scaled to a square grid of $0.05'' \times 0.05''$ duplicating the pixels on the longer dimension. In addition to the reduction provided by the pipeline, dedicated procedures were developed under IDL to perform flux calibration and the stellar continuum subtraction. Also, though the wavelength calibration was carried out by the reduction pipeline, using calibration lamp images, a more accurate calibration was accomplished using the sky OH lines from the sky images. I explain these steps in detail in the following sections.

Wavelength calibration

In order to carry out the best kinematical study, the best spectral resolution possible is required. SINFONI characteristics, in the configuration used in our observations, offer a very good spectral resolution (100 km/s in H band and 75 km/s in K band) with a velocity dispersion of $\sim$ 35 km/s. However, the wavelength calibration provided by the pipeline proved not to be accurate enough.

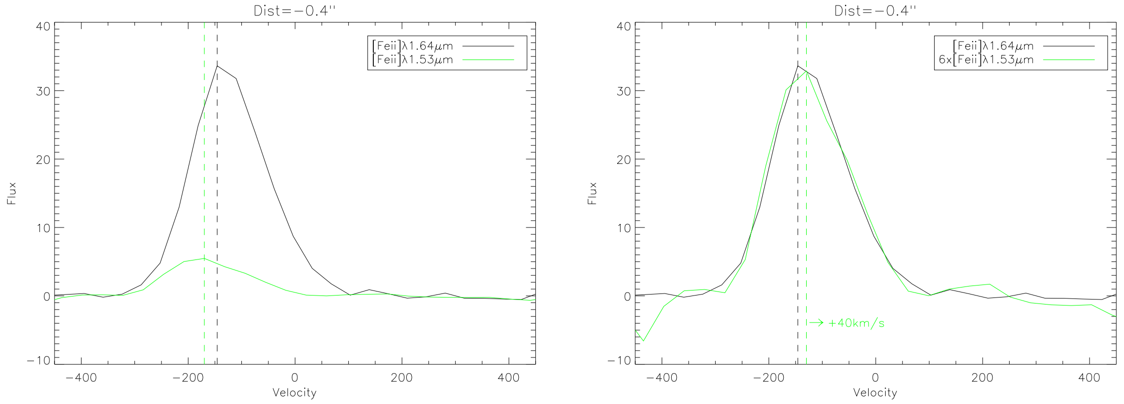

Figure 6.2: Velocity calibration problem: line profiles for $\lambda 1.53\mu$m (green) and $\lambda 1.64\mu$m (black) lines at a distances of 0.4″ from the star in the blue jet. Two lines show a shift of almost 50 km/s. Left: profiles after continuum subtraction. Right: same profiles but the $\lambda 1.53\mu$m profile was multiplied by 6 and shifted of 40 km/s to show the similarity between the two profiles.

During the study of the iron lines at 1.53μm and 1.64μm we realized the existence of suspicious shifts between the two lines of $\sim$50 km/s keeping the same profile shapes. Figure 6.2 shows the two line profiles at an example distance of 0.4″ from the star in the blue side of the jet. I mark the line peaks with dashed lines to show this shift between the two lines. On the right panel of Fig. 6.2 the profile of the $\lambda 1.53\mu$m line is shifted and the flux is multiplied by 6 to show the similarity with the $\lambda 1.64\mu$m profile. This is an important problem for the kinematical analysis. In order to understand the origin of these significant and not physical shifts, several possibilities in the data reduction process, using the proposed SINFONI pipeline, were tested. We realized that the origin was in the wavelength calibration step.

The standard pipeline reduction uses calibration lamps to carry out the wavelength calibration, instead of using sky OH lines as it is usual in IR spectroscopy. Some quality control files are produced in this step in order to be able to test the wavelength calibration accuracy. These files have information about the line fits achieved for the different spectral lines of the lamp placed along the wavelength interval, for each band and in the different positions on the detector. Figure 6.3 shows, for the two bands and for a central region on the detector the difference between the measured wavelength (or velocity) and the theoretical values, for all the measured lamp lines. Surprisingly, some expected brilliant lines were not measured causing, in some cases, holes in the wavelength interval coverage and reducing the accuracy in these regions. Moreover, variations up to ± 50 km/s around the theoretical value were found. I note that in Fig. 6.3, in the K band, all the shifts are positives but it is only a position example, in other detector positions both negative and positive shifts were found.

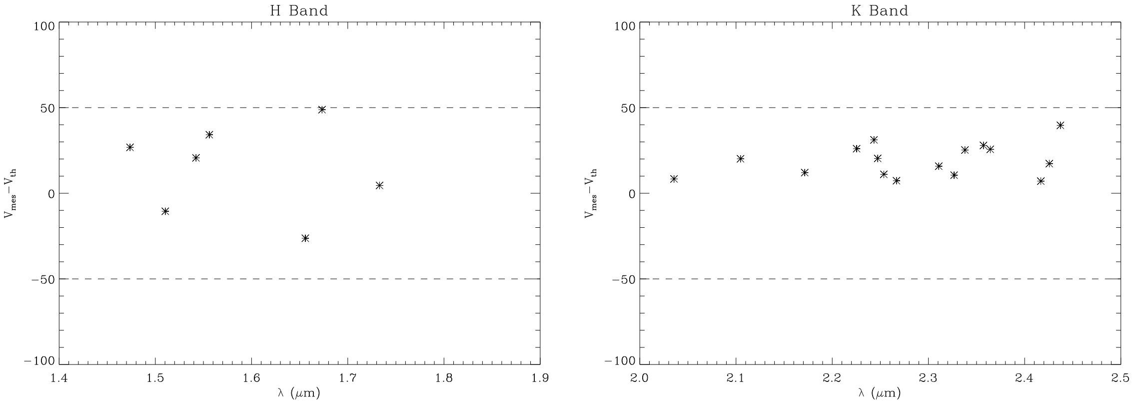

Figure 6.3: Velocity differences between the measured values and the theoretical value for the detected lamp lines in a central position on the detector. The H Band on the right and K Band on the left.

An error of ± 50 km/s is too big for the aims of the kinematical study and to determine the jet velocity with a reasonable accuracy since typical velocities in T Tauri jets are 200 or 300 km/s. With an insufficient accuracy in the calibration, we lose the advantage of the SINFONI quality and the power of this kind of observations.

To obtain a better calibration locally in the wavelength intervals where we are interested in, and better exploit our data, a more accurate velocity calibration using the OH lines placed near the lines of interest, on the sky cubes, was carried out in collaboration with Dr. Juha Reunanen. These sky images were reduced using the standard pipeline routine, therefore they are calibrated in wavelength with the lamp emission lines in the same manner of the science data. The difference between the theoretical value and the measured wavelength centroid on the OH lines, after pipeline reduction, gives the velocity correction to apply to our science data. We detect two bright OH sky lines on either side of the line of interest [FeII]$\lambda1.64\mu$m, one at $\lambda1.6128\mu$m and the second one at $\lambda1.6692\mu$m. The first line is more noisy than the second and it is also farther in wavelength from the iron line of interest, thus only the line at $\lambda1.6692\mu$m was used to improve the wavelength calibration in the corresponding spectral region. The left panel of Fig. 6.4 shows the

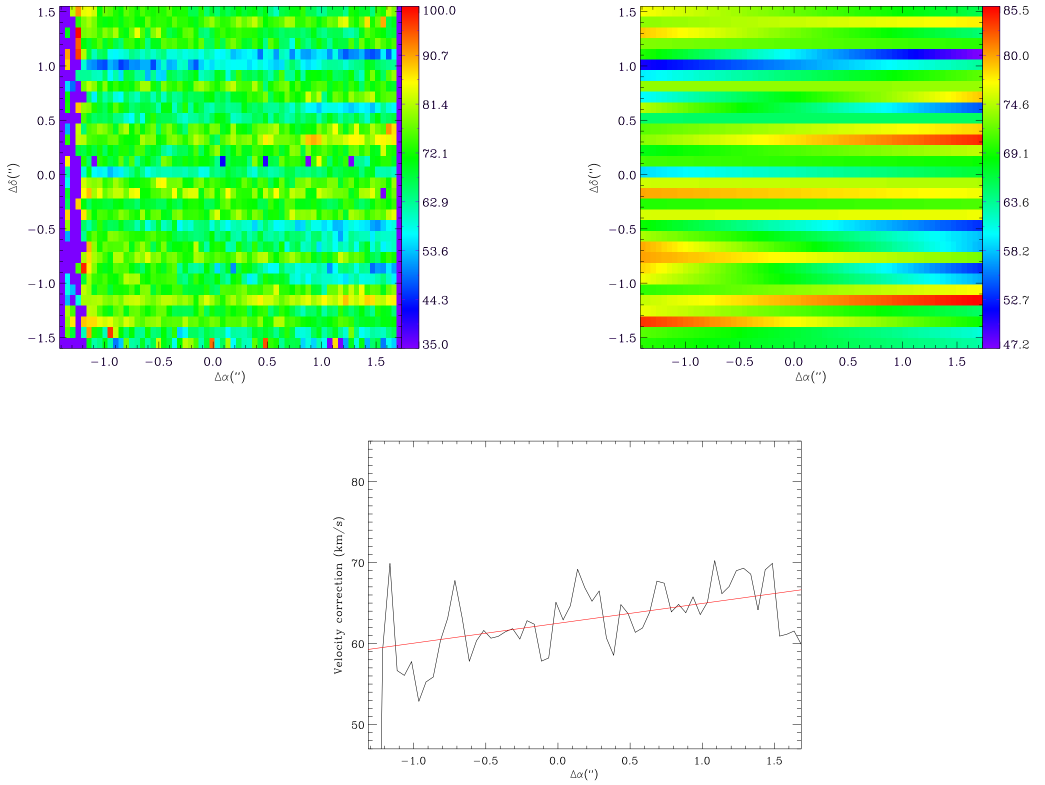

Figure 6.4: Upper-Left: Velocity correction to the previous wavelength calibration to the sky $\lambda 1.6692\mu$m line at each spatial position on the detector. Upper-Right: Velocity correction (Δv) in km/s derived as a linear fit carried out on the X direction of the detector on the previous image. Lower: Example of the fit achieve in one of the central slit.

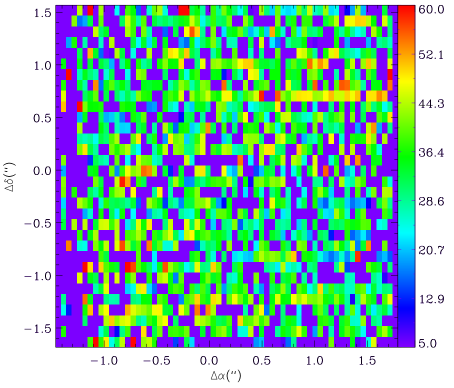

Figure 6.5: Velocity correction to apply in the region of the [FeII]$\lambda 1.533\mu$m line, measured from the OH sky line at $\lambda 1.53327\mu$m. The wavelength calibration in this spectral region was not finally corrected because it would introduce more noise to the corrected image.

velocity correction to apply to the OH line observed at $\lambda 1.6692 \mu$m. This figure clearly shows how the correction varies in all the detector positions, with corrections covering a large range, from 35 to 100 km/s. In average this correction is of 60-70 km/s. The OH lines detected in the region of the 1.533μm iron line are also quite noisy and the calibration was not improved in this region. Figure 6.5 shows the velocity shift measured in the closest OH line to the [FeII]$\lambda 1.533\mu$m line, at $\lambda 1.53327\mu$m. Other OH sky line, at $\lambda 1.52411\mu$m is as noisy as this.

This correction depends on the position on the detector and the wavelength interval. Hence, it is applied locally to the spectral interval close to [FeII]$\lambda 1.64\mu$m line in the H band. In the X direction on the detector the variation is smooth and a linear fit is carried out in this direction. The Y direction on the detector, each horizontal line in the figure, corresponds to the different slicers which in the original raw cube were not spatially close together on the detector. For this reason, the variation from one slicer to its neighbor is not continuous. Right panel in Fig 6.4 shows the fit applied to the measured velocity corrections.

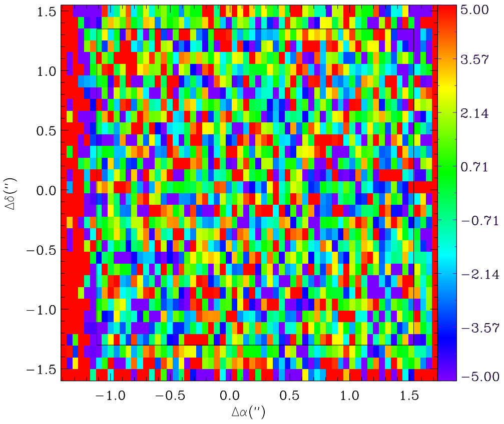

Figure 6.6: Difference between the velocity corrections derived from a linear fit, finally applied to the data, and the velocity corrections measured for each point on the detector. The standard deviation gives a lower limit to the error on the wavelength calibration. It is calculated inside the box because the outer parts of the detector are more noisy.

Figure 6.6 shows, for the H Band, the difference between the velocity corrections derived from the linear fit and the velocity corrections measured for each point on the detector. It gives us an idea of the error of the fit applied and the standard deviation gives a lower limit to the new wavelength calibration error, which is of ± 5 km/s (calculated on the region box plotted on Fig. 6.6). In addition to that, the standard deviation, measured in the same box, of the difference between the velocity corrections derived from the two OH lines bracketing the [FeII] line, gives an upper limit to the error in the new calibration of ± 10 km/s.

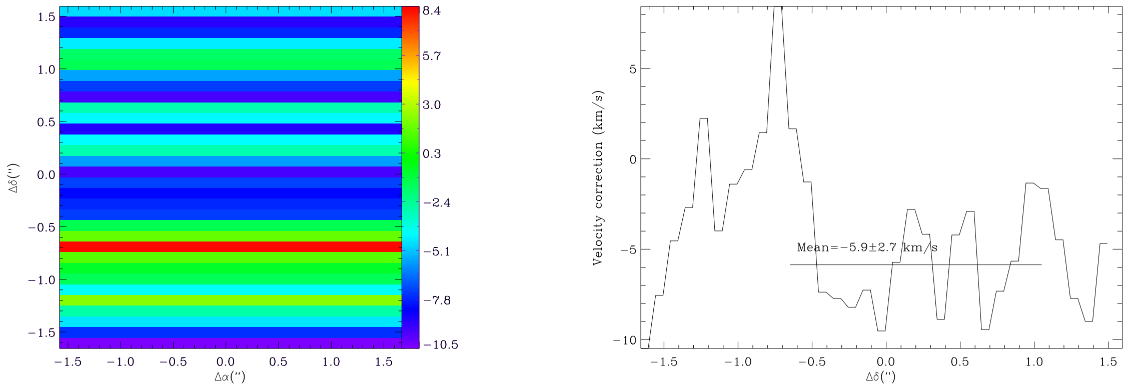

Figure 6.7: Left: Velocity correction, for each slit, measured from a Gaussian fit on a combination of the four OH lines detected around the $H_2\lambda2.12\mu$m line. Right: A cut in the Y direction of the detector. An average value was used to correct the wavelength calibration in this spectral region.

In the K band, we are interested in the region around the $H_2\lambda2.12\mu$m line. The corresponding sky image in the K band was used to detect OH line in this region. However, the signal to noise of this image was very poor. Four OH lines (two on either side of the H_2 line) were combined together, the resulting profiles were binned within the whole slitlet and a single velocity shift was measured by fitting a Gaussian to the final combined OH line profile. This fit is shown in the left panel of Fig. 6.7. The right panel shows a cut in the Y direction of the detector. Since the variation is not very important, an average value of 5.9 ± 2.7 km/s, averaged in the region where there is H_2 emission in our DG Tau observations, was used to improve the calibration at all the positions of the detector.

Telluric correction

The analysis will be centered on the strongest emission lines tracing the jet emission, that means the [FeII] lines at 1.64μm and 1.533μm, and the H_2 line at 2.12μm. The data reduction at these wavelengths is carefully verified to assure that the measured intensities are only due to jet emission. Figure 6.8 shows, for example, the raw spectrum at the position $\alpha \sim 0''$ and $\delta \sim 0.5''$, for the [FeII]$\lambda1.64\mu$m line. Over-plotted, in dashed line, there is the spectrum of the telluric standard star at the same wavelength interval, both spectra normalized to the continuum. This spectrum shows some telluric absorption lines but also a strong hydrogen recombination line, Br_{12-4}, formed at the star atmosphere. This Br line must be corrected from the standard spectrum before applying a telluric correction to the scientific spectra. However, the telluric contributions is less than 7% in the regions we are interested in and for each line of interest. Carrying out the telluric correction on the scientific data will introduce more noise than improvement to the data. Hence, this correction has not been performed. Nevertheless, a partial and local correction is accomplished at the same time as the photospheric stellar subtraction which is explain in Sec. 6.2.2.

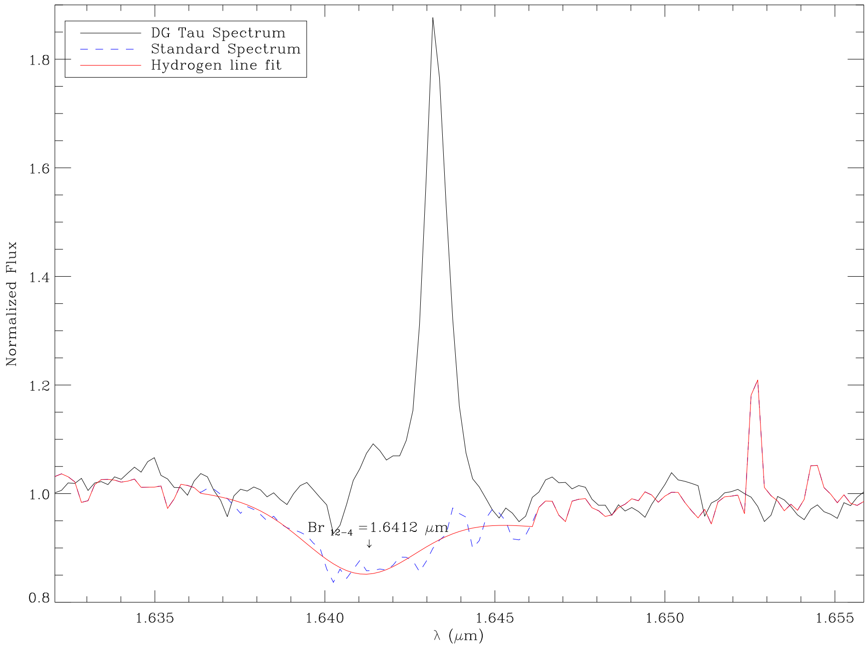

Figure 6.8: Spectrum at $\alpha \sim 0''$ and $\delta \sim 0.5''$ showing clear jet emission in the [FeII]λ1.64μm line. The telluric standard star spectrum is over-plotted, in dashed line, and in red solid line the fit to the Brackett Hydrogen line at 1.6412 μm is also included. Both spectra are normalized to the continuum. Telluric absorption lines contribute less than 7% to the emission.

Flux calibration

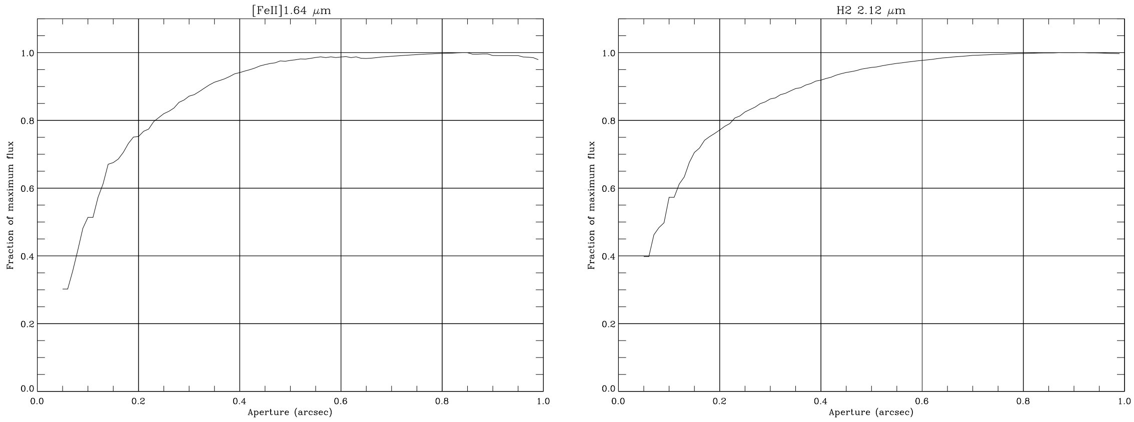

Figure 6.9: Measured flux normalized to the maximum in the telluric standards as a function of the aperture taken for integrating the flux. The H band on the left and the K band on the right.

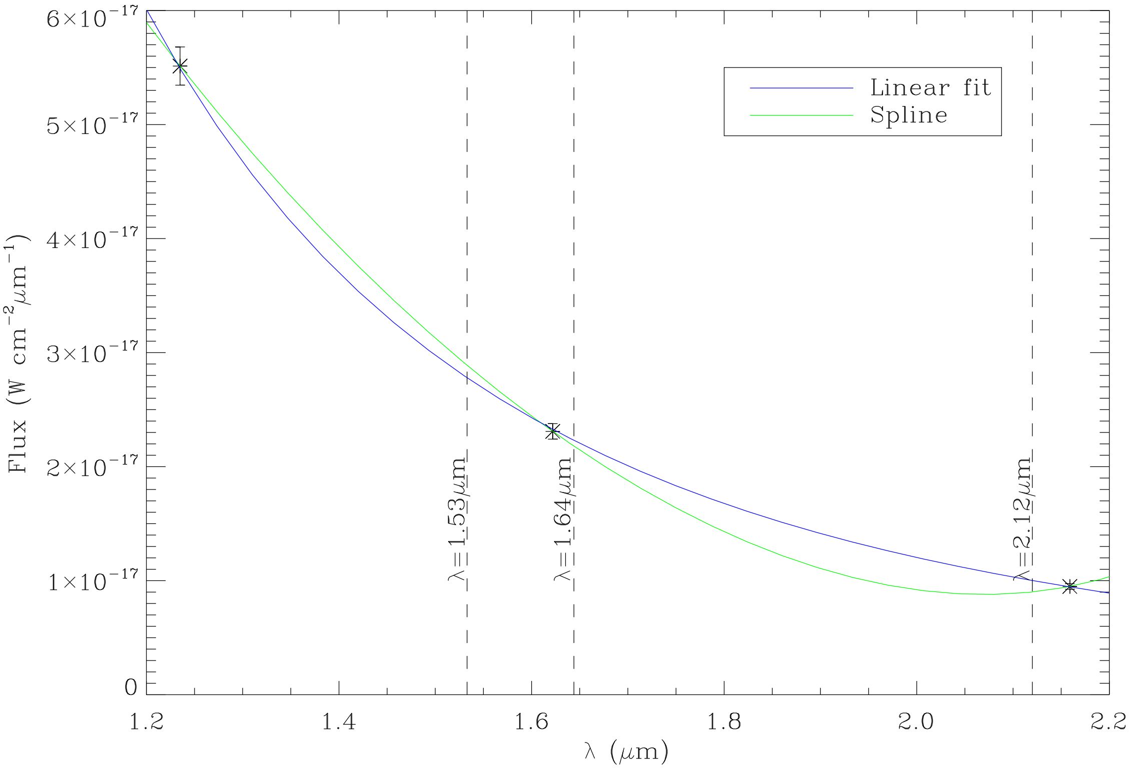

Figure 6.10: Interpolation between the flux calculated from the magnitudes in H, K and J bands from the 2MASS catalogue, for the star HIP 26686 (observed in the H band). Two methods were tested, a spline fit (green) and a linear fit (blue). Finally, the linear fit (in logarithmic scale), expected for a black body emission at this wavelength domain in the Rayleigh-Jeans approximation, was kept.

The flux calibration was carried out following the standard procedure. Given an aperture, the sum of the standard star spectra inside the aperture is calculate. The aperture is chosen big enough to take all the counts coming from the star but trying to introduce the less noise as possible. The required aperture for taking all the flux is 0.8″, Fig. 6.9, but an smaller aperture of 0.4″ is used to minimize the noise and then a factor correction is applied. Once the observed flux is measured, it has to be calibrated in physical units. In this case, this value was obtained from the star known magnitudes in the H, K and J bands of the 2MASS catalogue. The flux is obtained using the following expression:

$$F_{calib}(STD) = F_0(Band) \text{ x } 10^{-m(Band)/2.5} \tag{6.1}$$

where $F_0(Band)$ is the flux for a zero-magnitude star taken from 2MASS catalogue (Table 6.2), $m(Band)$ is the known magnitude in the band, taken from the literature, and $F_{calib}(STD)$ is the flux in the corresponding band. The corresponding values for the two observed standard stars are listed in the Table 6.3. The three fluxes derived for the star HIP 26686, for an example, are plotted in Fig. 6.10 (star symbols). Planck's law gives the energy law for a black body. It depends, expressed as a function of λ for a

Band	$F_0(Wcm^{-2}\mu m^{-1})$
J	$3.129\times10^{-13}\pm 5.464\times10^{-15}$
H	$1.133\times10^{-13}\pm 2.212\times10^{-15}$
K	$4.283\times10^{-14}\pm 8.053\times10^{-16}$

Table 6.2: Flux for a zero-magnitude star from the 2MASS catalogue.

Star name	Band	m	$F_{1.53}$	$F_{1.64}$	$F_{2.12}$
HIP 26686 (H Band)	J	9.385 ± 0.027	2.8×10^{-17}	2.2×10^{-17}	1.0×10^{-17}
	H	9.227 ± 0.024			
	K	9.136 ± 0.019			
HD 28107 (K Band)	J	7.557 ± 0.027	1.3×10^{-16}	1.0×10^{-16}	4.0×10^{-17}
	H	7.622 ± 0.046			
	K	7.625 ± 0.024			

Table 6.3: Names of the standard stars observed in the H and K band and the magnitude value for each band used in Eq. 6.1 to perform the flux calibration, obtained from the 2MASS catalogue. The last three columns give the extrapolated flux (in W cm$^{-2}\mu$m^{-1}) at each of the wavelengths of interest for the linear fit shown in Fig. 6.10.

given temperature, as $\propto \lambda^{-5}(e^{hc/\lambda kT}-1)^{-1}$. If $hc/\lambda kT < 1$ then the Rayleigh-Jeans' approximation could be applied and the intensity depends with λ as λ^{-4} (linear relation in log-log diagrams). At small wavelengths, Wien's approximation gives the intensity proportional to $\lambda^{-5}e^{-(hc/\lambda kT)}$. The standard star, HIP 26686, is a A2 spectral type star, thus with a temperature between 7500 and 10000K. For a wavelength of 1.6μm, the ratio $hc/\lambda kT \sim 1$, placing us between the two previous approximations. Hence, the three values are interpolated using two methods, a spline fit (in green in Fig. 6.10) and a linear fit (in blue). The spline fit is less reliable since it goes up for wavelengths at the end of the interval, which is not expected. Therefore, the linear interpolation (Rayleigh-Jeans approximation) was kept to obtain the corresponding theoretical flux at the wavelengths of interest (last columns in Table 6.3). It can be expressed as:

$$log_{10}F = -15.9 - 3.14 log_{10}\lambda$$

The same is made for the standard observed in the K band. Once the calibration factor, $calib\_cte$, derived, the flux calibration of the scientific data is immediate. However we have to take into account the different exposure time between the standard star, $t_{exp}(STD)$, and the object, $t_{exp}(OBJ)$:

$$Spec_{calib}(OBJ) = Spec_{obs}(OBJ) \text{ x } calib\_cte \text{ x } \frac{t_{exp}(STD)}{t_{exp}(OBJ)} = Spec_{obs}(OBJ) \text{ x } f \tag{6.2}$$

For the H band, at 1.64μm, we found a factor f of 2.73209$\times10^{-15}$ W m$^{-2}\mu$ m^{-1} arcsec^{-2} and 5.13088$\times10^{-15}$ W m$^{-2}\mu$ m^{-1} arcsec^{-2} for the K band, at 2.12μm.

Some sources of uncertainty in the flux calibration procedure are identified. The first and more obvious comes from the uncertainty in the 2MASS magnitudes, given in table 6.3 which translates in errors on the flux of 3%. But this is not the only source, others such as the uncertainty in the determination of the aperture containing the maximum flux must be kept in mind. Its importance can be estimated as the dispersion of the observed values from the maximum value in the last part of Fig. 6.9. I did this estimation for apertures greater than $0.6''$, and I obtained an error of 0.5% in the H Band and 0.6% in the K band. Finally, I note that, firstly, the star is assumed to be a perfect black body emitter when the linear fit is adopted (Rayleigh-Jeans approximation) and secondly, the scientific data and the standard star were not taken at exactly the same airmass introducing also an error when the flux calibration is applied. This last error can also be one of the most important, it depends on both the airmass difference between the standard and the object and also on the accuracy of the extinction coefficients and in the atmospheric conditions during the observation which can be translate in a higher extinction coefficient. For the differences in the airmass between the standard and the object of 0.4 both in the H and K bands, and for typical values of the extinction coefficients, the error in the flux can be of 2 or 3%. Taken into account all these error sources, the final error in the flux calibration will be of 4-5%.

Stellar continuum subtraction

The star photospheric continuum is very important in the whole field of view and it is especially strong very close to the star. Hence, in order to better analyze the jet in the nearest regions to the source, a careful continuum subtraction was developed in a similar way as for RY Tau (Ch. 5).

In the case of DG Tau a spectrum in the data-cube itself, without detectable spatial jet emission, was taken as representative of the photospheric stellar spectrum for each band. In the case of the H Band, the spectrum chosen is at α=$0.054''$ and δ=$-0.003''$ and for the K Band the reference spectrum comes from α=$0.07''$ and δ=$0.04''$. These spectra show the photospheric absorption lines coming from the star but also the telluric features coming from the earth atmosphere which were not corrected (Sec. 6.2.2). At each spatial position, this reference spectrum is scaled to the continuum level in the current spectrum, calculated locally on the continuum region on the both sides of the line of interest, and subtracted from the current spectrum. The residual profile is not only free of photospheric absorption lines but locally, at the position of the line of interest, also partially of telluric features since these telluric lines are presented in the same way in all the cube. Hence, even if the whole spectrum is not corrected from telluric lines, a partial and local correction is carried out in the interval chosen. The telluric features are well corrected when the spectrum is dominated by the continuum emission, close to the star, and less well corrected when line to continuum ratio is large.

I apply this method at distances $d<1.5''$ from the star in the H band and $d<0.5''$ in the K band, where the stellar continuum contributes significantly. At larger distances a

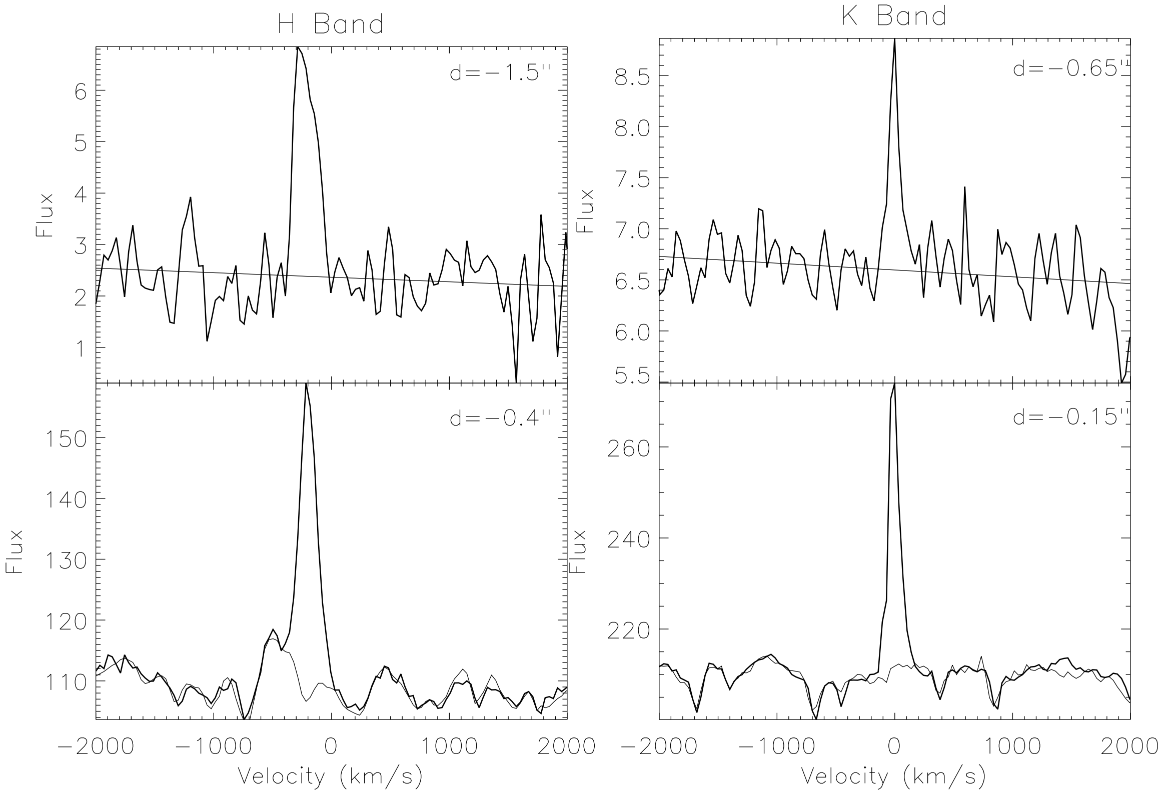

Figure 6.11: Observed spectra in the [FeII]$\lambda 1.64 \mu$m line in H band and in the $H_2\lambda 2.12\mu$m line in K band (thick lines) and fitted continuum (thin lines) at two positions along the blueshifted jet. In the H band we used a reference spectrum for distances to the star lower than 1.5$''$ and a linear fit in the rest. In the K band the limit was fixed at a distance of 0.5$''$ from the star (see text for more details).

simple linear baseline fit to the local continuum is used. Figure 6.11 shows for the two bands, two characteristic regions for these two different kinds of continuum subtraction. The importance of a good photospheric subtraction in evident in the lower panels showing the regions close to the star, especially in the case of the [FeII]$\lambda 1.64 \mu$m line region, where there is an important absorption close the line. Upper panels show that a linear fit is a good estimation of the local continuum for the more external regions.

Atmospheric refraction correction

A partial atmospheric refraction correction was performed when data are read. For each emission line of interest, data are read separately and spatially re-centering to the local continuum. The centroid of the continuum is measured in a reconstructed image, built from the continuum wavelength region which is near the emission line we are interested in. It is assumed that the atmospheric refraction is not varying over the small wavelength interval of interest.

6.3 Results

6.3.1 Morphology of atomic and molecular jet

Raw channel maps

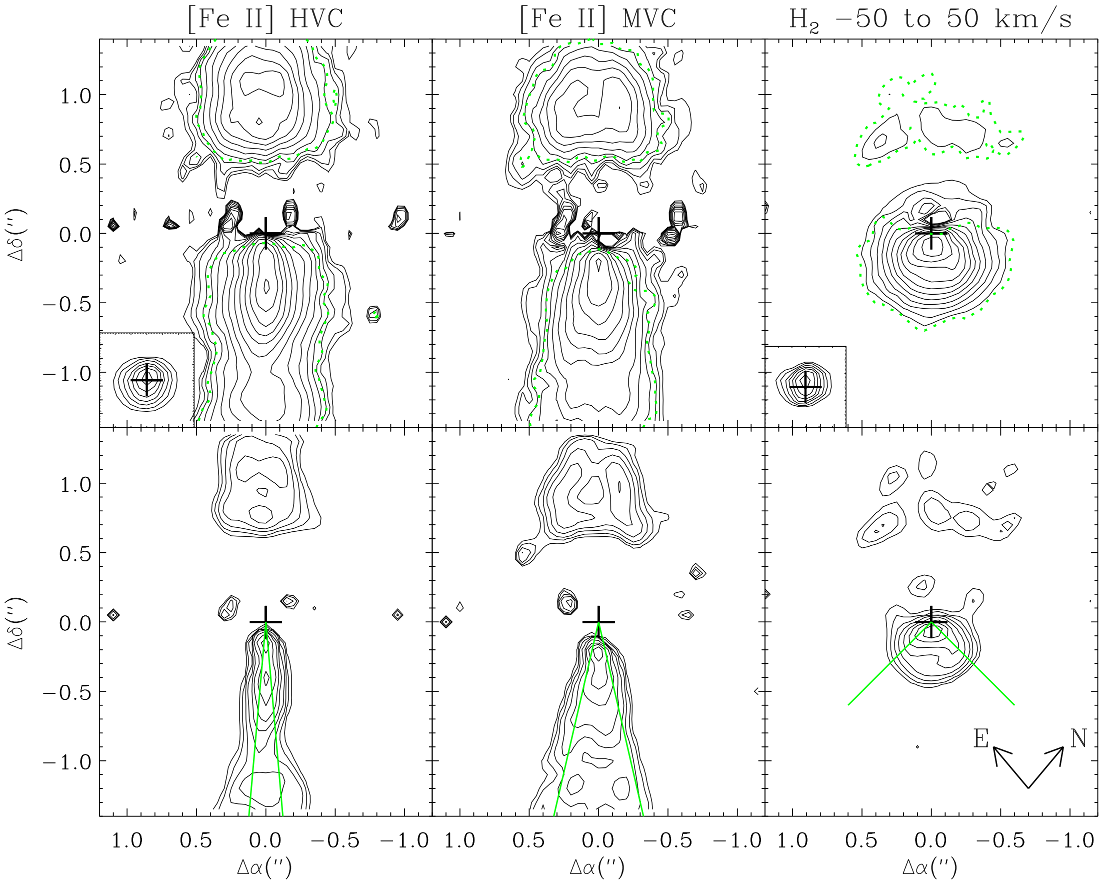

Figure 6.12: Continuum-subtracted maps for [FeII]$\lambda1.64\mu$m and $H_2\lambda2.12\mu$m lines. Atomic emission is centered on -233 km/s for the blue side of the HVC map and on +186 km/s for the red side of the same component, on -111 km/s for the blue MVC and on 29 km/s for the red part. The molecular emission is centered on -0.61 km/s. The cross gives the centroid position of the continuum emission and the dotted contour limits the region with SNR=5. Top panels are the raw data and bottom panels shows the same channel maps deconvolvoved. The opening angles for each blue velocity component are also represented. The notation $\Delta\alpha$ and $\Delta\delta$ are used to mark the spatial coordinates (X,Y) on the detector, the real orientation is given in the last panel. I keep this notation in the following figures. Inserts, in the HVC and H_2 maps, show continuum images derived from local fits.

Top panels in Fig. 6.12 shows raw continuum-subtracted line emission maps in both atomic [FeII]$\lambda1.64\mu$m and molecular $H_2\lambda2.12\mu$m lines. The emission is integrated in a high velocity component (HVC) and medium velocity component (MVC) in both sides of the atomic jet and in only one velocity interval for the molecular emission. The velocity intervals were chosen following the values of the two velocity components found by Pyo et al. (2003). The velocity intervals for the iron emission are as follows:

- The blue HVC (HVB, on the bottom of the image) is centered on -233.38 ± 70 km/s, which includes the following individual velocity channels: -181.38, -216.38, -251.38 and -286.38 km/s.
- The red HVC (HVR, on the top of the image) is centered on 186.11 ± 70 km/s, including the channels 133.61, 168.61, 203.61 and 238.61 km/s.
- The blue MVC (MVB), centered on -111.38 ± 52.50 km/s with individual channels -76.38, -111.38 and -146.38.
- The red MVC (MVR), centered on 28.61 ± 87.50 km/s includes the -41.38, -6.38, 28.61, 63.61 and 98.61 km/s individual velocity channels.
- Molecular emission is centered on -0.61 ± 52.50 km/s involving the -35.61, -0.61 and 34.38 km/s individual velocity channels.

The continuum position is calculated locally for each of the lines by a Gaussian fit in the two spatial directions. Since the images are referenced to the corresponding local continuum, they are actually corrected from the differential atmospheric refraction (DAR).

The atomic emission in the iron line does not show the very high velocity component at velocities higher than 300 or 350 km/s that is shown in the optical atomic emission of O, S^+ or N^+ in previous studies such those of Lavalley-Fouquet et al. (2000) or Bacciotti et al. (2000). However, the previous work in the same iron line, by Pyo et al. (2003), did not show a so high velocity component neither. In the optical, Lavalley-Fouquet et al. (2000) used the notation of LVB (Low Velocity Blue) for a component between -100 km/s and 10 km/s, IVB (Intermediate Velocity Blue) for a component in the range -250 to -100 km/s and HVB (High Velocity Blue) for a high velocity component at -400 to -250 km/s. However, Bacciotti et al. (2000) identify four different components in the [OI] emission: a LV for +73 to -57 km/s, MV between -58 to -188 km/s, HV from -189 to -319 km/s and a VHV (Very High Velocity) from -320 to -450 km/s. The components observed in the iron line would correspond more with the LVB and IVB of Lavalley-Fouquet et al. (2000) or the MV and HV of Bacciotti et al. (2000). Since our low component correspond to a channel centered at -100 km/s, we think that is more suitable to name them as medium and high velocity components, MVC and HVC.

Deconvolved channel maps

The upper maps in Fig. 6.12 were deconvolved with the continuum maps used as an estimate of the contemporary point spread function (PSF). Cuts through the peak of the continuum map associated to the [FeII] emission, in both directions of the detector, is shown in Fig. 6.13 and over-plotted there is a Gaussian fit. The continuum used to deconvolve the H_2 channel map shows similar profiles with FWHM equal to $0.16''$ and $0.14''$for

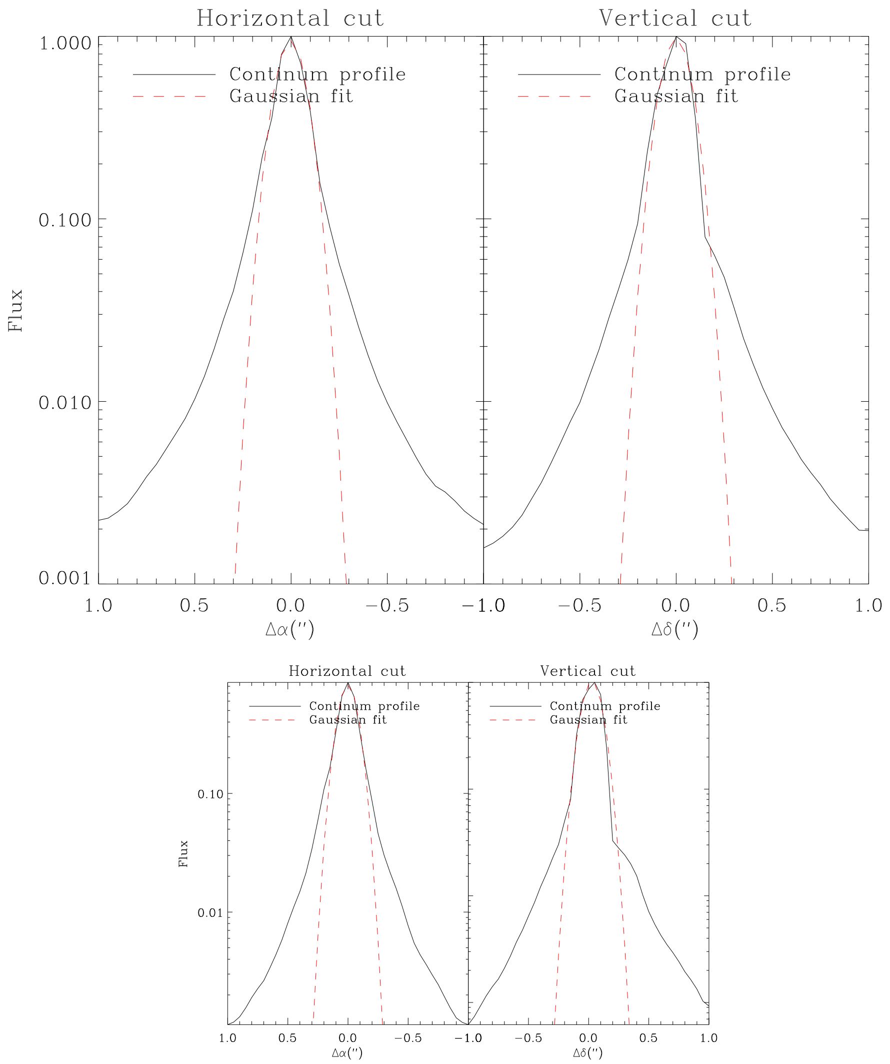

Figure 6.13: Cut, in both spatial directions, of the continuum image used as an estimate of the PSF to deconvolve the [FeII] velocity channel maps. In the α direction the FWHM=0.18″ and FWHM=0.15″ in the δ direction.

the α and δ direction, respectively. We use the LUCY restoration routine as implemented in the STSDAS/IRAF package, as it was done in the case of RY Tau (Ch. 5). We limited ourselves to 50 interactions (standard acceleration method). The final deconvolved image was obtained for a number of iterations of 40 and was determined by ensuring that the derive image FWHM did not change significantly with further iterations as shows Fig. 6.14 in the particular case of the [FeII] HVB. The final deconvolved maps are shown in the bottom panels of Fig. 6.12. The final resolution estimate is of 0.08″ in the case of [FeII] and $\leq 0.15''$ in the H_2 deconvolved channel map. Although the FWHM did not improve, the advantage of the deconvolution is to suppress the extended wings of the PSF due to partial AO correction.

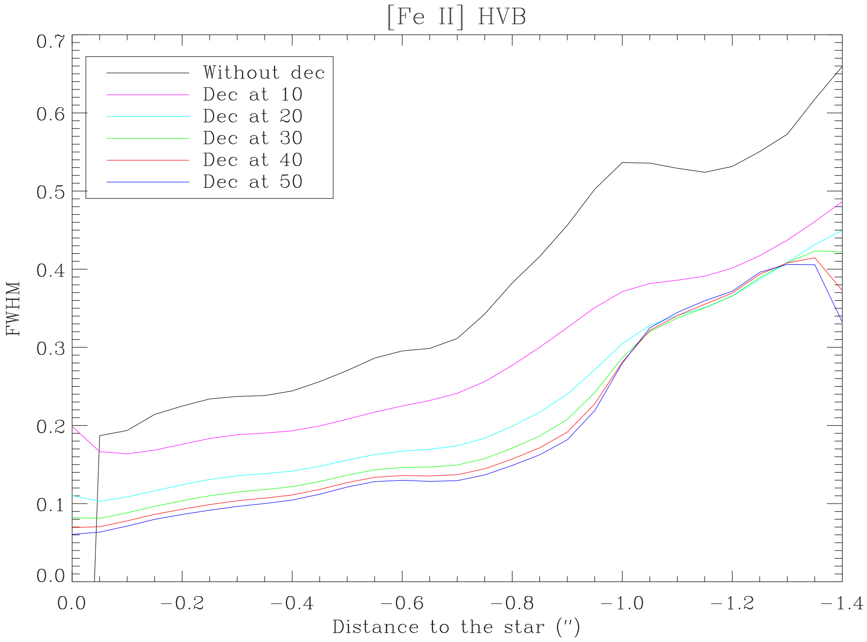

Figure 6.14: Measured FWHM of the jet on the different HVB [FeII] images resulting from different numbers of iterations in the deconvolution process. The maximum number was fixed at 40 iterations in the following.

In both raw and deconvolved images, some important properties of the atomic flow are observed. The atomic microjet is observed until the field limit in both sides of the jet, the emission extends outside the 3″ × 3″ FOV provided in these observations. The blue jet is more collimated at high velocities than medium velocities, with the HVB emission nested inside the MVB emission. This behavior has been previously noted in optical lines using OASIS at resolution of 0.4″ (Lavalley-Fouquet et al., 2000) and with HST/STIS observations over a FOV of ±0.2″ across the jet (Bacciotti et al., 2000) but the unique combination of the full coverage of the jet provided by SINFONI and the high angular resolution of 0.15″ reveal it even more clearly. The blueshifted emission shows at high velocities three distinct knots, at 0.1-0.2″, 0.35″ and 1.2″. On the contrary, the red counter-jet is only detected for distances larger than 0.5″, probably because the closer emission is hidden by the circumstellar disc, and it is wider than the blueshifted jet. It has a knot at 1.1-1.2″.

The molecular emission is confined to a small region (about 0.5″). In the blue side of the detected emission, the limb-brightened contours suggest a “hollow cavity” geometry as has seen already by Beck et al. (2008). The brightness drops steeply beyond 0.4″. The molecular H_2 emission is much broader than the atomic [FeII] with a constant full opening angle of $\simeq$45°. A strong emission peak slightly shifted from the continuum position is observed at 0.1″ along the jet axis.

The red lobe of the $H_2\lambda2.12\mu$m emission is very faint at it is restricted to a fragmented arc at 0.7-0.8″ from the star, emerging from the region without emission, which more or less encompasses the base of the bowshock seen in [FeII].

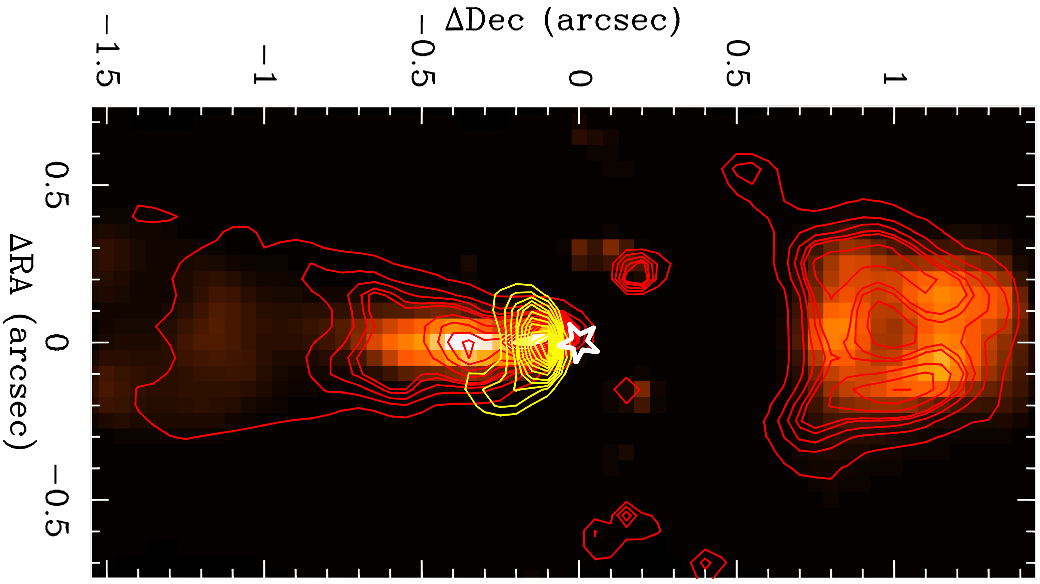

Figure 6.15: Superposition of the deconvolved images of [FeII]$\lambda1.64\mu$m (HVC (HVB+HVR) in the background image and MVC (MVB+MVR) in red contours) and $H_2\lambda2.12\mu$m (yellow contours).

For comparison of the atomic and molecular morphology, Fig. 6.15 shows the red and blue jet emission in the [FeII]$\lambda1.64\mu$m line (background image and red contours) and superimposed in yellow contours there is the $H_2\lambda2.12\mu$m flow. The molecular emission seems to be stopped at the atomic knot at -0.4″ and it seems to enclose the atomic knot. This nested structure between the two components, more evident in this image, favors the disc wind models.

Jet widths and collimation properties

Figure 6.16 shows jet width for both the [FeII] and H_2 emission, derived from deconvolved channels maps of Fig. 6.12, as a function of the projected distance from the star. For the atomic jet, both sides of the emission are plotted with the red counter jet width in red, and for the two kinematical components identified.

As it has been already noted from Fig. 6.12, the HVB is more collimated than MVB being nested inside this MVB component. The MVB emission has a conical shape with a constant full opening angle of 23°. On the contrary, the HVB keeps a particular high collimation with a full opening angle of ∼6°-7° until 0.9″ from the star. Beyond this point its width expands by a factor 2 showing an emission knot at 1.2″. The opening angle is measured by fitting the observed FWHM in Fig. 6.16 using a linear fit.

The red jet, at high velocities, is wider than the blue one, with FWHM $\simeq 0.4''$, but their widths become similar at $\sim$1.15″ which corresponds with the position of the main knot at both sides of the jet. The medium velocity component has a similar behavior. Closer to the star, the red emission is wider but at the position of knots placed at $\sim$1″ from the star in the red and blue sides, both jets have the same FWHM. Beyond this position, the MVR becomes narrower than the MVB, due to the bowshock morphology shown in Fig. 6.12.

Bacciotti et al. (2000) measure, from optical observations in [OI] taken with HST, a width of $\sim$0.18″ at a distance of 0.2″ for the low velocity component. The high velocity is hardly resolved with a width less than 0.1″ at the same distance. At this distance from the star, the atomic iron emission has similar widths in both the high and medium velocity components, $\sim$0.1″. Dougados et al. (2000) measure a FWHM of 0.21″ at 0.4″ from the star for [OI] observations, higher than our estimations at the same distance for the star. I note that this comparison must be considered only qualitatively since the values given in Dougados et al. (2000) and those shown here, are not subtracted by the PSF FWHM. However, the high velocity component has widths and opening angles comparable to those shown in Fig. 3 of Dougados et al. (2000) for RW Aur (OA of 3.9°) and CW Tau (OA of 3.3°) within the first 100 AU. In contrary, the iron medium velocity component is less collimated, with an opening angle of 23°, much higher. RY Tau widths, shown in Ch. 5, are also more comparable to those of the high velocity component in the iron emission than the medium velocity. In particular, the opening angle of 5° derived for the RY Tau microjet is also more similar to the OA measured in the first 0.8″ (112 AU) from the star for the HVB.

In the assumption of a disc wind and that the magnetic streamlines are opening with the distance to the source, these measurements give some constraints on the launching radius of the flow. The observed FWHM of 0.2″ at a distance to the star of 0.1″ in the $H_2\lambda2.12\mu$m indicates that the molecular flow, if tracing a wind, originates from a disc radius <0.1″=14AU. The constraint on the launching radius is more stringent on [FeII] emission for which the FHWM is less than 0.08″ ($\sim$10AU) for the same distance to the star, imposing then a launching radius less than 5 or 6 AU which is compatible with the limit already imposed by rotation studies in the optical of $\leq$ 3AU (Bacciotti, 2002; Anderson et al., 2003; Pesenti et al., 2004).

Jet wiggling

At high velocities, in the blue side of the atomic jet (HVB), variations of jet centroid position derived from Gaussian fits to the transverse intensity profile in the HVB map are observed, suggesting jet wiggling indicative of possible small scale jet axis oscillation. Left panel in Fig. 6.17 shows a zoom in the respective channel map (before and after deconvolution), the stars mark the centroid position at each distance to the star in the more collimated region. Right panel shows in detail these centroid measurements as a function of the distance to the star. Taking this region as the limits of a sinusoidal vari-

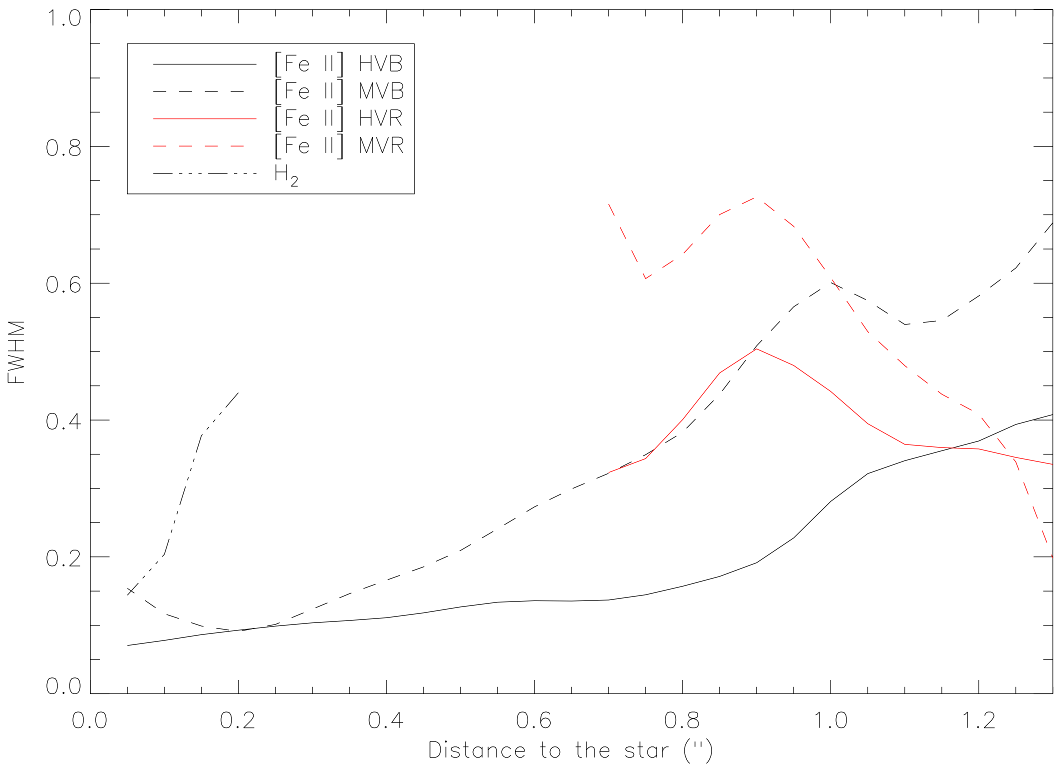

Figure 6.16: Jet width for both the [FeII] and the H_2 emission, respect to the projected distance from the star, derived from deconvolved channels maps of Fig. 6.12. Atomic HVC is in solid line and the MVC is in dashed line (black for the blue jet and red for the red one). H_2 width is in dashed double-dotted line.

ation, a wavelength of 1.2″ is derived. Assuming a jet velocity of 300 km/s at Taurus cloud distance (140 pc), a correspondent timescale of 3 yrs is derived. See the discussion section below for a discussion of a possible origin for this variation.

6.3.2 Kinematics

Centroid velocity maps

In order to have a 2D overall view of the kinematics of the emission, both atomic and molecular one, a one-component Gaussian fit was performed in each spectra, at each spatial position. Actually, two kinematical components are identified in the atomic jet with different properties and morphology, as was shown in the previous section. However, a global two-component Gaussian fit was not performed because the spectral resolution is not enough to well separate both components coherently. The resulting maps of centroid velocity and FWHM are shown in Fig. 6.18 for the atomic jet and in Fig. 6.19 for the molecular emission. Only the spectra with SNR higher than 5 at the line peak are plotted.

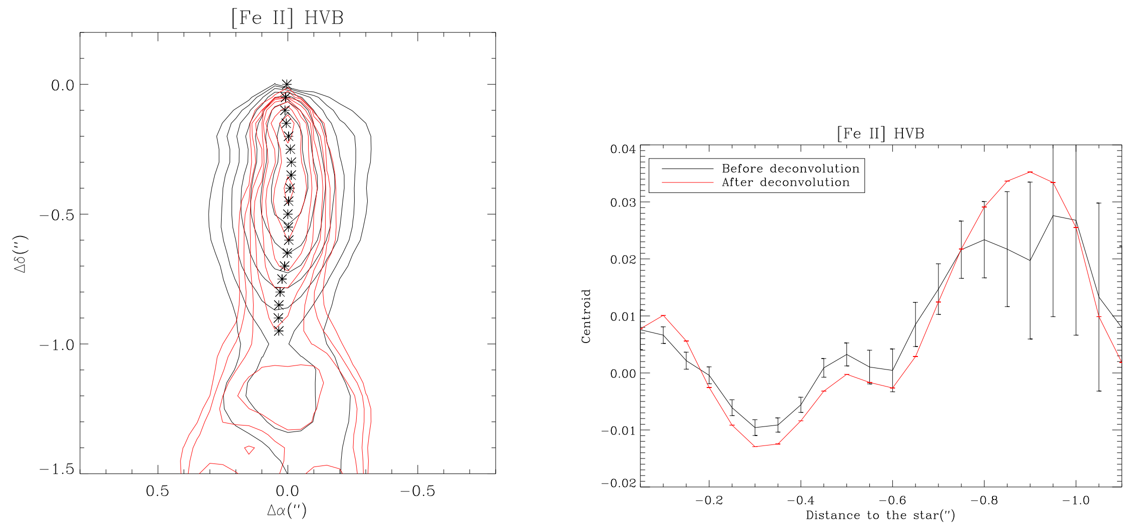

Figure 6.17: Left: HVB channel map, before deconvolution in black and after deconvolution in red. Stars mark the centroid position derived from a Gaussian fit to the transverse profiles. Right: The centroid positions in arcseconds as a function of the distance to the star, marked as stars in the left panel.

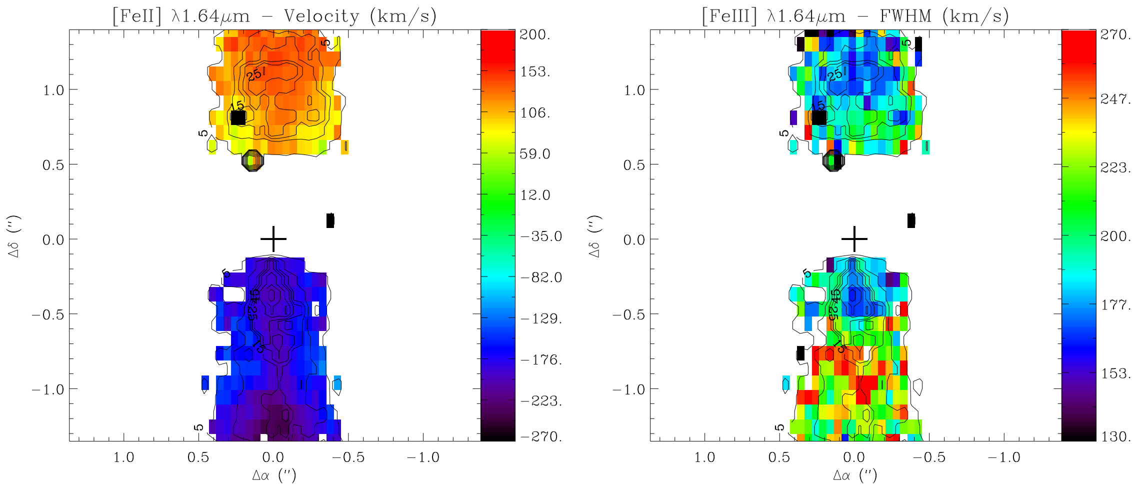

Figure 6.18: Maps of the centroid radial velocity (left) and velocity width (right) resulting of a one-component Gaussian fit to the [FeII]λ1.64μm line on each individual spectra. Contours give SNR at the line peak from 5 to 65 by step of 10. Only the spectra with SNR higher than 5 are shown. The cross marks the position of the star.

Following the same kind of calculation, based on photon noise statistics, carried out in the analysis of the RY Tau kinematics (Ch. 5), for a SNR $\geq$ 5 and FWHM between 170 and 250 km/s, observed in the blue atomic emission, the uncertainty in the centroid velocity derived from the Gaussian fit is $\leq$ 14-21 km/s. In the case of the molecular emission, it is typically less than 3 km/s for the typical FWHM of 100 km/s observed over the whole emission region and considering the uncertainty in the velocity calibration.

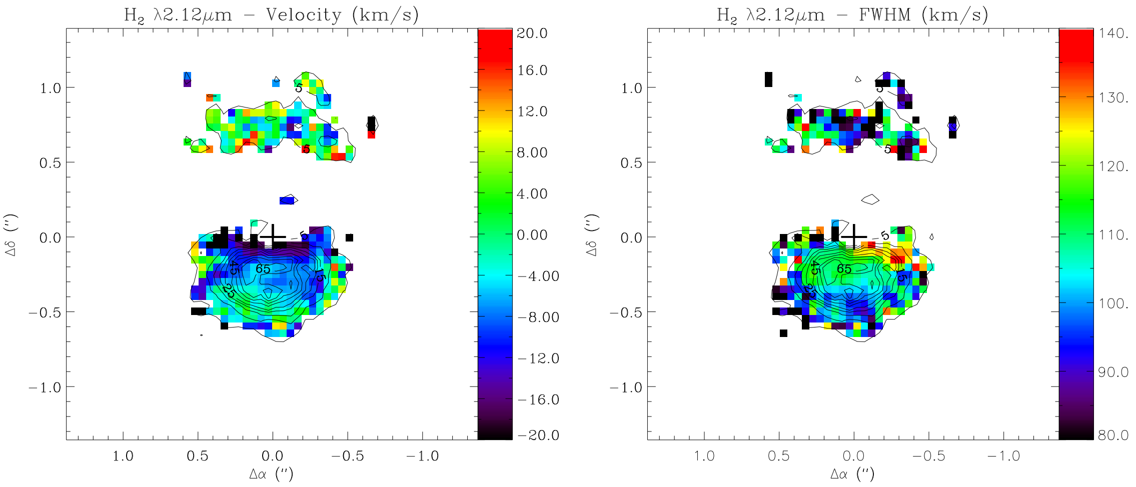

Figure 6.19: Same as Fig. 6.18 but for the $H_2\lambda2.12\mu m$ emission line.

Despite the fact that the on-component fit gives an average value between the two kinematical components identified, the centroid map for the blue [FeII] shows that the higher velocities (∼ 200 km/s) are concentrated towards the axis of the jet, corresponding to the HVB, and the external parts would correspond to the MVB with lower velocities of ∼ 130 km/s. This behavior is compatible with the fact that the high velocity component is more collimated and likely nested by the lower velocity component, as shown by the channel maps in previous section (Fig. 6.12). A peak in velocity is seen at the same position of the emission knot observed in the HVB channel map, at 1.2″ from the star. The profile width is between 220 and 250 km/s at distances further than 0.5″ and it becomes narrower at distances closer to the star, about 170 km/s. The SINFONI spectral resolution in the H Band is 110 km/s, thus the [FeII] emission in the blueshifted emission is spectrally resolved.

The red counter-jet shows a more uniform distribution with velocities of 125-150 km/s, being thus dominated by the HVR component. The profile is in general narrower than the blue jet and it reaches widths of 170-180 km/s at the position of the emission knot seen at 1.1-1.2″ in the high velocity red component.

The molecular emission shows a FWHM of ∼100 km/s over the whole emitting region, both in the blue and red sides of the emission, which means that part of the emission is resolved (SINFONI average spectral resolution in the K Band is ∼70 km/s). However, the emission is affected by the particular SINFONI spectral point spread function (PSF) shown in Fig. 6.20 which changes significantly for different regions in the detector. I also show an average H_2 profile simulating the same long-slit characteristics of the profile shown in Takami et al. (2004). We found that the resulting profile is quite similar to that of Takami et al. (2004) with similar centroid velocity. We are then confident in the centroid estimation from a Gaussian fit, but with a better spectral resolution of ∼30 km/s,

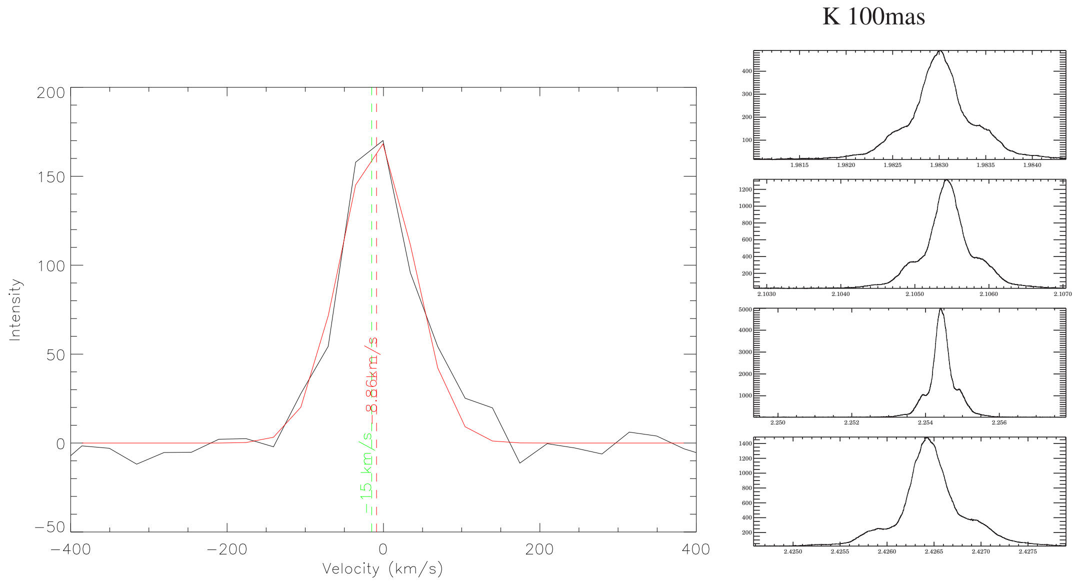

Figure 6.20: Left: Average profile of the H_2 emission, simulating the long-slit observations by Takami et al. (2004). The Gaussian fit to the profile is over-plotted in red. The radial velocity of -15 km/s observed Takami et al. (2004) and the centroid velocity from the Gaussian fit (-9 ± 3 km/s) are also shown. Right: SINFONI spectral PSF in the K band for the plate-scale used in our observations and for different regions on the detector.

Takami et al. (2004) marginally resolved the line, preventing us to definitively affirm that the molecular emission is resolved.

The centroid velocity map shows higher blueshifted velocities close to the star, of (-15)-(-20) km/s very close to the star and of -4 km/s in the "cavity" region. Further, the centroid velocities are compatible with 0 km/s, the same as in the emission which would correspond to the red counterpart. Beck et al. (2008), using NIFS at the Gemini Telescope and with R∼5300, also show kinematical maps of the $H_2\lambda2.12\mu$m line for DG Tau, but they calculate the velocity barycenter and dispersion instead of performing a Gaussian fit. Their map shows a median velocity of -2.4 ± 18.4 km/s over the whole emitting region, compatible with the median of -4.8 ± 7.5 km/s obtained from the Gaussian fit.

Kinematics along the jet axis

Atomic jet:

Figure 6.21 shows a position-velocity (PV) diagram along the jet in the [FeII]$\lambda1.64\mu$m line, assuming a 1″ pseudo-slit and sampling every 0.1″ along the jet. White contours limit the region with SNR higher than 3 and crosses mark the centroid velocity derived from one-component Gaussian fits to the line profiles. At distances to the star of ± 0.2″ the residuals from the stellar continuum subtraction are very important and this region is also delimited by a dotted-dashed line.

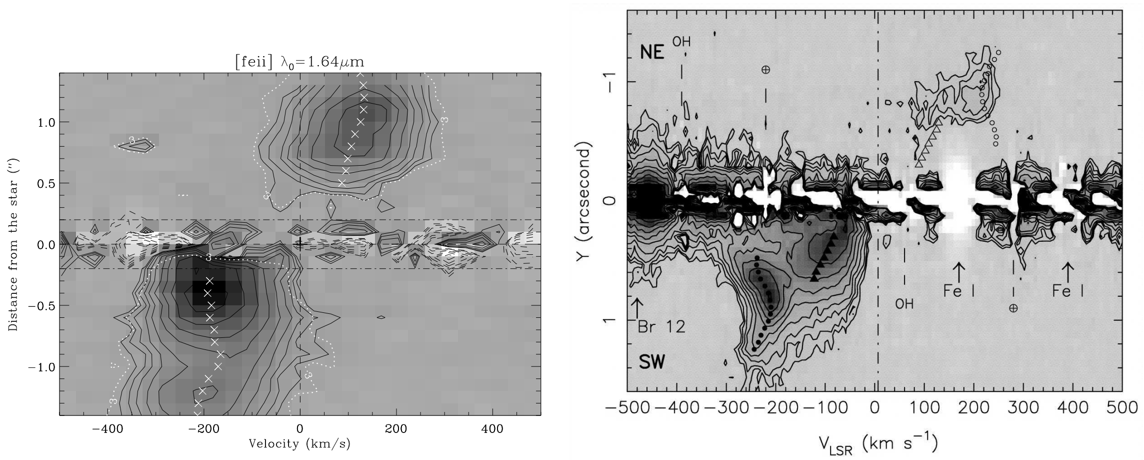

Figure 6.21: Left: Position-velocity map in the [FeII]λ1.64μm line, after continuum subtraction, for a 1″ wide pseudo-slit and sampled every 0.1″. Contours start at 2.43$\times$10^{-15} W m$^{-2}\mu$m^{-1}(″)$^{-2}$ and increase by factors of $\sqrt{2}$. Negative contours are shown with dashed lines. The white contour shows the SNR=3 level calculated on each average profile and crosses show the centroid velocity derived from a Gaussian fit. At distances ±0.2″, the PV are very affected by continuum subtraction residuals. Right: PV diagram shown by Pyo et al. (2003) for comparison, see text.

The blue jet emission is dominated by the high velocity component. It shows an average centroid velocity of ∼-190 km/s and two emission knots, one at -0.4″ from the star and the other at -1.2″. These two knots were already identified in the HVB channel map, Fig. 6.12. The knot at -1.2″ is faster than that at -0.4″, with a centroid velocity of -203 km/s, instead of -192 km/s for the second one. It is also wider in velocity, probably due to the contribution of the two symmetric knots observed in the MVB at this position in the corresponding deconvolved channel map. The MVB would contribute more at the PV diagram at distances of ∼0.9-1.0″.

The red lobe is also dominated by the HV component with an average centroid velocity of 115.8 km/s. The centroid radial velocities progressively decrease closer to the star. It shows a peak in velocity at 1.2″ from the star, symmetrically placed to the faster knot in the blue side, but with lower centroid velocity by a factor of 1.5, showing a velocity of 130 km/s.

Pyo et al. (2003) show a position-velocity diagram of the DG Tau microjet, obtained from long-slit IRCS observations (slit-width=0.3″) at Subaru Telescope, with a similar spatial resolution of 0.16″ but with a much better spectral resolution (R∼10 000) (Right panel in Fig. 6.21). They clearly detect two distinct velocity components with similar peak intensities. Their low velocity component, detected between ∼0.24″ and ∼0.7″ from the star, shows an average velocity of -100 km/s, similar to the center of the MVB interval identified in Fig. 6.12. Their high velocity component shows a distinct peak in the PV profiles between ∼0.4″ and ∼1.2″, with an average velocity of -220 km/s, which corresponds well with the center of our HVB interval. The average centroid velocity of -190 km/s, observed in Fig. 6.21, is in fact between the two velocity components detected by Pyo et al. (2003).

Pyo et al. (2003) also detect the red counter-jet at 0.7″ with velocities between 80 and 240 km/s and a peak of 200 km/s at 0.9″, but ten time weaker than the blue emission. The red peak emission in Fig. 6.21 occurs at 1″ from the star, but it shows a lower velocity of 125 km/s and an intensity only twice weaker than the blue peak at -0.4″ in the blue jet. This is mainly because we use a wide 1″ slit and the red lobe is broad.

I note that, even if similar knot velocities are observed between Pyo et al. (2003) and our observations, it is difficult to relate the two PV diagrams because the knots seen by them should have moved out of our field since the proper motion observed in the optical is 0.3″ and in four years, the gas have moved 1.2″.

Molecular emission:

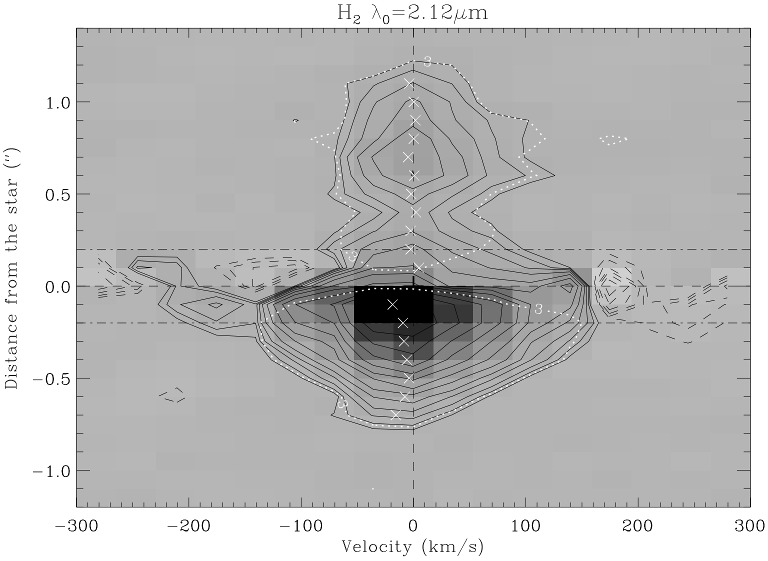

Figure 6.22: Position-velocity map for the $H_2\lambda2.12\mu$m line for a pseudo-slit of 1″ width and sampling every 0.1″. Contours start at 1.72×10^{-15} W $m^{-2}\mu m^{-1}('')^{-2}$ and increase by factors of $\sqrt{2}$. White contours and crosses are the same as in Fig. 6.21.

Figure 6.22 shows the position-velocity diagram for the $H_2\lambda2.12\mu$m line. In the blue-side emission, the average radial velocity is -7 km/s, excluding the point at -0.1″ from the star which shows a radial centroid velocity of -19 km/s. At this position, a peak in intensity is also shown. The wings at high velocities, ± 100 km/s are not real, they are part of the SINFONI spectral profile. The average profile width is of 88 km/s, at the resolution limit of 70 km/s.

The red-side of the diagram shows on average a radial velocity also very slightly blueshifted, with an average of -1 ± 2 km/s. There is a intensity peak at the base of the bowshock seen in [FeII] shown in the channel map (Fig. 6.12), at $\sim$0.7″. At this same position, a maximum in velocity is observed, but blueshifted, with a radial centroid velocity of -4.7 ± 2.7 km/s (the velocity calibration uncertainty).

However, the H_2 2.12μm emission is compatible with a zero velocity, as found by Beck et al. (2008), except for the bright H_2 2.12μm peak of $\sim$-18 km/s at -0.1″ into the blue jet. This peak is similar to that seen by Takami et al. (2004), using long-slit observations. They found a radial velocity of -15 ± 4 km/s integrating the outflow emission within ± 1.2″. Moreover, integrating in velocity, they found that the position of the emission is displaced 0.2″ towards the blueshifted flow.

Transverse position-velocity diagrams

In order to study the jet kinematics in the direction perpendicular to the jet axis, I show, in Fig. 6.23, transverse position-velocity diagrams of the [FeII]λ1.64μm and $H_2\lambda$2.12μm emission, and for several distances along the blueshifted jet, from 0.2″ to 0.5″. Beyond this distance, the H_2 is too weak. The velocity centroid obtained from a single-component Gaussian fit is indicated with asterisks and the SNR=3 limit is represented as a dotted contour.

Following the behavior shown in the position-velocity diagrams along the jet, the average centroid velocities for the iron emission are $\sim$-190 km/s, $\sim$-174 km/s through the four graphics. The average centroid velocities for the molecular hydrogen are $\sim$-5 to -7 km/s. In the case of the iron emission, the intensity peak is well centered in the jet axis, but in the case of the H_2, the peak is shifted 0.05″ from the jet axis for the four distances except for the plot at $d_{//}$=0.3″ where the shift is of 0.2″ because of the existence of the cavity.

The very different width and centroid velocity of [FeII] compared to $H_2\lambda$2.12μm seems to suggest no direct interaction between the two flow components as it was already noted by Takami et al. (2004) from their molecular observations in $H_2\lambda$2.12μm and also observed in HL Tau (Takami et al., 2007).

However, Fig. 6.24 shows the same plot as in Fig. 6.23 for a distance to the star of 0.3″ but adding the position-velocity at the same distance for [OI]λ6300Å, shown in Coffey et al. (2008) and kindly provided by Dr. Coffey. The top panel shows iron emission in black, compared to the H_2 emission in blue and in the bottom panel I compare [OI] emission and H_2. Black asterisks correspond to the centroid velocity obtained from a Gaussian fit to the [FeII] and the [OI] PV, and the blue ones correspond to the H_2. The Gaussian fit was carried out taking into account only one component when the [OI] shows two distinct components but it gives the value related to the dominant component.

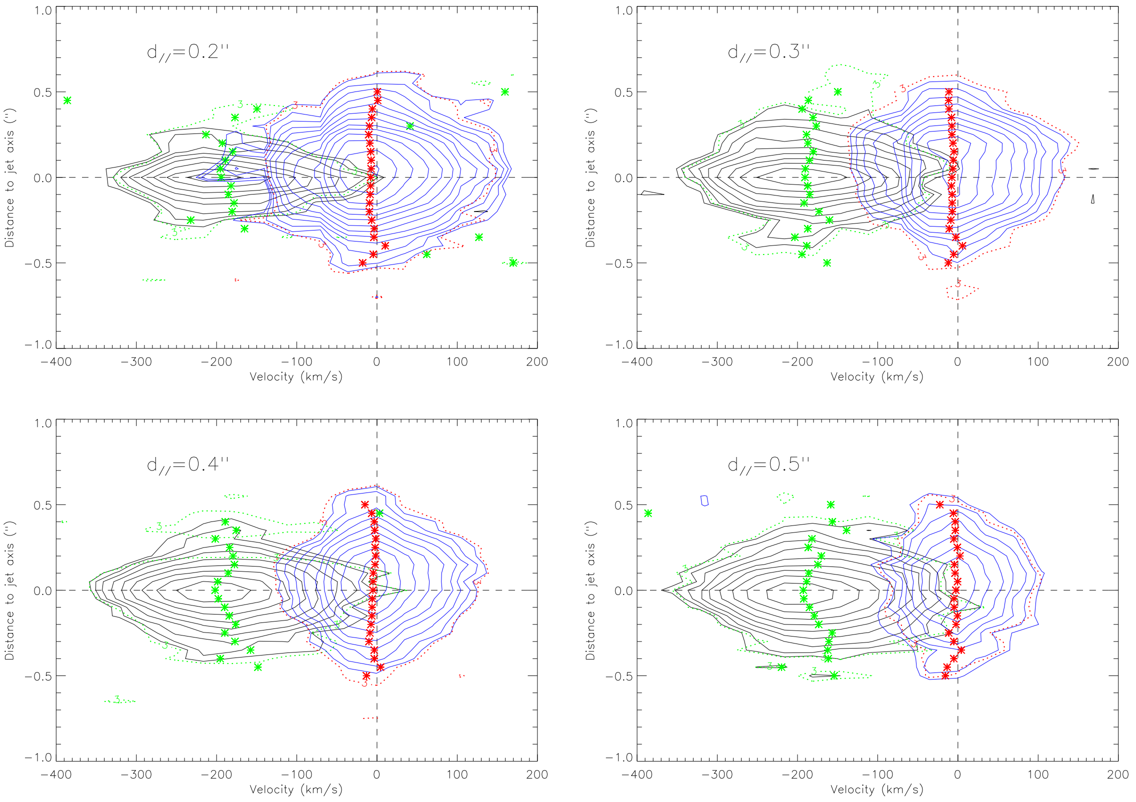

Figure 6.23: Transverse position-velocity diagram for distance to the star of 0.2″, 0.3″, 0.4″ and 0.5″. Iron is plotted in black and H_2 in blue. Centroids velocities from an one-component Gaussian fit are also plotted as green asterisks for the [FeII] and in red for the molecular emission. The dotted-line contours mark the SNR=3 limit. Emission up to ±100 km/s in H_2 are artefacts of spectral PSF of SINFONI.

From Fig. 6.24, it is evident that the transverse structure between the two atomic emissions, [FeII] and [OI], are different, being the iron emission more confined at high velocities. However, more remarkably is the fact that there is [OI] emission showing intermediate velocities filling the space between the [FeII] and the H_2 emission, and also that there is another component at low velocities, coincident in position and velocity with the H_2 emission, relating kinematically the [FeII] and H_2 components. Close to the jet axis the two atomic components have similar velocities whereas beyond 0.2″, the oxygen shows in fact the same velocities as the molecular component. Previous observations of the DG Tau jet in [OI] and [SII] had already showed a low velocity component with radial velocities dropping from -60 km/s on-axis to -30 km/s at 0.25″ (Bacciotti, 2002; Coffey et al., 2008). The velocity and transverse extent, intermediate between [FeII] and H_2 2.12μm, suggest that it might trace a "wide-angle" atomic flow surrounding the fast atomic jet and filling the H_2 2.12μm molecular "cavity". The [OI] at the same velocities as H_2 could be a different component. In fact, Lavalley et al. (1997) revealed the existence of a faint "halo" in [OI] with radial velocities of ∼-15 km/s which could be associated with the H_2 emission.

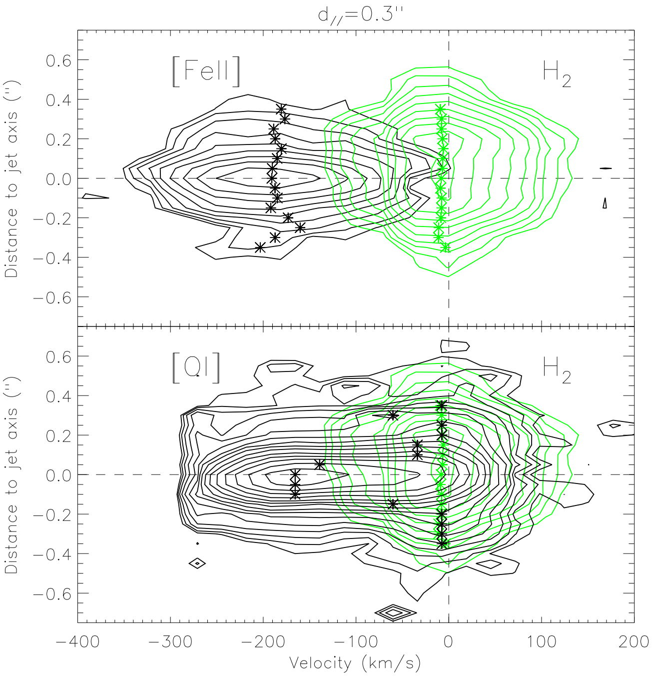

Figure 6.24: Top panel: Transverse PV diagram for the [FeII]$\lambda1.64\mu$m in black, $H_2\lambda2.12\mu$m in green contours. Bottom panel: [OI]$\lambda3600$ (data from Coffey et al. (2008), provided by Dr. Coffey) in black contours and $H_2\lambda2.12\mu$m in green contours. Centroid velocities from an one-component Gaussian fit are shown with asterisks (black for the iron and the [OI], green for the H_2.

6.3.3 Br_γ extent and luminosity

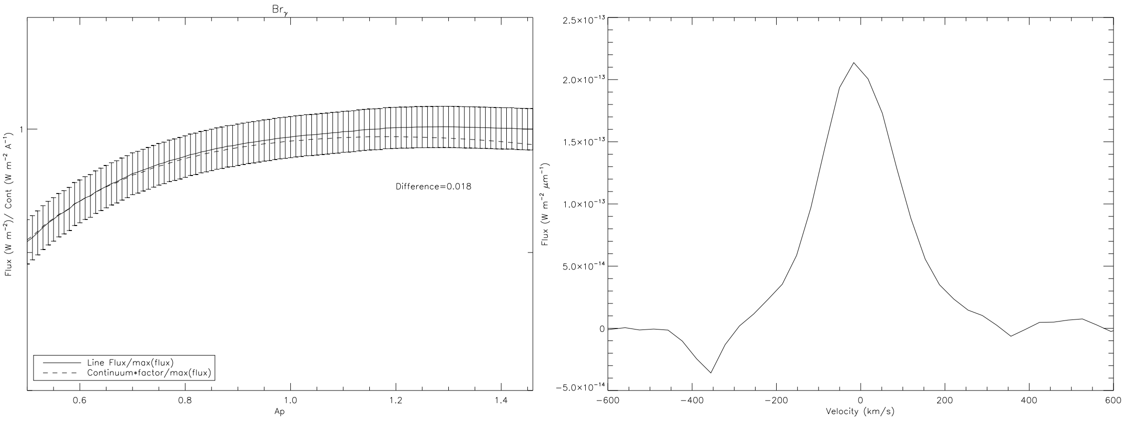

Figure 6.25: Left: Br_γ flux integrated in different aperture radius (solid line), compared to its local continuum (dashed line). Both curves are normalized to the maximum emission in Br_γ and the continuum curve is normalized to Br_γ one at small apertures. Right: Br_γ profile integrated in an aperture of 1.46″. This profile is integrated to derive the line luminosity.

Br_γ luminosity will be used to determine the mass accretion rate (see Sec. 6.4.4) and its contemporaneous measure with the mass ejection rate will allow a more reliable ejection-accretion ratio estimation than previous ones. Before obtaining the mass accretion rate, I further investigate the spatial extension of the Br_γ emission. Figure 6.25-left shows the luminosity measured in the Br_γ emission line for different integrating aperture radius, comparing to its local continuum. It shows the Br_γ flux in solid line and in dashed line the continuum emission multiplied by a factor of $\sim$5.6 to put it at the same level as the line emission for the first apertures. Both curves are normalized to the Br_γ flux measured with an aperture of 1.46″. The figure indicates that less than 2% of the Br_γ emission is resolved, thus the emission is dominated by shock accretion emission justifying its use in the accretion luminosity estimation.

The Br_γ luminosities were calculated by integrating over the whole line emission and over a circular aperture of radius 1.46″ (Fig. 6.25-right) as it was done to calculate the total standard star flux to carry out the flux calibration. I derive a Br_γ luminosity of 2.2×10^{-4} $L_\odot$ which is a factor 3-4 lower than that derived by Muzerolle et al. (1998b). This discrepancy comes directly from the method they use to estimate the Br_γ luminosity. Muzerolle et al. (1998b) obtained it from their measured equivalent widths and from the non-simultaneous mean photometric magnitudes given by Kenyon & Hartmann (1995). Muzerolle et al. (1998b) measure an equivalent width of 14.1Å, 2.5 times higher than ours of 5.6 Å. In addition, a factor a little higher than 1 in the photometric magnitude (6.74±0.19 used by Kenyon & Hartmann (1995) and 7.097 measured in our data) traduces in the final factor of 3.4 in the line luminosity.

6.3.4 Jet electron density

The IFS allows a two dimensional study of the electron density distribution from the [FeII]λ1.53/1.64μm ratio, being possible to study it, not only as a function of the distance to the star, as was done in traditional long slit spectroscopy, but also in the perpendicular direction to the jet axis. No significant difference is observed between the wings of the iron lines and a single value of electron density was calculated for the two kinematical components. For that, at each spatial point, we integrated both [FeII] lines spectrally, over the whole line. To convert our measured ratios to density values, we used the calculations carried out by Pesenti et al. (2003). They take into account only the first 16 levels of the Fe^+ atom, it is a simplified model but that gives a very good approximation of the level population distribution for excitation temperatures below 2×10^4 K. Fig. 6.26 shows the electron density distribution in both sides of the jet. The red counter-jet is more uniform than the blue jet with a value of $\sim 10^4$ cm^{-3}, even if there is a light asymmetry in the perpendicular direction to the jet axis, the electron density is higher for $\Delta\alpha > 0''$. We found the same asymmetry in the blue jet but in fact the blue jet shows a more complex structure. Close to the star, for distances less than 0.7″, a striking difference in n_e of about a factor 10 is observed between $\Delta\alpha > 0''$ and $\Delta\alpha < 0''$, one side being above the high density limit. On the contrary, far from the star, at distances higher than

1″ the jet shows values similar to that on the red counter-jet of $\sim 10^4$ cm^{-3} with also a faint asymmetry from West to East. If we now look along the jet axis, we observe that electron density decreases with distance, as we expected from previous studies in this star and other T Tauri stars (e.g. Lavalley-Fouquet et al., 2000; Bacciotti, 2002; Hartigan & Morse, 2007). This behavior is even clearer in the top panel of Fig. 6.31 shown in the next section, where we integrated also spatially in the transverse direction simulating a 1″ wide long slit observation and with a sampling of 0.1″. A deeper discussion of this figure and the electron density behavior with distance will be presented in the next section.

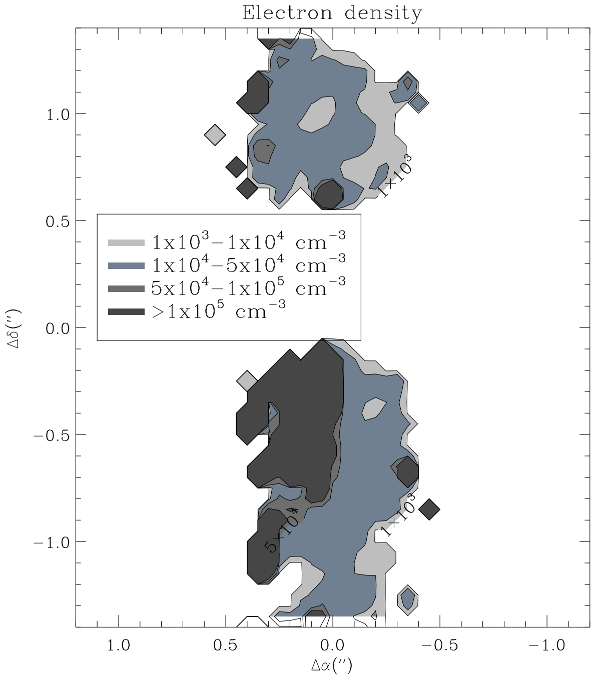

Figure 6.26: Electron density distribution in both the blue and red jet, obtained from the [FeII] $\lambda 1.53\mu$m/$\lambda 1.64\mu$m ratio and using the calculations of Pesenti et al. (2003). Close to the star, at the East we do not plot contours higher than 1 x 10^5 cm^{-3} because electron density in this region reach the high density limit of 5 x 10^5 cm^{-3}.

6.3.5 Column densities and mass of molecular emission

As I have already mentioned in Sec. 3.6.2 the flux-calibrated images in $H_2\lambda 2.12\mu$m can be converted into column densities in the upper level of the transition (V=1, J=3) through $N_{1,3} = F_{1-0S(1)} \times (4\pi)/(h\nu_{ul}A_{ul}) = 3.8 \times 10^{19} cm^{-2}(F_{1-0S(1)}/ergs^{-1}cm^{-2}sr^{-1})$. Assuming LTE at a temperature of 2000 K (as indicated by H_2 line ratios in DG Tau, (Beck et al., 2008)) the total column density of hot H_2 gas is given by $N_{H_2} = N_{1,3}/1.28 \times 10^{-2}$ (Takami et al., 2004). Hence, for a $H_2\lambda 2.12\mu$m line brightness of 0.013 erg s^{-1}cm^{-2} sr^{-1} at the peak of the image, placed at 0.1″ from the star, the corresponding total H_2 column density at 2000 K is 3.8$\times 10^{19}$ cm^{-2}. A column density of 9$\times 10^{18}$ cm^{-2} for the brightness averaged over the detected part of the blue lobe of 3$\times 10^{-3}$ erg s^{-1}cm^{-2} sr^{-1}.

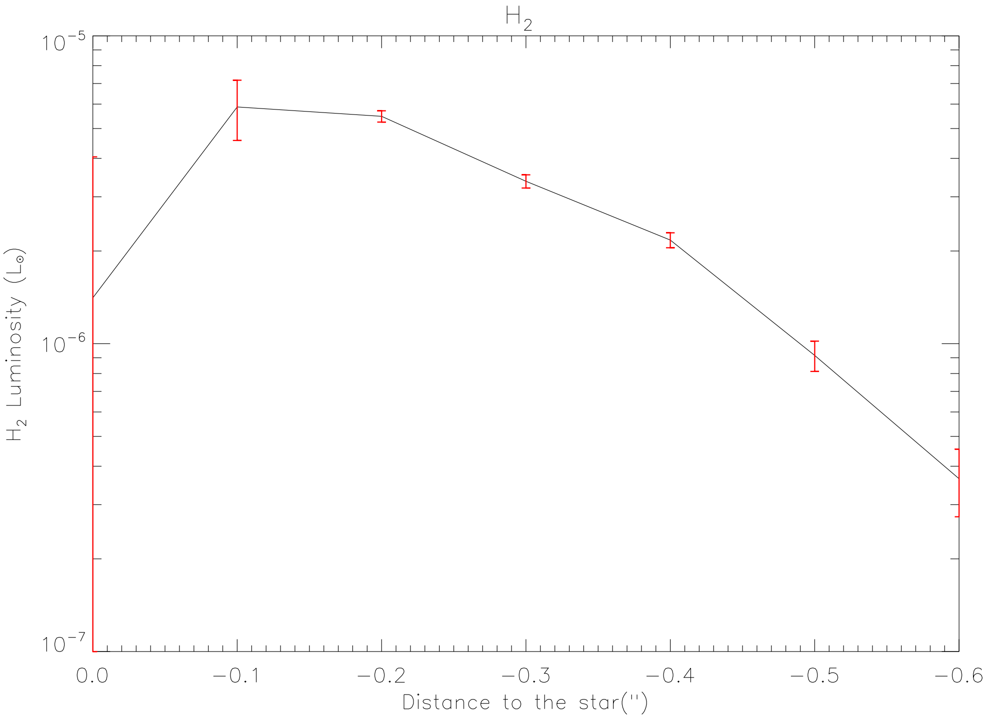

Figure 6.27: H_2 luminosity integrated over a pseudo-slit width of 1″ and sampled every 0.1″, plotted errors are at 3σ. A peak is observed at 0.1″ from the star and then it decreases with distance. The mass of H$_2$ (Eq. 3.45) and the mass-loss rate, in the case of volume emission, are proportional to the line luminosity.

Figure 6.27 shows the H_2 luminosity as a function of the distance to the star. The emission shows a peak at 0.1″ and then it decreases gradually with distance. The total luminosity integrated in the whole 0.5″ emitting region is 1.9×10^{-5} L$_\odot$ in good agreement with the value found by Takami et al. (2004). Therefore, using Eq. 3.45, the total mass of hot H$_2$ at 2000 K, assuming ELT, is 3×10^{-8} M$_\odot$.

6.4 Interpretation

6.4.1 Origin of jet wiggling

We investigate two possible scenarii for the observed wiggling of the DG Tau jet axis following the discussion conducted by Anglada et al. (2007) for the HH 30 jet: orbital motion of the jet source in a binary system and jet axis precession induced by a companion in a non-coplanar orbit with the jet source disc. We will assume circular orbits and use the same terminology as Anglada et al. (2007). Let m_1 be the mass of the jet source, m_2 the mass of the companion and $m = m_1 + m_2$ the total mass of the system. Let μ be the mass of the companion relative to the total mass, so that:

$$m_1 = (1-\mu)m, \quad m_2 = \mu m. \tag{6.3}$$

Let a be the binary separation. The orbital radius r_0 and orbital velocity V_0 of the jet source with respect to the system's center of mass are then given by: $r_0 = \mu a, V_0 = \frac{2\pi r_0}{\tau_0}$, where τ_0 is the orbital period. The total mass of the binary system can be expressed as:

$$\frac{m}{M_\odot} = \mu^{-3}(\frac{r_0}{AU})^3(\frac{\tau_0}{yr})^{-2} \tag{6.4}$$

6.4.2 Orbital motion of the Jet source

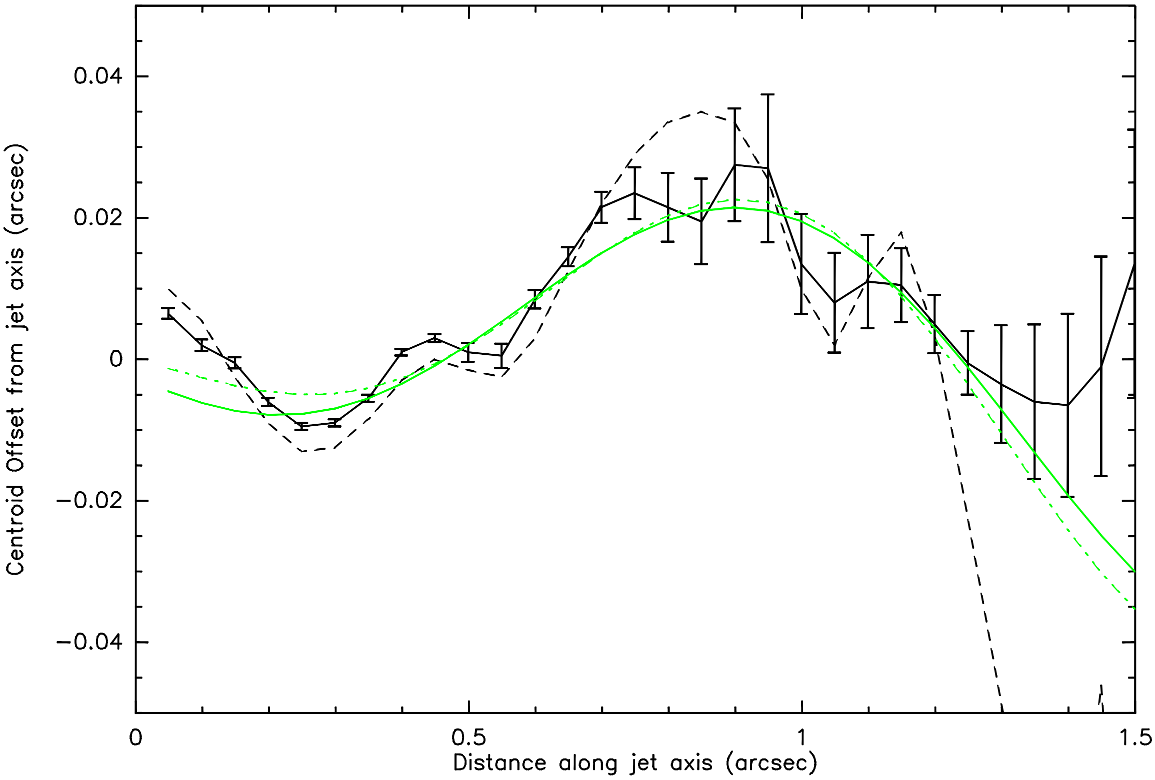

Figure 6.28: Observed wiggling in black, fit to an orbital motion in solid green line and to a jet axis precession in dot-dashed green line.

We first investigate the case of jet wiggling produced by orbital motion of the jet source. Eq.(8) of Anglada et al. (2007) gives the shape of the jet in the plane of the sky as a function of the observable parameters α, half-opening angle of the jet in the plane of the sky, and λ, observed angular period of the wiggles in the plane of the sky. These parameters are related to the orbital parameters of the jet source in the following way:

$$\frac{V_0}{V_j} = \tan\alpha \times \cos\phi, \quad r_0 = \lambda \times \tan\alpha \times D/2\pi \tag{6.5}$$

where V_j is the jet flow velocity, ϕ the inclination angle of the jet axis with respect to the plane of the sky and D the distance to the source. Applying a $chi2$ minimisation procedure, we derive the best fit of the observed shape of the DG Tau microjet for $\alpha = 1.35°$ (full opening angle of 2.7° and $\lambda = 1.72''$, which gives $r_0 = 0.9$ AU (Fig. 6.28). Using a radial velocity of 200 km/s and a jet inclination angle of 45°, we derive an orbital velocity $V_0 = 4.7$ km/s and an orbital period $\tau_0 = 5.75$ yr.

If we use an additional constraint on the mass of the most massive component, we can further constrain the mass and separation of the binary components. Hartigan et al. (1995) derive a mass estimate of 0.67 $M_\odot$ from a spectral type K5V and a stellar luminosity of 1.7 $L_\odot$. The recent study by White & Hillenbrand (2004) has revised the DG Tau mass estimate to 2.2 $M_\odot$ from high-resolution optical spectroscopic observations. White & Hillenbrand (2004) derive a spectral type of K3V and a stellar luminosity of 3.6 $L_\odot$ leading to this higher mass estimate. The origin of the discrepancy between these two mass estimates for DG Tau is not clear to us. Therefore, we take a conservative estimate of the primary mass between 0.5 and 2 $M_\odot$. If we use the additional constraint that the mass of the most massive component is in the range 0.5-2 $M_\odot$, we derive from Eq. 6.4 and Eq. 6.4.1 that μ is in the range 0.2-0.3 and the binary separation, $a = r_0/\mu = 3$-4.5 AU. The jet source would then be the primary component of the binary system and the mass of the companion is in the range 0.15-0.4 $M_\odot$.

A stellar companion with projected separation in the range ∼20-30 mas could have escaped detection since these scales are below the best angular resolutions achieved by single apertures in the optical and near-infrared domains ($\simeq 0.1''$). A companion within the FOV of the Keck interferometer (50 mas in the K band) could account for the low visibility observed ($V^2 = 0.37 \pm 0.02$) for DG Tau in the K band (Colavita et al., 2003). Lunar occultation observations conducted by (Leinert et al., 1991; Chen et al., 1992) detect an extended component at 2.2μm with FWHM=45 mas and flux contribution of 20.25%. It is not clear how this extended component would be related to the inferred companion. The companion could have escaped also lunar occultations since these observations probed three position angles spanning roughly 40°.

6.4.3 Jet axis precession

We investigate below the case where the observed jet wiggling is due to jet axis precession induced by tidal interaction between the disc and a companion in a non-coplanar orbit. In that scenario, the jet is assumed to originate from the circumstellar disc. Equation 13 of Anglada et al. (2007), derived from Masciadri & Raga (2002), gives the shape of the jet in the plane of the sky as a function of α and λ. The best fit of the observed DG Tau jet wiggling with this equation is obtained for $\alpha = 1.49°$ and $\lambda = 1.52''$. These observable parameters are related to the precession angle β and the precession period τ_p with the following relations:

$$\begin{aligned} \tan\beta &= \tan\alpha\cos\phi \qquad (6.6) \\ \tau_p &= \tfrac{\lambda D}{V_t cos\beta}, \qquad (6.7) \end{aligned}$$

where V_t is the tangential jet velocity ($= V_j\cos\phi$). From the above solution we derive the precession angle $\beta = 1.046°$ and the precession period $\tau_p = 5.066$ yr. With additional assumptions, it is possible to further constrain the orbital parameters of the companion. Assuming an outer disc truncation radius of $r_d \simeq 1/3a$, equation (14) of Anglada et al. (2007) gives the orbital period of the jet source τ_0 as a function only of τ_p and μ, the ratio of the companion mass to the total mass of the system. Combining this with Eq. 6.4, the total mass of the system can be expressed as a function of V_0, the orbital velocity of the jet source, and μ only:

$$m = 2.910^{-6} M_{\odot} \tau_p \times \cos\beta \times V_0^3/(\mu^2 \times \sqrt{1-\mu}). \qquad (6.8)$$

A maximum value for the orbital velocity of the jet source, V_0, is obtained from the requirement that the angular effect produced by the orbital motion of the jet source is smaller than the derived precession angle, ie $\frac{V_0}{V_j} < \tan(\beta)$. In the DG Tau case, we get $V_0 < 5.17$ km/s. It is possible to further constraint μ and a by combining this with a constraint on the mass of the primary. The jet source mass is given by $m_1 = m \times (1-\mu) \propto v_0^3 \times \sqrt{(}1-\mu)/\mu^2$. If we assume that the jet originates from the primary component (ie $\mu < 0.5$), the requirements that $0.5M_{\odot} < m_1$ combined with $V_0 < 5$ km/s imply $\mu < 0.06$ and a binary separation $a < 0.08$ AU ($a = r_0/\mu \propto V_0/\sqrt{(}1-\mu)$, tends towards a constant value $\propto V_0$ at low μ values). In addition for such low μ values, $m_2 \simeq \mu \times m_1$ so the additional constraint $m_1 < 2$ $M_{\odot}$ translates into $m_2 < 0.07$ $M_{\odot}$. The system would consist of a brown dwarf/giant exoplanet orbiting the jet source at very close separations. However, this solution is not compatible with the initial assumption $r_d/a = 1/3$ since it would imply an outer radius for the primary accretion disc, from which the jet originates, $r_d < 0.03$ AU ! Nevertheless, if one assumes that the jet source is the secondary, the requirement $m_2 > 0.5$ $M_{\odot}$ implies that $m_1/m < 10^{-5}$, i.e. the mass of the jet source would be unrealistically low! So no satisfactory solution seems to be found for the jet axis precession case.

6.4.4 Accretion rate

Different methods exist to estimate the mass accretion rate. The most obvious is from the infrared-excess continuum emission caused by viscous dissipation in the disc, but this is not the only possible source of infrared excess and it is complicated to distinguish between them. A more reliable method consist in measure the blue continuum excess emission observed in CTTs. Recent studies (Calvet & Hartmann, 1992; Edwards et al., 1994; Hartmann et al., 1994; Muzerolle et al., 1998a; Calvet & Gullbring, 1998) support the idea that this blue excess is emitted by an accretion shock produced when disc material following magnetic field lines impacts the stellar surface, being therefore a direct measure of the accretion rate. Another more easily obtainable estimation is from U-band photometry.

The problem with the measurements of the blue excess is that it is possible only in the case of low extinction. Hence, in order to study more reddened objects, an estimation from emission lines at longer wavelengths, therefore less dependent on the extinction measurements, are necessary. Muzerolle et al. (1998b) show that there is a tight correlation between the accretion luminosity and the Br$_\gamma$ line luminosity. Once the stellar parameters are known we can easily calculate the mass accretion rate. They also show the importance of well estimate the extinction in Class I objects to correctly measure the Br$_\gamma$ luminosity. In objects less embedded like T Tauri stars, this correction is less important. Moreover, in the case of DG Tau,Kravtsova (2003) found an upper limit for the extinction in the visible of 0.8 magnitudes, that means an extinction in the K band of only ~0.08 magnitudes (A$_K$ $\sim$ 0.1 A$_V$ (Becklin et al., 1978)). Hence, in the accretion luminosity estimation, I will neglect this factor.

K band data allow a contemporaneous estimation of the accretion rate, from Br$_\gamma$ line luminosity, to compare it with the mass loss rate measured from other emission lines. Using the relation given by Muzerolle et al. (1998b) (Eq. 6.9) to derive the accretion luminosity, the mass accretion rate, $\dot{M}_{acc}$, is easily obtained from the formula for disc accretion (Eq. 6.10) given by Gullbring et al. (1998).

$$log(L_{acc}/L_{\odot}) = (1.26 \pm 0.19)log(L_{Br_\gamma}/L_{\odot}) + (4.43 \pm 0.79) \tag{6.9}$$

$$\dot{M}_{acc} = \frac{L_{acc}R_*}{GM_*}\Big(1 - \frac{R_*}{R_i}\Big)^{-1} \tag{6.10}$$

For Eq. 6.10 I adopt a stellar radius of R_*=2.3 R$_\odot$ and stellar mass of M_*=0.7 M$_\odot$ (Hartigan et al., 1995). R_i is the inner radius of the accretion disc and as in Gullbring et al. (1998) a value of R_i=5 R$_*$ is assumed.

Br$_\gamma$ luminosity derived in Sec 6.3.3 is 2.2×10^{-4} L$_\odot$ that, following Eq. 6.9, gives us L$_{acc}$ = 0.66L$_\odot$, and therefore an inferred mass accretion rate of $\dot{M}_{acc}$ $\sim$ 8×10^{-8} M$_\odot$/yr from Eq. 6.10. However, Hartigan et al. (1995) found a value of the mass accretion rate of 10$^{-5.7}$ M$_\odot$/yr=2×10^{-6} M$_\odot$/yr that is a factor 25 higher than our estimation, taking the same values for the stellar radius and mass. They estimate the mass accretion rate assuming that the hot excess emission is originated in a boundary layer between the accreting disc and the stellar surface. They derive the accretion luminosity assuming that one-half of the emission is absorbed by the star, that the disc does not block any of the photospheric emission and that the boundary layer radiates like a black-body. On the contrary, Gullbring et al. (1998) fit the blue/UV excess assuming a scenario of magnetospheric accretion (Calvet & Gullbring, 1998), more accepted nowadays, which assumes that the excess emission is produced by the shock of the accreting material freely falling through the magnetic field lines when it shocks the stellar surface. They also assume optically thin slab of hydrogen to extrapolate the accretion luminosity from the veiling measurements and then they find less flux than for a blackbody assumption. Gullbring et al. (1998) obtain accretion luminosities and mass accretion rates for 16 stars also studied by Hartigan et al. (1995) and Valenti et al. (1993) and they accomplish a thorough comparison with the values obtained by these two previous works. They find discrepancies in the mass accretion rate of one order of magnitude between Hartigan et al. (1995) and Valenti et al. (1993). The values derived by Gullbring et al. (1998) are closer to those of Valenti et al. (1993) than Hartigan et al. (1995). The main difference is in the accretion luminosity derived which are higher by a factor of 5-6 in Hartigan et al. (1995) estimations. Besides, these discrepancies come from the different assumptions made in the two scenarios but also in the different extinctions adopted which can be up to 0.6-1.0 mag higher in Hartigan et al. (1995). Gullbring et al. (1998) conclude that typical mass accretion ratios in T Tauri stars are between 10^{-9}-10^{-7} $M_{\odot}$/yr and that the magneto-spheric accretion model gives lower estimations than the boundary layer model. A more recent work by Gullbring et al. (2000), also assuming a shock model, gives for DG Tau a $\dot{M}=5\times10^{-7}$ $M_{\odot}$/yr for a $M_{*}=0.5$ $M_{\odot}$, $R_{*}=2$ $R_{\odot}$ and a $A_{v}=1.6$, thus more coherent with our estimations than that of Hartigan et al. (1995).

In the following, we adopt 10^{-7}-5×10^{-7} $M_{\odot}$/yr as the range of accretion rate in DG Tau.

6.4.5 Tentative evidence for iron depletion in the jet

Iron is a refractory specie that in dense cool molecular clouds is found to be depleted in the gas phase due to condensation onto dust grains, thus iron gas phase abundance is a good indication of the dust content in the flow. Several studies have shown that iron is strongly depleted in the jets of young stellar objects (e.g. Nisini et al., 2005). In order to estimate the iron depletion in the DG Tau microjet, a comparison between [FeII] and [OI] luminosities was carried out, this method was first applied by Beck-Winchatz et al. (1994, 1996). Figure 6.29 shows the [FeII]$\lambda1.64\mu$m/[OI]$\lambda6300$ Å ratio which will give an estimate of the iron depletion into the grains, against the [FeII]$\lambda1.53\mu$m/[FeII]$\lambda1.64\mu$m ratio which traces the electron density in the jet. Asterisks mark the theoretical values from the planar atomic shocks by Hartigan et al. (2004) assuming no iron depletion into the dust. Models predict a flux ratio of ~1 when the density tracer is close to the high density limit, ie., close to the star. Triangles show the observational measurements with the [OI] luminosities obtained from Lavalley-Fouquet et al. (2000).

In order to minimize the effect due to the time between [FeII] and the [OI] observations, obtained in 2005 and 1998 respectively, I compare the [OI] observations with the [OI] luminosity obtained from the transverse PV diagram by Coffey et al. (2008), observed in 2003. The transverse PV was obtained at a distance to the star of 0.3″,

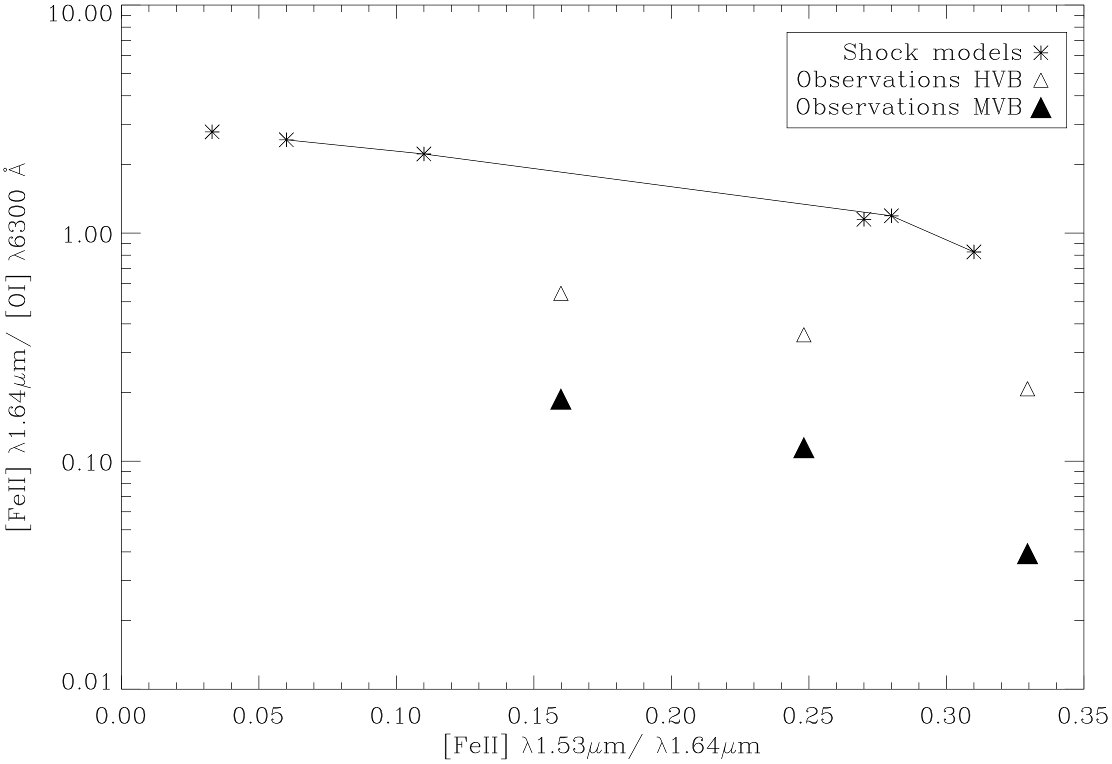

Figure 6.29: [FeII]λ1.64μm/[OI]λ6300Å ratio against the [FeII]λ1.53μm/[FeII]λ1.64μm ratio indicative of the electron density. [OI] observational points are obtained from Lavalley-Fouquet et al. (2000) and shocks models are those of Hartigan et al. (2004). Models with the same n_H=10^4 are connected.

with a slit width of 0.1″ and a spectral resolution similar to our data. The integrated [OI] line flux is 3×10^{-14} erg/s/cm^2 which correspond to a luminosity of 1.8×10^5 $L_\odot$. The luminosity observed by Lavalley-Fouquet et al. (2000), for the same velocity range (-250 km/s to 0 km/s), integrated over the first 0.5″is the same as Coffey et al. (2008), about 2×10^{-5} $L_\odot$. Therefore, the [OI] luminosity has not changed significantly between 1998 and 2002 and we can be confident in the comparison of the [FeII] luminosity observed in 2005 with the [OI] observations in 1998.

Hence, unless the [OI] flux drop strongly between 2002 and 2005, which seems unlikely, the discrepancies observed in Fig. 6.29 between the observed values and those from shock models (non depleted), are due to the iron depletion into the grains. From the Figure, the component at lower velocities is more depleted than the high velocity component. The MVB is 10 times lower than that predicted by the models, while for the HVB is 4, indicating that at least 80% of the iron is depleted into the grains. Podio et al. (2009) also find a higher depletion at lower velocity in the HH 111 jet. Two scenarios are possible, either part of the material in the jet comes from a region in the disc at inner distances than the evaporation radius or dust grains are more efficiently destroyed at higher shock velocity, in agreement with the predictions of theoretical models (Jones et al., 1994; Draine, 2004; Guillet et al., 2009). In addition, both components are more affected by depletion at higher densities (higher [FeII]$\lambda1.53\mu$m/[FeII]$\lambda1.64\mu$m ratio).

However, simultaneous observations in [OI] and in the [FeII] are required to better determine the quantity of iron which remains in the grains. We note that the observed depletion is lower than the factor 100 observed in dense molecular clouds, indicating partial destruction of dust grains (Savage & Sembach, 1996).

6.4.6 Jet mass-flux from [FeII]

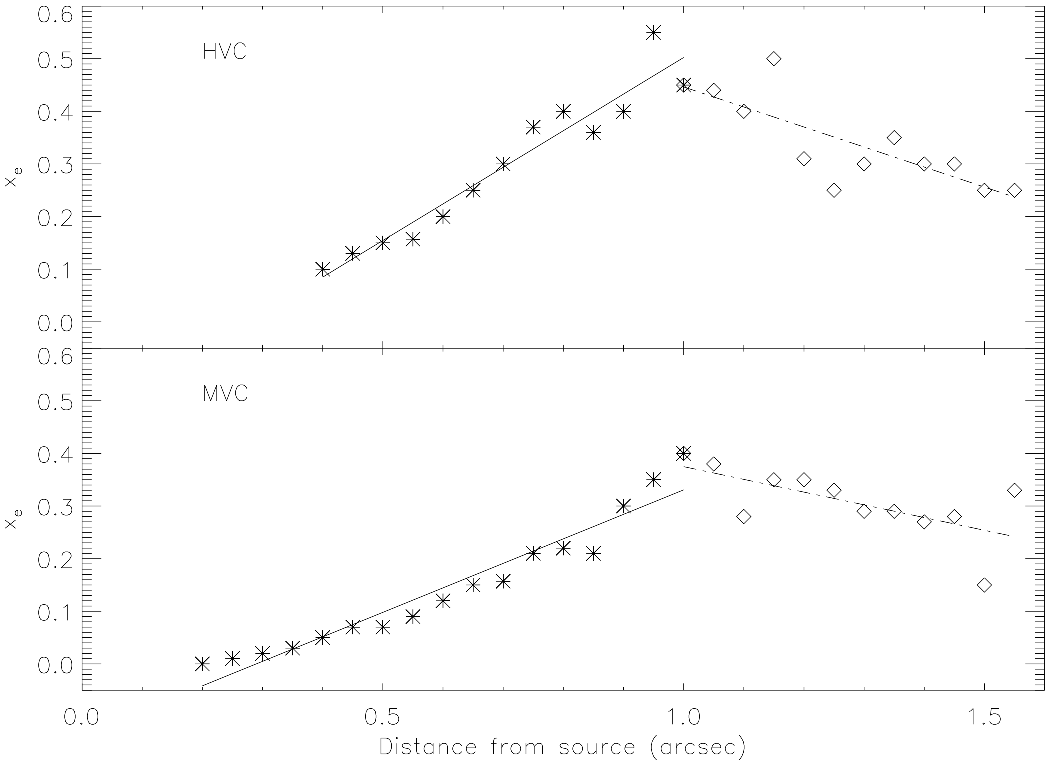

Figure 6.30: Derived ionization fraction values for different distances from the star and for the high and medium velocity components, from Bacciotti (2002). We carried out two linear fits for distances lower and higher than 1″ separately.

In the following, we concentrate the analysis on the blue-shifted jet. In order to have an estimation using the *Cross section and density* method described in Ch. 3, Sec. 3.6, of the mass-loss rate with distance along the jet we obtained all the parameters in Eq. 3.31 as a function of the distance. We used a single value of V_j for all the distances. We used a typical radial velocity of -220 km/s for the HVC and -100 km/s for the IVC, taken from Pyo et al. (2003). To obtain V_j we corrected the radial velocity by the inclination angle of the jet: $V_j = V_r/\cos(i)$ where i=42° to the line of sight (Lavalley, 2000). As an estimate of the jet radius, we take the intrinsic jet width defined as $FWHM = \sqrt{FWHM_{obs}^2 - FWHM_0^2}$ where FWHM$_{obs}$ is measured in the deconvolved maps as a function of the distance to the star, and we take as the effective resolution of the deconvolved images FWHM$_0$ $\sim$ 0.08″ at 0.1″ along the jet in Fig. 6.16. We also estimated the different values of n_e and x_e with distance along the jet. The electron density was obtained from lines ratios following the method described in section 6.3.4. Nevertheless, the lines needed to derive the ionization fraction, [NII]/[OI], were not measured in our observations so we looked in the literature the estimations obtained at a date as close as possible to our observations. Bacciotti (2002) measured the ionization fraction as a function of the distance along the optical jet in DG Tau and separately for the four velocity components that she identified. Observations were taken in 1999 with STIS (Space Telescope Imaging Spectrograph) aboard HST (Hubble Space Telescope) in high spatial resolution mode with a spatial sampling of 0.05″. She identified four velocity components labeled as LVC (low velocity component), MVC (medium velocity component), HVC (high velocity component) and VHVC (very high velocity component). We used her MVC (centered at -135 km/s) estimations for our intermediate velocity component and her HVC (centered at -260 km/s) for our high velocity component. Therefore, we obtain a ionization fraction as a function of the distance to the star for our two velocity components as a linear fit to the derived observational values given in Fig.5 of Bacciotti (2002). The ionization increases with distance from the star, up to a maximum at 1″ and then it decreases, so we conducted two different linear fits, one for distances lower than 1″ and the other for distances higher. The result of the fits, over-plotted to the observational values of Bacciotti (2002) are shown in Fig. 6.30. For distances lower than 0.3″ Bacciotti (2002) does not have estimations for our MVC and the fit in the HVC gives very low values of x_e so at 0.3″ we took the values derived by Coffey et al. (2008), x_e=0.02 for the high velocity component and 0.05 for the medium velocity component. For distances even lower than 0.3″ we fixed it to a minimum value of 0.01.

Figure 6.31 shows the electron density, ionization fraction and total hydrogen density used in the calculations, and presented in Table 6.4 for both the HVC and MVC and as a function of distance, electron density was assumed the same for both components because no significant differences were observed in our data between the two wings of the iron line. I over-plot, with symbols, the estimations obtained by Lavalley-Fouquet et al. (2000), obtained from optical observations. Their values of x_e in the HVC and IVC are quite consistent with the values used here, but their LVC, comparable to our medium velocity interval, shows lower values in factors of 5 or 6. In addition, similar studies of the ionization fraction with distance show similar values and variations, close to the star the ionization fraction is very low and increases with distances reaching some times a plateau and then it declines again. Hence, we are confident about the validity of the use of values by Bacciotti (2002) in our estimations.

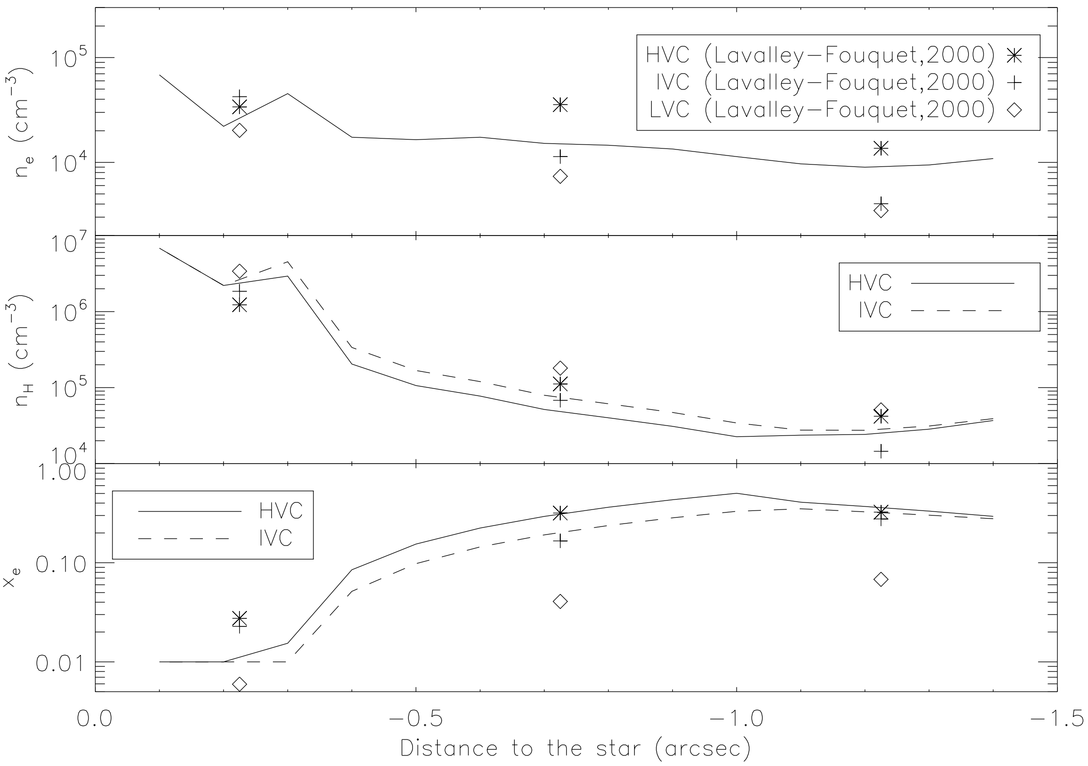

Figure 6.31: Electron density, ionization fraction and hydrogen density against distance to the star used in the calculations of the mass loss rate, for the HVC in solid line and for the MVC in dashed line. The electron density is same for both velocity components. Symbols show the values obtained by Lavalley-Fouquet et al. (2000) for the three velocity components detected in their optical observations.

For the *uniform slab* method, we used the same values of n_e as a function of the distance to the star as in the first method. We also use the same typical radial velocity values for each velocity component to obtain V_t ($V_t = V_r * tg(i)$ with i the inclination angle to the line of sight). The length of the beam projected on the sky where we calculated the luminosity (integrated in a pseudo-slit of width=1″) for different distances to the star is l_t=0.1″=2×10^{14} cm (at 140pc) that is the spatial sampling on the detector along the jet. But this method is independent of l_t as long as brightness variations are smooth over l_t.

For the *shock* method, we assumed the presence of one shock every 50 AU following the example of HH30 (Hartigan & Morse, 2007), that means that the luminosity coming from a region of 0.3″ ($\sim$ 50AU at Taurus distance) comes from one single shock. The luminosity showed in Fig. 6.32 is integrated every 0.3″ along the jet axis, starting at 0.2″ from the star to obtain the four points given in Table 6.4. Following the finding of Lavalley-Fouquet et al. (2000), the shock mass loss rate is corrected by v_j/v_s=4 to derive the mass loss rate in the jet.

General overview

The values obtained for the three methods are plotted in Fig. 6.32 as a function of the distance to the star in the blue atomic jet and separately for each velocity component. The measured luminosity for each velocity component, used for the *uniform slab* and *shock* methods are also shown. Stars show the two values given by Coffey et al. (2008) using the same first method based on jet density and cross-section as us. Table 6.4 sumarizes these values as well as the values used in their estimation for all the distances to the star.

For the HVC, shown in the top panel of Fig. 6.32, the three methods show similar values between 10^{-9} and 10^{-8} $M_{\odot}$/yr. In contrary, the medium velocity component shows clear differences between the three methods, even if the mass-loss rate remains at the same order of magnitude as HVC. In both cases, our values at $0.3''$ are lower than those found at the same distance by Coffey et al. (2008) using observations in the optical.

Let us start looking to top and bottom panel separately and discuss the main uncertainties of each method and the differences between them. The first method considered, based in cross section and density measurements, obviously depends strongly on the jet width and the total density, as shown in Eq. 3.31. The other parameter playing an important role in the estimations is the velocity, which is easy to obtain accurately from observations. In addition, I note that variations with distance for a given velocity component are small, about 5% for $d < 1''$, and thus a representative velocity for each kinematical component, and constant with distance, is actually considered. In contrary, as I have already mentioned, this method is very dependent of the jet width by means of the square of the FWHM, measured in line profiles. This dependence is clear in Fig. 6.32, the corresponding curve follows the same behavior with distance as the observed FWHM (Fig. 6.16), increasing with distance. The first point at $0.3''$ is higher than the point at $0.4''$, contrary to the width tendency, because of a peak in density. Actually, close to the star the electron density reaches the high density limit, thus the values close to this limit are less accurate. However, the main source of uncertainty is in the conversion of the electron density to n_H. The uncertainty in this parameter comes on one hand from the uncertainties in the electron density, but even more important from the uncertainties in the estimation of x_e, which are very difficult to quantify because of the low [NII]/[OI] signal to noise ratio, especially close to the central star. Hence, this parameter is not easy to obtain from observations, there are very few studies of this parameter as a function of the distance from the central star. However, knowing x_e with distance results crucial to derive a good estimation of the mass loss rate along the jet. Fig. 6.30 shows the derived ionization fraction by Bacciotti (2002) as a function of the distance to the star, showing remarkably different excitation conditions in a small scale of some arcseconds, from 0.01 at $0.3''$ to 0.4 or 0.5 at $1''$ from the star. If a mean constant value along the jet of $\sim$0.2 is considered, the x_e obtained will be up ten times the real value close to the star. Hence, we consider the observed values from Bacciotti (2002) in our calculations despite there is a difference of 6 years between the two set of observations.

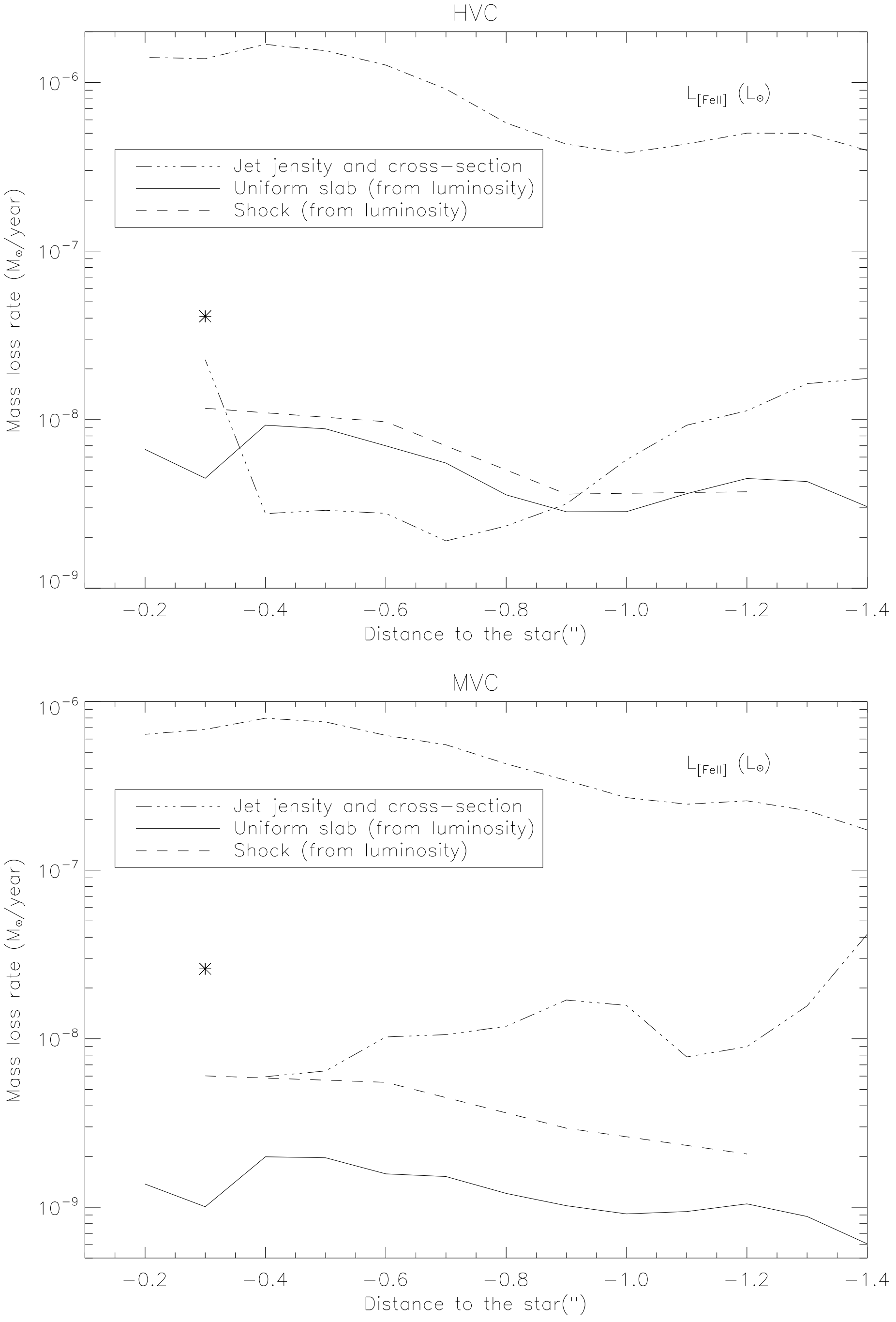

Figure 6.32: Mass-loss rate for the atomic jet in [FeII]$\lambda1.64\mu$m for the three methods described in the text as indicating in the legend and for the two velocity components identified, HVC on the top and MVC on the bottom. The line luminosity for each velocity component, used in the two methods based in the luminosity, is also represented. Stars indicate the value found by Coffey et al. (2008) for optical observations.

HVC

d (arcsec)	n_e (10^4 cm^{-3})	x_e	n_H (10^5cm^{-3})	FWHM$_{obs}$ (arcsec)	L$_{1.64}$ (L$_\odot$)	$\dot{M}_1$ $(M_\odot/yr)$	$\dot{M}_2$ $(M_\odot/yr)$	$\dot{M}_3$ $(M_\odot/yr)$
0.2	2.21	0.01	22.06	0.09	14.1	-	0.67	
0.3	4.52	0.01	29.35	0.10	13.8	2.27	0.45	1.17
0.4	1.74	0.08	2.04	0.11	16.8	0.28	0.93	
0.5	1.64	0.15	1.06	0.13	15.4	0.29	0.88	
0.6	1.74	0.22	0.77	0.13	12.7	0.28	0.70	0.97
0.7	1.52	0.29	0.52	0.14	9.15	0.19	0.55	
0.8	1.45	0.36	0.40	0.16	5.76	0.23	0.36	
0.9	1.34	0.43	0.31	0.19	4.30	0.32	0.28	0.36
1.0	1.13	0.50	0.25	0.28	3.81	0.58	0.28	
1.1	0.97	0.41	0.24	0.34	4.31	0.93	0.36	
1.2	0.99	0.37	0.24	0.37	5.01	1.13	0.45	0.37
1.3	0.94	0.33	0.28	0.41	5.00	1.63	0.43	
1.4	1.09	0.29	0.34	0.37	3.95	1.75	0.30	

MVC

d (arcsec)	n_e (10^4 cm^{-3})	x_e	n_H (10^5cm^{-3})	FWHM$_{obs}$ (arcsec)	L$_{1.64}$ (L$_\odot$)	$\dot{M}_1$ $(M_\odot/yr)$	$\dot{M}_2$ $(M_\odot/yr)$	$\dot{M}_3$ $(M_\odot/yr)$
0.2	2.21	0.01	22.06	0.09	6.40	-	0.14	
0.3	4.52	0.01	45.25	0.12	6.84	-	0.10	0.60
0.4	1.74	0.05	3.38	0.16	7.97	0.59	0.20	
0.5	1.64	0.10	1.68	0.21	7.58	0.64	0.20	
0.6	1.74	0.14	1.20	0.27	6.30	1.02	0.16	0.55
0.7	1.52	0.19	0.79	0.32	5.54	1.06	0.15	
0.8	1.45	0.24	0.61	0.38	4.28	1.18	0.12	
0.9	1.34	0.28	0.47	0.51	3.41	1.70	0.10	0.29
1.0	1.13	0.33	0.34	0.60	2.69	1.58	0.09	
1.1	0.97	0.35	0.27	0.54	2.46	0.78	0.09	
1.2	0.99	0.33	0.27	0.58	2.56	0.90	0.10	0.21
1.3	0.94	0.30	0.31	0.69	2.26	1.57	0.09	
1.4	1.09	0.28	0.39	0.89	1.73	4.17	0.06	

Table 6.4: Values of mass-loss rate (in units of $10^{-8} M_\odot/yr$) obtained for the three methods and for different distances to the star, plotted in Fig. 6.32. High velocity component in the blue side (HVC) on the top and the medium velocity component (MVC) on the bottom. I also give the values of electron density, ionization fraction, hydrogen number volume density ($n_H = n_e/x_e$) and jet width used to estimate the mass-loss rate and shown in Fig. 6.31 and in Fig. 6.16. Luminosity is given in units of 10^{-7} L$_\odot$, obtained by integrating in a pseudo-slit of width $1''$ perpendicular to jet and sampling every $0.1''$ along the jet.

I remind the reader that, in this method, we are assuming the filling factor equals to one, which implies the assumption of a homogeneous distribution of material within the jet, but also that the densest regions dominate the observed emission, giving in fact an upper limit to the real mass flux. As expected, this method gives an upper limit in the case of the MVC but it is no the case for the HVC that it is lower than the other two methods by a factor up to 3 until a distance of 0.9″. This could indicate that we underestimate the width of the HVC component in the closest parts to the star related to the MVC. Another possibility is that the electron density could be underestimated near the star where the density reaches the saturation limit. On the other side, projection effects in this portion of the jet which is marginally resolved and with strong density stratification, probably results in a non reliable estimate of jet mass flux.

The other two methods used, *uniform slab* and *shocks*, based on [FeII] luminosity estimates, follow the same behavior as the luminosity decreasing with distance from the star. In the case of shocks this dependency is obvious from Eq. 3.41, where the n_H and V_s dependency is evaded. The only dependence kept is with the luminosity (assumed a solar abundance, but we will discuss the dependence with abundance more in detail later).

In the case of luminosity of a uniform slab method, besides the luminosity and Fe abundance dependence, the choice of l_t is also important if the emission is not resolved along the jet over a length greater than l_t. In the case of long-slit spectroscopy this l_t is the slit width and it can be larger than the real emitting beam giving in this case a lower limit to the real $\dot{M}$. For our SINFONI data, the spatial resolution allows integration beams of 0.1″.

The dependence with electron density in this last method comes from the line emissivity which depends on the electron temperature too. Coffey et al. (2008) find 2.5x10^4 K for their HVC and 0.5x10^4K for their LVC. Hence, the emissivity was calculated assuming an electron temperature of 10^4 K and fitting the curve computed by Pesenti et al. (2003) for this temperature, as I showed in Ch. 3 (Fig. 3.10). One part of the uncertainty in the mass flux comes from the goodness of the fit performed, the fit is very good for the electron density representative in the case of DG Tau ($n_e >$ 1x$10^4 cm^{-3}$). In addition, the fact of assuming a fixed temperature of 10^4 K along the jet, also introduces an error in the estimation of the emissivity used. However, the mass loss rate value will be affected by the electron density accuracy. Lavalley-Fouquet et al. (2000), Bacciotti (2002) and Coffey et al. (2007) shows that the electron density is higher in the axial region, in the more collimated and higher speed components (which was already known to be very dense at the base of the jet (Solf, 1997). Here, the same electron density is assumed for both velocity components and comparing with the values by Lavalley-Fouquet et al. (2000), the electron density assumed would result in an underestimation or overestimation of a factor 2, depending on the distance.

However, the main source of uncertainty in this two last methods is the adopted iron abundance in gas phase. As I showed in the precedent section, the iron depletion onto the dust grains is important, resulting in a factor to apply to the mass loss estimation of 4 for the HVC and of 10 for the MVC. For the following comparison with previous works using oxygen lines, not affected by depletion, these factors are taken into account.

In addition, in the case of shocks, the assumed ratio between the shock and the jet velocity is also an important source of uncertainty.

Comparison with previous works

Figure 6.33 shows the same as Fig. 6.32 but estimations for the two models depending on the luminosity were corrected by iron depletion and the results obtained by Lavalley (2000) using the same methods as us, are also shown for comparison. Our HVC, centered at -234 km/s, is compared with her IV (intermediate velocity component) centered at -175km/s and our MVC, centered at -111 km/s, is compared with her LV (low velocity component) centered at -50km/s. Her estimations were obtained from measurements in the [OI]λ6300Å line. As in Fig. 6.32, observations from Coffey et al. (2008), obtained in the same [OI] optical line and using the method based on the jet density and the jet width is shown. Coffey et al. (2008) found a value higher by a factor 2 than our estimations for the same method. The discrepancy mainly comes, on the one hand from a jet radius twice our estimation (they do not correct for instrumental PSF) and because of the quadratic dependence, this results in a factor 4. On the other hand, the total density obtained by Coffey et al. (2008) is a factor 3 lower than ours which compensates the factor 4 from the jet width. The difference in MVC may also be due to the fact that the authors do not correct the MVC with by the area filled by HVC, which we do.

If we compare the two set of optical observations, Lavalley (2000), using also the same method as Coffey et al. (2008), find higher values, being the differences up to one order of magnitude close to the star. Relating to our estimations, Lavalley (2000) also find higher values, being at some distances even higher than one order of magnitude. However, at 1.4″, for both components, the two estimations become coherent. That may indicate that the optical component are wider than the iron one in the internal parts of the jet or, as I said before, that we either underestimate the jet width for these regions or the density or both of them. In addition, in the MVC the important difference in x_e are compensated by the difference in the electron density. However, a discrepancy of a factor 3-4. in the hydrogen density still remains between our values and those of Lavalley (2000).

The two models obtained from the iron luminosity, once corrected by the iron depletion, give values higher than that of Coffey et al. (2008) for the *shock* method and lower for the *uniform slab* method. In the case of the HVC, the estimations obtained using the *shock* method from iron luminosity are remarkably similar to those obtained from oxygen luminosity. However, considering all the uncertainties in the parameters for each method, we obtain similar values to previous estimations within a factor 5. Over the central 1″ from the star a mean value, from the *uniform slab* and *shock* methods, of 3×10^{-8} $M_\odot$/yr is obtained for the HVC and of 10^{-8} $M_\odot$/yr for the MVC, in this case from an average of the three considered methods, giving a total mean mass loss rate of 4×10^{-8} $M_\odot$/yr. Considering the derived values for the mass accretion rate, the ejection-accretion ratio ranges between 0.08 and 0.4.

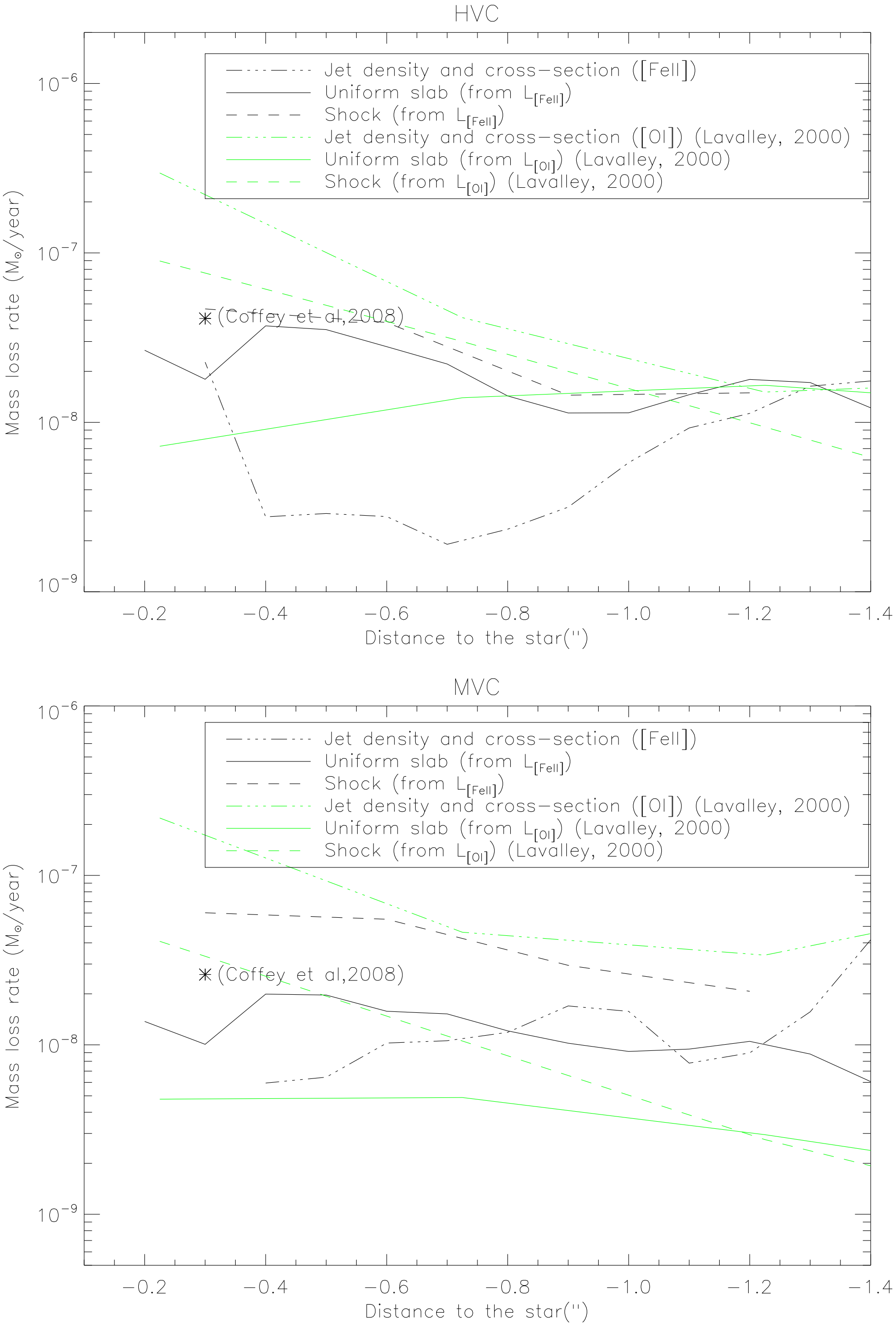

Figure 6.33: Same as Fig. 6.32 (models depending on the luminosity were corrected by iron depletion) but values obtained by Lavalley (2000), using the optical line [OI]λ6300Å and the same methods, are showed for comparison.

If we assume that the jet is originated in an extended MHD disc wind, a constrain in the launching radius range can be derived. We considered the warm solution with λ=13 whose predicted velocity is in excellent agreement with the HVC in the observed DG Tau position-diagram (Cabrit, 2007b), and the predicted transverse PV diagram also fits well the observed one (Pesenti et al., 2004). For this solution, we derive a external/internal ratio of $r_e/r_i > 45$. Typically, from observational constrains the external radius is about 5AU and we expect that internal radius is at >0.05 AU, giving a range in radii of a factor 100, compatible with the estimations derived here.

6.4.7 Possible heating mechanisms for the H_2 emission

Molecular emission as that shown in this section for DG Tau was observed in other T Tauri stars (e.g. Beck et al., 2008) and several scenarios, combined with several possibilities for the excitation mechanisms dominating the emission, are proposed to explain its origin. However, none of those are clearly rejected or accepted. I will review all this possibilities using the additional information derived from the data analyzed in this chapter for the DG Tau outflow. I will start by the three heating processes proposed which were already noted and discussed in-depth by Takami et al. (2004) and Beck et al. (2008). The first one is the UV photo-dissociation in a PDR, the second is assuming shocks and the last one is heating by ambipolar diffusion.

(1): UV PDR:

Le Petit et al. (2006) show the predictions from the revised Meudon model of photon-dominated region (PDR) for, among other, infrared H_2 lines and for high FUV field, G_0, values (up to 10^7, in units of the local interstellar radiation field, taken to be equivalent to a one-dimensional flux of 1.6×10^{-3} erg s^{-1} cm^{-2} in the 6-13.6 eV band (Habing, 1968)). The extinction-corrected DG Tau FUV flux measured on earth is 2×10^{-13} erg/s/cm^2/Å at 1400-2000 Å (Gullbring et al., 2000). Hence, at the distance of the emission peak, at 0.1″ (14 AU), the FUV field of DG Tau would be ~0.4 erg/s/cm^2/Å and thus the UV radiation field coming from DG Tau is $G_0=2.5\times10^5$ at the peak of the emission. For this G_0, models obtain line ratios compatibles with observations for total densities between 10^6 and 10^7 cm^{-3}. All the ratios shown in Beck et al. (2008), measured centered at the peak emission, are well reproduced by the models within the observational uncertainty, although the 1-0 S(2)/1-0 S(1) flux ratio seems to require lower UV radiation field or higher densities and 2-1 S(3)/1-0 S(1) seems to require a stronger UV radiation. However, the 1-0 S(1) flux is no so well reproduced by the models and it is lower than observed by a factor of 5. At 14 AU, the observed flux is 0.013 erg s^{-1} cm^{-2} sr^{-1},whereas the predicted flux is 0.0025 erg s^{-1} cm^{-2} sr^{-1} (for a density of 10^7 cm^{-3}).

It is important to note that PDR models by Burton et al. (1990) predicted [OI] emission, for these high densities of 10^6-10^7 cm^{-3} and $G_0>10^5$, at the same temperature as the H_2, as showed by observations (Fig. 6.24). The models predict H_2/[OI] ratios of 3.3 for a density of 10^6 cm^{-3} and 0.18 for a density of 10^7 cm^{-3}, both predictions for a $G_0=10^5$.

The discrepancy in the flux at the peak position, can be due to projection effects since the predicted flux are obtained for a face-on geometry. It can be also due to a possible and no-resolved shock produced a this position. If we consider the average flux of 3×10^{-3} erg s^{-1} cm^{-2} sr^{-1} at an average distance to the source of 0.25″= 35AU, the UV radiation field coming from DG Tau is $G_0=4\times10^4$ and the expected flux, for densities between 10^6 and 10^7 cm^{-3}, is 0.001, still lower than the observed one, but now only by a factor 3.

Concerning the predicted gas temperature, for both $G_0=2.5\times10^5$ and 4×10^4, and the high densities considered, it is between 2000 and 2500 K in good accord with observations. One could think that the real UV radiation field arriving to the molecular emission region would be partially absorbed for the existing material between the star and the PDR region. In this case, models would not reproduce the observed fluxes and ratios even at high density. However, a moderate extinction is expected from the inner material since moderate iron depletion is observed in the gas phase ($A_v/n_H < 1/10\ (A_v/n_H)_{ISM}$).

(2): Shocks:

Takami et al. (2004) support this idea based on the fact that shocks are already observed in outflows of various young stellar objects, but also because the observed line flux ratios measured in the molecular emission of DG Tau are similar to those found in shock-excited extended outflows, indicating thermal temperatures of 1000-4000K.

Beck et al. (2008) show that the small range in temperature obtained from the level populations suggest a thermalized gas and the observed line ratios are also in good agreement with C type shock calculations by Smith (1995). However, they conclude that in all the stars of their study, it is not possible to distinguish between UV and shock excitation as the main excitation mechanism for the H_2 emission. In the particular case of DG Tau, authors favor the explanation of a shock excited emitting region coming from a wide and slow component of the wind, based on the decreasing $1/r^2$ flux law showed by this object.

To analyze this possibility in the data studied here, the models computed by (Kristensen et al., 2008) are used. As I briefly explain in Sec. 3.6.2, these models, both J and C-shocks, compute the flux in different H_2 lines depending on three parameters: the magnetic field, the shock velocity and the total density.

Figure 6.34 shows the computed H_2 brightness in the $\lambda2.12\mu$m line against the computed 2-1 S(1)/1-0 S(1) ratio in the case of J-shocks. Different colors correspond to different total pre-shock densities. The grey box marks the region compatible with obser-

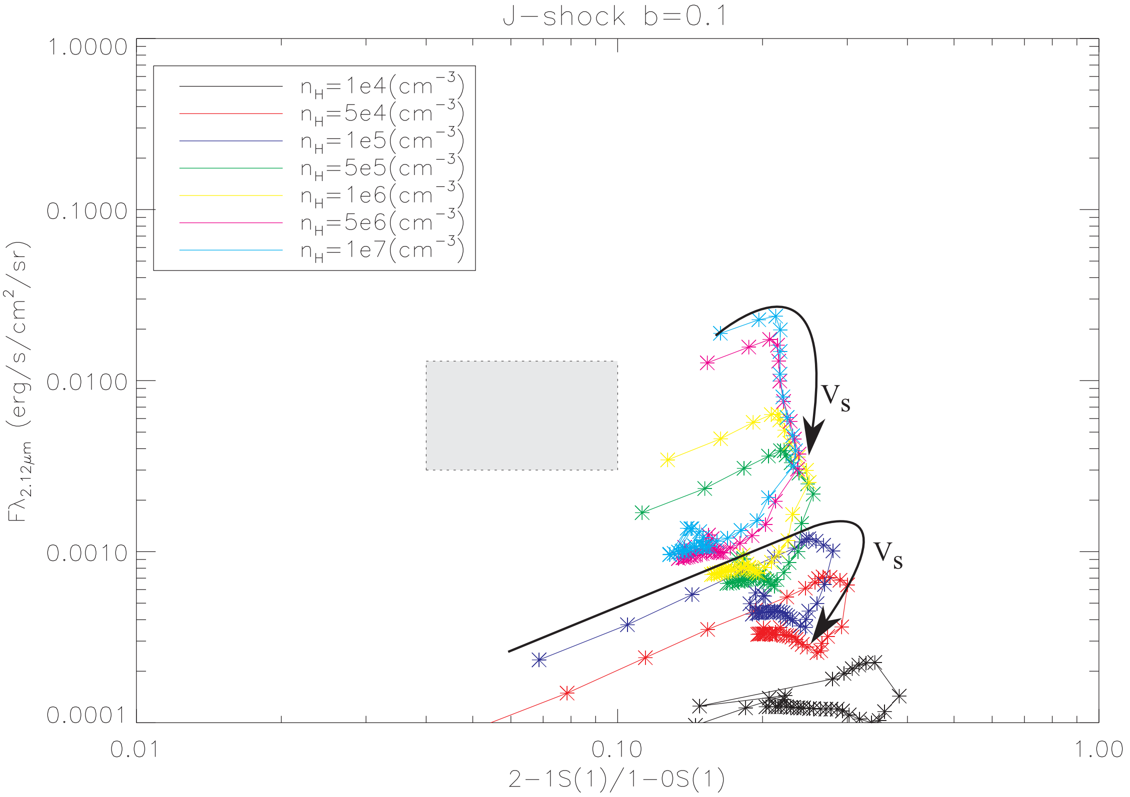

Figure 6.34: Computed H_2 brightness in the 1-0 S(1) (λ=2.12μm) line against the computed 2-1 S(1)/1-0 S(1) ratio by Kristensen et al. (2008) for J-shocks. The direction of increasing v$_s$ is shown. The gray cube shows the observed measurements indicating that J-shocks are not valid in this case.

vations, a 2-1 S(1)/1-0 S(1) line ratio of 0.07±0.03 (Beck et al., 2008) and a brightness between 0.003 erg/s/cm^2/sr and 0.013 erg/s/cm^2/sr, corresponding to the average and peak values derived here. It is clear from the image that the J-shock are excluded in the case of DG Tau H$_2$ emission. The ratio of 2-1 S(1)/1-0 S(1) is well under the value of 0.2 typical for these models. Moreover, even if very low shock velocity J-shocks models, with n$_H$=10^4-10^5 cm^{-3}, could reproduce the observed ratio, the average brightness would be severely underestimated by a factor 10-20.

Hence, I will focus the analysis in the different models proposed in the case of C-shocks. First of all, these models will allow me to constrain the shock velocity depending on the total density and magnetic field assumed. Figures 6.35, 6.36 and 6.37 show the H$_2$ brightness and the 2-1 S(1)/1-0 S(1) ratio as a function of the shock velocity and for seven values of hydrogen density, obtained from three C-shock models with three different transverse magnetic field quantified by b=B(μG)/$\sqrt{n_H(cm^{-3})}$= 0.5, 1.0 and 2.0 respectively for each figure. For each curve of density the highest velocities correspond to the points at higher line flux and higher line ratio. As in Fig. 6.34, the gray box shows the range of compatible H$_2$ brightness and 2-1 S(1)/1-0 S(1) ratio obtained from observations and

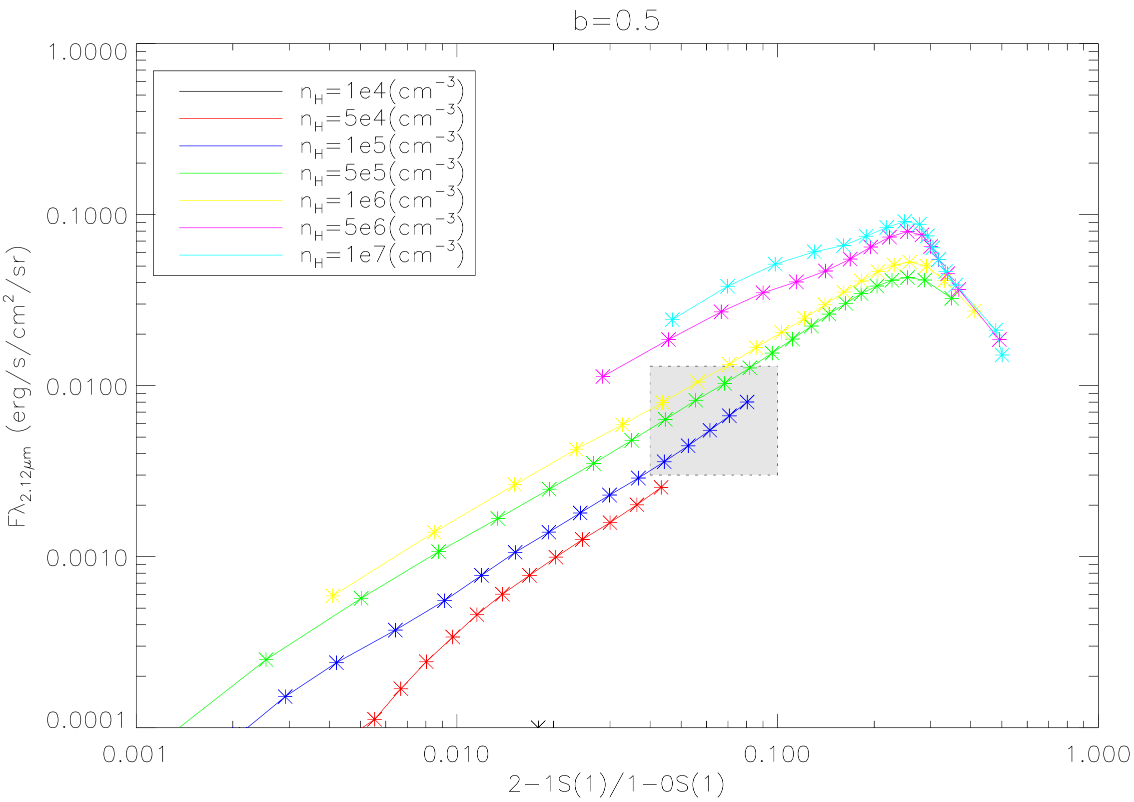

Figure 6.35: Computed brightness in the $H_2\lambda2.12\mu$m line against the computed 2-1 S(1)/1-0 S(1) ratio from models by Kristensen et al. (2008). Different colors correspond to different values of hydrogen density, n_H=1×10^4 cm^{-3}, 5×10^4 cm^{-3}, 1×10^5 cm^{-3}, 5×10^5 cm^{-3}, 1×10^6 cm^{-3}, 5×10^6 cm^{-3} and 1×10^7 cm^{-3}, and the small gray cube shows the observational values. This model is for a C-shock with b=0.5.

Table 6.5 summarizes the shock velocity populating this region for the different values of b and n_H. Observations are not always consistent with models, theses cases are noted in the table with a cross. The shock velocities derived are higher for higher magnetic fields models but lower for higher hydrogen densities. Three extra models with b=3, b=4 and b=10 are shown in the table. For all the values of b, densities higher than 1×10^6 cm^{-3} are completely excluded and low densities, between 1-5×10^4 cm^{-3}, are only compatible for b$\geq$ 1. In particular, for the highest b computed in the models, b=10, the shocks velocities are between 81 and 91 km/s and the only total density compatible with observations is n_H=1×10^4 cm^{-3}. Thus, for the derived compatibles values of n_H and b, the transverse magnetic field is limited between 100μG and 1000μG.

Once the shock velocity estimated, the mass-loss rate in the shock can be derived using Eq. 3.48 (showed in Sec. 3.6.2) for b $\leq$ 2 where the assumption of the $H_2\lambda2.12\mu$m is the main cooler is valid. For b $\geq$ 3, the post-shock temperature is lower and this line is not longer the main cooler. Hence, in this case, the shock mass-loss rate is obtained from the n_H and v_s, constrained from the previous figures, and from an estimate of the shock

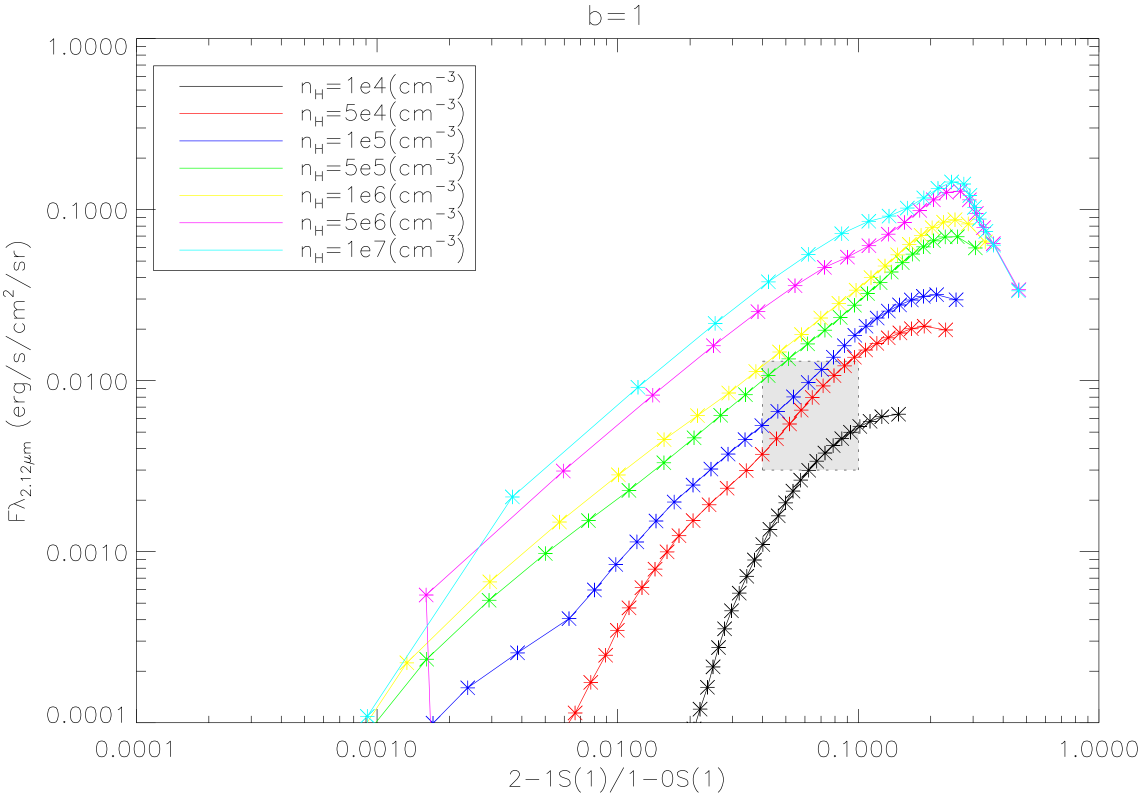

Figure 6.36: Same as Fig. 6.35 but for a C-shock with b=1.0.

n_H (cm^{-3})	b=0.5	b=1.0	b=2.0	b=3	b=4	b=10
1×10^4	X	50-54	53-60	57-65	60-69	81-91
5×10^4	X	37-43	43-46	48-49	52	X
1×10^5	27-31	33-36	40	X	X	X
5×10^5	18-21	22	X	X	X	X
1×10^6	15-16	19	X	X	X	X
5×10^6	X	X	X	X	X	X
1×10^7	X	X	X	X	X	X

Table 6.5: Shock velocity ranges, in km/s, derived from models shown in Fig. 6.35, 6.36 and 6.37. Crosses mean that no shock velocity is compatible with observations for the corresponding magnetic field and hydrogen density.

surface. This shock surface is obtained by comparing the flux integrated in the emitting region with the average surface brightness, resulting in a shock surface of 2×10^{30} cm^2. The final mass-loss rate in the shock ($\dot{M}_s=\mu m_H n_H v_s S_s$) ranges between 6×10^{-9} $M_\odot$/yr (for a b=10, $n_H=10^4$ cm^{-3} and v_s=91 km/s) and 3.4×10^{-8} $M_\odot$/yr (for a b=0.5, $n_H=10^6$ cm^{-3} and v_s=15 km/s).

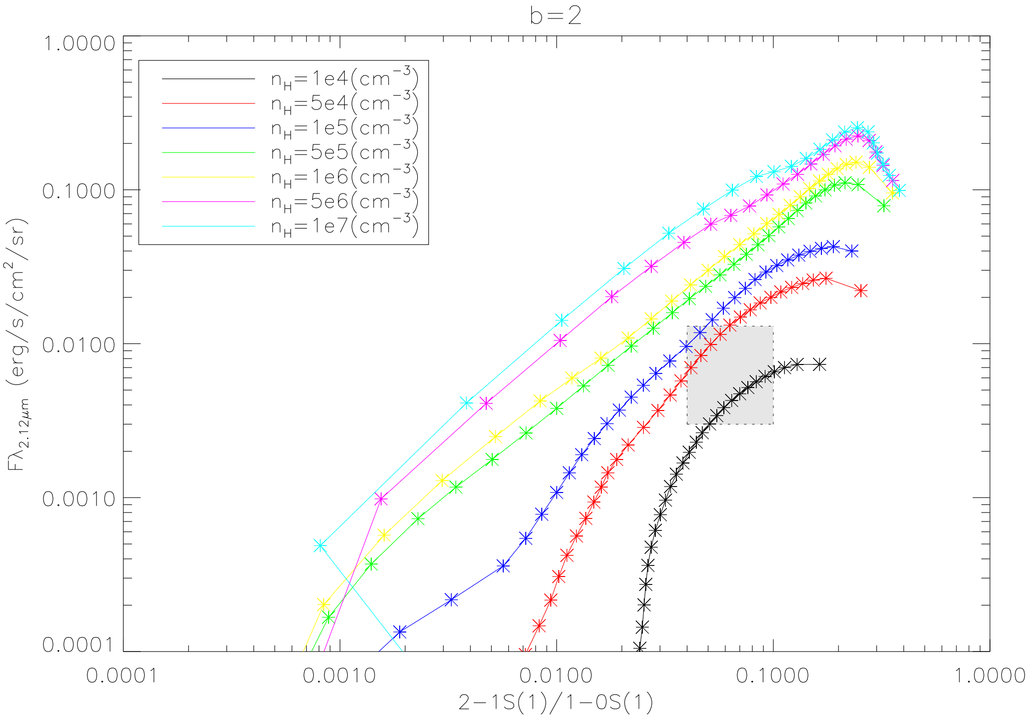

Figure 6.37: Same as Fig. 6.35 but for a C-shock with b=2.0.

(3): Ambipolar diffusion:

Recently, Panoglou et al. (2009) carried out a thorough study of the thermal and chemical structure of a flow on a disc wind model. In the article, the authors describe the results found for a *slow and dense* (Casse & Ferreira, 2000) disc wind model. Fig. 6.38 shows the overall geometry of the MHD disc wind solution used by the authors. The heating mechanisms taken into account in the code include the ambipolar diffusion by elastic scattering between the neutral fluid and charged ions, the Ohmic heating by the drift between ions and electrons, the photoelectric effect on grains irradiated by the UV field of hot accretion spots and stellar X-rays and cosmic-rays irradiation. The authors demonstrate that the H_2 molecule can survive in the context of a protostellar MHD disc wind for distances greater than 1 AU and despite the FUV field and the strong ambipolar diffusion heating (panel h of Fig. 6.39). However, they show that the main heating mechanism remains the ambipolar diffusion. They also show that for typical emitting spatial scales, about 9 AU, and $\dot{M}_{acc} \sim 10^{-6}$-$10^{-7}$ $M_\odot$/yr, the temperature reach a plateau of 2000-4000 K (panel a of Fig. 6.39) which is compatible with the observed temperature in the case of DG Tau (Beck et al., 2008). I will discuss more in detail this scenario in the next section where I will review the different possibilities for the origin of the molecular emission, including the disc wind scenario.

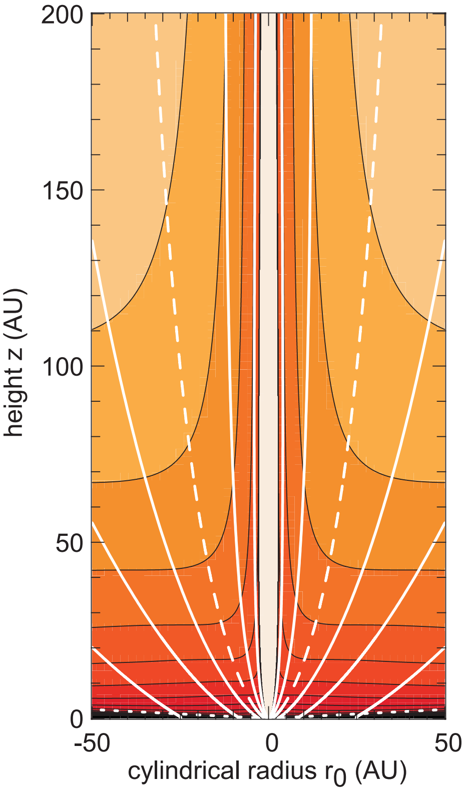

Figure 6.38: Overall geometry of the MHD disc wind solution of Casse & Ferreira (2000) used in the predictions by Panoglou et al. (2009). Solid curves show flow lines and the color scale shows the density. The white line denotes the slow magneto-sonic wind surface at $z \simeq 0.05r$.

6.4.8 Origin of the molecular emission: the disc wind hypothesis and its alternatives

In this section I will discuss the possible origins proposed for the low velocity H_2 molecular cavity observed in DG Tau. Based on the results shown previously and the discussions presented in the precedent sections, I will try to give some constraints which limit the number of possibilities. These origins can be separated into three main types: (1) origin in a molecular MHD wind (2) origin in a shocked disc atmosphere and (3) origin in a photo-dissociation region which produces a wind by photo-evaporation of the disc material. Figure 6.40 shows in a very schematic way this three main scenarios. However, variants or adding components can be imaged in each scenario. In the first scenario two possible cases are presented assuming an excitation by shocks: the emission shows a bow-shock structure if the shocks are produced internal to the wind or the shock can be against a static disc atmosphere or ambient medium. This last possibility seems more coherent with the observed morphology in the case of DG Tau. However, below, I will discuss more in detail this different possibilities within an excitation by ambipolar diffusion origin in the case of a MHD wind. In the representation of a shocked disc atmosphere, I show the hypothesis of a stellar wind causing the shock against the disc atmosphere, but one can imagine, for an example, an internal atomic MHD wind or a X-wind. In

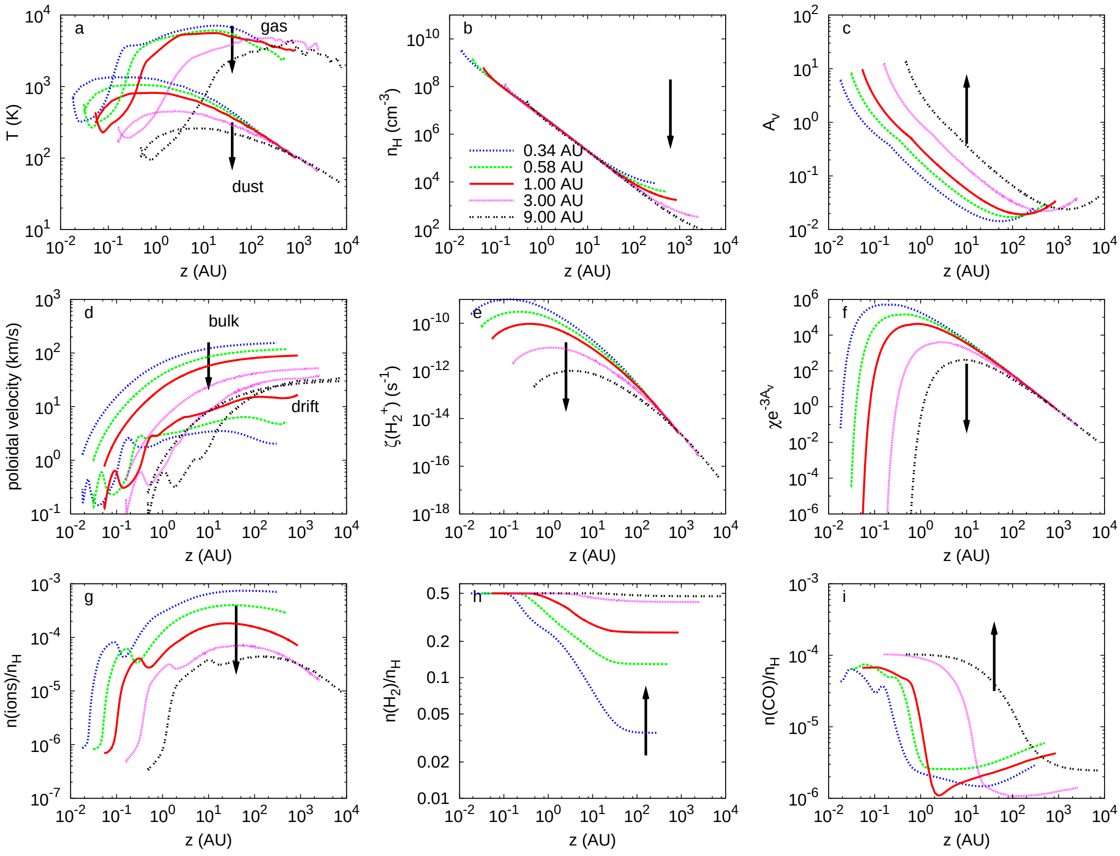

Figure 6.39: Model predictions for a Class II object, $\dot{M}_{acc} \sim 10^{-6}$ $M_\odot$/yr, and different streamlines launched from 0.34, 0.58, 1.00, 3.00 and 9.00 AU, obtained by Panoglou et al. (2009) (private communication). (a) the gas temperature and dust temperature (lower curves); (b) the number density of hydrogen nuclei; (c) the visual extinction A_v to the star, in magnitudes; (d) the poloidal components of the bulk flow speed (top curves) and the calculated drift speed (lower curves); (e) the X-ray H_2 ionization rate; (f) the effective radiation field in Draine units (attenuation factor appropriate for carbon photoionisation); (g) the fractional abundance of ions; (h) the fractional abundance of H_2; (i) the fractional abundance of CO.

the last scenario, I only show the molecular wind produced by the stellar radiation, but a more complicated configuration can be consider, with an internal stellar or MHD wind or a photo-evaporated atomic contribution to the wind.

(1): Origin in a molecular MHD wind component, extension of the atomic wind:

Takami et al. (2004) favor the origin of the molecular flow in the disc for several reasons: (1) the "onion-like" kinematic structure of the molecular emission, following the atomic component and which is also observed in our data. (2) from ^{13}CO observations, there is no matter surrounding the jet to be entrained by the fast, collimated jet. Within the two magneto-centrifugal wind models suggested and which predict the onion-like

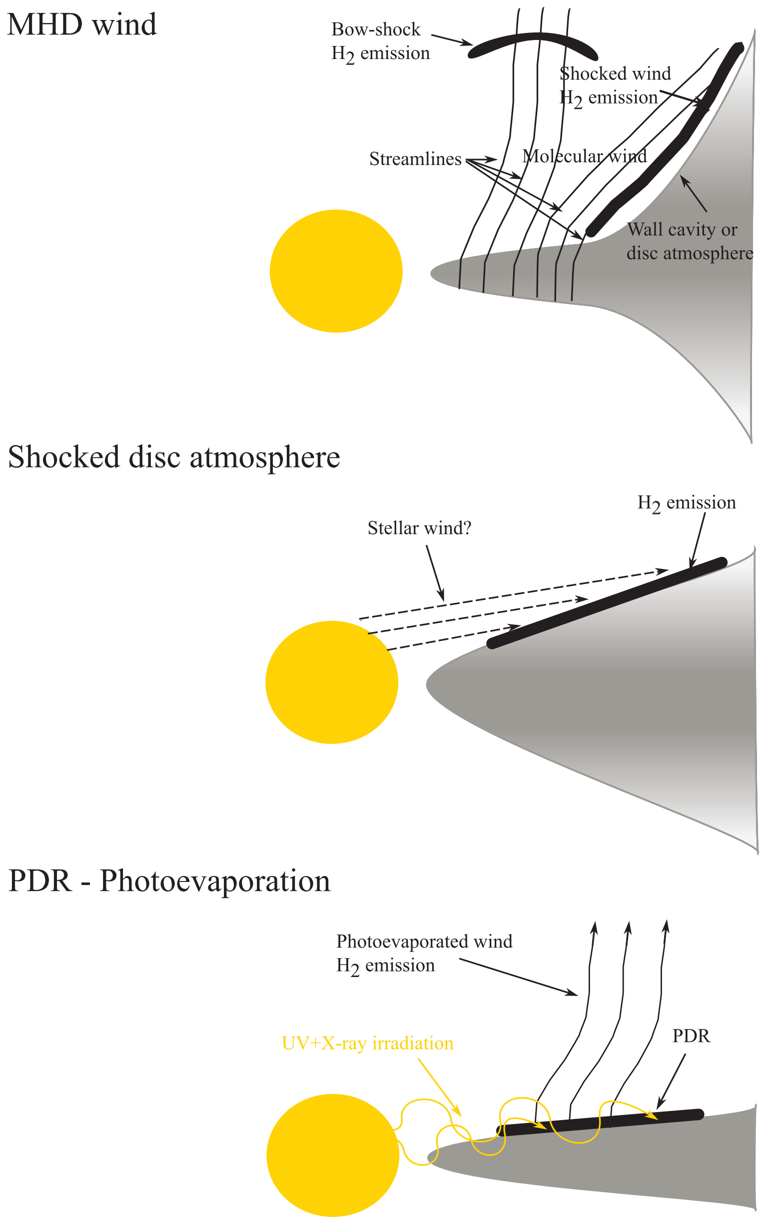

Figure 6.40: Schematic representation of the three main scenarios discussed in this section for the origin of the molecular emission in DG Tau.

structure mentioned but with different jet launching regions, Takami et al. (2004) note that the disc wind model can easily explain the presence of H_2 molecules whereas for the X-wind model it is not clear.

In the context of a disc wind, some constraints can be fixed from the observed flow velocity and the observational limit in the launching radius, r_0 (Ferreira et al., 2006). The terminal poloidal velocity, v_p^∞, can be expressed in terms of the keplerian velocity, v_k, at the radius r_0, and the magnetic lever arm, λ=(r_A/r_0)^2, by $v_p^\infty \sim v_k\sqrt{2\lambda - 3}$ where $v_k = \sqrt{GM_*/r_0}$.

Moreover, there are two more simple expressions relating the magnetic lever arm with the ejection efficiency, ξ, and with the ratio between the external, r_e, and the internal, r_i, radius from which the wind is launched:

$$\xi = \frac{1}{2(\lambda - 1)} \qquad 2\frac{\dot{M}_j}{\dot{M}_{acc}} = \xi \; ln\Big(\frac{r_e}{r_i}\Big)$$

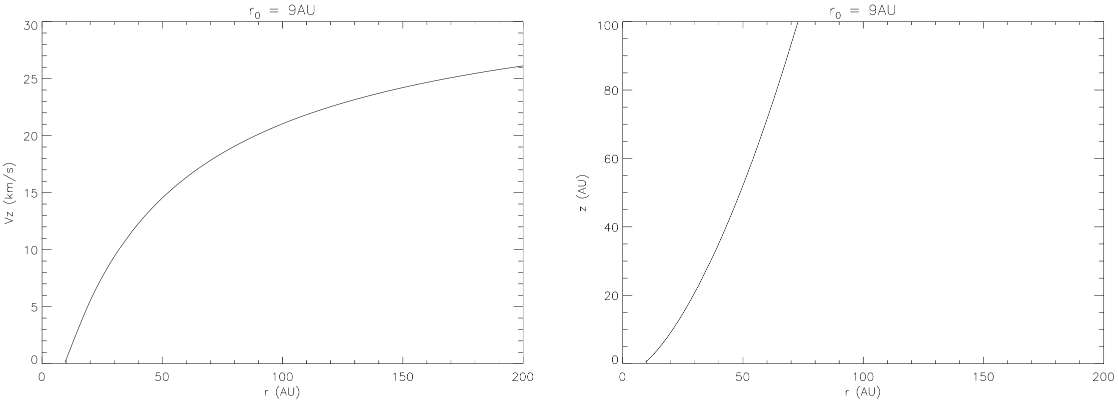

Figure 6.41: Left: Velocity predicted by models by Casse & Ferreira (2000) as a function of the disc radius for the streamline at r_0 = 9 AU. For distances of $\sim$ 50 AU, the predicted velocity is $\sim$15 km/s, as observed, and the terminal velocity is reached at higher distances. Right: For the same solution, the morphology of the streamline is in good accord with the observed morphology.

Pesenti et al. (2004), in order to explain optical observations of the jet rotation for DG Tau in the medium velocity component (MVC) of $\sim$ 50 km/s, fit to a model with λ=13 and a r_0= 3 AU. If we consider this solution in the case of the molecular emission, λ=13 results in $\xi \sim$ 0.04 and in a $v_p^\infty \geq$ 39.5 km/s, for $r_0 \leq$ 10 AU, which is higher than the observed velocity. However, this discrepancy in velocity is solved if the observed H_2 streamline does not achieve the terminal velocity on the observed spatial scales (z=20-200 AU). In this case, the solution found by Pesenti et al. (2004) gives a velocity of $\sim$ 15 km/s at the same spatial scales, as shown in Fig. 6.41 from models by Casse & Ferreira (2000) for the corresponding streamline at r_0=9 AU. In addition, the morphology expected for this streamline is very similar to that observed in the same spatial scales, right panel in Fig. 6.41.

Keeping in mind all these calculations, I will discuss the implications and the coherence of the excitations mechanisms previously discussed within this physical scenario for the origin of the H_2 emission in DG Tau.

-PDR in the wind:

Takami et al. (2004) derive an emitting region of 4×10^{30} cm^2 needed to account for their observed luminosity assuming a 1-0S(1) surface brightness of 10^{-3} erg/s/cm^2/sr. They procure the surface brightness from predictions by models by Burton et al. (1990) for an incident FUV of $G_0=10^5$ (the maximum value computed by the model) and a density of 10^7 cm^{-3}. Then, assuming a typical column density of the H_2 of 10^{21} cm^{-2} (Burton et al., 1990) and taking their observed flow velocity of 20 km/s, the derived mass of H_2 is 5×10^{-6} $M_\odot$ which is 100 times the mass of hot H_2 at 2000 K derived here. They thus obtain a momentum flux of 7×10^{-6} $M_\odot$km/s/yr, also too large compared to the typical values for Class I protostars of 2×10^{-6} $M_\odot$km/s/yr or lower (Bontemps et al., 1996). Based on their derived momentum flux, Takami et al. (2004) rule out this process as the excitation mechanisms causing the H_2 emission.

However, the FUV field of DG Tau would be $\sim$0.4 erg/s/cm^2/Å at a distance of 0.1″ (14 AU) (extinction-corrected FUV flux measured on earth is 2×10^{-13} erg/s/cm^2/Å at 1400-2000 Å (Gullbring et al., 2000)). Hence, the impinging G_0 would be 2.5×10^5, higher than the maximum value considered in the PDR models of Burton et al. (1990). If we assume the same velocity of $\sim$ 20km/s but the emitting region considered here, twice lower than that considered by Takami et al. (2004), and a characteristic time twice that of Takami et al. (2004), the momentum flux obtained is then 1.75×10^{-6} $M_\odot$km/s/yr. This value is four times lower that the value derived by Takami et al. (2004) and it is more compatible with typical values expected for this class of objects. In addition, most of the emitting area is at velocity lower than 20 km/s giving even lower momentum flux.

In addition, in this scenario, the emitting region is only a small fraction of the total mass placed in the boundary layer with the atomic jet, receiving the direct UV radiation from the star. The estimations of the mass-loss rate and the momentum flux, obtained from the assumption of a total H_2 column density of 10^{21} cm^{-2} assumes that all the gas is moving at the same velocity as the emitting gas, which is in fact against the observation that the velocity is very low except at the H_2 peak and against the assumption of a extended disc wind in which each streamline has a different velocity, lower for increasing distances. The momentum flux is actually an upper limit to the real one.

In summary, this argument is not very strong because in the case of a MHD wind, the comparison with static PDR models is not very coherent and, as I have already mentioned, Panoglou et al. (2009) shows that for the disc wind model, the ambipolar diffusion is the dominant heating mechanism, rather than the UV radiation coming from the star.

-Heating by ambipolar diffusion:

Panoglou et al. (2009) show that the H_2 can survive in the disc for distances greater than 1 AU and that the temperature is coherent with that observed. Assuming that all the 0.5″ emitting region contributes uniformly to the emission (*Volume method*, Sec. 3.6.2) and that the gas moves at a velocity of $\sim$ 15 km/s (derived t_{dyn}= 22yr), a mass flux of $\sim$1.4×10^{-9} $M_\odot$/yr is thus found, in good agreement with Takami et al. (2004) estimations ($\dot{M} \geq$ 2.2×10^{-9} $M_\odot$/yr), since the H_2 luminosity and velocity observed are similar. Hence, assuming that all the H_2 is hot at $\sim$2000 K, and taking the previously calculated accretion rate, the derived ejection-accretion ratio in the case of volume emission, is $\geq$ 0.014.

For the λ= 13 solution and this ejection-accretion ratio, a constrain in the external-internal radius ratio of $r_e/r_i \geq$ 2 is obtained. For a $r_e \leq$ 10 AU, the internal radius would be $\leq$ 5 AU, compatible with constraints on the outer radius of atomic wind (3 AU) from rotation studies (Pesenti et al., 2004). However, more detailed comparison of observations with synthetic observations, using thermal and chemical structure, computed by Panoglou et al. (2009) is needed.

The problem with this scenario is that the derived n_H in the case of a disc wind, from Panoglou et al. (2009), is 10^4-10^5 cm^{-3} which is too low to have LTE in H_2 rovibrational levels and then too low H_2 flux and ratios are maybe expected, related to the values obtained here and by Beck et al. (2008).

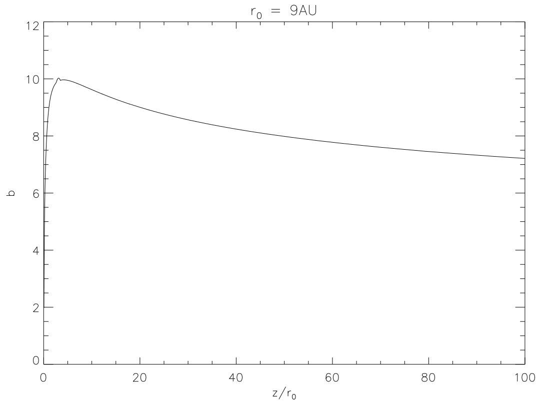

Figure 6.42: Predicted b=B/$\sqrt{n_H}$ as a function of z/r_0 for the solution with λ= 13 and r_0 = 9 AU (Casse & Ferreira, 2000).

-Heating by shocks:

In our data, the bow-shock morphology of the red emission seems compatible with internal jet shocks. In contrary, the morphology of the blue H_2 emission rules out internal jet shocks (except for the peak at 0.1″ with 15 km/s). Hence, the shock could be produced by the wind against the disc or cloud material. Top panel in Fig. 6.40 shows these two possibilities. In the case of a wind shocked against the disc, an outer disc thicker is required to explain the observed morphology, which is expected in a transition between a magnetized and a standard disc (Combet & Ferreira, 2008). As I showed before, the densities pre-shocks predicted are $\leq 10^6$cm^{-3} for shock velocities ranging between 15 and 91 km/s depending on the total density and the magnetic field considered in the model.

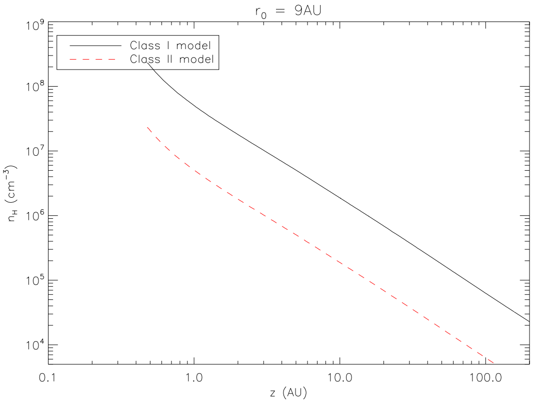

Figure 6.43: Predicted n$_H$ as a function of z for the solution with λ= 13 and r$_0$ = 9 AU (Casse & Ferreira, 2000). The class I model corresponds to a mass accretion rate of 10^{-6} M$_\odot$/yr and the class II model corresponds to 10^{-7} M$_\odot$/yr.

For b=10, as expected from the solution with λ= 13 and r$_0$ = 9 AU from Casse & Ferreira (2000) at z/r$_0$$\sim$10 (Fig. 6.42), the observed ratios and fluxes thus favor the densities of 10^4-10^5cm^{-3} and strong shocks velocities. The densities predicted by shocks are in very good agreement with the n$_H$ $\sim$ 10^4-10^6 cm^{-3}, depending on the mass accretion rate considered, shown in Fig. 6.43 for the streamline of r$_0$= 9AU at vertical scales in the disc of 10-50 AU. However, the jet velocity predicted of $\sim$106 km/s (for an observed velocity of 15 km/s and a shock velocity of $\sim$91 km/s, then jet velocities is the sum of the two), is too fast compared to disc wind predictions for a r$_0$= 9 AU. The alternative fast wide-angle wind (X-wind) coming from the inner disc could be a possibility. However, if the shock is oblique as expected if the wind is impinging on disc atmosphere at $\sim$45°, one would expect to see post-shock radial velocities comparable to the derived shock velocities, which is not observed.

In order to derive the mass-loss rate in the jet, the shock mass-loss rate is corrected from the ratio between the jet and shock velocities. Hence, in the case of b=10, n$_H$=1×10^4 cm^{-3} and v$_s$=91 km/s, the mass-loss rate is $\dot{M}_w$=7.37×10^{-9} and the ejection-accretion ratio is $\geq$0.09. For the solution at λ=13, this ejection-accretion ratio constrains the external-internal radius ratio at $\geq$90. From an observed limit at 10AU for r$_e$ and a probably internal radius of 1AU for which Panoglou et al. (2009) find a significant amount of H$_2$, the expected r$_e$/r$_i$ is rather 10 than 90.

On the contrary, if we consider the other extreme model compatible with observations, with shock velocities similar to the observed radial velocity, b=0.5, n_H=1×10^6 cm^{-3} and v_s=15 km/s, then the mass-loss rate is 7.96×10^{-8} $M_\odot$/yr, and then the ejection-accretion ratio is 0.9 which is not a very physical solution, in addition to the fact that b=0.5 is not compatible with a MHD wind.

The DG Tau H_2 seems complicated to explain assuming shocks in a MHD wind. However, here I only discuss the MHD solution at λ=13 for which detailed predictions were obtained. A detailed analysis of the parameter space is require to find a more suitable solution or to definitively exclude the shocks as the dominant excitation mechanism in the case of th DG Tau molecular emission. Even, at this solution, the intermediary velocities and densities compatibles with observations must be analyzed in more detail taking into account projection effects and the detailed morphology of the emission.

(2): Origin in a shocked disc atmosphere:

The emission observed comes from the disc atmosphere, or the outer walls of a cavity, shocked by a wide angle atomic wind, either stellar or from the disc, as the low velocity component observed in [OI] emission (Lavalley et al., 1997; Coffey et al., 2007) (Middle panel in Fig. 6.40). In this case, the disc is initially at rest, then the shock velocity is similar to the observed line of sight velocity. The shock velocity of the oblique shocks against the disc will be low as observed for the molecular emission in DG Tau. The densities predicted by the shock models at low velocities of 10^5-10^6 cm^{-3}, and a small value of b, agree with the values predicted by the disc atmosphere models by Nomura et al. (2007) at the observed spatial scales (r=10-100 AU and z/r∼0.8). But this models are computed for TW Hya which has a mass accretion rate 10 times lower than that of DG Tau. The difference in the mass accretion rate has a direct influence in the surface density in the disc, then the predicted total density is 10^6-10^7 cm^{-3}. Some solutions are still compatible with the values obtained from the shock models.

The problem in this case is that one expect a redshifted emission and an expansion of the cavity in quite short timescales, unless the ejection of material against the disc is episodic.

(3): Irradiated disc

- **Static photo-dissociation region (PDR) in disc atmosphere**: In this scenario the system is formed by a star emitting UV and X-ray radiation and a disc which is heated by the star radiation and a photo-dissociation region is formed in the disc atmosphere.

Beck et al. (2008) argue against the possibility of excitation by UV-Xray emission coming from the star based on the models by Nomura & Millar (2005); Nomura et al.

(2007). These models derive H_2 emission from a disc irradiated by both X-rays and UV photons from a central T Tauri star. They predict temperatures less than 1000 K for distance to the star of 30-50 AU. Hence, they reproduce neither the H_2 level populations of 2000 K nor the H_2 observed at distances higher than 30 AU. Beck et al. (2008) note that this models can be valid in the case of DG Tau if they underestimate the excitation temperature and spatial scales of the emission in a factor of 2 or 3. But they also note that this seems unlikely. However, it is important to keep in mind that the models by Nomura & Millar (2005); Nomura et al. (2007) are matched to the case of TW Hya, an evolved CTTs with an order of magnitude lower accretion rate and with a FUV flux 60 times lower than that of DG Tau. A model with higher FUV from the central star and taking into account the H_2 as cooling, which is not the case in the current models by Nomura, are required.

Nomura et al. (2007) improve their models of Nomura & Millar (2005) by including the X-ray emission in their calculations. They show that the UV radiation dominates the excitation of the $H_2\lambda2.12\mu$m line but that X-ray radiation can be important. In fact, Gustafsson et al. (2008) conclude than in the case of the T Tauri star T Tau N, the combination of of X-ray and UV-photos are necessary in order to explain the H_2 flux in the context of this scenario. In our case, the expected flux, in units of 10^{-15} erg s^{-1} cm^{-2}, at the Taurus distance is 0.25 if only the X-rays are considered, 2.07 for UV radiation and 3.32 when the X-ray and the UV radiation are combined. The integrated flux for DG Tau is 3×10^{-14} erg s^{-1} cm^{-2} which is a factor 10 higher than the model, even when both X-ray and UV radiation are considered. However, this discrepancy can be solved if we keep in mind that these models are obtained for the particular case of TW Hya which has a mass accretion rate 10 times lower than that of DG Tau. Hence, the predicted total density for spatial scales of z/x=0.8-1 AU (for a x=10AU) are also 10 times lower than the predictions of PDR models (Le Petit et al., 2006) to reproduce the observed fluxes and line ratios.

Relating to the total density, the values predicted by static PDR models are 10^6-10^7cm^{-3} for $G_0=10^5$-3×10^5 (Le Petit et al., 2006), which are one order of magnitude higher than densities predicted by Nomura et al. (2007) for disc atmospheres at 45° and z$\sim$10-100 AU. But again, these models are built for TW Hya and I showed that a simple scaling multiplying by 10 gives densities more compatibles. Hence, a PDR disc model adapted to DG Tau properties is required to fully exclude this alternative.

- **PDR + Photo-evaporation in the disc** (Font et al., 2004). If we only consider a PDR in the disc, we cannot explain the blueshifted emission, an outflow must be created. In this scenario the disc surface is heated by EUV and X-ray radiation coming from the star and a wind is created by photo-evaporation of the disc (bottom panel of Fig. 6.40). The FUV photons can heat the molecular hydrogen by photoelectric effect on grains and if the thermal velocity of the gas exceeds the escape velocity of the disc surface, a flow can be created.

The characteristics radius for thermal evaporation is (Dullemond et al., 2007):

$$r_g \sim 100AU\Big(\frac{T}{1000K}\Big)^{-1}\Big(\frac{M_*}{M_\odot}\Big) \tag{6.11}$$

For the mass of DG Tau, M_*=0.7 $M_\odot$, and the temperature of 2000 K observed for the molecular emission, r_g= 35 AU. Then the photo-evaporation occurs outside $r_{cr} > 0.15\ r_g$ (Dullemond et al., 2007), which corresponds to a $r_{cr} > 5$ AU and 1 AU for the molecular and the [OI] emission respectively. From Fig.6 from Font et al. (2004), the acceleration scale will be within $4r_g$=140 AU and $4r_g$=28 AU for the molecular and atomic emission which could explain the low velocity observed, but this scales would be easily resolved with the current instruments.

However, models by Burton et al. (1990) predict emission in [OI]λ6300Å at the same temperature of H_2 if CO is photodissociated. This is coherent with the transverse PV diagram, Fig. 6.24, where the co-existence of the two emissions is evident. Assuming then the same temperature of 2000 K for the two components, they would be produced at $r_{cr} > 5$ AU. Font et al. (2004) show that the terminal velocity is achieved at distances of $4r_g$=140 AU with a value of three times the sound speed. With sound speed of $\sim$ 5 km/s, the terminal velocity obtained is $\sim$15 km/s, the observed maximum velocity in the molecular emission.

For the atomic component, the mass loss rate due to photo-evaporation can be obtained by (Hollenbach et al., 1994):

$$\dot{M}_{wind} \simeq 4\times10^{-10}\Big(\frac{\Phi}{10^{41}s^{-1}}\Big)^{1/2}\Big(\frac{M_*}{M_\odot}\Big)^{1/2}M_\odot yr^{-1} \tag{6.12}$$

For Φ of 10^{41}-10^{44} photos s^{-1}, typical for CTTs, the mass loss rate for the atomic component will be between 2.9×10^{-10}-1.2×10^{-8} $M_\odot yr^{-1}$. An estimation of the mass loss rate in the low velocity "halo" observed in [OI] by Lavalley et al. (1997) would be desirable in order to test this scenario.

6.5 Conclusions

In this chapter I presented SINFONI observations, in both H and K bands, for the microjet associated to the DG Tau classical T Tauri star. A thorough analysis of the [FeII] atomic and H_2 molecular emissions was carried out. The main conclusions are the following:

Atomic emission:

- A nested velocity structure, already observed in the optical domain, is observed. The observed high velocity component with opening angles of 6°-7° would be nested by the medium velocity component which shows an opening angle of 23°.

- Important asymmetries in the transverse density close to the star are detected. These asymmetries could be related to the jet axis wiggling detected in the blue high velocity component which can be reproduced by a low mass stellar companion at 3-4.5 AU and of 0.15-0.4 $M_\odot$.

- A qualitative analysis of the iron depletion is present, showing that it is more important at medium velocities than for the higher ones. I showed that for the medium velocities, the correction factor to apply is up to 10 to the medium velocities and 6-7 for the high velocity component.

- Revised mass-flux are given, taking into account the iron depletion in the methods using the iron luminosity. An average value in the central 1″ of 4×10^{-8} $M_\odot$/yr is obtained.

- A comparison with predictions from a MHD wind model with λ=13, well reproducing previous optical observations and showing synthetic PV diagrams compatible with the observed iron HVC, gives a range in the launching radii > 45.

Molecular emission:

- The observed low velocity cavity in H_2 extends the nested structure observed in the atomic component. From the transverse PV, no direct connection is seen between the H_2 emission and the [FeII], but with the [OI] emission at very low velocities. It is not clear if this low emission in [OI] is the same atomic component observed at higher velocities or a new one.

- Origin of this emission
  - In the case of a MHD wind, only the solution at λ=13 was analyzed. For this solution, the emission seems difficult to be explained by excitation by shocks and a excitation by ambipolar diffusion seems more compatible. In this last case, a constrain in the internal radius of 5AU has been found. However, in the case of ambipolar diffusion the predicted densities are maybe too low to achieve the LTE in the level population and the expected flux are too low compared to the observed one. Nevertheless, this is only one of the possible solutions, a detailed analysis of parameter space for the MHD solutions is strongly required to favor or reject one or both scenarios.
  - An origin in a shocked disc atmosphere seems unlikely because one expect an expansion of the cavity in short-time scales due to the shock velocity. Moreover, the emission is expected to be redshifted, but this is not a very strong argument since the observed velocity is in average compatible with zero velocity. In contrary, a photo-dissociation region in the disc surface and a evaporated wind produced by the irradiation by the star is a promising scenario for this wide and low molecular emission which must be study in more detail.

In summary, the aim of this analysis was to give some clues for future deep analyses. The analysis is limited first to only one MHD solution, in the case of the MHD hypothesis and the models by Panoglou et al. (2009) does not consider yet the shocks in the computation, which will be a very important improvement within predictions for the line fluxes and line ratios. On the other side, the disc models by Nomura et al. (2007) are adapted to the particular case of TW Hya, a star with a mass accretion rate 10 times lower than that of DG Tau and with a UV radiation also much lower. A model adapted to the particular case of DG Tau is desirable.

In addition, a more detailed kinematics of the H_2 cavity, within a more completed study of the connection between the [OI] and the H_2 emissions, at different positions along the jet, are required to better constrain these scenarios.

7

Conclusions

The work carried out in this thesis was motivated at the beginning by an evident need in the community to obtain observational constrains which allow to probe the existing scenarios and models to explain the jet phenomenon, not only related to young stellar objects but also to the broad kind of objects showing jets.

Since the first observational evidences of the existence of jets associated to young stellar objects, models to explain the ejection mechanism have been strongly improved, also based in a very important observational finding which relates this phenomenon with the accretion material coming from the surrounding disc and falling onto the star (Cabrit et al., 1990; Hartigan et al., 1995). However, distinguishing between an origin in the disc, the region of interaction between the stellar magnetosphere and the disc or in the star itself, was and still remains very complicated. All the efforts carried out to obtain more and more detailed models were evidently supported by a big observational effort. The works carried out by Hartigan et al. (1995) or Hirth et al. (1997) over a significant number of sources gave the first clues to analyze in more detail the more promising sources. The necessity as clear to observe these objects at the highest spatial and spectral resolution possible to reach the regions where the ejection and collimation process occur. Following this aim, the works by Lavalley et al. (1997) or Dougados et al. (2000) using adaptive optics, or those by Bacciotti et al. (2000) or Woitas et al. (2002) using space observations with HST and the work by Lavalley-Fouquet et al. (2000) using IFS techniques led to important advances in our understanding of the accretion-ejection phenomenon (Sec. 2). However, when I started my thesis, the number of sources studied in detail with high resolution techniques was still very small, only 15 were observed using HST/STIS and only 3 using IFS. In my thesis I studied two objects, RY Tau and DG Tau, combining IFS and AO techniques to carry out a thorough morphological and kinematical study simultaneously, with a very good angular resolution and a medium spectral resolution. Each one of the two sources was chosen to answer two particular distinct issues included and described within the objectives of this thesis in Sec. 2:

- *What is the effect of the source properties on the jet properties?*

  – Effect of the stellar mass

When I started my thesis, any study of the variation of the jet properties with the central source mass had not been achieved in detail. For this purpose, the star RY Tau was observed. This star, of 2 $M_\odot$, allows me to analyze the properties of the jet in the case of a mass intermediate between the classical T Tauri stars and the Herbig Ae/Be star.

The similarity in the jet properties for RY Tau, in morphology, kinematics and in the mass-loss rate estimate, compared to those in other T Tauri stars with a lower mass supports the idea that the jet launching mechanism is universal over a broad range of stellar masses. Firstly, it shows a similar morphology, with jet widths of 30-40 AU and a full opening angle of 5° on spatial scales of 20-280 AU. Secondly, the mean jet centroid radial velocity is -70 ± 5 km/s but it shows a peak of -90 km/s at the same position as a peak in emission, at $1.35''$ from the star. An intermediate jet inclination to the line of sight between 45° and 77° was estimated and true flow velocity between 100 and 300 km/s was derived, also compatible with lower mass CTTs.

Finally, the transverse jet kinematic structure near the knot position shows a 3σ transverse velocity shift which can be caused by the wings of a bowshock placed at the peak emission or by jet rotation. The angular resolution of the data is insufficient to distinguish between the two possibilities.

The analysis of the atomic emission in the NIR [FeII]$\lambda1.64\mu$m line of the DG Tau star, with a typical classical T Tauri stellar mass of 0.7 $M_\odot$, also supports this idea. However, the DG Tau jet shows a more complex morphology.

DG Tau is one of the most studied CTTs, and it has already been studied using IFS in the optical (Lavalley-Fouquet et al., 2000) and in the NIR using high spectral resolution long-slit observations (Pyo et al., 2003), but a detailed study of the morphology, kinematics and the excitations conditions had not been carried out simultaneously using spectro-imaging in the NIR.

The analysis carried out here reveals a nested structure with the gas at higher velocities being more collimated and nested inside the gas at medium velocities. The red emission is partially hidden by the circumstellar disc. In the bueshifted jet, an opening angle of 6°-7° is measured until $0.9''$ from the star for the high velocity component and beyond this distance it is twice broader and shows an emission knot at $1.2''$. The velocity component at medium velocity shows an opening angle of 23°.

The red emission shows a clear bowshock morphology and is in average wider than the blue jet. This behavior is compatible with previous observations in the optical.

The kinematics of the atomic emission shows also velocities similar to other T Tauri stars, including RY Tau. A high velocity component at -230 km/s and a medium velocity component at -110 km/s are observed in the blueshifted emission. In this case, a low velocity component is not observed. The corresponding velocities in the redshifted emission are lower than in the blue jet, 186 km/s and 29 km/s for the high and medium velocity component respectively.

Studies of more sources comprising a large range in central source masses, not only T Tauri stars, is needed to be able to establish some global conclusions about the effect of the central source mass on the jet properties. Up to know, studies such as that by Perrin & Graham (2007) have shown that the properties of Herbig Ae jets are similar to those of T Tauri stars. In particular, Perrin & Graham (2007) studied the star LkH$_\alpha$ 233, a star more massive than RY Tau (with a revised mass of 4 M$_\odot$), and they found that with an opening angle of 9° and a mass flux of $1.2 \pm 0.3\times10^{-7}$ M$_\odot$/yr, it shows similar properties of kinematics, collimation, knotty appearance, electron density and estimated mass flux than for other T Tauri stars. On the other side of the mass spectrum, studies in brown dwarf (e. g. Whelan et al., 2009) show also the presence of jets similar to those found in CTTs, also observed in FEL. In particular they detect an outflow component to the LS-RCrA 1 H$_\alpha$ line and a LVC to the FELs. They even detect a molecular component to the optical outflow of LS-RCrA 1 and ISO-Oph 102. However they demonstrate that mass loss rate in BDs is comparble to the accretion mass rate.

– Effect of the source multiplicity

This was one of the objectives of this thesis and the star RY Tau was chosen for its binary status to probe the jet properties in a binary system. However, the good agreement between the measured jet PA and the expected PA for the binary system, obtained from the photocenter variations in the Hipparcos observations, calls into question the interpretation of binarity. An alternative interpretation to the photocenter variations is that they could be caused by UXOr-like occultation events and/or contribution from a scattering cavity.

In contrary, the measured jet wiggling in DG Tau could indicate a possible companion at 3-4 AU. A companion at this distance could have an important influence especially in the atomic wind if we assume a disc wind origin (predicted launching radius for the atomic component of ∼3 AU), but probably also in the accretion onto the star.

The binarity of the RY Tau and DG Tau stars must be tested in order to clarify this issue. On the other hand, other sources, proved to be part of a multiple system and showing evidence of having jets, should be studied to determine the possible effect on the jet or jets properties and which finally could not be analyzed here.

– Mass loss rate estimates

The mass flux is a very important parameter to contrain models but which is difficult to estimate accurately. The previous estimates should be reviewed with better resolution instruments and as a function of the distance to the star. For example, our estimate of the mass loss rate in the case of RY Tau is 4 times higher than the previous estimates from integrated spectroscopy.

Different methods have been used to determine the mass loss rate in the jet in both RY Tau and DG Tau. The different methods give similar results considering the uncertainties in the parameters used for their estimate. The values range between 0.16×10^{-8} and 2.6×10^{-8} $M_\odot$/yr for RY Tau and between 8×10^{-9} and 7×10^{-8} $M_\odot$/yr for DG Tau, depending on the considered method. An average value of $4\ \times10^{-8}$ $M_\odot$/yr give an ejection-accretion ratio ranging between 0.08 and 0.4 for DG Tau and between 0.02 and 0.4 for RY Tau, with a most probable value of 0.1 in the two cases.

- *What is the origin of the near-IR molecular emission in CTTs what is its relation with the atomic emission?*

Very few spatially resolved studies have been made of the near-infrared molecular emission in CTTs and different origins have been proposed and discussed. I carry out a similar discussion about the molecular emission observed in DG Tau. The main properties of this emission are the low velocities, compatibles with 0 km/s, and the wide morphology which in the case of DG Tau shows in addition a cavity morphology. I discussed all the scenarios which in my opinion could be the origin of this emission and I tried to give as many constraints as possible to clarify this issue. The large number of parameters and possibilities for each of the scenarios make the discussion very complicated. With the only aim of giving some clues to more detailed future works, I limit the analysis of the MHD models to one of the solutions, λ=13, which explains satisfactorily previous observations of the transverse structure of the DG Tau. However, any of the scenarii presented cannot be completely excluded from our data and in a first analysis. A deeper analysis and study of the models cquoted are required to definitely favor one over another.

However, among all the possible scenarii, the *X-wind* is difficult to reconcile with the observations because of the high fluid velocity predicted by this kind of model and the low velocity observed. In the context of a *disc wind*, on the other hand, an excitation by shocks seems difficult to explain the observations. The model considering heating by ambipolar diffusion is more promising. An alternative solution, a *photo-evaporated wind* coming from a PDR at the disc surface, explains on one side the morphology and velocities of the molecular H_2 emission, but also the coexistence of the atomic [OI] emission at very low velocities with the H_2 emission.

7.1 Perspective and future work

Among all the open questions related to ejection mechanism in young stellar objects, only two of them were the main subject of this thesis work. Important results have been obtained and when a definitive conclusion was not possible, the most restrictive constraints as possible were given, indicating directions for future works. However, new problems have also been revealed.

Despite the detailed analysis carried out here for RY Tau and DG Tau, more similar spectro-imaging studies, both in the optical and near-IR domain, in other objects are required to be able to consolidate global conclusions and results which really constrain the models. In particular, to confirm the finding that the jet properties does not change with the mass of the central star, as shown here. But also, to test the influence of other parameters, as the binary status, which could not be explored here. One of the most important parameters for constraining models, the mass loss rate, must be determined for more stars and at different positions from the star. The determinations obtained here using spectro-imaging observations showed that the previous estimatesfrom long-slit spectroscopy can be wrong by an order of magnitude because they assume a uniform density and they overestimate the size scale of the emission. Two future projects, MUSE at the VLT and NIRSPEC at the JWST, are particularly interesting for the jet study in order to improve these kind of studies.

In addition, extending the common studies in the optical to the near infrared is also important to test the jet properties in different excitation conditions and to clarify the origin of the molecular component observed in some objects. Is this molecular component common in all the T Tauri stars? Do its properties change with the properties of the central star? What is the exact relationship with the atomic component?

In particular, from a point of view of modelling, in order to advance in the understanding of the near-IR H_2 molecular emission (as that shown in this thesis), existing models have to be improved to adapt them to the particular physical conditions of gas in T Tauri stars. For example, in the case of MHD models, a thorough study of the parameters space is crucial to determine the best solution for these kind of objects. Then, the models by Panoglou et al. (2009) should include shocks in their calculations. In the particular case of DG Tau, since it is one of the most observed CTTs, it is desirable to have predictions as those shown by the PDR disc surface models by Nomura et al. (2007) for a central star with similar properties as DG Tau. In addition, the evidence of depletion in dust grains must be also modelled and the effect of dust in shocks must be analyzed.

More general, non-stationary numerical models have been recently developed. Murphy and collaborators have numerical simulations of the evolution of a MHD jet reaching large scales comparable with those observed by the current instruments. Besides, in order to better constrains the models, it is also required that models obtain more predictions in line fluxes and line ratios and if it is possible to product also predicted position-velocity diagrams and emissions maps for direct comparison with observations. These predicted diagrams must also take into account the projection effects and the instrumental limitations inherent to observational data, like the spectral and spatial resolutions and the instrumental response. An important effort considering this is being carried out. A project of a pipeline called OpenSESAMe [1] which can produce synthetic PV and channel maps has started within the Jetset European Marie Curie research and training network[2].

From the observational point of view, I showed that the dust depletion is a very promising tool to constrain the launching regions in jets. As Nisini et al. (2005) showed in the case of HH1, and I also showed here in the case of DG Tau, Fe gas phase depletion onto the dust grains can be up to 80% and must be taken into account in the mass loss rate estimations using methods based in the iron luminosity. To obtain an accurate value of the iron depletion, lines not affected by depletion, like for example [OI] lines, must be observed simultaneously with the iron lines. An observational project leaded by Dr. Podio is already proposed at spatial scales of >1000 AU but studies at scales less than 100 AU are required. In the near-IR it is also possible to observe simultaneously Iron and Phosphorus lines to estimate depletion. Oliva et al. (2001) suggested to use the ratio between [FeII]$\lambda 1.25\mu$m and [PII]$\lambda 1.18\mu$m since Phosphorus is also a non-refractory specie and the excitation conditions between these two lines are similar..

In addition, DG Tau has a particularity which has not been taken into account here but which must be considered in future works. DG Tau is the only CTTs showing spatially extended X-ray emission from a jet (Güdel et al., 2005, 2008). It shows soft emission extending out to 5$''$, not compatible with a point source origin (Güdel et al., 2008). The authors show that the soft emission comes from the base of the jet and Schneider & Schmitt (2008) find a spatial offset between the soft and the hard central components, supporting this idea. Very recently, Günther et al. (2009), analyze these observations using a simple, analytical model for outflow where the outer wind is launched from the disc whereas the origin of the inner jets could be either the inner disc region or the star. They assume a simple cylindrical geometry for the post-shock flow and the innermost outflow region moves at a velocity high enough to heat the post-shocked material to X-ray emitting temperatures. They found that the emission is well explained by a shock, even if the cause of the shock is not completely clear. The emission would arise from the fastest and innermost component of the optical outflow, with densities higher than 10^5 cm^{-3}. This region would be a thin layer,since only a small fraction of the total mass loss is needed to

---

[1] http://homepages.dias.ie/~jgracia/OpenSESAMe/

[2] http://www.jetsets.org/home.html

explain the observed luminosity. This emission, combined with the emission coming from the star should be considered in the disc models, since this emission is distributed above the inner accretion disc and therefore it will illuminate the disc in near normal incidence, maximizing the irradiation effects in the outer disc. X-ray emission like that observed in DG Tau have been first observed in HH 2 (Pravdo et al., 2001) and HH 154 (Favata et al., 2002). This last one was satisfactory explained by a two-dimensional hydrodynamic numerical model by Bonito et al. (2007). As noted by Güdel et al. (2008), this kind of jet X-ray emission is probably present in other proto-stellar jets but it is difficult to detect because of absorption effects. This is a very recent domain of research but it must be studied in more detailed and taken into account by the future models.

However, the main problem remains the same, we need to reach the most internal parts of the system to have access to the spatial scales where the ejection and collimation take place. Hence, instruments and techniques achieving even better angular resolution are crucial. The more promising techniques to achieve sub-AU resolution are IR interferometry with the spectrograph AMBER at the VLT or spectro-astrometric analysis. Spectro-astrometry is a powerful technique which recovers important spatial information from a spectrum beyond the limitations of the seeing. It could be used for example to measure the position of the source very accurately by fitting a Gaussian to the spatial profile across the whole wavelength range. This technique is already been used in the study of young stellar outflows, in particular, it has been used to dis-entangle outflow components within lines such as H_α or Pa_β (Whelan et al., 2004) and to discover the first outflow from a brown dwarf (Whelan et al., 2005). Of particular interest is to apply this technique to 2D IFS observations. On the other hand, interferometry provides a unique mean for direct investigation of the inner regions of the jet and of the accretion funnels flows, on sub-AU scales. Pioneering studies are already conducted on Herbig AeBe stars by Dr. Benisty and an observational campaign to extend these studies to T Tauri stars driving large scale jets is in project. The combinations of spectro-imaging and AMBER/VLTI data on a few selected objects will allow to study the link of the flow properties between sub-AU to 10 AU scales, i.e., precisely the region where collimation is achieved and terminal velocities are reached.

Finally, the ALMA interferometer will allow to extend the study of the warm molecular emission detected in the near-IR H_2 lines to the cold molecular jet component, probing the outer layers of the flow, with unprecedent spatial resolution (a few AUs). These observations will allow to establish the link between the two molecular components and they will provide additional constraints for launching models: indeed the survival of molecules in the outer layers of the flow restricts the range of possible launching radii.

In the forthcoming years, the very promising future improvements both in observational instruments, such VLTI or ALMA, and in modelling, with the increasing number of numerical simulations, will allow major advances in the understanding of the ejection-accretion problem in young stellar objects, but also applicable to other astrophysical domains.

Bibliography

Agra-Amboage, V., Dougados, C., Cabrit, S., Garcia, P. J. V., & Ferruit, P. 2009, *A&A*, 493, 1029

Allington-Smith, J. & Content, R. 1998, *PASP*, 110, 1216

Anderson, J. M., Li, Z.-Y., Krasnopolsky, R., & Blandford, R. D. 2003, *ApJ*, 590, L107

Andre, P. 1997, in IAU Symposium, Vol. 182, Herbig-Haro Flows and the Birth of Stars, ed. B. Reipurth & C. Bertout, 483–494

Andre, P., Ward-Thompson, D., & Barsony, M. 2000, Protostars and Planets IV, 59

Anglada, G., López, R., Estalella, R., et al. 2007, *AJ*, 133, 2799

Appenzeller, I., Oestreicher, R., & Jankovics, I. 1984, *A&A*, 141, 108

Arnaud, M. & Rothenflug, R. 1985, *A&AS*, 60, 425

Arribas, S., Mediavilla, E., García-Lorenzo, B., del Burgo, C., & Fuensalida, J. J. 1999, *A&AS*, 136, 189

Asplund, M., Grevesse, N., & Sauval, A. J. 2005, in Astronomical Society of the Pacific Conference Series, Vol. 336, Cosmic Abundances as Records of Stellar Evolution and Nucleosynthesis, ed. T. G. Barnes, III & F. N. Bash, 25–+

Bacciotti, F. 2002, in Revista Mexicana de Astronomia y Astrofisica, vol. 27, Vol. 13, Revista Mexicana de Astronomia y Astrofisica Conference Series, ed. W. J. Henney, W. Steffen, L. Binette, & A. Raga, 8–15

Bacciotti, F., Chiuderi, C., & Oliva, E. 1995, *A&A*, 296, 185

Bacciotti, F. & Eislöffel, J. 1999, *A&A*, 342, 717

Bacciotti, F., Mundt, R., Ray, T. P., et al. 2000, *ApJ*, 537, L49

Bachiller, R., Martin-Pintado, J., Tafalla, M., Cernicharo, J., & Lazareff, B. 1990, *A&A*, 231, 174

Bacon, R., Adam, G., Baranne, A., et al. 1995, *A&AS*, 113, 347

Bally, J., Reipurth, B., & Davis, C. J. 2007, in Protostars and Planets V, ed. B. Reipurth, D. Jewitt, & K. Keil, 215–230

Basri, G., Martin, E. L., & Bertout, C. 1991, *A&A*, 252, 625

Bautista, M. A. & Pradhan, A. K. 1998, *ApJ*, 492, 650

Beck, T. L., McGregor, P. J., Takami, M., & Pyo, T.-S. 2008, *ApJ*, 676, 472

Beck-Winchatz, B., Bohm, K. H., & Noriega-Crespo, A. 1994, *PASP*, 106, 1271

Beck-Winchatz, B., Bohm, K.-H., & Noriega-Crespo, A. 1996, *AJ*, 111, 346

Becklin, E. E., Neugebauer, G., Willner, S. P., & Matthews, K. 1978, *ApJ*, 220, 831

Bergin, E. A., Aikawa, Y., Blake, G. A., & van Dishoeck, E. F. 2007, in Protostars and Planets V, ed. B. Reipurth, D. Jewitt, & K. Keil, 751–766

Bertout, C. 1989, *ARA&A*, 27, 351

Bertout, C., Basri, G., & Bouvier, J. 1988, *ApJ*, 330, 350

Bertout, C., Robichon, N., & Arenou, F. 1999, *A&A*, 352, 574

Binette, L., Cabrit, S., Raga, A., & Cantó, J. 1999, *A&A*, 346, 260

Bonito, R., Orlando, S., Peres, G., Favata, F., & Rosner, R. 2007, *A&A*, 462, 645

Bontemps, S., Andre, P., Terebey, S., & Cabrit, S. 1996, *A&A*, 311, 858

Burton, M. G., Hollenbach, D. J., & Tielens, A. G. G. M. 1990, *ApJ*, 365, 620

Cabrit, S. 2002, in EAS Publications Series, Vol. 3, EAS Publications Series, ed. J. Bouvier & J.-P. Zahn, 147–182

Cabrit, S. 2007a, in Lecture Notes in Physics, Berlin Springer Verlag, Vol. 723, Lecture Notes in Physics, Berlin Springer Verlag, ed. J. Ferreira, C. Dougados, & E. Whelan, 21–+

Cabrit, S. 2007b, in IAU Symposium, Vol. 243, IAU Symposium, ed. J. Bouvier & I. Appenzeller, 203–214

Cabrit, S., Codella, C., Gueth, F., et al. 2007, *A&A*, 468, L29

Cabrit, S., Edwards, S., Strom, S. E., & Strom, K. M. 1990, *ApJ*, 354, 687

Calvet, N. & Gullbring, E. 1998, *ApJ*, 509, 802

Calvet, N. & Hartmann, L. 1992, *ApJ*, 386, 239

Calvet, N., Muzerolle, J., Briceño, C., et al. 2004, *AJ*, 128, 1294

Canto, J. & Raga, A. C. 1991, *ApJ*, 372, 646

Casse, F. & Ferreira, J. 2000, *A&A*, 361, 1178

Chen, W. P., Howell, R. R., Simon, M., & Benson, J. A. 1992, *ApJ*, 387, L43

Chrysostomou, A., Bacciotti, F., Nisini, B., et al. 2005, in Protostars and Planets V, 8156–+

Coffey, D., Bacciotti, F., & Podio, L. 2008, *ApJ*, 689, 1112

Coffey, D., Bacciotti, F., Ray, T. P., Eislöffel, J., & Woitas, J. 2007, *ApJ*, 663, 350

Coffey, D., Bacciotti, F., Woitas, J., Ray, T. P., & Eislöffel, J. 2004, *ApJ*, 604, 758

Colavita, M., Akeson, R., Wizinowich, P., et al. 2003, *ApJ*, 592, L83

Combet, C. & Ferreira, J. 2008, *A&A*, 479, 481

Content, R. 2006, New Astronomy Review, 50, 267

D'Antona, F. & Mazzitelli, I. 1994, *ApJS*, 90, 467

Davis, C. J., Berndsen, A., Smith, M. D., Chrysostomou, A., & Hobson, J. 2000, *MNRAS*, 314, 241

Davis, C. J., Ray, T. P., Desroches, L., & Aspin, C. 2001, *MNRAS*, 326, 524

Decampli, W. M. 1981, *ApJ*, 244, 124

Dopita, M. A. & Sutherland, R. S. 1996, *ApJS*, 102, 161

Dougados, C., Cabrit, S., Ferreira, J., et al. 2004, *Ap&SS*, 292, 643

Dougados, C., Cabrit, S., Lavalley, C., & Ménard, F. 2000, *A&A*, 357, L61

Draine, B. T. 2004, in The Cold Universe, Saas-Fee Advanced Course 32, Springer-Verlag, 308 pages, 129 figures, Lecture Notes 2002 of the Swiss Society for Astronomy and Astrophysics (SSAA), Springer, 2004. Edited by A.W. Blain, F. Combes, B.T. Draine, D. Pfenniger and Y. Revaz, ISBN 354040838x, p. 213, ed. A. W. Blain, F. Combes, B. T. Draine, D. Pfenniger, & Y. Revaz , 213–+

Dullemond, C. P., Hollenbach, D., Kamp, I., & D'Alessio, P. 2007, in Protostars and Planets V, ed. B. Reipurth, D. Jewitt, & K. Keil, 555–572

Edwards, S. 1997, in IAU Symposium, Vol. 182, Herbig-Haro Flows and the Birth of Stars, ed. B. Reipurth & C. Bertout, 433–442

Edwards, S., Cabrit, S., Strom, S. E., et al. 1987, *ApJ*, 321, 473

Edwards, S., Hartigan, P., Ghandour, L., & Andrulis, C. 1994, *AJ*, 108, 1056

Eisenhauer, F., Abuter, R., Bickert, K., et al. 2003, in Presented at the Society of Photo-Optical Instrumentation Engineers (SPIE) Conference, Vol. 4841, Society of Photo-Optical Instrumentation Engineers (SPIE) Conference Series, ed. M. Iye & A. F. M. Moorwood, 1548–1561

Esposito, S. & Pinna, E. 2008, in Lecture Notes in Physics, Berlin Springer Verlag, Vol. 742, Lecture Notes in Physics, Berlin Springer Verlag, ed. F. Bacciotti, L. Testi, & E. Whelan, 45–+

Favata, F., Fridlund, C. V. M., Micela, G., Sciortino, S., & Kaas, A. A. 2002, *A&A*, 386, 204

Ferreira, J., Dougados, C., & Cabrit, S. 2006, *A&A*, 453, 785

Ferreira, J., Pelletier, G., & Appl, S. 2000, *MNRAS*, 312, 387

Flower, D. R. & Pineau des Forêts, G. 2003, *MNRAS*, 343, 390

Font, A. S., McCarthy, I. G., Johnstone, D., & Ballantyne, D. R. 2004, *ApJ*, 607, 890

Fragile, P. C., Anninos, P., Gustafson, K., & Murray, S. D. 2005, *ApJ*, 619, 327

García, P. 1999, PhD thesis, Université Claude Bernard, Lyon

Garcia, P. J. V., Cabrit, S., Ferreira, J., & Binette, L. 2001a, *A&A*, 377, 609

Garcia, P. J. V., Ferreira, J., Cabrit, S., & Binette, L. 2001b, *A&A*, 377, 589

García-Díaz, M. T., López, J. A., García-Segura, G., Richer, M. G., & Steffen, W. 2008, *ApJ*, 676, 402

García-Segura, G., López, J. A., & Franco, J. 2005, *ApJ*, 618, 919

Giannini, T., McCoey, C., Nisini, B., et al. 2006, *A&A*, 459, 821

Güdel, M., Skinner, S. L., Audard, M., Briggs, K. R., & Cabrit, S. 2008, *A&A*, 478, 797

Güdel, M., Skinner, S. L., Briggs, K. R., et al. 2005, *ApJ*, 626, L53

Gueth, F. & Guilloteau, S. 1999, *A&A*, 343, 571

Guillet, V., Jones, A. P., & Pineau Des Forêts, G. 2009, *A&A*, 497, 145

Gullbring, E., Calvet, N., Muzerolle, J., & Hartmann, L. 2000, *ApJ*, 544, 927

Gullbring, E., Hartmann, L., Briceno, C., & Calvet, N. 1998, *ApJ*, 492, 323

Günther, H. M., Matt, S. P., & Li, Z.-Y. 2009, *A&A*, 493, 579

Gustafsson, M., Labadie, L., Herbst, T. M., & Kasper, M. 2008, *A&A*, 488, 235

Habing, H. J. 1968, *Bull. Astron. Inst. Netherlands*, 19, 421

Hartigan, P. 2008, in Lecture Notes in Physics, Berlin Springer Verlag, Vol. 742, Lecture Notes in Physics, Berlin Springer Verlag, ed. F. Bacciotti, L. Testi, & E. Whelan, 15–+

Hartigan, P., Edwards, S., & Ghandour, L. 1995, *ApJ*, 452, 736

Hartigan, P. & Morse, J. 2007, *ApJ*, 660, 426

Hartigan, P., Morse, J. A., & Raymond, J. 1994, *ApJ*, 436, 125

Hartigan, P., Raymond, J., & Pierson, R. 2004, *ApJ*, 614, L69

Hartmann, L., Avrett, E., & Edwards, S. 1982, *ApJ*, 261, 279

Hartmann, L., Hewett, R., & Calvet, N. 1994, *ApJ*, 426, 669

Hartmann, L. & MacGregor, K. B. 1980, *ApJ*, 242, 260

Hirth, G. A., Mundt, R., & Solf, J. 1997, *A&AS*, 126, 437

Hollenbach, D., Johnstone, D., Lizano, S., & Shu, F. 1994, *ApJ*, 428, 654

Johns-Krull, C. M. 2009, Hot Inner Winds from T Tauri Stars, ed. Tsinganos, K., Ray, T., & Stute, M. (Springer Berlin Heidelberg), 33–41

Jones, A. P., Tielens, A. G. G. M., Hollenbach, D. J., & McKee, C. F. 1994, *ApJ*, 433, 797

Kenyon, S. J. & Hartmann, L. 1995, *ApJS*, 101, 117

Kingdon, J. B. & Ferland, G. J. 1996, *ApJS*, 106, 205

Koenigl, A. 1991, *ApJ*, 370, L39

Konigl, A. & Pudritz, R. E. 2000, Protostars and Planets IV, 759

Kravtsova, A. S. 2003, Astronomy Letters, 29, 463

Kristensen, L. E., Ravkilde, T. L., Pineau Des Forêts, G., et al. 2008, *A&A*, 477, 203

Kuhi, L. V. 1964, *ApJ*, 140, 1409

Kwan, J. & Tademaru, E. 1988, *ApJ*, 332, L41

Lada, C. J. 1987, in IAU Symposium, Vol. 115, Star Forming Regions, ed. M. Peimbert & J. Jugaku, 1–17

Landini, M. & Monsignori Fossi, B. C. 1990, *A&AS*, 82, 229

Lavalley, C. 2000, PhD thesis, AA(Université Joseph Fourier (Grenoble 1))

Lavalley, C., Cabrit, S., Dougados, C., Ferruit, P., & Bacon, R. 1997, *A&A*, 327, 671

Lavalley-Fouquet, C., Cabrit, S., & Dougados, C. 2000, *A&A*, 356, L41

Le Petit, F., Nehmé, C., Le Bourlot, J., & Roueff, E. 2006, *ApJS*, 164, 506

Leinert, C., Haas, M., Mundt, R., Richichi, A., & Zinnecker, H. 1991, *A&A*, 250, 407

López-Martín, L., Cabrit, S., & Dougados, C. 2003, *A&A*, 405, L1

Lucy, L. B. 1974, *AJ*, 79, 745

Masciadri, E. & Raga, A. C. 2002, *ApJ*, 568, 733

Matt, S. & Pudritz, R. E. 2005, *ApJ*, 632, L135

Melnikov, S., Woitas, J., Eislöffel, J., et al. 2008, *A&A*, 483, 199

Melnikov, S. Y., Eislöffel, J., Bacciotti, F., Woitas, J., & Ray, T. P. 2009, *A&A*, 506, 763

Mendoza, C. 1983, in IAU Symposium, Vol. 103, Planetary Nebulae, ed. D. R. Flower, 143–172

Meyer, M. R., Calvet, N., & Hillenbrand, L. A. 1997, *AJ*, 114, 288

Mora, A., Merín, B., Solano, E., et al. 2001, *A&A*, 378, 116

Motta, V. 2003, PhD thesis, Instituto de Astrofísica de Canarias

Mundt, R. 1984, *ApJ*, 280, 749

Muzerolle, J., Calvet, N., & Hartmann, L. 1998a, *ApJ*, 492, 743

Muzerolle, J., Hartmann, L., & Calvet, N. 1998b, *AJ*, 116, 2965

Nisini, B., Bacciotti, F., Giannini, T., et al. 2005, *A&A*, 441, 159

Nisini, B., Caratti o Garatti, A., Giannini, T., & Lorenzetti, D. 2002, *A&A*, 393, 1035

Nomura, H., Aikawa, Y., Tsujimoto, M., Nakagawa, Y., & Millar, T. J. 2007, *ApJ*, 661, 334

Nomura, H. & Millar, T. J. 2005, *A&A*, 438, 923

Nussbaumer, H. & Storey, P. J. 1988, *A&A*, 193, 327

Oliva, E., Marconi, A., Maiolino, R., et al. 2001, *A&A*, 369, L5

Osterbrock, D. E. 1989, Astrophysics of gaseous nebulae and active galactic nuclei, ed. U. S. Books (University Science Books)

Panoglou, D., Cabrit, S., Pineau des Forêts, G., et al. 2009, *A&A*, in prep.

Perrin, M. D. & Graham, J. R. 2007, *ApJ*, 670, 499

Pesenti, N., Dougados, C., Cabrit, S., et al. 2004, *A&A*, 416, L9

Pesenti, N., Dougados, C., Cabrit, S., et al. 2003, *A&A*, 410, 155

Petrov, P. P., Zajtseva, G. V., Efimov, Y. S., et al. 1999, *A&A*, 341, 553

Pety, J., Gueth, F., Guilloteau, S., & Dutrey, A. 2006, *A&A*, 458, 841

Podio, L., Bacciotti, F., Nisini, B., et al. 2006, *A&A*, 456, 189

Podio, L., Medves, S., Bacciotti, F., Eislöffel, J., & Ray, T. 2009, *A&A*, 506, 779

Pravdo, S. H., Feigelson, E. D., Garmire, G., et al. 2001, *Nature*, 413, 708

Pudritz, R. E., Ouyed, R., Fendt, C., & Brandenburg, A. 2007, in Protostars and Planets V, ed. B. Reipurth, D. Jewitt, & K. Keil, 277–294

Pyo, T.-S., Kobayashi, N., Hayashi, M., et al. 2003, *ApJ*, 590, 340

Ray, T., Dougados, C., Bacciotti, F., Eislöffel, J., & Chrysostomou, A. 2007, in Protostars and Planets V, ed. B. Reipurth, D. Jewitt, & K. Keil, 231–244

Ray, T. P., Mundt, R., Dyson, J. E., Falle, S. A. E. G., & Raga, A. C. 1996, *ApJ*, 468, L103+

Raymond, J. C. 1979, *ApJS*, 39, 1

Richardson, W. H. 1972, Journal of the Optical Society of America (1917-1983), 62, 55

Romanova, M. M., Ustyugova, G. V., Koldoba, A. V., & Lovelace, R. V. E. 2009, *MNRAS*, 399, 1802

Sauty, C., Trussoni, E., & Tsinganos, K. 2002, *A&A*, 389, 1068

Sauty, C. & Tsinganos, K. 1994, *A&A*, 287, 893

Savage, B. D. & Sembach, K. R. 1996, *ARA&A*, 34, 279

Schneider, P. C. & Schmitt, J. H. M. M. 2008, *A&A*, 488, L13

Shang, H., Li, Z.-Y., & Hirano, N. 2007, in Protostars and Planets V, ed. B. Reipurth, D. Jewitt, & K. Keil, 261–276

Shu, F. H., Najita, J. R., Shang, H., & Li, Z.-Y. 2000, Protostars and Planets IV, 789

Siess, L., Dufour, E., & Forestini, M. 2000, *A&A*, 358, 593

Smith, M. D. 1995, *A&A*, 296, 789

Smith, M. D., Khanzadyan, T., & Davis, C. J. 2003, *MNRAS*, 339, 524

Smith, M. D. & Mac Low, M.-M. 1997, *A&A*, 326, 801

Solf, J. 1997, in IAU Symposium, Vol. 182, Herbig-Haro Flows and the Birth of Stars, ed. B. Reipurth & C. Bertout, 63–72

St-Onge, G. & Bastien, P. 2008, *ApJ*, 674, 1032

Sternberg, A. & Dalgarno, A. 1989, *ApJ*, 338, 197

Strom, K. M., Strom, S. E., Edwards, S., Cabrit, S., & Skrutskie, M. F. 1989, *AJ*, 97, 1451

Takami, M., Bailey, J., & Chrysostomou, A. 2003, *A&A*, 397, 675

Takami, M., Bailey, J., Gledhill, T. M., Chrysostomou, A., & Hough, J. H. 2001, *MNRAS*, 323, 177

Takami, M., Beck, T. L., Pyo, T.-S., McGregor, P., & Davis, C. 2007, *ApJ*, 670, L33

Takami, M., Chrysostomou, A., Ray, T. P., et al. 2004, *A&A*, 416, 213

Taylor, S. D. & Raga, A. C. 1995, *Ap&SS*, 233, 139

Valenti, J. A., Basri, G., & Johns, C. M. 1993, *AJ*, 106, 2024

Valenti, J. A. & Johns-Krull, C. M. 2004, *Ap&SS*, 292, 619

Whelan, E. T., Ray, T. P., & Bacciotti, F. 2009, *ApJ*, 691, L106

Whelan, E. T., Ray, T. P., Bacciotti, F., et al. 2005, *Nature*, 435, 652

Whelan, E. T., Ray, T. P., & Davis, C. J. 2004, *A&A*, 417, 247

Whelan, E. T., Ray, T. P., Randich, S., et al. 2007, *ApJ*, 659, L45

White, R. J. & Hillenbrand, L. A. 2004, *ApJ*, 616, 998

Woitas, J., Bacciotti, F., Ray, T. P., et al. 2005, *A&A*, 432, 149

Woitas, J., Ray, T. P., Bacciotti, F., Davis, C. J., & Eislöffel, J. 2002, *ApJ*, 580, 336